Conductive ferroelectric domain walls in PZT for neuromorphic applications

THÈSE No (XXXX)

PRÉSENTÉE
À LA FACULTÉ DES SCIENCES ET TECHNIQUES DE L'INGÉNIEUR
LABORATOIRE DES DISPOSITIFS NANOÈLECTRONIQUES
PROGRAMME DOCTORAL EN MICROSYSTÈMES ET MICROÉLECTRONIQUE

ÉCOLE POLYTECHNIQUE FÉDÉRALE DE LAUSANNE

POUR L'OBTENTION DU GRADE DE DOCTEUR EN SCIENCES

PAR

Felix Risch

acceptée sur proposition du jury:

Prof. Guillermo Villanueva, président du jury
Dr. Igor Stolichnov, directeur de thèse
Prof. Beatriz Noheda, rapporteur
Prof. Paul Muralt, rapporteur
Prof. Marty Gregg, rapporteur

Lausanne, Suisse, 2024

Acknowledgements

-

Bern, – – 2024 Felix Risch

Abstract

Over the last decades, the digital revolution has continuously increased the demand for more computational power. However, with the exponential rise of artificial intelligence applications in virtually every aspect of today's life, these additional demands can not be met by relying on the already decreasing Moore's law scaling of classical transistor technology. Moreover, the standard von Neumann architecture for information processing presents a bottleneck for AI-driven neural network algorithms in terms of energy efficiency and computation speed. To overcome these limitations, novel computation schemes are being explored to meet the needs of the rising AI industry by transferring brain-inspired algorithm concepts into direct hardware implementations. Such concepts, often referred to as neuromorphic computing, not only demand a new bottom-up architecture design but also advanced memory and information processing devices. Promising candidates for novel in-memory elements are memristors, which resistance is based on previous signals, functioning similarly to synapses in the human brain. Implementing such plastic, history-dependent properties into single nanoelectronic elements is a promising approach to address the need for advanced functionalities. One pathway includes the integration of new material systems like ferroelectric or phase change materials offering fundamentally new properties at the nanoscale.

This thesis explores the unique potential of ferroelectric domain walls for enabling advanced functionalities and developing novel memristive devices. By investigating their distinctive properties and incorporating them into innovative device structures, this work aims to advance the field of domain-wall nanoelectronics and the understanding of domain wall conductivity. In this thesis, the properties of conductive domain walls in archetypical ferroelectric $Pb(Zr,Ti)O_3$ thin films are studied with the goal of exploiting the conductive domain wall-channels for devices with memristive functionalities. Detailed studies on the growth conditions of highly tetragonal PZT films on $DyScO_3$ substrates were carried out, leading to reliable methods for creating PZT films with both pristine and artificially created conductive domain walls. Within the thesis, the first observations of highly conductive normally neutral 180° domain walls are reported. A combination of studies, including high-resolution AFM-based techniques such as PFM and cAFM, temperature dependent measurements and cryogenic current transport experiments together with phase-field simulations as well as STEM-cross section analysis, revealed the complex and distorted structure of the thought-to-be straight 180° domain walls. The explored intrinsic conduction mechanism is facilitated by charged domain interfaces created through the interaction of the ferroelectric and ferroelastic domain boundaries. The integration of graphene electrodes allowed the stabilization of multi-domain states in the fabricated Gr/PZT/SRO capacitors enabling the confinement of the highly conductive domain walls inside the device area. Memristive functionalities are achieved by gradual altering of the created mixed-domain states through electrical stimuli. A different approach to control and stabilize domain walls for device applications is demonstrated by the introduction of high-resistive platinum electrodes. The finite resistivity of the electrodes enabled a controlled switching of individual domains and the precise positioning of the 180°-domain walls. The combination of these techniques resulted in fully symmetric and linear memristive properties and the development of the first proximity-sensitive domain wall memristor.

The outcomes of this thesis highlight the potential for the strain mediated stabilization of charged domain walls and proposes new device concepts relying on an advanced control over the domain wall position. By combining novel materials and device concepts the presented results provide a foundation for further advancements in the field of domain wall-nanoelectronics and contribute to a deeper understanding of the underlying origin of domain wall conductivity.

Keywords: ferroelectric materials, neuromorphic computing, conductive domain walls, memristors, two-dimensional (2D) materials, lead zirconium titanate (PZT), atomic force microscopy (AFM)

Zusammenfassung

In den letzten Jahrzehnten hat die digitale Revolution die Nachfrage nach mehr Rechenleistung kontinuierlich erhöht. Mit dem exponentiellen Anstieg von Anwendungen der künstlichen Intelligenz in nahezu allen Bereichen des heutigen Lebens können diese zusätzlichen Anforderungen jedoch nicht durch das bereits abnehmende Moore'sche Gesetz der klassischen Transistortechnologie erfüllt werden. Darüber hinaus stellt die Standard-von-Neumann-Architektur für die Informationsverarbeitung einen Engpass für KI-gesteuerte neuronale Netzalgorithmen in Bezug auf Energieeffizienz und Rechengeschwindigkeit dar. Um diese Einschränkungen zu überwinden, werden neuartige Berechnungsschemata erforscht, um die Bedürfnisse der wachsenden KI-Industrie zu erfüllen, indem gehirninspirierte Algorithmen direkt in Hardware implementiert werden. Solche Konzepte, oft als neuromorphes Rechnen bezeichnet, erfordern nicht nur ein neues Bottom-up-Architekturdesign, sondern auch fortschrittliche Speicher- und Informationsverarbeitungsgeräte. Vielversprechende Kandidaten für neuartige In-Memory-Elemente sind Memristoren, deren Widerstand auf vorherigen Signalen basiert und ähnlich wie Synapsen im menschlichen Gehirn funktionieren. Die Implementierung solcher plastischen, geschichtsbasierten Eigenschaften in einzelne nanoelektronische Elemente ist ein vielversprechender Ansatz, um den Bedarf an fortschrittlichen Funktionalitäten zu decken. Ein Weg beinhaltet die Integration neuer Materialsysteme wie ferroelektrische oder Phasenwechselmaterialien, die grundlegende neue Eigenschaften im Nanobereich bieten.

Diese Arbeit untersucht das einzigartige Potenzial von ferroelektrischen Domänenwänden zur Ermöglichung fortschrittlicher Funktionalitäten und zur Entwicklung neuartiger memristiver Geräte. Durch die Untersuchung ihrer besonderen Eigenschaften und deren Integration in innovative Gerätestrukturen zielt diese Arbeit darauf ab, das Feld der Domänenwand-Nanoelektronik und das Verständnis der Leitfähigkeit von Domänenwänden voranzutreiben.

In dieser Arbeit werden die Eigenschaften leitfähiger Domänenwände in archetypischen ferroelektrischen $Pb(Zr,Ti)O_3$-Dünnschichten untersucht, um die leitfähigen Domänenwandkanäle für Geräte mit memristiven Funktionalitäten zu nutzen. Es wurden detaillierte Studien zu den Wachstumsbedingungen hoch tetragonaler PZT-Schichten auf $DyScO_3$-Substraten durchgeführt, die zu zuverlässigen Methoden zur Erstellung von PZT-Schichten mit sowohl ursprünglichen als auch künstlich erzeugten leitfähigen Domänenwänden führten. Innerhalb der Dissertation werden die ersten Beobachtungen hoch leitfähiger normalerweise neutraler 180°-Domänenwände berichtet. Eine Kombination von Studien, einschließlich hochauflösender AFM-basierter Techniken wie PFM und cAFM, temperaturabhängigen Messungen und kryogenen Stromtransportexperimenten zusammen mit Phasenfeldsimulationen sowie STEM-Querschnittsanalysen, enthüllte die komplexe und verzerrte Struktur der vermeintlich geraden 180°-Domänenwände. Der untersuchte intrinsische Leitfähigkeitsmechanismus wird durch geladene Domänengrenzflächen erleichtert, die durch die Wechselwirkung der ferroelektrischen und ferroelastischen Domänengrenzen entstehen.

Die Integration von Graphenelektroden ermöglichte die Stabilisierung von Multi-Domänen-Zuständen in den hergestellten Gr/PZT/SRO-Kondensatoren und ermöglichte die Eindämmung der hoch leitfähigen Domänenwände innerhalb des Gerätebereichs. Memristive Funktionalitäten werden durch allmähliche Veränderung der erzeugten gemischten Domänenzustände durch elektrische Reize erreicht.

Ein anderer Ansatz zur Kontrolle und Stabilisierung von Domänenwänden für Anwendungen wird durch die Einführung hochresistiver Platinelektroden demonstriert. Der endliche Widerstand der Elektroden ermöglichte ein kontrolliertes Schalten einzelner Domänen und die präzise Positionierung der 180°-Domänenwände. Die Kombination dieser Techniken führte zu vollständig symmetrischen und linearen memristiven Eigenschaften und der Entwicklung des ersten proximitätssensitiven Domänenwand-Memristors.

Die Ergebnisse dieser Arbeit heben das Potenzial der Stabilisierung geladener Domänenwände hervor und schlagen neue Anwendungskonzepte vor, die auf einer fortschrittlichen Kontrolle über die Position der Domänenwand basieren. Durch die Kombination neuer Materialien und Konzepte bieten die hier präsentierten Ergebnisse eine Grundlage für weitere Fortschritte im Bereich der Domänenwand-Nanoelektronik und tragen zu einem tieferen Verständnis des zugrunde liegenden Ursprungs der Leitfähigkeit von Domänenwänden bei.

-

Stichwörter: ferroelektrische Materialien, neuromorphes Rechnen, leitfähige Domänenwände, Memristoren, zweidimensionale (2D) Materialien, Blei-Zirkonium-Titanat, Rasterkraftmikroskopie

Contents

List of Figures

Acronyms

1D	One Dimensional
2D	Two Dimensional
3D	Three Dimensional
AFM	Atomic force microscopy
Au	Gold
BFO	Bismuth ferrite
cAFM	Conductive atomic force microscopy
Cr	Chromium
DC	Direct Current
DSO	Dysposium scandate
DW	Domain wall
e.g.	exempli gratia
eBeam	Electron beam
EELS	Electron energy loss spectroscopy
FE	Ferroelectric
FeFET	Ferroelectric field-effect transistor
Gr	Graphene
H-H	Head to Head
ICT	Information and communication technologies
IoT	Internet of Things
LNO	Lithium niobate
LTD	Long term depression

LTP	Long term potentiation
N_2	Nitrogen
O_2	Oxygen
PFM	Piezoelectric force microscopy
PLD	Pulsed laser deposition
PZT	Lead zirconium titanate
RT	Room temperature
Si	Silicon
SRO	Strontium ruthenate
STDP	Spike timing-dependent plasticity
STEM	Scanning transmission electron micrsoscope
T-T	Tail to Tail

1 Introduction

Starting from the middle of the last century, the invention of the computer and the following efforts to create artificial human intelligence have relentlessly propelled the integration of technology into every facet of our life, dramatically transforming the landscape of communication, productivity, and scientific discovery. However, as the adoption of artificial intelligence continues to deepen across all sectors, traditional computing architectures are being pushed to their limits. The von Neumann architecture, which has long been the gold standard for data processing, faces significant challenges in terms of energy efficiency and computational speed, particularly when tasked with the ever increasing size of the neural network models.
As technology evolves to accommodate the expanding complexity and volume of data, the limitations of conventional computational systems have become increasingly apparent. These systems, designed with separate memory and processing units, are inefficient for the tasks demanded by modern AI applications, leading to excessive energy use and slower processing speeds. This inefficiency is exacerbated by the exponential growth of interconnected devices, the Internet of Things (IoT), the scaling limit of classical transistor technology and emerging demands of edge computing, which require more sophisticated and energy-efficient computing solutions to manage the vast networks of data in real-time.
To address these challenges, a paradigm shift in computing architecture is essential. Inspired by the biological processes of the human brain, neuromorphic computing emerged as a fundamentally novel approach. This new field seeks to overcome the boundaries of traditional computing by developing systems that emulate neural processes and integrate brain-like functionalities like in-memory computations to increase the energy efficiency. To enable these advanced functionalities for single nanosized artificial neuron and synapse elements, new materials and technologies need to be studied and integrated.

This thesis focuses on the development of such devices with brain-like functionalities for neuromorphic applications by studying ferroelectric materials. Within the ferroelectric material, emphasis is put on the inherently nanometer size two-dimensional boundaries of ferroelectric domains, the domain walls, which hold promise to be implemented as reconfigurable elements with memristive functionalities.

1.1 The need for emerging computational approaches and materials

The digital revolution has fundamentally transformed how people access, sort, and share information since the middle of the last century after the invention of the transistor in 1947 [1] and the following realization of the first transistor based computer (TRADIC) in 1954 [2]. The scaling of the still young semiconductor industry was predicted by Gordon Moore in 1965. "Moore's Law" states that the number of transistors within an integrated circuit would double every two years [3], a trend which remained valid for decades and only recently started to slow down [4] (see Fig. 1.1). The increased power consumption, heat dissipation issues, and the approaching atomic scale at which quantum effects begin to interfere with traditional transistor operation present fundamental limits for continuous classical scaling of the complementary metal-oxide-semiconductor (CMOS) technology [5].

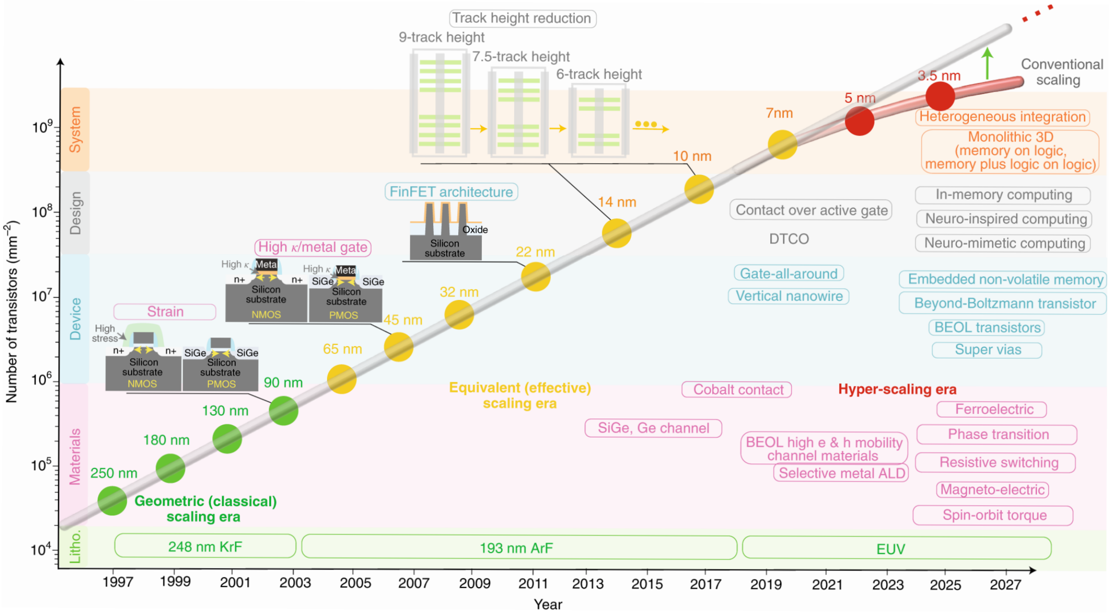

Figure 1.1: *The evolution of transistor scaling can be divided into three eras: geometric scaling, equivalent scaling, and hyper-scaling. Geometric scaling involved scaling various aspects of the transistor such as the channel and junction doping concentration, physical dimensions of the channel, gate oxide, and drain-source regions. Equivalent scaling introduced innovative materials such as high-k dielectrics, strained channels, and 3D structures for the transistor. To push the limits further and enter the hyper-scaling era, innovations in materials, co-integrating both logic and memory functions in one device, and heterogeneous integration technologies will be necessary. Adapted from [4].*

Besides the advancements of the semiconductor industry, other key inventions like the "world wide web" at CERN in 1989 [6] resulted in an unprecedented global connectivity. While less than 1% of the world population were using the internet in 1995 [7], due to the fast growing connectivity of smart objects the total number of Internet of Things (IoT) devices already surpassed the 10 billion mark [8] (Fig. 1.2) and is expected to reach more than 50 billion by 2025

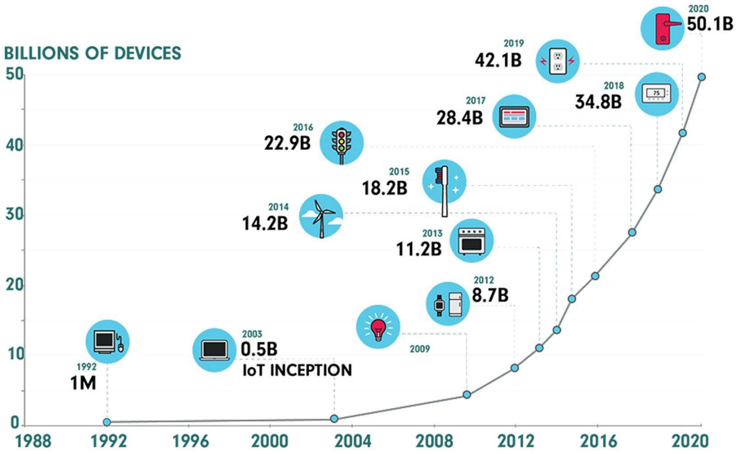

Figure 1.2: *Growth of the total number of IoT devices during the last decades. Adapted from [12].*

[9]. Together with the increase of smart connected devices like wearables, sensors, actuators or smartphones which need to store transmit and process information, an exponential increase in data creation and traffic is seen. Current data handling easily exceeds 1 zettabyte (10^{21} bytes, ZB) [10], a trend which needs to be adequately addressed to avoid an unsustainable explosion in energy consumption. Predictions of the energy consumption of the information and communication technology (ICT) sector are as high as 20% of the worlds total energy by 2030 [11].

With the rise of the information era, vastly available new data and increasing computation performance, another field quickly established itself as one of the dominant technologies of the century. Artificial intelligence (AI) algorithms and associated applications have expanded in nearly every aspect of life and are getting integrated into newly evolving technologies, from the education sector to producing music, art or design, medical applications and early-stage disease prediction, autonomous drive and intelligent chat bots as well as speech or image recognition [13, 14, 15, 16, 17, 18]. Hugely driven by the wide success of advanced large language models (LLMs), which were one of the first (publicly) available general-purpose text-generation programs, AI-programs are quickly maturing and heavily increasing their size [19]. Larger and larger models are developed to enhance the performance by an incredible rate, doubling their computation demand every 3.4 months, easily surpassing the decreasing scaling of Moore's Law [20] (compare Fig. 1.3). Additionally, due to the inefficient implementation of the underlying neural network structure of modern AI-algorithms the energy consumption needed to train the models exacerbate the increasing energy demand and costs further. Training of Open AI's GPT-3 alone is estimated to require nearly 5 million USD, over 1000 MWh of total energy and a duration of over 10 days [21, 20].

The inefficient use of energy and speed limitation by AI-algorithms stems from their implementation on classical computing platform. Despite their astonishing performance, fundamental

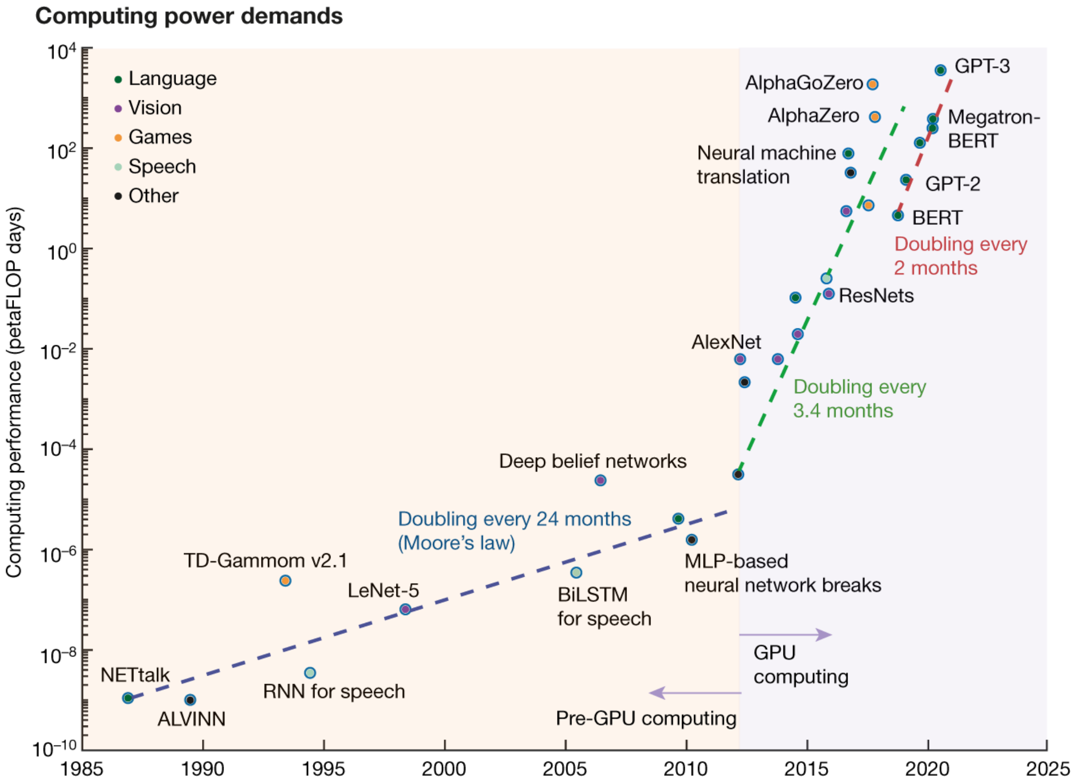

Figure 1.3: *The increase in computing power demands over the past four decades expressed in petaFLOPS days. Until 2012, computing power demand doubled every 24 months; recently this has shortened to approximately every 2 months. The colour legend indicates different application domains. Adapted from [20].*

factors impede the achievement of efficient computations. The most important problem, known as the von-Neumann bottleneck, refers to the separation of computation and memory in classical computer architectures [22]. The underlying AI-models however are implemented in highly connected neural network structures, which require a vast amount of calculations and continuous weight updates of the interconnected layers and nodes of the network. For comparison, inside the brain 10^{11} neurons are innterconnected with 10^{15} synapses, while the GPT-3 model does work with around two times as many parameters ($17.5 \cdot 10^{10}$) as there are neurons in the brain, the complex interconnection provided by the trillions of synapses is still unmatched and will push research for more complex AI-models in the future [23].

To address the challenges of the increasing demand in computation power by advancing AI-models together with the problematic energy consumption based on the current implementation of the algorithms, new ways of computing for AI are needed. To fuel novel breakthroughs and AI-applications, especially for edge-computing and real-time processing for which cloud-based services are unavailable, novel highly efficient computation platforms are necessary.

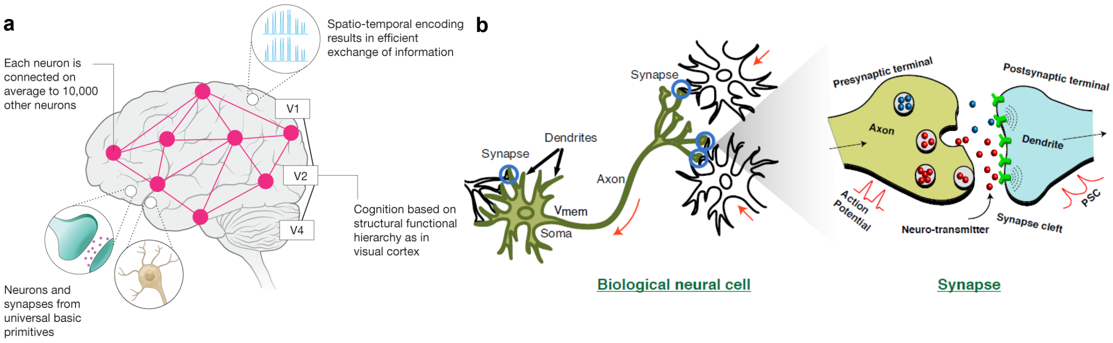

Figure 1.4: a) Schematic of the organizational principles of the brain. The intertwined network of neurons and synapses with temporal spike processing enables rapid and efficient flow of information between different areas. b) Schematic of a basic biological neural cell and synapse. Neurons and synapses are the fundamental elements of a neural network, and the transmission of action potentials through synapses plays a crucial role in neural communication. Adapted from [24, 25].

Neuromorphic computing concepts, which try to mimic the function of the human brain are one promising trend, which is heavily explored at the moment. The human brain excels at ulta-high energy efficiency. For example: with an energy budget of 1 MWh, which is a fraction of the needed energy for a state of the art AI-model, the brain could operate for 6 years [23] with an estimated average energy consumption of 20 W. The brain's remarkable capability is thought to be attributed to three foundational observations from neuroscience: vast connectivity, structural and functional organizational hierarchy, and time-dependent neuronal and synaptic functionality. Neurons are the computational primitive elements of the brain that exchange or transfer information through discrete action potentials or 'spikes,' and synapses are the storage elements underlying memory and learning (see Fig. 1.4).

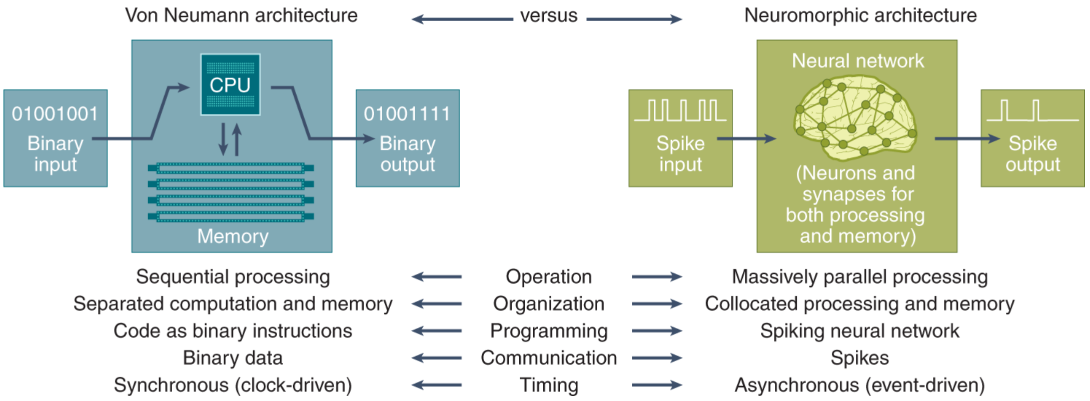

Figure 1.5: Comparison of the von Neumann and neuromorphic architectures, showing their fundamental differences and structures. Adapted from [26].

The term neuromorphic computing was first conceptualized by Carver Mead in the late 1980s [27], referring to the implementations of artificial neurons and synapses, with functionalities which are inspired by the human brain [26] and arranged in neural network circuits. Unlike classical von Neumann computers, which have separate CPUs and memory units, neuromorphic computers integrate processing and memory within neurons and synapses, called in-memory computing. Neuromorphic systems receive spikes as input, where the timing, amplitude, and shape of the spikes encode information, in contrast with the binary values used in traditional computers. They are inherently scalable, stochastic, event driven and offer the possibility of highly parallel operation (compare Fig. 1.5). These properties allow them to calculate with increased energy efficiency and allow for direct implementation of the neural network structured AI-algorithms. Several physical realizations of spike-dependent neuromorphic systems have been developed in academia such as SpiNNaker [28] and BrainScaleS [29] or from industry such as IBM's TrueNorth [30] and Intel's Loihi [31]. These systems are used to run large scale neuroscience simulations, solving image or speech recognition tasks or to advance existing spike-time dependent algorithms.

While the before mentioned neuromorphic systems could showcase the potential of spiking neural networks, their implementations to date are based on classical CMOS-technology with their associated problems of limited energy efficiency, large space requirements and limited interconnectivity [32].

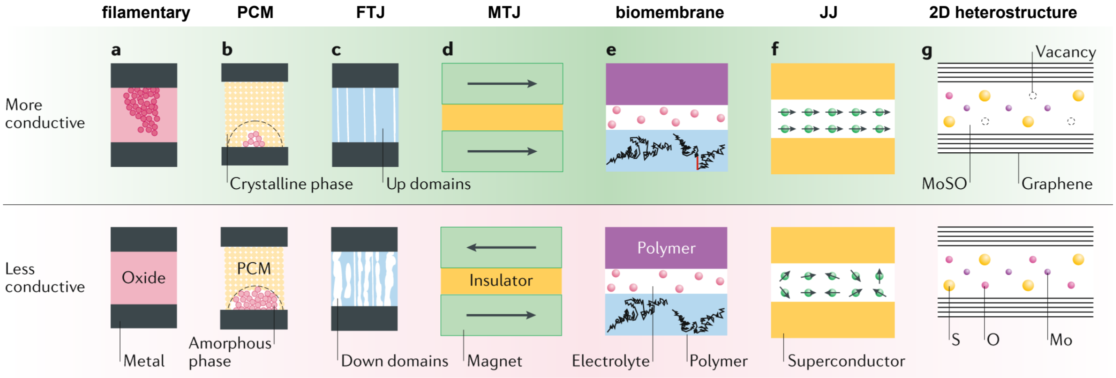

Figure 1.6: *Novel hardware implementation of synaptic functionalities in different material systems. The top row depicts the high-conductivity synaptic states, and the bottom row depicts the low-conductivity synaptic states. a) A filamentary device (oxide or conductive bridge). b) A chalcogenide-based phase-change memory (PCM). c) A ferroelectric tunnel junction (FTJ). d) A magnetic tunnel junction (MTJ). e) An organic electrochemical device. f) A Josephson junction (JJ) with a magnetic barrier. g) A graphene/MoSO/graphene van der Waals heterostructure. Adapted from [23].*

Recently, research has shifted to focus on direct AI-hardware implementation. Developing advanced materials and material properties for novel fundamental devices would allow for a full analog-computing neuromorphic hardware [33, 34, 35]. Such hardware could address the energy-efficiency, scalability and computation in real-time due to a better level of mimicking and more direct implementation of the brain-functionalities such as spike-time dependent plasticity (STDP) learning, neuronal integrate and fire model or direct in-memory weight update.

Different materials and their associated functionalities and working principles are currently investigated such as phase-change materials, ferroelectric materials, filamentary materials, 2D materials or chanel-doped biomembranes [36, 37, 38, 39] (see Fig. 1.6). One promising approach within these different material systems is to develop devices with memristive functionalities, inspired from the fundamental circuit element, the memristor, proposed by Chua in 1971 [40]. Memristive elements, broadly defined as resistive switchable elements based on their history of applied charge, would allow for in-memory computing as they co integrate memory and resistor [41, 42] (compare Fig. 1.7). Such properties are essential for realizing artificial synapses. As research in this field is ongoing, it is yet to be seen if one of the material classes will prevail or if several systems will establish themselves with different advantages and disadvantages.

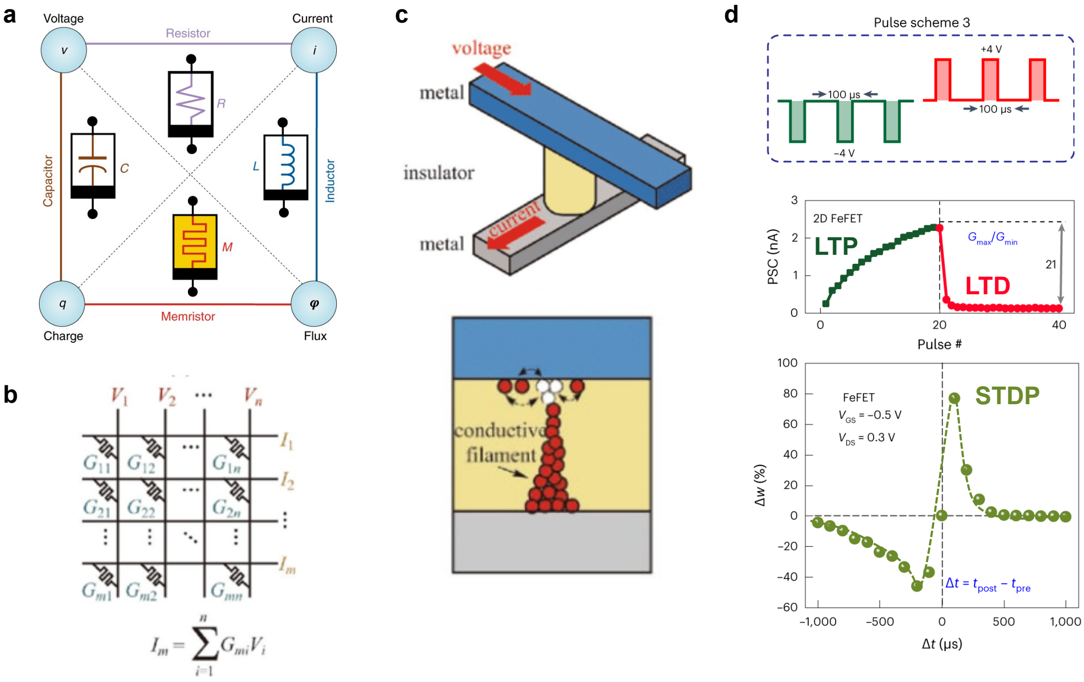

Figure 1.7: *a) Four fundamental passive circuit elements and their relationships. The memristor is defined by a relationship between flux (ϕ) and charge (q). b) Schematics of the matrix–vector multiplication (MVM) operation mapping into a memristor crossbar array by exploiting Ohm's law and Kirchhoff's law. c) Illustration of a memristor with a metal/insulator/metal sandwiched structure based on the conductance tuning mechanisms of a conductive-filament type device. d) Long-term potentiation (LTP) and long-term depression (LTD) curves for a FeFET synaptic device under a pulse number modulation scheme together with an experimental STDP curve for the same device. Adapted from [43, 25].*

Among the heavily studied and interesting concepts, this thesis focus on ferroelectric materials, to be implemented in novel elements for neuromorphic hardware. Especially, one functional class within the ferroelectric system will be studied, the two dimensional boundary between ferroelectric domains, the domain wall. As it will be explore later, ferroelectric domain walls have great potential to function as highly reconfigurable channels with memristive properties for neuromorphic devices and circuits.

1.2 Ferroelectric domains and domain walls

Ferroelectric materials are well known and used in today's semiconductor industry as actuator and sensors [44, 45], in memories [46, 47] or supercapacitors [48, 49] and recently investigated also for novel neuromorphic devices [25, 33]. Discovered in 1921 [50] and named after the analogues ferromagnetic materials, ferroelectricity is a material property characterized by a spontaneous electric polarization that can be reversed by an external electric field [51]. As a subclass of piezoelectric materials (characterized by the appearance of an electric field under mechanical stress), ferroelectric materials need to posses a non-centrosymmetric crystal structure, which allows for a stable formation of an electric dipole moment. Under the application of an electric field, this dipole can reversibly switch orientations between at least two energetically-equal ground states. The stable, but reversible electrical polarization is characterized by a hysteretic behaviour in the polarization vs. electric field (P-E) diagram as seen in Figure 1.8 b).

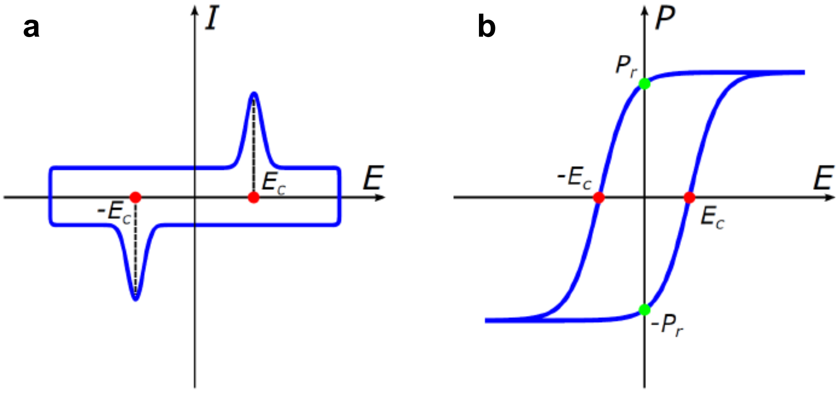

Figure 1.8: *a) Displacement current vs. electric field b) Hhysteresis P-E loop. Adapted from [52].*

During switching, the change of the polarization direction is accompanied by a sharp current spike, which results from the change of bound charges at the surface, compare Fig. 1.8 a). The electric field needed to switch the polarization is denoted as the coercive field (E_c). Ferroelectric materials posses a so called Curie-Temperature (T_c) above which they transition from the ferroelectric phase to the paraelectric phase, illustrated in Figure 1.9. More information about the fundamentals of ferroelectrics can be found elsewhere, e.g. in ref [53].

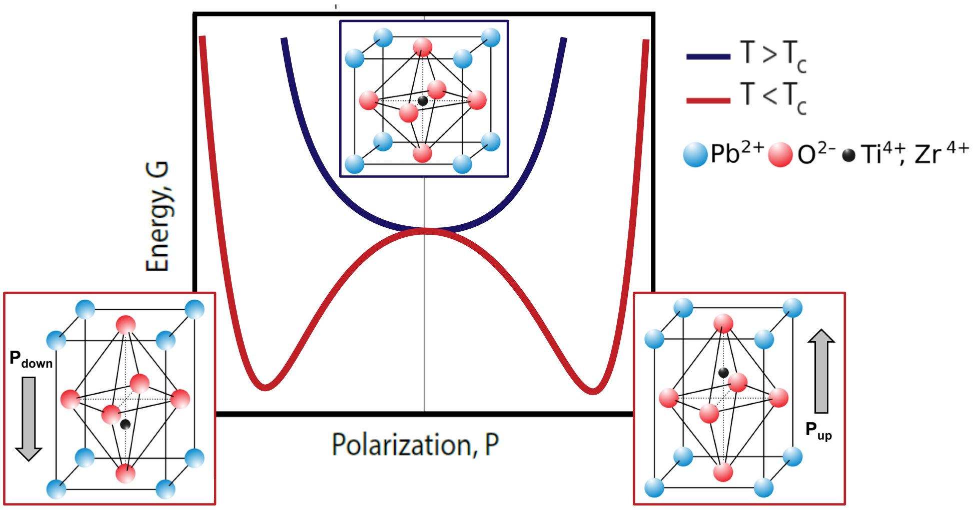

Figure 1.9: *Schematic of the energy landscape in the ferroelectric phase ($T < T_c$) and in the paraelectric phase ($T > T_c$). The small inserts represent the crystal lattice structure of PZT for the paraelectric phase and for the two polarization states of the ferroelectric phase. Adapted from [52, 54].*

To date the most used ferroelectric materials are ceramics processed as thin films [55]. As inorganic compounds, they offer good chemical stability, high or partial crystalline structure and insulating properties. Within the wide class of ceramics, perovskite materials are of particular interest, e.g. due to their high dielectric constant [56]. Their crystal structure is described as ABX_3, with A and B usually being a bigger and smaller cation respectively and X commonly occupied by oxygen. Some of the most prominent perovskites, which also posses ferroelectric properties include $BaTiO_3$ or $Pb(Zr,Ti)O_3$ [51, 57]. Another non-perovskite ferroelectric, which has found a lot of interest in industry is HfO_2 due to a CMOS compatible fabrication process [58].

Regions within the ferroelectric material, where the electric polarization is uniformly aligned are called domains. The formation of these domains is a result of the material's effort to minimize its overall energy, balancing the electrostatic energy, elastic energy, and domain wall energy [59]. The configuration and size of ferroelectric domains are influenced by the crystal structure, boundary conditions, and processing methods such as thin film deposition versus bulk crystal growth techniques [60]. While an amorphous material is characterized by a lack of long range order of the atoms, a single crystal or mono crystalline structure reflects a system in which the whole sample possesses a continuous identical crystal structure with high symmetry. In between the two extremes, the poly crystalline structure is made from areas of single crystalline regions called grains. The crystal orientation between grains can be randomly oriented. Amorphous materials typically are not ferroelectrics due to the missing order of the crystal structure, while poly crystalline and single crystalline materials can show ferroelectric behaviour. In general, poly crystalline films can be fabricated faster and cheaper and with shorter process time compared to single crystal growth which necessitates highly optimized growth parameters and ideal conditions [61]. However single crystal samples for ferroelectric applications are highly desirable due to the confinement of the polarization direction by the continuous crystal structure, a reduced defect density and generally enhanced electrical and mechanical properties. Within the single crystals, especially thin film fabrication has emerged as an important technique to fabricate materials with well defined thicknesses, atomically flat surfaces and controllable material properties. Deposition techniques such as pulsed laser deposition (PLD), molecular beam epitaxy (MBE) or radio-frequency magnetron sputtering allow for an epitaxial layer growth with which highly oriented single crystalline thin films can be produced [62].

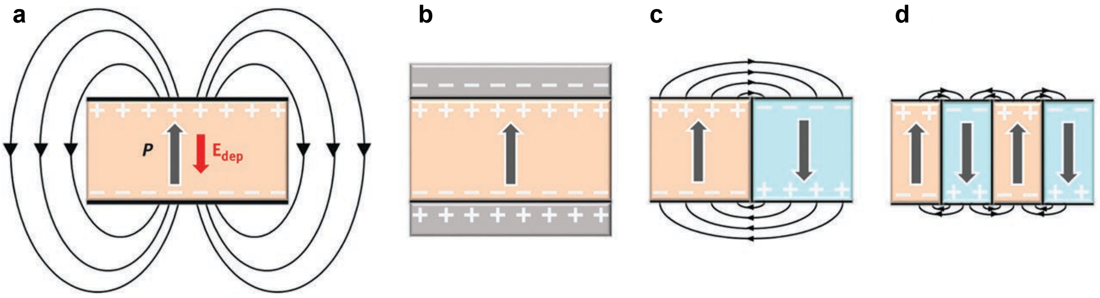

Figure 1.10: *Domain formation in ferroelectrics. Black field lines represent the electric stray field. (a A ferroelectric monodomain state. The grey arrow shows the polarization direction, P. The build-up of stray electric fields induces a field in the opposite direction, the depolarizing field,* E_{dep}*, indicated by the red arrow. (b) Complete screening of the ferroelectric polarization by surface charges. (c) A 180° domain wall leading to a smaller electric stray field that reduces the internal depolarizing field. (d) Representative multidomain state showing the much smaller electric stray fields. Adapted from [63].*

In ferroelectrics, the domain formation is accompanied by the appearance of bound charges, which introduce a so called depolarizing field (E_{dep}) with opposing direction of the spontaneous polarization [63], see Fig. 1.10 a). Since the accumulating bound charges counteract on the domain formation, one way to reduce them is to screen them by surface charges or with metallic electrodes in capacitor structures, see Fig. 1.10 b). Other mechanisms to mitigate the depolarizing field include the formation of poly domain states in which domains with alternating polarization directions are formed, effectively cancelling the effect on a macroscopic scale, see Fig. 1.10 c) and d). Different parameters can influence the available screening charges or the formation and strength of the depolarizing field. Temperature, oxygen pressure [64] or crystal-induced strain [65] will influence the final domain configuration as well as the inherent crystal structure of the ferroelectric material.

Another important aspect is the crystal structure of the ferroelectric material itself. Simple systems like the tetragonal $PbTiO_3$ (PTO) posses a tetragonal structure with spontaneous polarization along the c-axis. They are therefore switchable in the [001]-direction with two stable configurations. $BiFeO_3$ (BFO) however forms in the rhombohederal structure with its ferroelectric polarization along the [111]-direction, which results in a total of 8 different polarization directions and much more complex domain patterns, as seen in Figure 1.11.

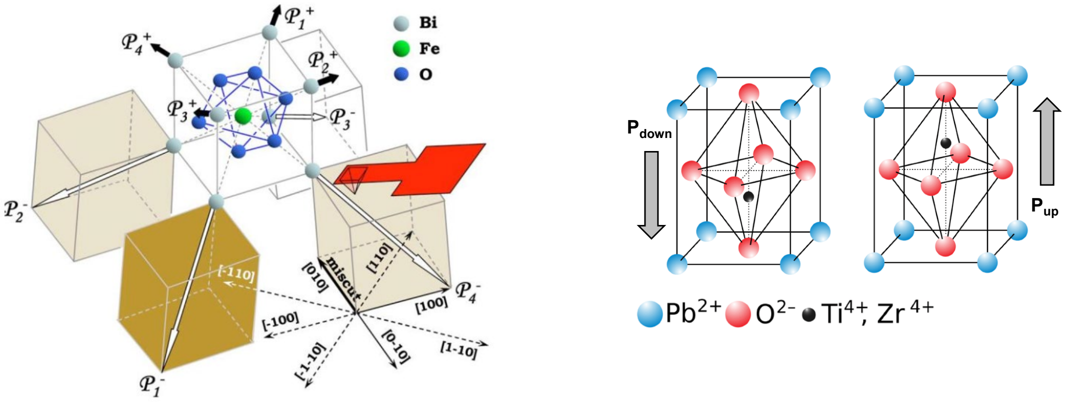

Figure 1.11: *Comparison of the rhombohedral BFO (left side) and the tetragonal PZT (right side) lattice structure with their ferroelectric polarization directions. Adapted from [54, 66].*

Especially in epitaxially grown thin films, induced strain effects from the substrate material further complicate the domain landscape as domain formations can get pinned or the formation of ferroelastic domains can be promoted. For the important material of this thesis, $Pb(Zr,Ti)O_3$ (PZT), the before mentioned effects as well as other processing parameters for film growth, domain and domain wall formation and tuning of their properties are discussed in more detail in Chapter 1.4.

While most applications in previous ferroelectric devices exploit the properties of the domains, their polarization direction, or the controlled switchability, recently the research focus has shifted to the domain boundaries. The two dimensional interfaces which separate domains of different polarization direction, known as domain walls, were long disregarded. Partially due to their intrinsic size, with widths between a unit cell and a few nanometers, only recently advanced functional characterization techniques with high enough resolution like atomic force microscopy (AFM) and transmission electron microscopy (TEM) allowed researches to study their structure and exploit the unique properties of these topological defects [67].

Interface physics is know to provide a wide range of interesting and novel functionalities like p-n junctions in semiconductors or the control of electronic transport at oxide interfaces [68, 69, 70]. Contrary to interface-enabled functionalities, which make use of the interaction region of two heterogeneous materials, as seen in the emergence of a 2D electron gas at the $LaAlO_3/SrTiO_3$ interface [71], domain walls represent interfaces within a homogeneous material.
Due to their intrinsic size advantage compared to the bulk domains, the possibility to control their position and presence by manipulation of the domain configuration with external stimuli and the experimental demonstration of unique intrinsic properties like enhanced conductivity [72], domain walls have become an independent research field. Devices in which

the functional element is represented by a 2D domain wall offer novel design concepts for nanoscale electronic building blocks or circuits, which give rise to the field of domain wall nanoelectronics [73, 74].

1.2.1 Conducting domain walls

One of the most interesting novel properties, which traces back to predictions from Vul et al. in 1973 [75], was first observed at domain walls in $BiFeO_3$ in 2009. Seidel et al. showed that 109° and 180° domain walls in the multiferroic system exhibited robust conductive traces [72] with orders of magnitude enhanced conductivity compared to the insulating bulk of the domains. With this discovery a new field was born and shortly after, conductive properties coupled to the existence of domain walls were found in a multitude of proper and improper ferroelectrics and in different kinds of domain walls. Some of the most prominent examples include $BaTiO_3$ [76] as well as $LiNbO_3$ single crystals [77, 78]. Thin film PZT [79, 80] and the before mentioned BFO-systems [81, 82, 83] as well as in improper ferroelectric single crystals like $ErMnO_3$ [84], $YMnO_3$ [85] and many others [86, 87, 88].

Domain walls can be classified depending on the the angle created between the two polarization directions ($\mathbf{P}_1$ and $\mathbf{P}_2$) of the adjacent domains with respect to the domain wall normal vector ($\mathbf{n}_{DW}$) [89]. In the case of neutral domain walls (nDW), the polarization directions are aligned side by side by 180° preserving the polarization continuity at the domain wall while charged domain walls (cDW) either face to or away from each other, giving rise to a polarization discontinuity and a formation of an electrostatic field. The electrostatic field creates bound charges σ_P, which can be calculated by:

$$\sigma_P = (\mathbf{P}_2 - \mathbf{P}_1) \cdot \mathbf{n}_{DW} \tag{1.1}$$

For neutral walls, the bound charges are $\sigma_P = 0$, while for charged walls a net bound charge arises $\sigma_P \neq 0$. Depending on the direction of the polarization, the formed cDW can be categorised into Head-to-Head (H-H) and Tail-to-Tail (T-T) DWs as seen in Figure 1.12 a) (neutral DWs are classified as Head-to-Tail or Tail-to-Head DWs). The creation of bound charges need to be screened with mobile charges (electrons, holes or mobile ions), so that the electrostatic energy of the DW is reduced and the DW is stabilized [73]. In general, due to the increased energy cost of charged domain walls, their presence needs to be further stabilized by other factors like strain induced boundary conditions [90].
Due to the high bound charges found at charged domain walls and a distortion of the band structure due to the local electric fields, and the therefore accumulated free carriers, in most cases, an enhanced conductivity can be observed at cDWs. While neutral DWs do not promote the accumulation of free charges by the creation of bound charges, they can still sometimes show a conductive response [79]. However the corresponding charge carriers accumulating at

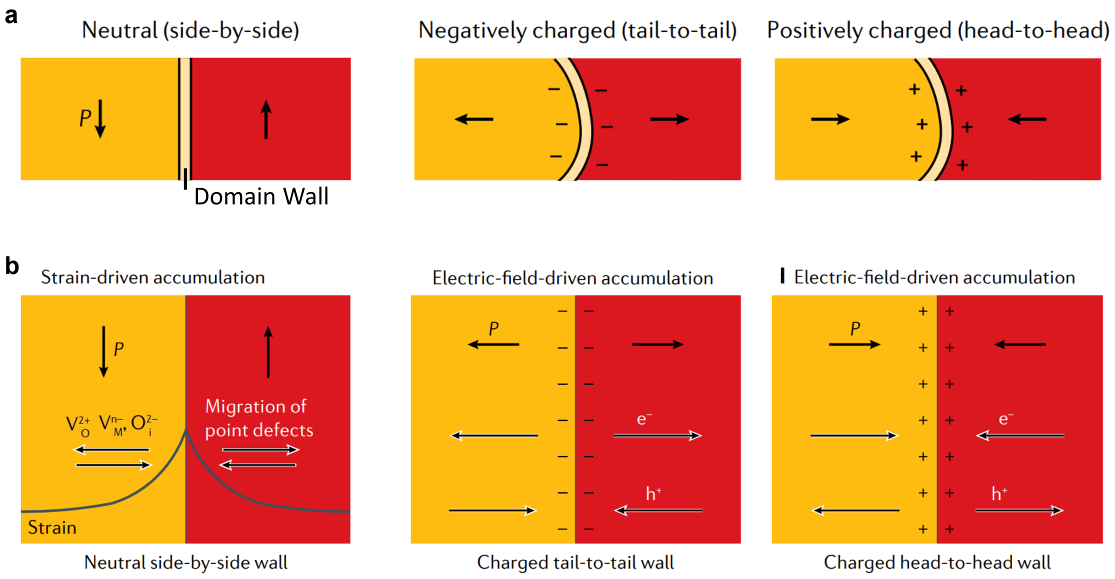

Figure 1.12: *Comparison of neutral and charged domain walls. a) Schematics of a neutral DW, a Tail-to-Tail DW and a Head-to-Head DW. b) Schematics of different types of charge accumulation depending on the type of domain wall. For neutral DWs a strain-driven accumulation takes place, while for charged DWs an electric-field causes the accumulation of either positive or negative charges. Adapted from [73].*

neutral walls originate from charged defects, mostly oxygen vacancies (V_O^{2+}), impurities or interstitial ions [67]. Point-defects are known to locally change the materials symmetry and since domain wall are regions in which the material symmetry breaks, these defects can get attracted by the DWs to compensate for the strain induced energies [91, 73]. The comparison for different types of accumulation at domain walls are shown in Figure 1.12 b) for the neutral and charged DWs.

Based on their underlying effect the conduction mechanisms can be classified into an extrinsic effect (for the neutral strain-driven) and intrinsic effect (for electrostatic field-driven). The influence of the extrinsic and intrinsic mechanism onto the band diagram promoting the conduction at the domain walls are shown in Figure 1.13. Defect-mediated accumulation at neutral walls lead to defect sites between the conduction and the valence band, while H-H or T-T DWs lead to a electric field induced local shift in the band structure. Moreover, high-resolution TEM mapping of the local polar displacements and domain orientations showed that in reality domain walls are often distorted or bent and are rarely perfectly straight at the nanoscale [92], which leads to a mixed-type effect of extrinsic and intrinsic conduction.
Other distinguishing factors between the defect assisted conduction and intrinsic electron or hole mediated conduction are the observation of persistent conductive footprints of erased domain walls for the case of extrinsic conduction [93]. Metallic-like or non-thermally activated conduction [94, 76, 95], which is in line with an intrinsic mechanism, could be measured by temperature dependent electrical measurements of DWs as well as in cryogenic experiments,

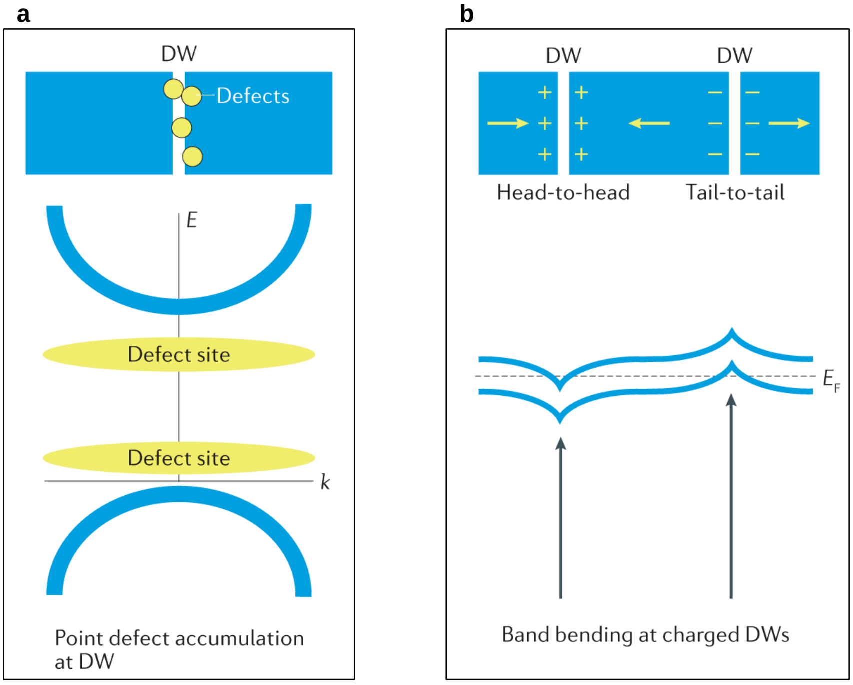

Figure 1.13: *Extrinsic and intrinsic effects on the band structure at the domain wall. a) Intra-bandgap defect states between the conduction band (top semicircle) and the valence band (bottom semicircle). Usually, intra-bandgap states are caused by defects. b) Shift of the band structure induced by local electric fields associated with local head-to-head (giving positive bound charges, +) and tail-to-tail (giving negative bound charges, -) configurations of the polarization. Adapted from [67].*

in which new conductive DWs are created and erased at 4K. Thermally activated effects could be measured for defect assisted extrinsic conduction transports governed by oxygen vacancies [79, 81, 96, 97]. Especially the role of oxygen vacancies has been studied in more detail. Since oxygen vacancies can easily be controlled during film growth by playing with the oxygen pressure, experimental studies revealed that chemical tuning of the V_O^{2+} density can lead to enhanced conduction at the DWs [97].

Other ways to control the conductivity of DWs have been studied by direct observations of the relation between charge state of the domain walls (which can be seen as the amount of bound charges) and conductivity. An ideal scenario to study differently charged DWs is presented for the improper hexagonal manganites systems [73]. Because the electrical polarisation is not the primary order parameter, the formation of ferroelectric domains encounter more flexible boundary conditions, which result in the spontaneous formation of a variety of different domain and charged DW structures normally unobserved for proper ferroelectrics.

In the hexagonal manganites, characteristic six-fold vortices form at the meeting point of gradually curved DWs. In Figure 1.14 a), a vortex plus the 6 differently oriented domains (3 colors plus black and white arrows for up and down) in a $YbMnO_3$ crystal can be seen together

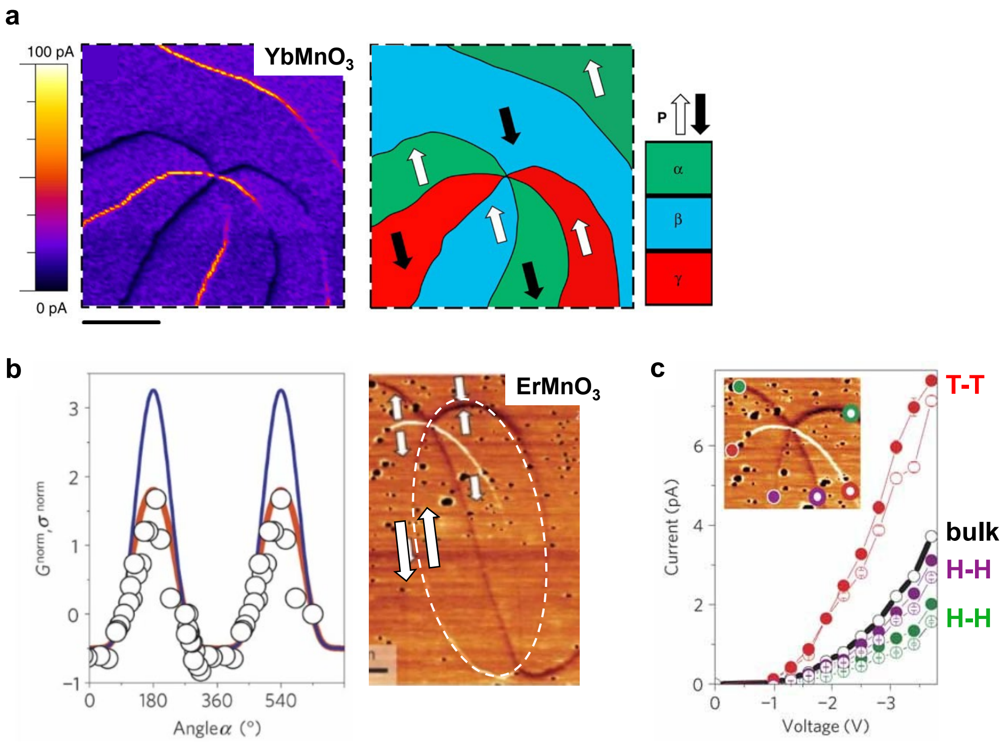

Figure 1.14: *Domain structure and conductive response of curved domain walls in the hexagonal manganites YbMnO$_3$ and ErMnO$_3$. a) cAFM image of a vortex showing the gradual change of conductance along the different DWs on the left side and an illustration of the different domain directions on the right side. b) Plot of the angular dependency of the conductivity of a DW in the ErMnO$_3$ crystal. c) IV curves for different DW configurations from the same area as in b). Adapted from [98, 84].*

with a conductive AFM (cAFM) image showing the gradual conductance change of the DWs [98]. In Figure 1.14 b) and c), a ErMnO$_3$ crystal is studied and the angular dependence of the DW conductance is shown as well as point IV curves for the H-H and T-T DWs compared to the bulk [84]. It is obvious that T-T DWs in these systems show an enhanced conductivity, which is gradually decreased for a lowering of the T-T angular state of the DW. Interestingly the H-H DWs showed an even lower conductance than the bulk, indicating a depletion region of free carriers.

These experiments not only highlight the gradual dependency of the DW conductivity with respect to the charge state but also experimentally prove the different kind of carrier accumulation (or absence) at different DW types. Pioneering work to determine the sign of carriers as well as measuring quantitative carrier densities have been carried out by exploiting the Hall-effect in AFM-based experiments [98, 99, 100] and were able to experimentally prove the expected p-type nature of T-T DWs with holes as the most likely carriers.

While in the manganites system differently curved DWs can be observed and studied, they remain fixed elements and the change of conductance is only observed by a local change of

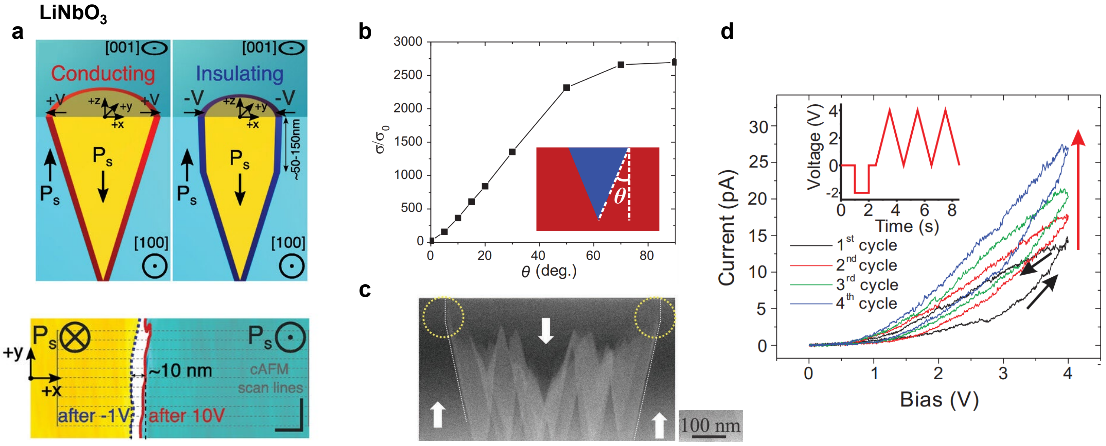

Figure 1.15: *Formation and effect of surface angle tilt of domain walls in LiNbO$_3$. a) Schematic of the conductive and insulating state of the cone shape polarization domain in the LNO crystal together with the resulting domain size change observable by AFM-imaging. b) Plot of the conductance change based on the change of the surface angle. c) TEM cross-section image of the cone shape domains. Yellow circle indicate the regions of the adjustable surface angle. d) IV curves with multiple pulses showing an increased in the readout current based on the amount of applied pulses. Adapted from [101, 102].*

position. In other systems such as LNO, a direct manipulation of the charge state of electrically written DWs was demonstrated, see Figure 1.15. Vertical domains in a capacitor structure exhibit a surface angle of the DWs with respect to the z-axis. To minimize its energy, the DW-angle tends to straighten up and reduces its charge state and conductivity. By applying short poling pulses, the angle can become inclined with H-H DW configurations and based on the amount of pulses the degree of the surface angle can be tuned. The change of the DW angle directly results in an conductive switching of the DWs with a gradual tunability as seen in Fig. 1.15 d).

Similar results are obtained for PZT systems in which a repeated resistive switching is observed for poled nanodomains based on an application of a pulse-probe waveform, tuning the local domain angle to induce the resistance change, see Figure 1.16 a)-c) [80]. The dynamic tuning of DW conductivity in BFO systems seen for the application of consecutive voltage pulses is believed to arise from a different mechanism. Slight domain distortions observed in high-resolution PFM images from before and after the tuning [83] (compare Figure 1.16 d) and e)) are believed to be at the origin of the tunable conductance.

Ongoing research also focuses on the intrinsic properties of the DW conductivity, which inherently is difficult to access due to the two-probe geometry inherent to the cAFM technique. In addition to the before mentioned Hall-effect measurements, carefully designed planar AFM-electrode measurements were performed to learn more about the intrinsic resistivity of the DW rather than the often dominating interface effects [103, 104]. Other experiments tried to fit different conduction models like Fowler-Nordheim Tunneling, Schottky-Emission or Hopping

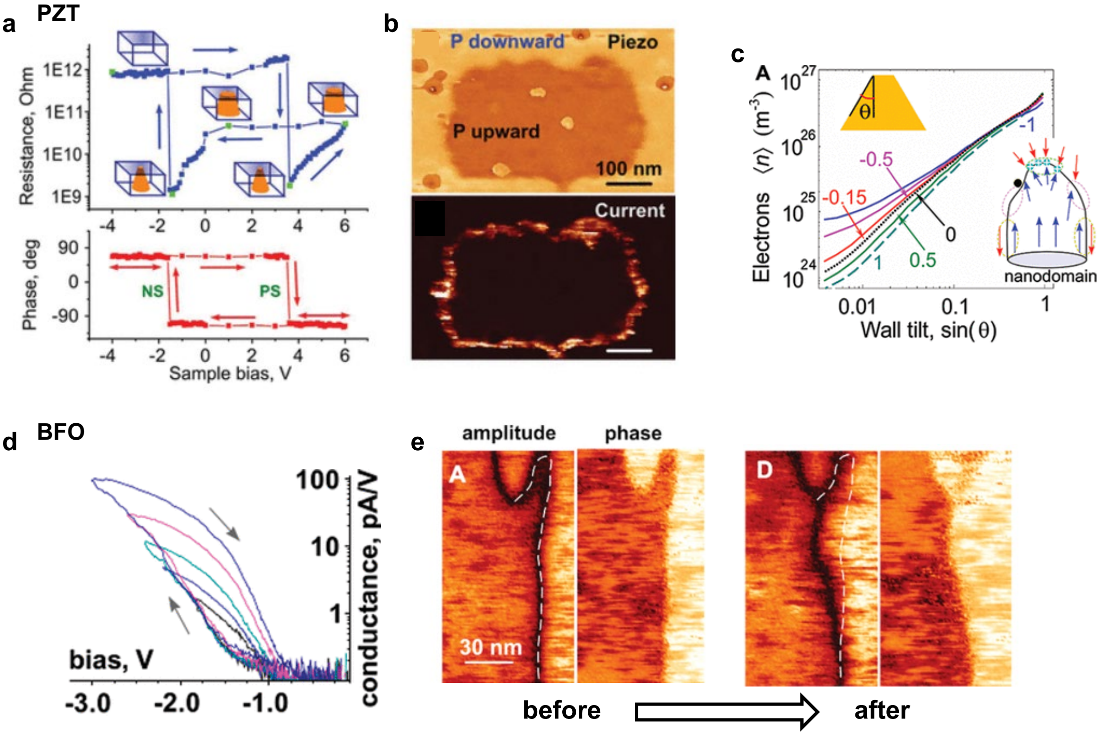

Figure 1.16: *Dynamic conductivity of DWs in PZT and BFO systems. a) Top: local resistance of a PZT film acquired using a pulse-probe waveform. Cartoon schematics show nanodomains of upward polarization orientation (orange) believed to be formed at various instances of the resistance curve (green points). Bottom: phase of local piezoresponse accompanying the resistance curve. b) Simultaneously acquired PFM and cAFM images. c) Dependence of the carrier concentration on the domain wall tilt. d) A series of hysteretic I-V curves obtained sequentially on the surface of BiFeO3 film. e) Evolution of the domain wall profile along the surface when it is subject to conductive measurements. Adapted from [80, 83].*

conduction to their experimental data to evaluate the dominant conduction mechanism for the DW-type. However, as the DWs are confined in nanoscale volumes and their conduction also heavily depend on their adjacent interface materials and boundaries, for most cases the conductive response and the observed resistive switching needs to be treated to arise from the whole DW-system including its interfaces.

1.2.2 Domain wall control

While it was shown in the previous chapter that a lot of research effort has been performed to entangle the different extrinsic and intrinsic conduction mechanisms and the role of point defects to better understand the physics of the conduction origin [67] and help to deterministically control properties at the domain wall for domain wall-based nanoelectronics, one other major persisting challenge is the reliable control over the domain wall dynamics. As most DW-based devices and prototypes to date use a degree of control over the creation/erasure and positioning/density of DWs for device applications it is important to have engineering solutions to hand which are applicable for the different material systems and device architectures. For device applications, which will be presented in detail in Chapter 1.3, not only the positional control of the DWs are important also stability concerns of charged DWs and tunability of the static conductivity, which have been discussed previously.

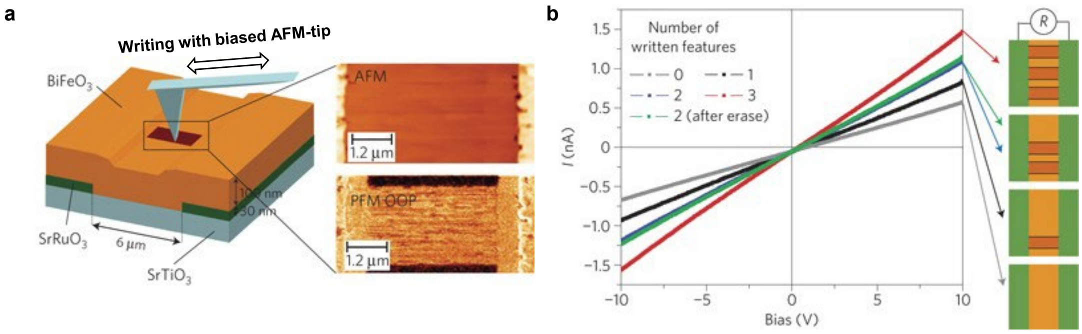

Figure 1.17: *Direct change of the resistive state of a device prototype by writing of DWs with a biased AFM-tip. a) Schematic of the poling procedure creating DWs which connect the left and right SRO bottom electrode. b) Iv curves for the different states depending on the number of written DWs. Adapted from [72].*

Since the DWs are created and positioned (mostly) through ferroelectric domain manipulation, electrical stimuli is an important knob for controlling the domain walls. While in principle other mechanisms like mechanical or magnetic stimuli can be used to control the ferroeelectric domains by the flexoelectric or ferromagnetic effect (for certain materials), they are rarely applied in device concepts. One way to change the ferroelectric domain configuration is by locally controlling the electric field. Probably the most simplest way of doing so is by writing domains with a biased AFM-tip. By doing so one can readily connect e.g. two planar electrodes with domain walls by partially switching the domains in the direction of the electrode. By creating more poled strips, a discrete number of domain walls can be written and connected to the device electrodes [72] as done in one of the first prototype concepts in BFO, see Figure 1.17. While this techniques allows a high degree of control over the nucleation area of the domains and the position of the DWs by choosing the area contacted by the biased tip, it is only useful for demonstration purposes as a moving tip presents a highly cumbersome approach to manipulate functional elements in a device.

If one removes moving parts another way to tailor the electric field is by shaping the electrode design. By doing so inhomogeneous electric fields are created with enhanced areas of the e-field which promote switching in these pre-designed locations compared to areas of lower electric fields. Some examples are shown in Figure 1.18 a, in which a nanometer sized contact is put in front of a larger electrode to create non straight DWs connecting the planar electrodes [105] and in 1.18 b, in which "spike-like" modifications at the electrode border result in an enhanced electric field perpendicular to the spike with a preferential domain switching and DW injection [106]. The advantages of such designed electric fields are the precise modeling

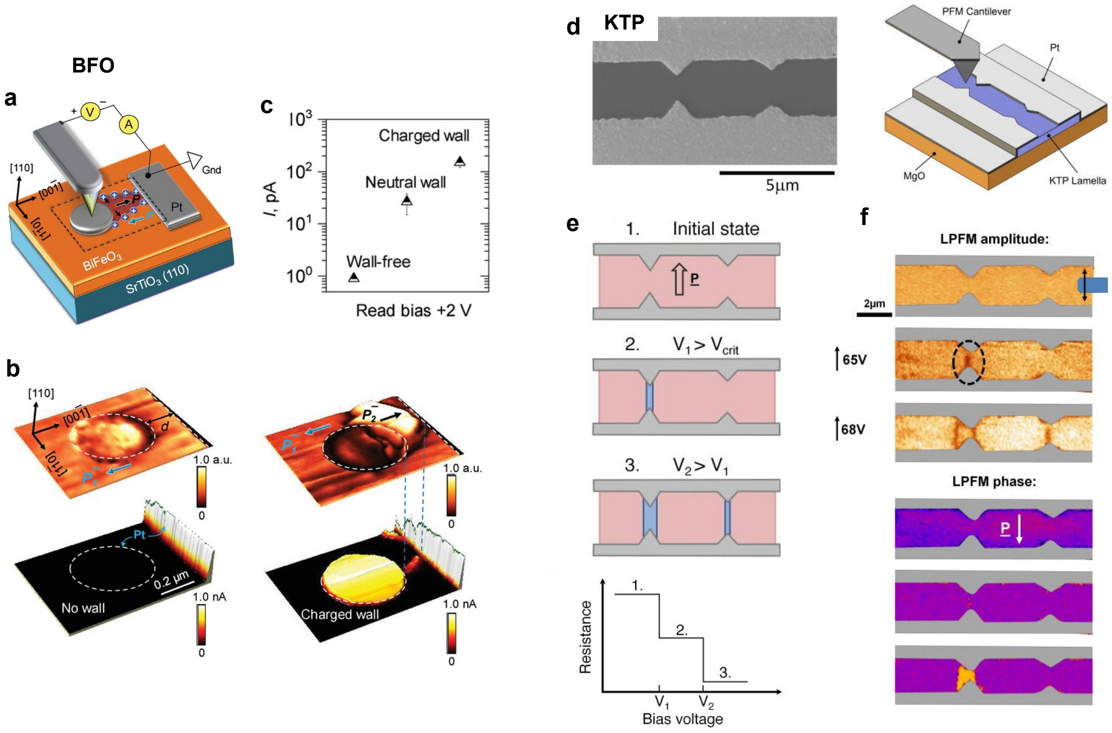

Figure 1.18: *Modifying the electric poling field through the electrode design. a) Schematic of device with a nanoelectrode in front of a larger Pt pad resulting in an asymmetric electric field. b) PFM and cAFM image of the device off-state without domain walls and on-state with connecting non-straight domain walls. c) Different current levels for the different kind of DWs. d) SEM image of notched electrodes on platinum sputtered KTP lamella created via FIB milling and a schematic of the experimental setup for PFM investigations. e) Schematic of the different states of varying resistance based on the voltage V_2. f) Lateral-PFM amplitude and phase images showing the different states depending on the formation of the DWs. Adapted from [105, 106].*

through simulations which results in deterministic switching behaviours and control over the parameters like necessary applied biases or electrode dimensions. Also as seen in Fig. 1.18 b by adjusting, multi-switching or cascade-like switching can be achieved, which is potentially interesting for multi-state or voltage dependent memories.

Similar to these approaches, instead of changing the electrode shape to create an modified electric field, it is also possible to introduce defects or pinning centers by chemical doping inside the active material to create "hot-spots" at which nucleation and therefore the injection of DWs are promoted and at which DW can be stabilized. Defect-engineering is a wide research field in its own studying the effect of doping and defect chemistry on the material properties like e.g. enhanced ferroelectric polarization, modified hysteresis loops, enhanced electrical properties or increased retention and endurance cycling. For controlling nucleation sites, DW positioning and domain expansion speed, the material is only locally modified. Some

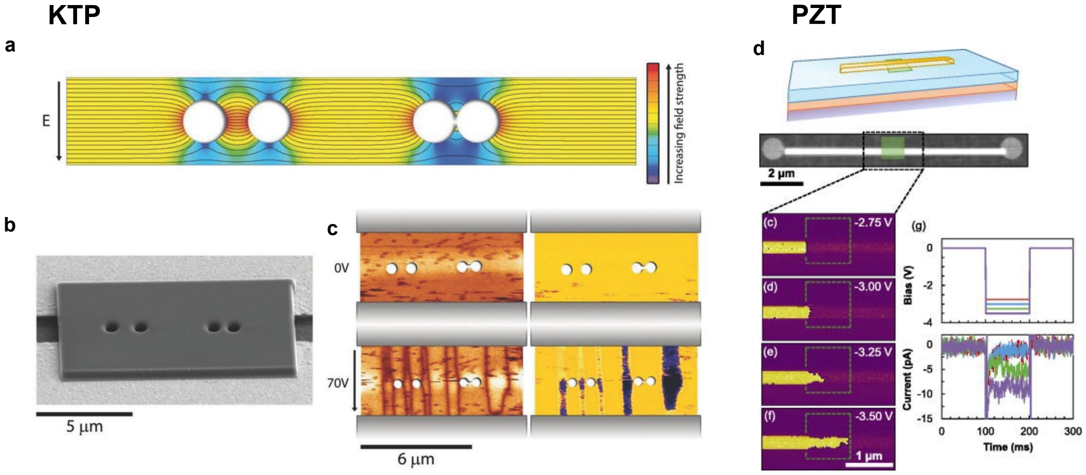

Figure 1.19: *Modifying the effective electric field through defects and chemical doping. a) Electric field model of KTP lamella with milled circles showing the creation of field hot-spots left and right of the defects. b) SEM image of a KTP lamella with milled circular defects. c) PFM images of amplitude (left) and phase signals (right) showing a mono-domain state (top) and domain nucleations aligned with the field hot-spots (bottom). d) Domain wall interaction with a 1 μm wide defect region (green). Schematic representation of the structure at the top and sequence of PFM images showing the domain wall pinned at the defect region (green dotted outline) and then depinned at high bias magnitudes in the bottom images. Adapted from [107, 108]*

examples include the creation of material defects like drilling of holes [107] while others rely on the locally applied chemical doping [108] as presented in Figure 1.19. Especially precise locally doping with Ga^+ ions show potential in capacitor device geometries as pinning and defect sites allow to control the domain structure inside the otherwise not accessible sandwiched active region [109].

One drawback of the before mentioned concepts are that irreversible changes are necessary to create such inhomogeneous electric fields either in the electrode shape which needs to be predefined or by locally altering the material itself, which could additionally effect the properties of the DWs. Furthermore, even when working reliably these concepts are rigid and provide no dynamical changeability compared to neuronal connections in the brain which can be reconfigured. As domain walls as functional elements are inherently interesting not only due to the ability to inject and erase them on demand but also to control their position and allow them to form (inter-)connections in more complex ways.

As mentioned earlier, mechanical stress has also been used to control not only the creation and formation of domains, but also to limit DW motion in a less controlled way compared with electric-field driven approaches. Mechanical switching through a top electrode was shown by exploiting the flexoelectric effect in BTO [112] as well as controlled writing and positioning of conductive domains by locally applied stress [113, 94]. Additionally it has been

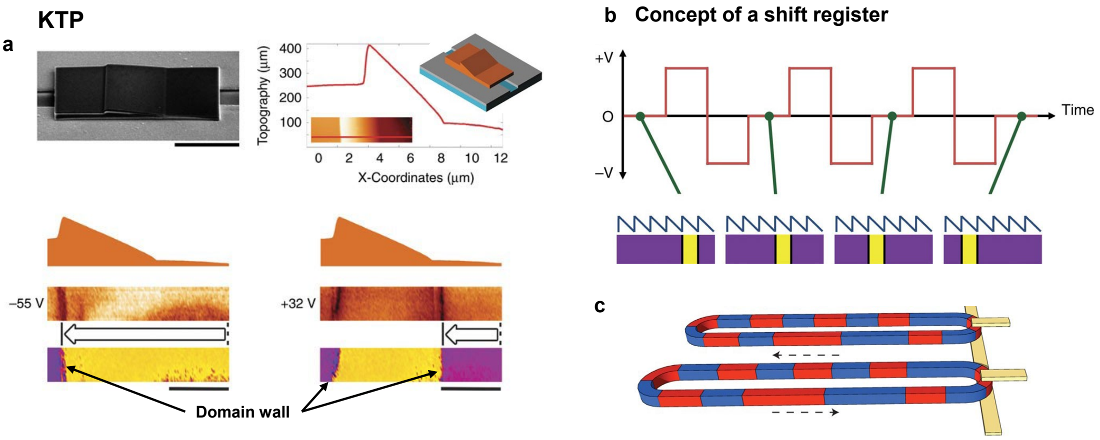

Figure 1.20: *Ferroelectric domain wall-motion diode. a) KTP lamella with a sawtooth cross-sectional morphology. Top: SEM image of the real device together with a line profile of the lamellar surface topography. Bottom: a new domain wall has been injected and progressed from right to left up the ramp and over the sawtooth edge, left side. The state after a further bias pulse was applied, right side. A domain wall of the opposite polarity has been injected into the device and moved to the base of the ramp. b) Domain-wall shift register based on ratchet-like domain-wall motion for successive alternating field pulses. c) Possible implementation of a shift register in a memory device. Adapted from [110, 111].*

shown that ferroelastic domains, which are sensitive to mechanical stress can interact with the ferroelectric switching dynamics [114].

Other novel and advanced concepts of asymmetric domain wall movements were presented by demonstrating a ferroelectric "motion-diode" [110] in close relation to the ferromagnetic counterpart of a shift-register [111]. Here, the domain walls movement is restricted in one direction irrespective of their polarity, as a result of a cross-sectional sawtooth profile of the poling electrode, see Figure 1.20. Successful demonstrations showed that domain walls could only propagate in the direction of increasing thickness of the sawtooth electrode, paving the way for implementing a series of diodes for a ferroelectric DW-shift-register potentially usable for "race-track" memory [115] concepts.

Another clever way to manipulate the effective electric field for poling the ferroelectric domains is by using electrodes, which offer a time dependent non-uniform electric field distributions. High-resistive (high-R) electrodes have been shown to successfully confine and guide the electric field due to a limited charge-movement inside the electrode. The advantage over patterned electrodes is the flexibility over the evolving domain which can be controlled by the amplitude, dwell time or amount of poling pulses compared to rigid electrodes which are only able to produce one domain pattern through the applied electric field. McGilly et al. [116, 117] successfully applied this concept by using high-R platinum electrodes, shown in Figure 1.21. The increased spread resistance caused a voltage gradient within the electrode, which resulted in controlled DW-dynamics. Of course high-R electrodes also present challenges, e.g. in the

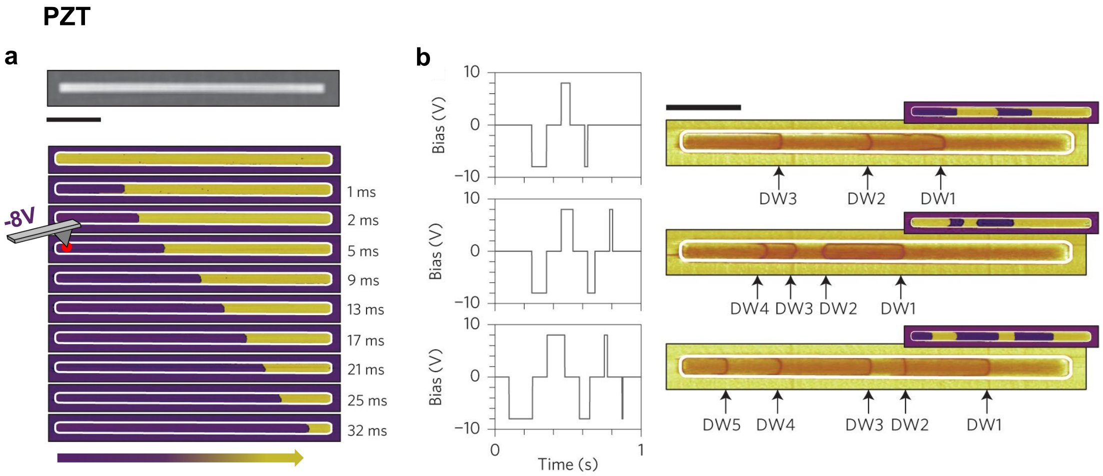

Figure 1.21: *Controlling domain walls with high-resistive electrodes. a) Top: topography image of a line electrode made from high-resistive platinum. Bottom: series of PFM images monitoring the DW motion based on an increase of the applied voltage pulse duration. b) PFM images of the injection of multiple DWs based on a voltage pulse profile with alternating positive and negative pulses. Adapted from [116].*

higher resistivity of the electrodes, worse interface contact with DWs or potentially enhance fatigue effects.

1.3 State-of-the-Art domain wall electronics

While different challenges still impede the technological integration of domain wall based devices to date, prototypes with various functionalities based on the different DW-types have been realized. A variety of foremost non-volatile memory devices as well as logic units have been demonstrated.

Standard concept rely on a resistance change of the device based on the creation or erasure of conductive domain walls between an inter-electrode gap. In BFO systems, often a planar electrode architecture was used as shown in Figure 1.22. In the first approach a nanometer sized electrode is placed in front of a big electrode and a voltage bias is applied. The in-plane domains in the area between the electrodes switch and 2 domain walls are connecting the small an big electrode. Based on the distance of the gap, the DW-curvature and therefore its charge state is controllable yielding higher readout currents for smaller gap distances. In another approach, center-type topological quadrant domains in an BFO film are used, which showed a reliable switching between an on-state and off-state by changing the quadrant domain wall structure from the H-H to their T-T configuration. The realized memory devices showed excellent stability of the created H-H DW state due to the topological confinement. In other works on memory elements from DWs in BFO thin films, three-terminal devices were created in which a partially switching of domains is used together with only temporary

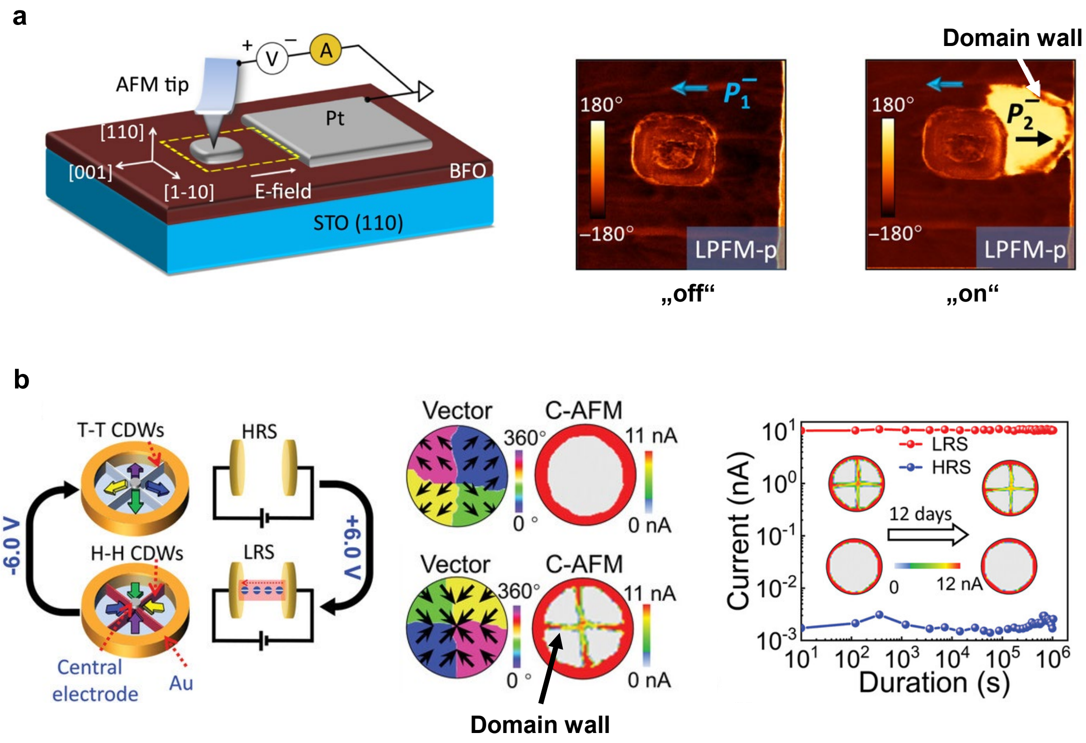

Figure 1.22: *Ferroelectric domain wall based memory devices. a) Schematic of the BFO memory device with PFM images of the pristine monodomain P_1 off-state and on-state with a poled domain P_2 and associated DWs. b) Left: DW-based memory device using a switching of the center-type quadrant domain states changing between its H-H and T-T formation. A gold ring top electrode and an AFM tip placed in the center of the device is used to promote the switching. Middle: cAFM image of the off-state and on-state showing the conductive DWs together with a representation of the polarization directions of the quad-domains. Right: Retention tests of the HRS and LRS over a duration of 12 days showing no change in the on- or off-state. Adapted from [118, 119].*

formation of charged DWs under a readout voltage. An enhanced endurance is claimed for this type of operation, while still preserving the non-volatility of written information.

Logic operations are demonstrated by BFO nanoislands, in which conductive domain walls are stabilized due to the mechanical clamping, and precise creation or breaking of DW-paths are used for logic operations [120], see Figure 1.23. In LNO coplanar capacitor structure the diode-behaviour of the cone like charged domain walls are used to construct logic gates (AND or OR gates) as well as rectifier and electrical diodes [102].

In other works, the neurological behaviour of synapses are emulated by LNO-systems. Plasticity shown as potentiating and depression behaviour as well as different short to long term-memory functionalities are observed when working with spike rate dependent tuning schemes. Clever ways of implementing the driving voltage bias also gives rise to spike time dependent plasticity, a known learning mechanism of the biological brain [121]. In self-assembled BFO

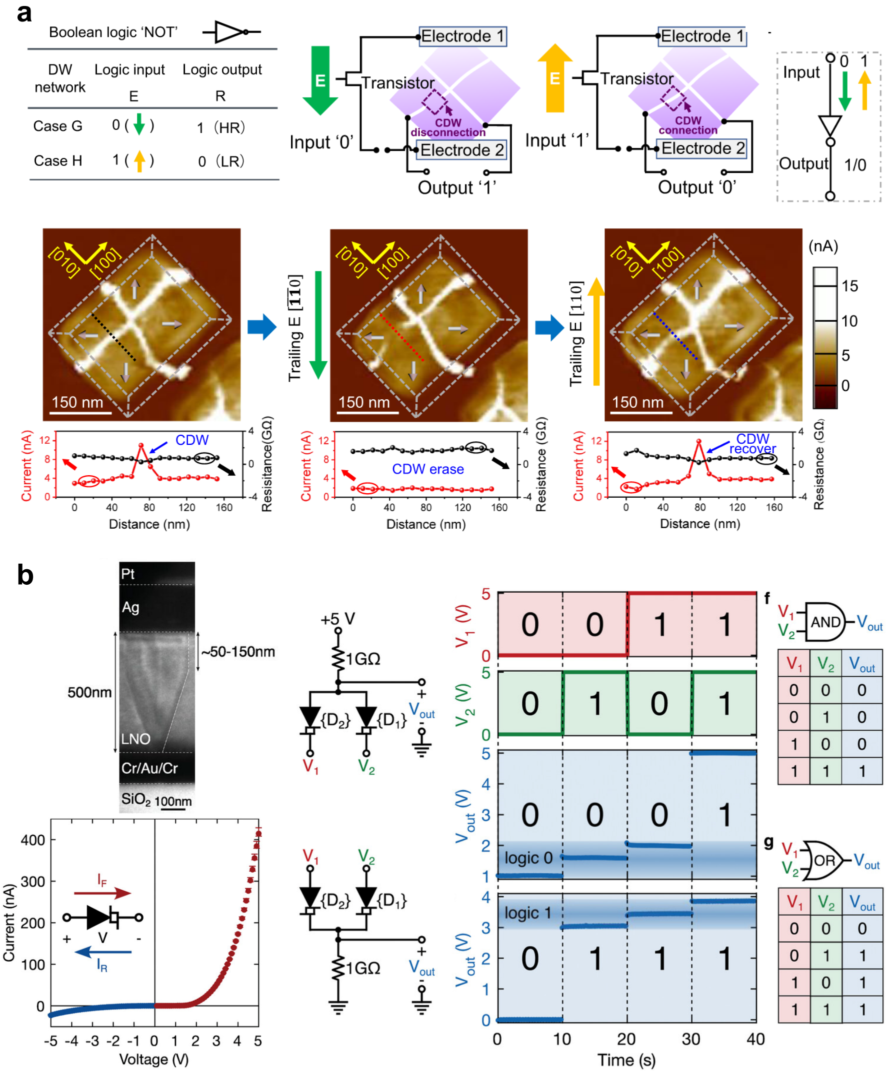

Figure 1.23: *Ferroelectric domain wall based logic. a) DW-based logic units based on the connecting of a charged DW segment in connected BFO nanoislands. b) Experimental demonstration of "AND" and inclusive "OR" logic gates based on the diode-like behaviour of LNO DWs with stable and distinguishable "0" and "1" output states. Adapted from [120, 102].*

DW-networks, no direct domain manipulation by poling operations are used but the memristive properties of the highly interconnected DW network are investigated with potential to apply reservoir-computing schemes [122, 123]. Studies on other application-relevant aspects include their technological integration especially to allow CMOS-compatible processes [124, 125], high-temperature stability [126], domain wall p-n junctions [127] and tunable in-plane DWs [128].

Besides standard binary memory applications, advanced memristive functionalities are one of the sought-after advantages potentially realisable within domain-wall devices. Non-volatile

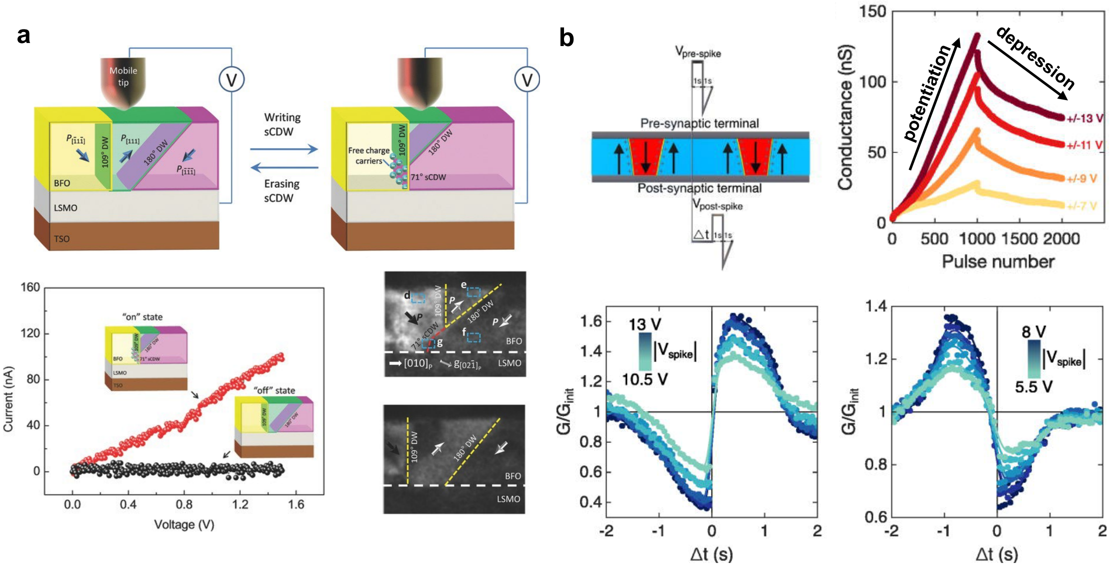

Figure 1.24: *Tuning of charged domain walls and spike time dependent characteristics. a) Top: schematic of the tuning of the charged DW-segment inside a BFO film by applying voltage through a mobile tip. Bottom: IV characteristics of the on-state for which the charged DW-segment is created and the off-state for which the charged-segment is removed. TEM images of the two states prove the formation of the charged DW. b) Creation of a STDP characteristic dependent on the time difference of a pre- and post-synaptic pulse within a LNO capacitor device. The STDP characteristic is achieved due to the conductance change of the charged DW segments based on the pulse amplitude and polarity. Adapted from [129, 121].*

multi-resistive state tuning based on DW-functionalities due to previously received input signals would open the door for single in-memory computing devices with nanometer size dimensions.

So far, proposed concepts showed multi-resisitve state switching within the realm of DW-based ferroelectric systems in two ways: either by changing the conductivity of single domain walls or by controlling of the domain wall density. For single-DW tuning, various approaches were studied, including, e.g. changing of the surface angle in cone shaped DWs in LNO [130], modifying the proportion of the charged segments within DWs in BFO [129] or dynamic tuning of the DW conductivity by consecutive pulses [122, 83] (see also Chapter 1.2.1). Multi-domain capacitor devices with tunable domain wall density [131, 72] usually offer higher accessible current output and simplified device architecture, however concepts are hindered by issues with retention and high-voltage operations. The tunable multi-state DW-based memristors, which have been demonstrated on LNO crystals are promising, however the conductive states associated with the charged DWs still show a drift of the conductance state due to relaxation of the domain wall inclination angle [130, 121]. Low-voltage memristive operations for a limited number of conductance states have also been shown in perovskite thin films, in particular in BFO, demonstrating the general feasibility of a multi-state DW-memristor [72, 118]. However its practical implementation within a simple two-terminal device is impeded by either direct domain writing via a biased AFM-tip or a limited degree of control over the domain formation and propagation needed to reliably address a multitude of resistive states.

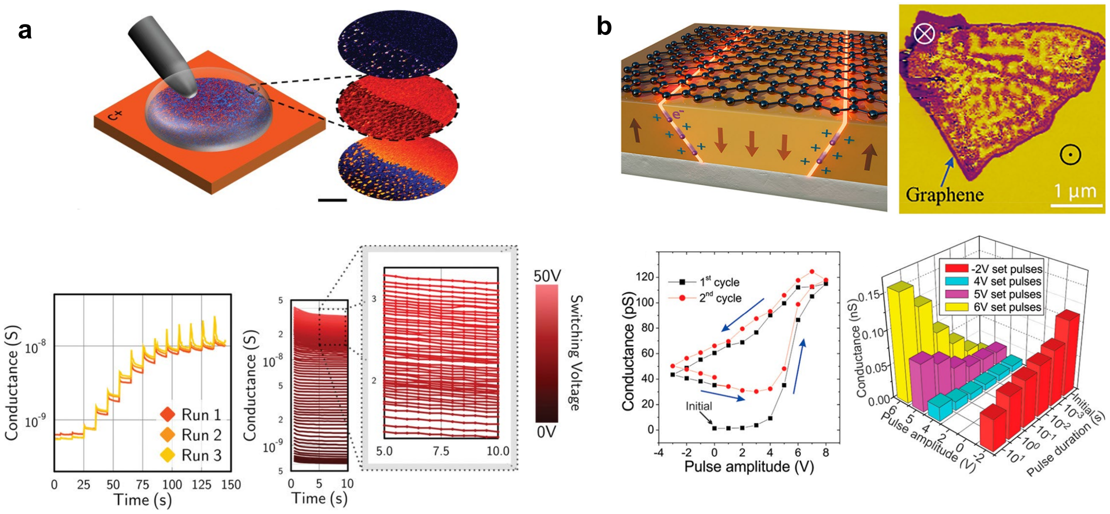

Figure 1.25: *LiNbO$_3$ domain wall memristors with multitude of resistance states. a) Creation and accessing hundreds of resistive states based on a DW density manipulation by the application of consecutive pulses applied through a liquid top electrode. b) DW-density modulation inside a Gr/LNO capacitor with sub-coercive field tuning of the surface angle of the charged DWs for an expanded resistive tuning. Adapted from [131, 130].*

Further progress in the field is still hindered by the relatively low current outputs or needed high voltages of DW-based memristors and the lack of stability (even through concepts have been established which actively use the time dependent variation of the conductance states [121]). Strongly charged DWs inherently counteract the need for stability while complex poling operations by trailing fields also complicate the integration of such methods in solid-state devices. For devices based on the tuning of the DW-density, the stochastic formation and modification of poled domains can cause problems for the repeatability and addressability of distinct conductance states. More progress is expected in advancing techniques to reliably control the nucleation and positioning of DWs as well as a better understanding of the underlying conduction mechanisms which should allow for a enhanced tunability of the single-DW conductivity.

1.4 Lead Zirconium Titanate

Lead zirconate titanate (PZT) is a solid solution with the chemical formula Pb(Zr$_x$Ti$_{1-x}$)O$_3$ (0 ≤ x ≤ 1). PZT was first developed in the 1950s at the Tokyo Institute of Technology by Shirane et al. [132, 133], following an increasing interest in ferroelectricity, previously studied in BaTiO$_3$. PZT is a ceramic perovskite material with ABO$_3$ lattice structure in which the 'A' site is occupied by Pb and the 'B' site by either Zr or Ti [134, 135]. It is well known for its piezoelectric properties and a cornerstone in many micro-electro-mechanical systems (MEMS) due to its high Curie

Temperature, and its exceptional piezoelectric and ferroelectric properties. Only in recent years a shift towards alternative piezoelectric materials for MEMS system is seen due to an urge for a lead-free industry. However, 98% of all commercial piezoelectric are still based on PZT [136].

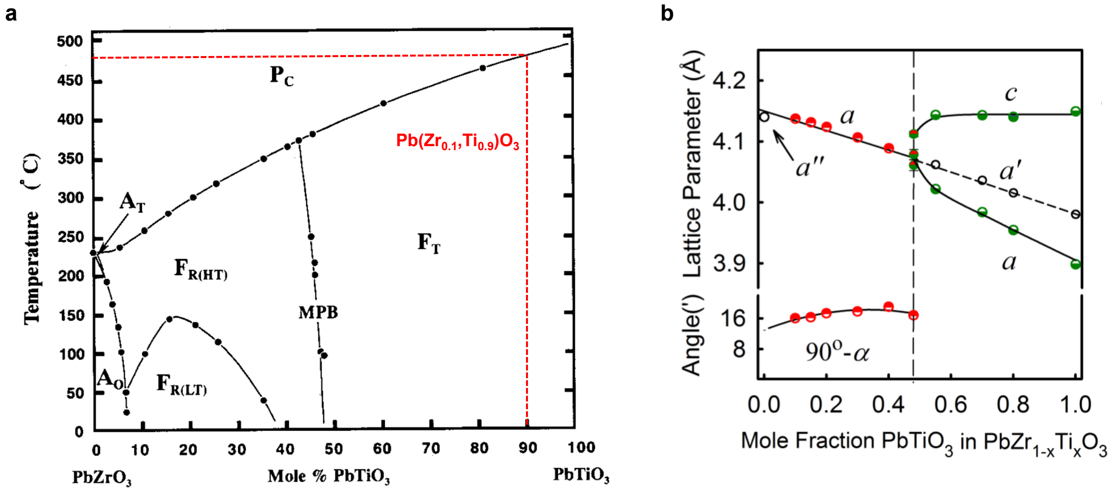

Figure 1.26: *a) Phase diagram of $Pb(Zr_xTi_{1-x})O_3$. The in this thesis used composition of Zr:Ti of 1:9 is indicated by the red line. b) PZT crystal lattice parameter change depending on the mole fraction of PbTiO3. Adapted from [137, 138].*

PZTs phase diagram is displayed in Figure 1.26a, which was first studied by Jaffe et al. in 1954 [137]. The composition, which is used and studied in this thesis is 1:9 for Zr:Ti. As it can be seen in the phase diagram, for this composition a phase transition takes place at around 460°C from the high-symmetric cubic to tetragonal phase (with space group P4mm). This phase transition gives rise to the ferroelectric property as it is explained in Chapter 1.2. Noteworthy is the nearly temperature independent morphotropic phase boundary (MPB) which occurs at a Zr/Ti ratio of around 0.45–0.5 [135] separating the Ti-rich tetragonal and Zr-rich rhombohedral phase, which gives rise to an enhanced piezoelectric response. Since this thesis focuses on ferroelectric domain walls within PZT materials, a tetragonal Ti-rich composition offering ferroelectric properties is required. In particular, the next chapter will focus on thin film fabricated single crystalline PZT films.

1.4.1 Ferroelectric PZT thin films

Ferroelectric thin films have found their way in ferroelectric devices such as non-volatile memories or capacitors [139]. To date, the most exploited functionality of the PZT films are linked to their high remnant polarization and ideal switching characteristics due to the tetragonal crystal lattice. Main applications focus on manipulation of the domains with out of plane polarization direction as well as controlling the switching dynamics and the resulting domain states to store information. As discussed in Chapter 1.2 and 1.2.1, besides the ferroelectric domains, recent research is targeting the 2D domain walls as functional elements to achieve new functionalities and reduced device dimensions.

Most PZT films are grown using pulsed laser deposition (PLD) as it allows to preserve the stoichiometry of the target material during deposition (more details on the PLD technique can be found in Chapter 2.2 and 3). For most applications poly-crystalline films can be used, however since the crystallographic directions of different grains (with grain sizes of several µm) in poly-crystalline films are randomly oriented their use for high-precision applications by harvesting and manipulating properties on the nanoscale is difficult and single crystal films are needed. Single crystal oxide films can be grown by epitaxial layer-by-layer formation with the PLD technique. To allow a defect-free growth several parameters have to be optimized but one of the most important one is the choice of the substrate material. The substrate on which the materials are grown onto present a boundary to which the formed layer tries to adapt. Therefore, substrate materials and their crystal lattice constants need to be carefully chosen. A so called lattice-matching is needed, such that the differences between lattice constants of the substrate and the film are minimized. This results in a decreased elastic strain during growth (and cooling) resulting in defect-free continuous films. Depending on the composition, the PZT crystal has different lattice parameter as seen in Figure 1.26b [138]. In this work, PZT with a ratio of 1:9 will exclusively be used, which exhibits high a tetragonality (ratio of c/a) and lattice parameters of: a_{PZT}=0.3914 nm and c_{PZT}=0.4138 nm [94]. Classic substrate materials for the PZT growth include foremost $SrTiO_3$ (STO) and members of the rare earth scandates family ($ReScO_3$) (more details in Chapter 3).

STO is a perovskite material, which has a centrosymmetric cubic crystal structure at room temperature making it an ideal substrate for growth of a wide range of oxides with a lattice parameter of a_{STO}=0.3905nm. Rare earth scandates, which exhibit a distorted perovskite structure can also be used for high-quality crystal growth. A perovskite oxide's (pseudo)cubic unit cell can be visualized as a stack of alternating AO and BO_2 layers along the [001] direction [140]. By taking the pseudo-cubic lattice parameter, rare earth scandates provide lattice constants in a range between 0.39 4nm and 0.405 nm [141]. By choosing substrates with different lattice mismatches, different strains are applied to the grown functional material as it adapts to the substrate lattice. For example, using a $DyScO_3$ substrate with pseudo cubic lattice constants of $a_{DSO,1}$=0.3951 nm and $a_{DSO,2}$=0.3947 nm, results in a lattice mismatch of 0.93% and 0.84% at room temperature with respect to the a-lattice parameter of $Pb(Zr_{0.1},Ti_{0.9})O_3$. Comparing this to the STO case, with its smaller lattice constant a mismatch of only -0.23% exists at room temperature.

Therefore also resulting PZT thin film exhibit different morphology at the nanoscale when grown onto DSO or STO substrates. While the STO substrates with the low lattice mismatch show smooth topography, the surface of PZT on DSO grown substrates show deformations arranged in a cross-hatch pattern. When choosing substrates with a even higher lattice mismatch such as $SmScO_3$ (SSO) with $a_{SSO,1}$=0.3991 nm and $a_{SSO,2}$=0.3983 nm the lattice mismatch is in the order of 1.97% and 1.77%. Resulting thin films of PZT show a dense

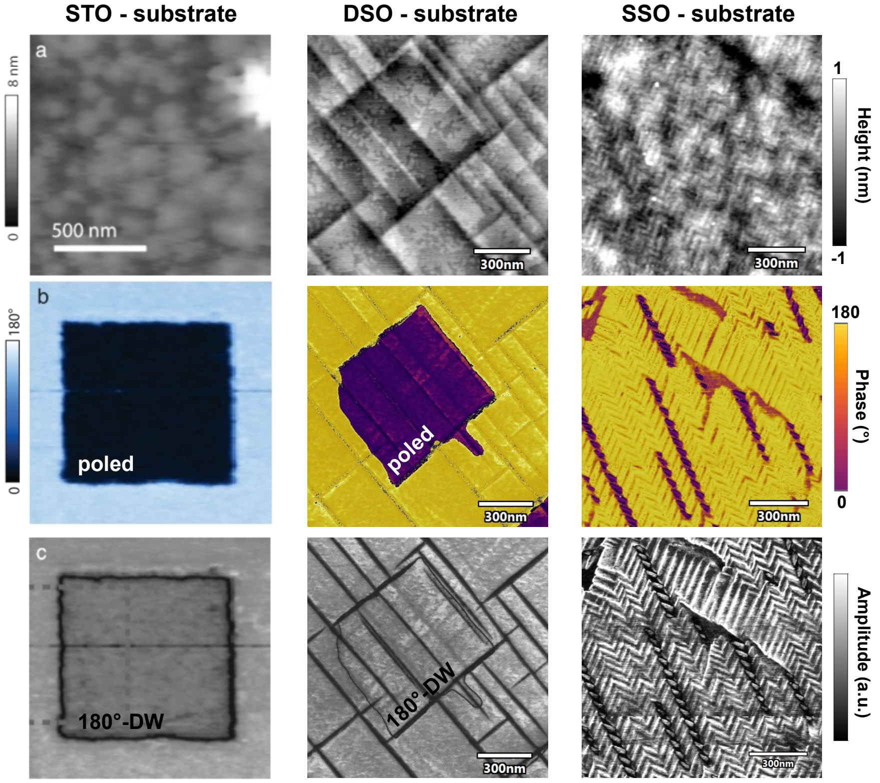

Figure 1.27: *PZT thin films deposited on different substrates with increasing lattice mismatch. From left to right column: PZT on STO, DSO and SSO substrates, respectively, with increasing lattice mismatch to the deposited PZT film. Topography and PFM images are displayed, showing the formation and increase of ferroelastic a-domains (seen in the amplitude image as the cross-hatch pattern for the DSO substrate and herringbone pattern for the SSO substrate) for increasing lattice mismatch. Adapted from [79].*

pattern of stripes also called herringbone pattern, compare Figure 1.27. The emergence of these patterns are due to the formation of ferroelastic a-domains, which form to reduce the strain introduced by the substrate lattice. Therefore an increase in a-domains is observed for substrates with higher lattice mismatch. Ferroelastic a-domains are in-plane oriented compared to the dominantly observed ferroelectric out of plane c-domains. The ferroelectric c-domains can be switched by an electric field, applied e.g. with a biased AFM-tip, whereas the a-domains only react to the electric field by rearrange due to the polarization switching of the c-domains. To map and distinguish the c-domains and a-domains, piezoforce microscopy imaging (PFM) can be used. In Figure 1.27, partially polarized c-domains of PZT samples on STO and DSO substrates are seen. In the case of the STO, a clear phase change is observed in the phase image indicating the differently polarized c-domains. The border between these polarized domains, a 180°-DW is seen in the amplitude as a thin black line. For the DSO sample, also a 180°-phase change is observed with an associated thin black lines in the amplitude image corresponding to the 180°-DW. However on top that, the observed deformations seen in the topography image as cross-hatch pattern are also visible in the amplitude image. Since the classic vertical PFM-technique is only sensitive to the out-of plane component of the polarization, a-domains can be identified as (thin) black areas of low response.

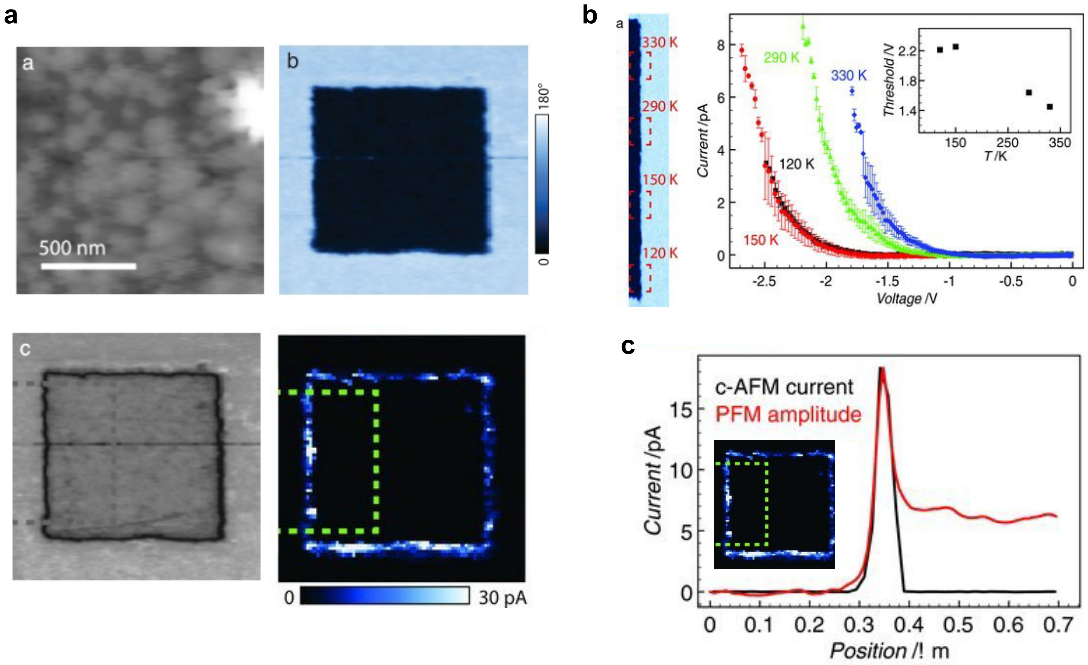

Figure 1.28: *PZT thin films deposited on STO with thermally activated conducting 180°-DWs a) Topography, PFM and cAFM images of poled area of the PZT film. The switched c-domain (black square in the PFM-phase image) with its associated 180°-DWs (black lines in the PFM amplitude image) are visible. The 180°-DWs show a conductive response in the cAFM image (blue lines in the bottom right image). b) IV characteristics of 180°-DW segments at different temperatures showing the increase in conductivity for elevated temperatures. c) Cross-section profile of the cAFM and PFM-amplitude image proving the perfect overlap of the conductive trace with the 180°-DW position. Adapted from [79].*

In work by Jill Guyonnet et al. [79], $Pb(Zr_{0.2},Ti_{0.8})O_3$ samples were grown on STO substrates and the 180°-DWs, which were created by partially poling of c-domains were investigated by conductive AFM (cAFM), see Figure 1.28. The experiment revealed a weak conductive response at the 180°-DW location. The conduction was fully switchable, that means it was removable by erasing the DW itself, and showed a thermally activate behaviour. In successive work [142], the origin of the conduction at the neutral 180°-DWs was shown to be influenced by reversible annealing steps, which proofed the role of oxygen vacancies. One reason for this observation is believed to arise from the highly localized electric fields at the AFM-tip, which are used to create the 180°-DWs. The highly increase electric fields may drive the reorganization and/or injection of oxygen vacancies, which then preferentially segregate to newly formed DWs, providing trap states for hopping mediated conduction along the walls.

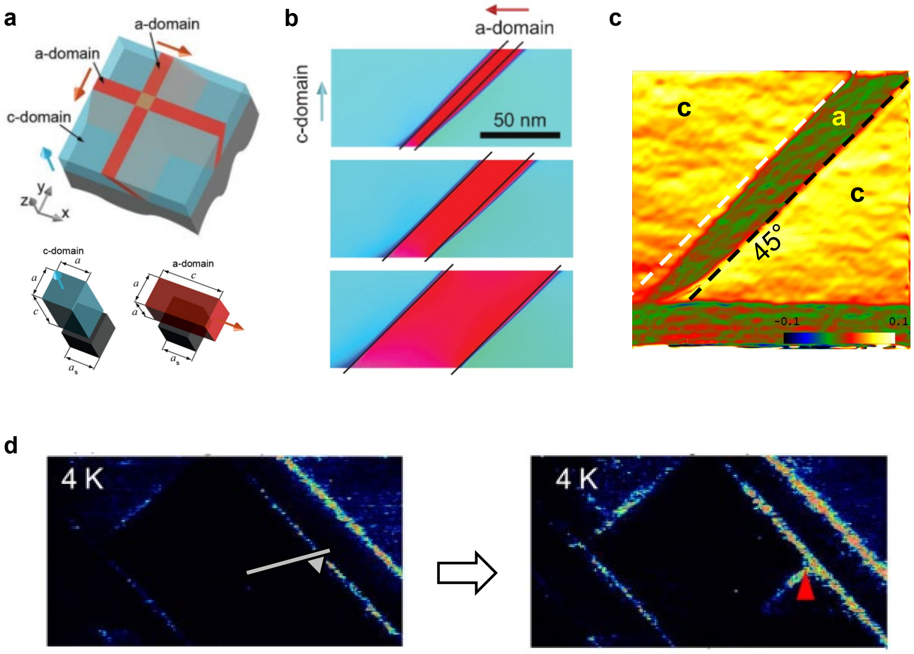

Figure 1.29: *PZT thin films deposited on DSO with non-thermally activated conducting a-DWs. a) Schematic of the a/c-domain cross hatch pattern. b) Simulations of the a-DW bending depending on the a-domain thickness. c) TEM strain map visualization of an a-domain in a PZT sample showing its 45°-structure and its slight deviation from that neutral position at the bottom interface. d) cAFM images of the conducting a-DWs at cryogenic temperatures of 4K. From left to right: an applied pressure by the AFM tip results in the formation of a new conductive a-DW. Adapted from [94].*

Moreover, not only the 180°-DWs in PZT film on STO showed conductive properties, also a-domains, which emerge due to the previously described lattice mismatch on DSO substrates exhibit an enhanced conductivity [94, 143], see Figure 1.29. Cross-section transmission electron microscopy (TEM) imaging revealed the structure of a-domains to be nearly 45° tilted compared to the c-axis of the film. This tilting is necessary to comply to the electrostatic boundary conditions to form neutral Head-to-Tail DWs. However, due to a slight bending from the neutral 45° angle, due to the lattice strain, the a-DWs can become slightly charged. Simulations showed that precise thicknesses of the film and widths of the a-domains are needed for the conductance to emerge. A widening of the a-domains as well as increasing of the film thickness results in a straightening of the a-domains and a vanishing of the conduction. Films in which a conductive response of a-domains were measured possessed thicknesses between 50-70nm and formed a-domains were 10-15nm wide. AFM experiments down to cryogenic temperatures at 4K could show a non thermally-activated conduction, in contrast to the observations of Jill Guyonnet and coworkers. Furthermore, the creation of new conductive a-domains at cryogenic temperatures ruled out an extrinsic conduction mechanism as defects are essentially frozen at such low temperatures.

These above observations show that different types of conduction mechanisms can be present at DWs in PZT-systems. Oxygen vacancies but also free carriers associated with charged walls offer a wide range of tuning parameters to enhance and control the DW conduction and to enable DW-based devices with ferroelectric PZT films.

2 Methods

In this chapter, the utilized main measurement instruments and deposition machines are introduced. Especially, it will focus on atomic force microscopy techniques such as piezoforce microscopy and conductive atomic force microscopy and on the pulsed laser deposition technique for the material growth. The key advantages are presented together with developed specific measurement protocols while differences to other commercially available systems are highlighted.

In this chapter the main measurement instrument, the atomic force microscopy (AFM) is introduced together with the main deposition technique, pulsed laser deposition (PLD). At the end of the chapter a short section gives more details for the STEM experiments and lamella fabrication, which will be shown in Section 4.2.4. Since both AFM and PLD are well established techniques in research as well as in industry, this chapter will not explain the fundamental principles of the systems but rather focuses on practical details with a direct link to the here presented work. A detailed introduction into the fundamentals of the techniques with their available modifications and underlying physical principles can be found elsewhere, e.g. in ref [144, 145] for AFM-techniques and ref [146, 147] for PLD-techniques. For the AFM section in this chapter, the influence of the environment control, different type of AFM-tips used or specific cleaning protocols are discussed. For the PLD section, a focus is put onto the specific system which was used for this thesis, the Solmates SMP 800 Large Area PLD system located at EPFL's cleanroom CMi, highlighting both its advantages and disadvantages compared to other PLD systems.

2.1 Atomic Force Microscopy

In this section, a detailed look will be given to the main instrument to acquire not only topographic data of the ferroelectric films but also to perform functional measurements. Atomic force microscopy (AFM) is an imaging technique that relies on the interaction of a nanometer-sized sharp tip with the sample surface to probe material properties with nanometric precision. The offered versatility of the AFM principle has led to the development of advanced techniques such as conductive AFM (cAFM) and piezoresponse force microscopy (PFM). While cAFM measures local conductivity, PFM utilizes the piezoelectric response to study ferroelectric polarization switching. Both techniques use a metallic (or metallic coated) AFM tip as a top electrode, to apply highly localized electric fields to create and image nanometric domains and sense local current paths of the sample [59].

All AFM measurements shown in this study are performed with an Oxford Instruments Asylum Research Cypher-AFM system. For the used AFM system an "Environmental Scanner" (ES) modification was available, which offered a controlled gas environment close to the sample plus a temperature control between room temperature and 250°C. The advantages of the environmental chamber were used for all functional AFM measurements (that is PFM and cAFM scans) presented in this thesis. Standard topography measurements were equally done with or without the ES module with in no noticeable changes. For conduction measurementsa a Cypher Dual Gain ORCA Holder (capable of measuring between 1 pA and 10 μA) was used. The ORCA holder also provided the acquiring of PFM images, such that an easy switch between the two AFM modes was possible to image the same sample area with both techniques. Due to its versatile use, nearly all AFM-experiments are performed with the ORCA holder. Because of the circuitry of the ORCA holder all biases to the sample are applied with respect to the bottom SRO electrode while the tip (top electrode) was kept at virtual 0 V.
The tips predominantly used in this thesis (especially useful for cAFM images) were stiff (40 N/m) conductive boron doped diamond coated tips from ADAMA Innovations "AD-40-AS" with standard tip sharpness (tip radius: 10±5 nm) and "AD-40-SS" for high resolution images (tip radius: <5 nm), offering both excellent tip contact to the sample surface paired with stiff and non-degrading scanning properties. The cryogenic measurements in Section 4.2.2, also employed diamond coated tips but from a different company, NaDiaProbes with a nominal spring constant of 5±1 N/m were used. For measurements in which only topography images were taken, uncoated tips from BudgetSensor were used ("Tap300Al-G"), yielding exceptional resolution (especially in z-direction) when used in AC-mode. For the measurements on monolayer graphene electrodes, shown in Section 5.2.2, the stiff diamond coated ADAMA tips were exchanged for softer (2.8 N/m) Ti/Ir coated tips from Oxford Instruments "Asyelec 01-R2" to minimize the wear onto the single graphene layer during contact scans.

Especially cAFM imaging proved to be very sensitive to the environmental conditions as well as to the used tip. A high relative humidity and water absorbents at the surface of the oxide film are know to influence the functional measurements of the AFM [148]. The enhanced electric field at the tip apex can further result in unwanted chemical reactions with the oxide surface or higher degradation of the tip [149]. One effective way to limit these effects is to remove excess of humidity by heating the sample above 120°C combined with a constant flow of N_2 gas. Furthermore, after cooling down, a small flux of N_2 is maintained to ensure a non-reactive gas environment (inert gases can be used equally). This procedure greatly enhanced the repeatability of measurements both for PFM polarization switching studies but especially for the contact sensitive cAFM measurements.

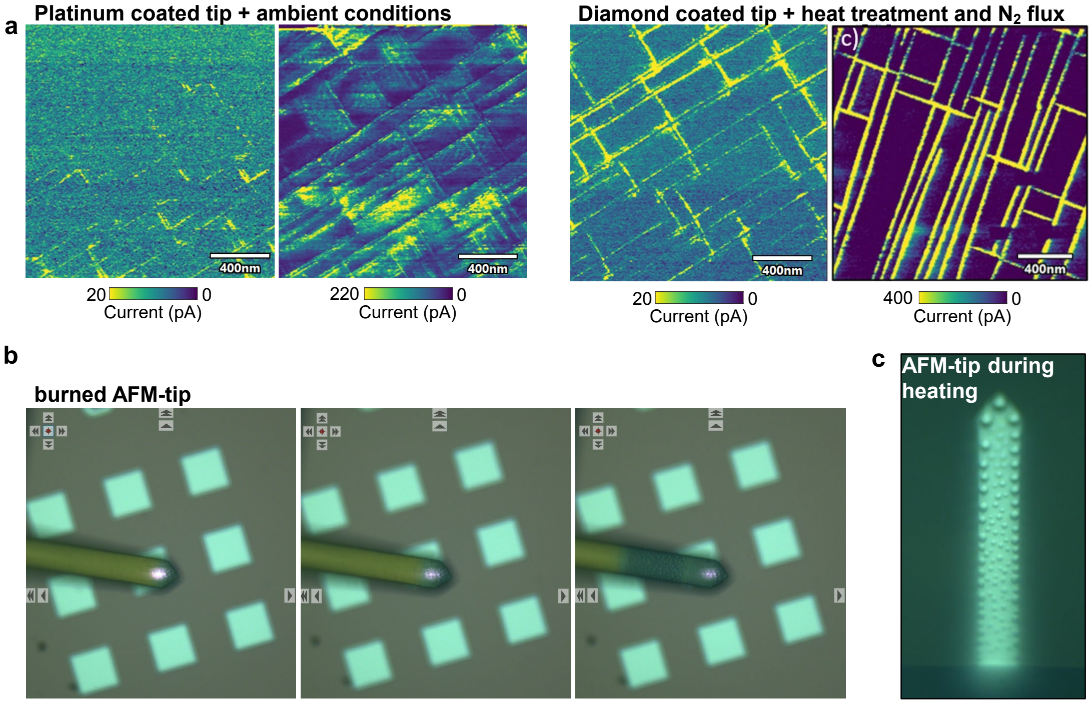

Figure 2.1: *Environmental influences on AFM-imaging. a) Left side: cAFM images of conductive a-DWs with a platinum coated tip without the environmental control. Right side: the same sample is imaged by cAFM with a diamond coated tip and previous applied pre-treatments inside the ES chamber. The pre-treatment involved the heating above 120°C together with a constant N_2 flux. b) Optical images by the AFM objective showing the irreversible altering of an diamond tip due to a high current flow. c) Optical image of an AFM tip during the heating cycle of the pre-treatment when positioned far away from the sample. Water droplets condense on the back side of the tip.*

In Figure 2.1 a), two cases of cAFM measurements of the conductive a-domain wall network are shown. On the left side, a platinum coated tip is used without the environmental control chamber and on the right images a ADAMA diamond tip is used together with the above described pre-treatment. It is obvious that the right side shows much clearer well defined images due to reduced artifacts in the images. For the left side, an often observed "on-off" switching is observed due to a changing contact during contact scanning. For some lines the tip picks up contaminants from the surface and loses electrical contact to the sample until it recovers from it by continuous scanning. In the right image of the left side, an effect known as "double-tip" can be observed. A modified apex of the tip leads to an overlap of a second image, slightly shifted compared to the first one.

Moreover, diamond tips showed to exhibit excellent wear characteristics. Some of the employed tips lasted for over 400 contact scans (both PFM and cAFM together with electrical readouts) without noticable degradation of its conductive property or contact resistance. Such characteristics are important since they allow to establish comparable results not only within one session but between different sessions and over longer timespans.

Figure 2.1 b) and c), shows two effects, which were observed during and before scanning which, if not taken care of can result in greatly distorted results. In b), a "burned" diamond coated AFM tip is seen. Too high voltages were applied and the investigated capacitor devices got leaky leading to high currents passing through the tip and irreversibly altering it. In c) the occurrence of condensed water drops on the back side of the AFM tip are observed. This happened during the heating process before a measurement due to the high temperature gradient between the sample surface and the tip position. This effect could reliably be prevented by placing the tip in close proximity to the surface prior to the heating step. By doing so the temperature gradient is reduced and no water condenses on the tip back side.

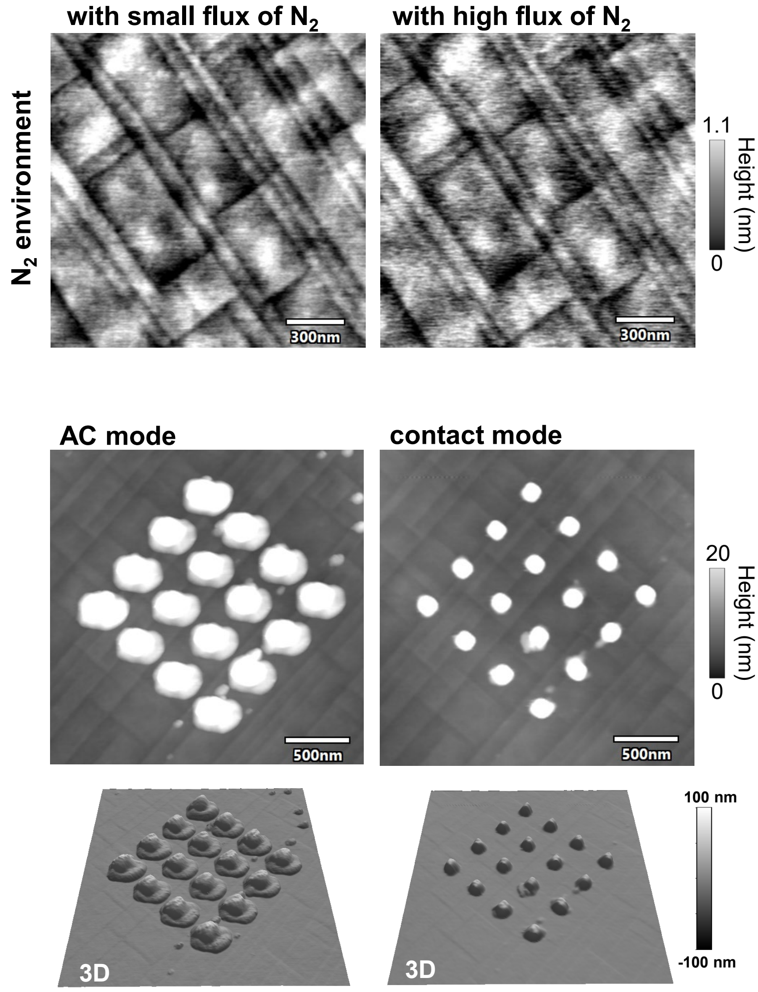

Figure 2.2: *Imaging problems during AFM scans - N_2 flux and AC-mode. Top: topography AC images while a small (left side) or high (right side) flux of N_2 is applied. Bottom: Comparison of AC-mode and contact mode scans of the same pattern of Cr/Au electrodes with a diamond tip. Unexpected interactions of the diamond tip in the AC-mode lead to strong distortions of the topography images.*

Figure 2.2 shows two other observed effects. In the first one at the top of the figure, the difference between a high and low N_2 flux during scanning is shown. Despite the changes being minor, an increased flux during scanning can lead to a reduced resolution especially in the AC-mode. In the bottom of Fig. 2.2, a strange interaction of diamond tips used in AC-topography mode on Cr/Au electrodes are shown. The left side shows the AC image of a 4x4 electrode pattern. The same area is imaged in contact mode (shown on the right side) revealing the actual electrode geometry. One explanation could be that electrostatic interactions between the tip and the electrodes (which dominantly effect the AC-mode scan) distort the resulting image. Therefore critical evaluation of acquired images is recommended together with a comparison of different techniques to rule out potential artifacts as seen here.

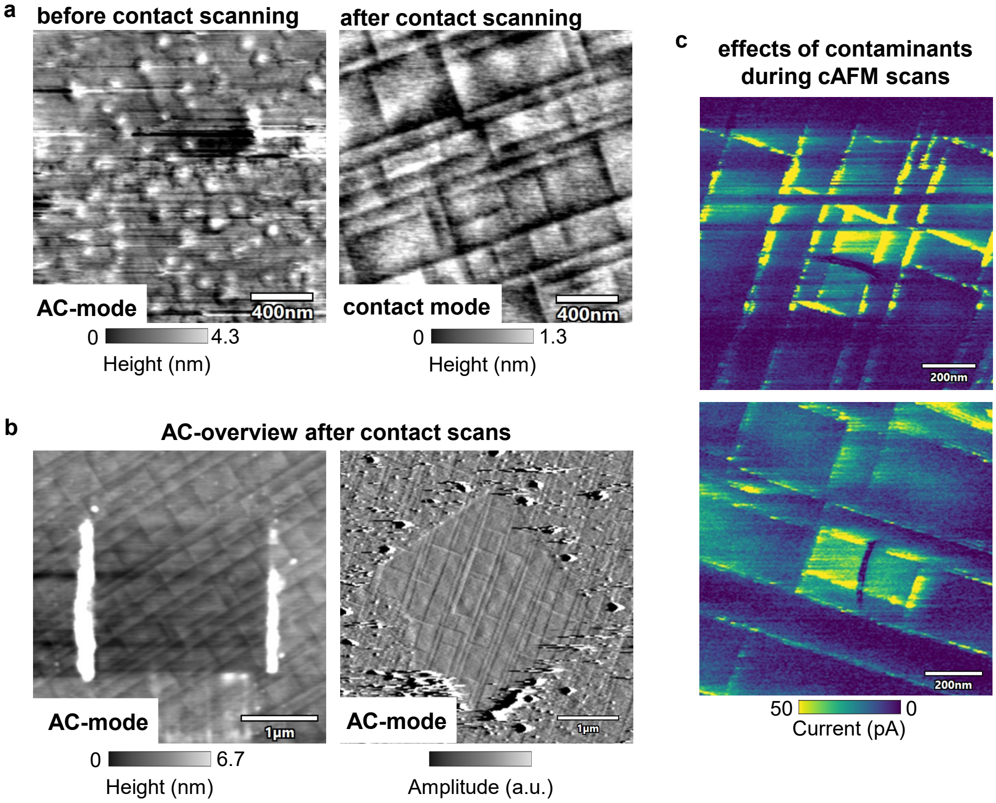

Figure 2.3: *Effect of sample surface cleaning by AFM contact scans. a) Before (AC-mode) and after (contact mode) images of the same area after several scans in contact mode. b) AC-overview images of areas, which were scanned in contact mode. c) Suboptimal cAFM scans of conductive a-DWs. An on-off behaviour of the tip-surface contact is observed as well as drag-artifacts of the conductive traces.*

In Figure 2.3, the sample surface before and after AFM contact scans is evaluated. It is obvious from Fig. 2.3 a) and b), that the scanning in contact mode resulted in a "cleaning" of the surface. Nanosized contaminants accumulated at the surface are removed and pushed away by the contact scanning AFM-tip. Such small particles can not be removed by standard sample cleaning procedures like acetone immersion, sonication or lens tissue scrubbing. It is noted here that the amount of such particles which needed to be removed before reliant imaging could be performed, were present especially in older samples compared to freshly created ones. This cleaning effect is another reason why in this work diamond tips proved to provide a great enhancement. The hardness and stiffness of the used ADAMA tips excelled in the "cleaning"-scans to enable good surface contact without losing their conductive properties due to tip-wear. Finally in Fig. 2.3 c), some cAFM images are shown for which the samples were not properly cleaned and resulting drag-artifacts of the conductive traces and the previously discussed "on-off" behaviour can be observed.

All in all, it can be summarized that an increased care has to be taken when acquiring functional contact scans relying on a good and stable electrical contact between the tip and the sample surface. Different effects can have strong influence on the taken images and lead to false or at least reduced quality of images and deducted material characteristics. Procedures like contact-cleaning steps and pre-treatments such has heat-cycling and N_2 environments are presented, which resulted in an enhanced reliability of the AFM scans.

2.2 Pulsed Laser Deposition

The PLD system used to growth SRO and PZT films in this thesis is a Solmates SMP 800 Large Area PLD system located in the cleanroom of CMi at EPFL. The SMP 800 was designed to allow for large wafer scale, reproducible, high-throughput deposition of thicker layers up to several micrometer. As it will be shown later, this optimized system allowed for faster growth of samples compared to standard research PLD-systems. A downside is that some of the parameters necessary to control the epitaxial thin film growth are not easily accessible or even limited.

The advantages of the system are a fully automatized loading and unloading of wafers, fast and controlled ablation of the targets and fast processing times. A standard process of thin film growth with 10 Hz frequency, and short deposition times (which reduces the temperature stabilization time) of around 10 min can be done within a total of 2 h including sample mounting, loading and unloading. Mounting samples was done by gluing the crystal substrate to a silicon test wafer with silver paste which was then inserted into the loading block.

However there are also disadvantages associated with with the fully automatized PLD-system. Only during the previous year, the system was upgraded to allow slow frequencies below 10Hz. Another inconvenient point is the limited pressure range of 1 mbar. Chamber pressures up to 200 mbars and above are often used in other PLD-systems. Moreover and probably the biggest point of concern is the temperature control. First, for the growth chamber of PZT, there exist no direct temperature sensor at the sample position. The temperature is controlled by setting of the heater power based on a provided calibration curve measured from a silicon wafer [150], strongly limiting the precise control of the actual temperature of the substrate. Furthermore, during cooldown the only method so far involves simply shutting down the heater power associated with an highly nonlinear cooling rate. Another inconvenient point is the missing RHEED-signal, which has established itself as a highly useful tool for the in-situ monitoring of the layer by layer growth for epitaxial thin films [151].

Heater Setpoint (%)	Temperature °C
0	RT
15	110
20	230
25	360
30	460
35	530
40	600
45	660
50	710

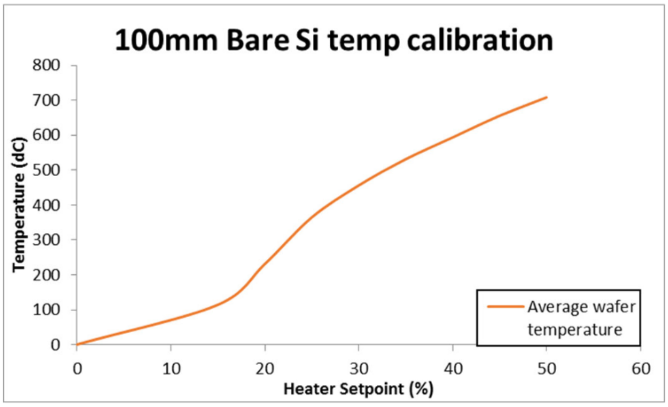

Figure 2.4: *Right: temperature calibration curve, measured for a silicon wafer inside the Solmates PLD chamber, relating the setpoint of the heater power in % to the actual temperature after a sufficient stabilization time. Left: a table with given values for the Heater setpoint and the according temperatures of the silicon wafer. Adopted from [150].*

In Figure 2.4 the calibration curve for the temperature of a silicon wafer is given based on the manual provided by Solmates. As it can be seen, a heater setpoint around 43% should correspond to a temperature of 620°C while 39% should lead to a stable temperature of around 580°C. These temperatures correspond to standard process temperatures of SRO and PZT layers respectively. It needs to be noted here that these settings provide only a rough estimate as the real temperature on the crystal substrate glued onto a silicon wafer by silver paste is expected to differ from the given values. Also a change over time due to degrading of the heating element without a recalibration can lead to a shift in the temperature curve.

While a thermocouple temperature sensor (TC1) is provided inside the chamber, it is not meant to acquire the actual temperature data but rather serves as a safety measure to observe unreasonable changes in the temperature as the measured temperature can differs from the actual temperature by over 100°C.

In Figure 2.5, the temperature of the chamber according to the temperature value of TC1 for a cooldown process is shown. At minute 48, the temperature curve shows a stabilized region of around 450°C, however in this process the heater setpoint was set to 40% which should result in a temperature of about 600°C and is expected to be much closer to the real value than the measured 450°C. Nevertheless, the behaviour during cooldown can be demonstrated by the change in the TC1 value. After entering the cooldown-phase the heater setpoint is put to 0% and the temperature decreases. The non-linearity is shown in Fig. 2.5 together with some intermediate values depicted. In the beginning a fast cooling rate is observed with over 30°C/min which saturates after 10 min to less than 15°C/min.

One way to potentially resolve this non-linear cooldown, which has not been tested so far, would be to add consecutive heating steps with decreasing heater setpoints and short waiting times for each step.

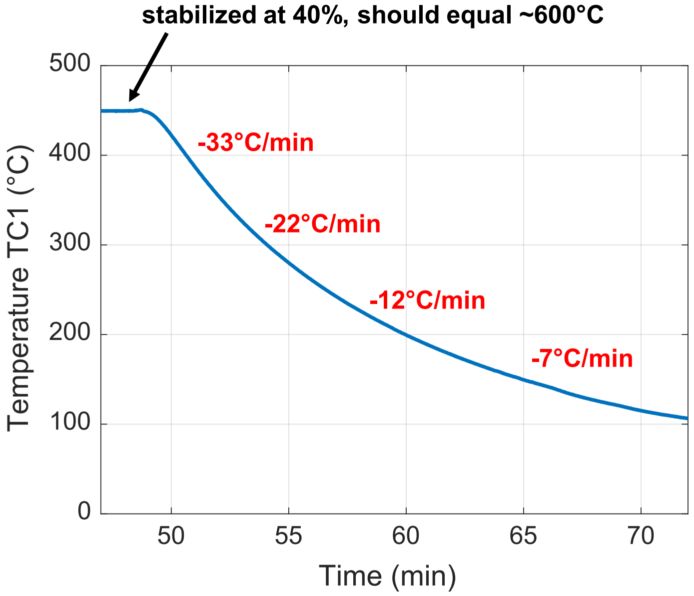

Figure 2.5: *Temperature decrease in the Solmates PLD chamber measured by a thermocouple (TC1). The measured temperature seen for the stabilized plateau on the left side of around 450°C hugely differs from the actual temperature, which was set to be around 600°C (the value is assumed based on the calibration curve from Solmates). A nonlinear temperature decrease is seen for the cooldown after the heater power is turned off.*

Nevertheless the presented specific characteristics of this PLD system highlights the difficult assessment of some major parameters, like e.g. the temperature, preventing a detailed quantitative analysis of the parameter studies in Chapter 3. Despite the disadvantages, once a recipe is found which produces good growth conditions, the systems does provide the possibility of fast processing of epitaxial grown films and a high-throughput.

2.3 Scanning transmission electron microscopy

In this section, details on the scanning transmission electron microscopy (STEM) experiments from Section 4.2.4 are presented, which also can be found in ref [152]. The STEM images and analysis of the polar displacements are used to study the formation and structure of the domains and domain walls in the PZT samples. Especially the 180°-DWs, which are created by PFM polings before preparation of the lamellas are investigated. STEM provides unique insights beyond the surface, allowing cross-sectional image analysis to reveal the structures of domain walls that are undetectable by AFM techniques inside the sample.

Atomic characterization of the PZT domains and DWs was performed using a Thermo Fisher Titan 60-300 transmission electron microscope (TEM), operated at 300 kV. The microscope is equipped with a high-brightness Schottky field emission gun (X-FEG) and a Wien-filter monochromator, a CETCOR corrector for the condenser system to provide sub-Å resolution, and a Gatan Imaging Filter Tridiem 866 ERS for electron energy loss spectroscopy (EELS).

High-angle annular dark field (HAADF) and annular bright field (ABF) imaging in STEM mode were used to capture both the cationic and oxygen sublattices simultaneously. Annular dark field (ADF) imaging was used to highlight diffraction contrast associated to the presence of domain walls. Lab-made TEM scripts were employed to collect sets of 10 consecutive HAADF and ABF images. These images were acquired with a short dwell time (<1 μs/pixel), realigned with subpixel resolution and averaged to correct for residual spatial drift and reduce electronic noise.
The atomic displacements of Zr/Ti and O columns along the in-plane (Δx) and out-of-plane (Δz) direction were calculated by measuring the shift from the centrosymmetric position defined by the A sites of the perovskite structure (Pb). The initial positions of the atomic columns were found using a blob detection algorithm tracing intensity maxima in the image and then refined by applying successive center-of-mass and 2D Gaussian fits using Atomap python package [153]. Finally, detailed polar displacement maps were constructed via the Temul package [154]. In-plane and out-of-plane deformation maps were measured by applying geometric phase analysis (GPA) on HAADF-STEM images, to assess the local lattice deformation at the DWs.

Electron energy loss spectroscopy (EELS) in STEM was performed to assess the oxygen content of the DWs and identify the type of carriers that lead to conduction. The spectra were collected though a line scan of the electron beam on top of the DWs with acquisition time of 0.5 s per spectrum. In total 100 spectra were collected in each interval from which approximately 4 were collected from a DW. The electron beam was monochromated and reached a value of 0.2eV FWHM and the GIF resolution was set 0.05 eV.

Cross-sectional TEM lamellas were prepared with an FEI Helios 650 Dual Beam microscope. Specimens were extracted with their zone axis (ZA) parallel to the [100]pc and [110]pc directions of the DSO substrate (pc: pseudocubic). The final thinning and polishing of the specimens were performed at low current (<7 pA) and voltage (5 kV) to minimize structural damages and DW motion due to heat dissipation and Ga+ bombardment.

3 PZT thin film growth

This chapter describes the fabrication of strained epitaxial PZT samples by PLD with the aim of achieving conductivity at the domain walls. Throughout this work DSO substrates are used due to their specific lattice mismatch with the employed highly tetragonal PZT films. At the beginning of this chapter in Section 3.1 the influence of the DSO surface quality and A/B-site termination is discussed with respect to the growth of the SRO and PZT layers. Detailed growth studies with varying parameters are performed to evaluate and optimize growth conditions for continuous and flat epitaxial films. The second part of the chapter, Section 3.2 discusses PZT samples fabricated with a SRO bottom electrode onto DSO substrates which are studied with respect to the out-of-plane conductivity of the domain walls. AFM-techniques are used to study and confirm the ferroelectric behaviour of the samples as well as to investigate the conductive properties of the domain walls. Focus is put onto the two known types of conductive domain walls, self-assembled 90°-DWs and artificially created 180°-DWs. Based on these results, we try to draw conclusions to the key processing parameters and film properties which are necessary to achieve stable and strong conductivity at the domain walls. Two final outcomes are highlighted, which are the achieved fabrication of samples with self-assembled nanoislands with an observed strong conductive response and secondly samples with flat continuous PZT films with conductive 90°-DWs and 180°-DWs.

3.1 $DyScO_3$ substrate and $SrRuO_3$ bottom electrode

In the following section we will explore in detail the substrate used for our PZT samples - $DyScO_3$ (DSO). We will discuss why DSO is an ideal candidate for our specific aim of engineering conductive domain walls in PZT films and look at the needed preparation steps to achieve ideal growth conditions of the PZT and SRO layers. After that, we shortly discuss the used bottom electrode $SrRuO_3$ and focus on its ideal growth conditions and dependence on various process parameters as well as substrate quality.

3.1.1 The choice of substrate - DSO

As it is explained in more detail in Section 1.4.1 and 2.2, to grow epitaxial, defect-free layers of complex oxide films with smooth surfaces by techniques such as pulsed laser deposition (PLD) or molecular beam epitaxy (MBE) it is crucial to ensure a good lattice match between the deposited material and the substrate crystal lattice [155]. In this work, highly tetragonal (Zr/Ti = 1/9) PZT layers are used, which have lattice constants of a_{PZT}=0.3914nm and c_{PZT}=0.4138nm [94]. Therefore a substrate material needs to be used which provides similar lattice parameters to ensure a smooth growth. A matching for the in plane lattice parameter a_{PZT} is chosen such that the resulting PZT films grow with their c-axis in the [001] direction.

Dysprosium scandate is a member of the rare earth scandates ($REScO_3$) family which - like PZT - posses a perovskite structure. The perovskite structure is represented by the formula (ABX_3), with X usually being oxygen (O) and A and B being two positively charged cations. In the case of rare earth scandates, the 'A'-sites are occupied by a rare earth ion while the 'B'-site is occupied by a Sc ion. In the case of the $REScO_3$, the ideal cubic crystal lattice is distorted to a orthorhombic crystal. Importantly, the pseudocubic lattice parameters of (some) $REScO_3$ crystals are in a similar range to those of interesting functional oxides such as PZT.

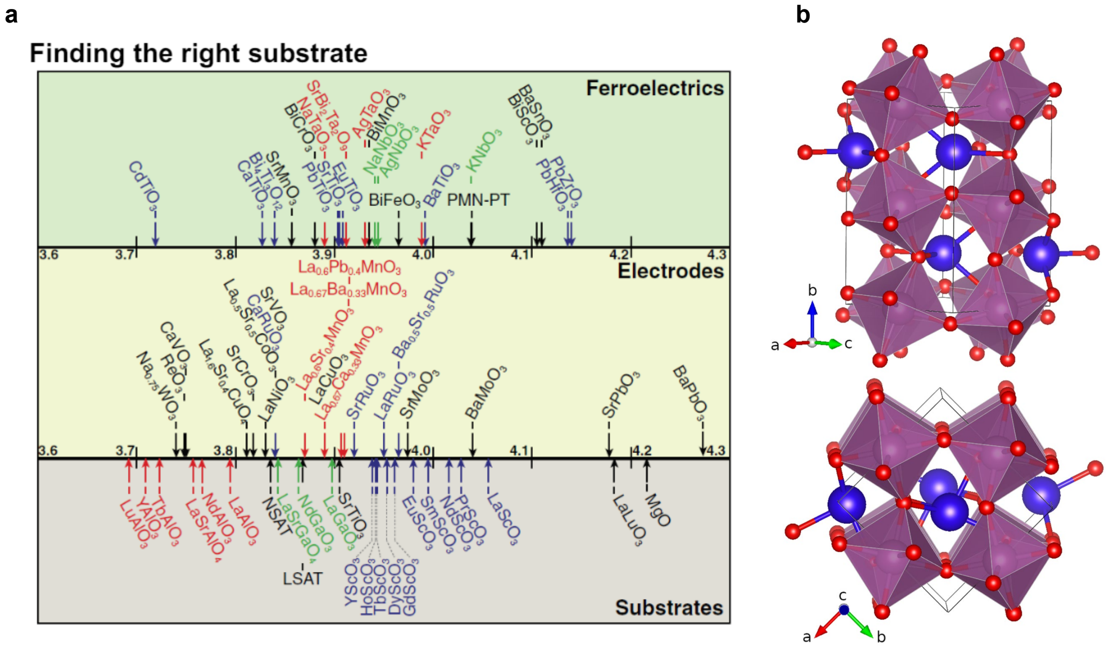

Figure 3.1: *a) Comparison of lattice parameters of commercially available substrate materials (bottom section), a select list of perovskite electrode materials (middle section), and ferroelectric, incipient ferroelectric, and anti-ferroelectric materials (top section). b) othorhombic distorted perovskite structure of $DyScO_3$. ScO_6 octahedra of the structure are shown in magenta, oxygen in red and Dy cation are shown in blue. Adopted from [156, 157]*

Depending on the choice of the rare earth ion, different pseudo cubic lattice constants can be achieved. As it can be seen in Figure 3.1a, the rare earth scandates can be found between 3.94Å and 4.05Å and fall within a range of 0.6-3.5% lattice mismatch with regards to PZT at room temperature [156]. Therefore, depending on the choice of the substrate different lattice strains can be engineered to act onto the epitaxial film and modify its properties, growth conditions or domain formations.

For practical reasons, we note that based on previous studies on PZT films [158, 143], it was found that dysprosium offered a nice balance of not exceedingly high induced strain, but still high enough to promote the formation of ferroelastic a-domains (more details can be found in Section 1.4). Since it has been shown that specific strain conditions promote the formation and stabilization of charged walls (see Chapter 1.2.1), strain engineering can be used to control and tune properties of the DWs. Previous works showed the formation of charged ferroelastic a-domains [94, 143], which is one of the reason why DSO is chosen as a substrate for PZT thin film in this thesis. Of course not only the lattice strain through substrate selection is important for the formation of charged DWs and the emergence of conductivity. For charged a-domains, experimental results as well as theoretical studies revealed a strong correlation of a-domain width and film thickness on the effective charge state of the a-domains [159, 94], while oxygen vacancies have been shown to tune conductive properties of neutral DWs [79].

As we will see in the next chapters and especially in Section 4, the interaction of charged ferroelastic domains, created by using DSO substrates and precisely tuned growth conditions, in combination with normally neutral DWs result in highly enhanced conductive properties to emerge at 180°-DWs.

3.1.2 DSO treatment - to do or not to do?

In this subsection we will look at the different DSO substrate treatments tested throughout this work and the associated advantages and disadvantages.

For this work DSO substrates (with sizes of 5x5mm and 10x10mm) were purchased from Crystek GmbH. The DSOs are cutted with respect to the (110) orientation with a small 0.07°-0.1° miscut angle. The top surfaces are polished and showed to be very clean without any additional cleaning steps needed.

Pristine out of the box substrates were put into the AFM and imaged with the AC-topography mode (see Fig. 3.2). The underlying terrace structure which results from the miscut angle is visible for both cases while more steps are present for the substrate with the higher miscut. Rough step edges are observed with partial overlapping of more than one step (more pronounced in the case of the 0.1° miscut). It is know in literature that e.g. for STO substrates, specific pre-deposition treatments are needed before SRO and/or other functional oxide layers can be defect-free grown [160]. The surface treatment of STO, which consists of a HF-etching step followed by an annealing step, is widely acknowledged, proven and used [122]. For the lesser popular DSO substrate the case is not as clear. The reason for surface treatments in general

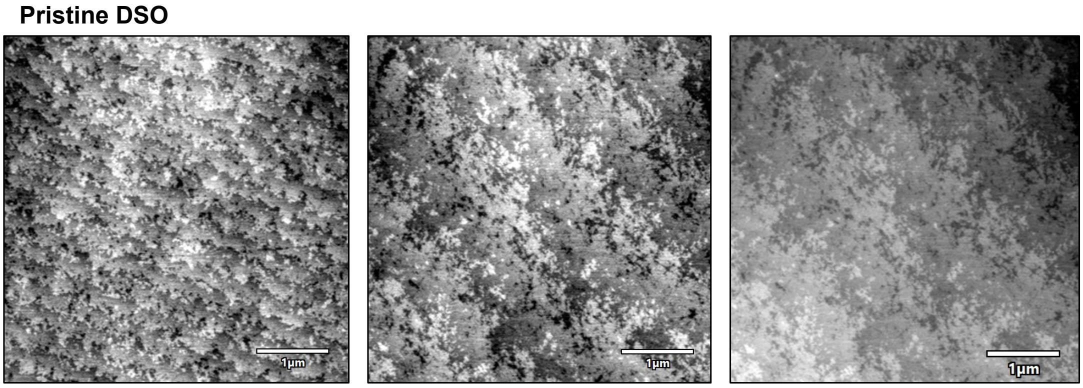

Figure 3.2: *AFM topography images of pristine (110) DSO samples. Left: 0.1° miscut DSO sample with smaller step width. Center: DSO substrates with 0.07° miscut angle. Right: Same image as in the center, besides the image is flattened to show the different height of following steps.*

is to obtain atomically flat and well defined surfaces with a single termination [160] which allows for a smooth growth due to limited dislocations and controlled nucleation especially of the first layers. Additionally for growths of some materials even the type of termination (A- or B-type) is important due to the chemical interactions of the surface layer with the material to grow [122, 161, 162].

The pseudo-cubic crystal lattice in the [001] direction of DSO can be represented by alternating layers of DyO and ScO_2 layers as shown in Figure 3.3 and 3.1b. The height of one layer is equal to half of the unit cell, which is around 0.2nm. In general, as received substrates should show a mixed termination meaning a variety of DyO and ScO_2 layers at the surface with disordered step edges and height variations of 0.2nm, 0.4nm, 0.6nm or 0.8nm depending on the amount of overlapping layers (see Fig. 3.3b).

As seen in the AFM scans of the pristine DSO sample (Fig. 3.2), this scenario is observed (due to the degree of disorder of the step edges, the lateral size of islands and the resolution limit of the AFM-scans reliant step measurements were not possible for the pristine samples). According to literature, as described above, this scenario is unfavorable for a controlled growth and efforts were made to develop an etching recipe for rare-earth scandates similar to the STO-recipe to achieve a single terminated surface and straight step edges [163]. As it has been shown by R. Egoavil et al., SRO layers preferentially grow on Sc-terminated surfaces [162], therefore by monitoring the final SRO layers the quality of surface termination can be judged. The proposed recipe from Kleibeuker et al. involved an initial annealing step followed by an alkaline etching step using NaOH. Based on the experiments in the paper the single annealing step already resulted in straight step edges due to reorganization of the uppermost layers, but not to a full single termination as steps of 1.5 times the unit cell height remained and trenches in the SRO film are observed. Due to the following selective etching step with significantly different etch rates for the DyO and ScO_2 layers, a well defined single terminated

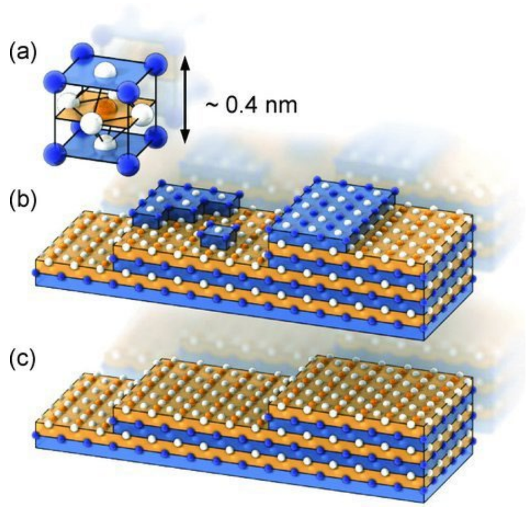

Figure 3.3: *Schematic representation of ABO_3 crystals with ordered and mixed terminated surface. a) The ABO_3 unit cell, where A is typically a rare earth (here Dy), and B is often a transition metal ion (here Sc). b) A schematic representation of a mixed-terminated surface with steps of 0.2, 0.4, and 0.6 nm high. c) A single-terminated ScO_2 surface with steps of 0.4 nm high. The blue blocks correspond to the DyO layer and the orange blocks to the ScO_2 layer, with blue, orange, and white circles corresponding to Dy, Sc, and O ions, respectively. Adopted from [163].*

ScO_2 surface is reached. While this recipe for the surface treatment has been successfully employed by various groups, some newer works proposed alternative scenarios for which these cumbersome etching recipes might not be necessary and pristine substrates could be usable [164].

As the epitaxial growth of functional oxides, the underlying growth dynamics, chemical interactions as well as substrate treatments and layer formations are a research field in its own, the following analysis focuses on the practical implementation of the different surface treatments of DSO substrates for the growth of SRO and PZT layers. To evaluate, if the employed methods are beneficial the final outcome of the SRO/PZT grown layers will be judged. Ideally, the final SRO layer will show a defect/hole free surface with well defined edges and steps of a unit cell height. By observing these characteristics, we can assume that ideal growth conditions are reached and smooth layer-by-layer formation took place. Similar to the SRO, for the PZT layers we want to achieve a smooth and defect/hole free surface. However due to the formation of ferroelastic domains, observations of well defined step edges are not expected, but rather the strain driven emergence of a-domains (compare Fig. 1.27).

First the annealing step was investigated. For this, pristine DSO samples (cleaning of the pristine out of the box samples were done occasionally prior to this step without any noticeable differences in the amount of particles or contaminants) were put into a quartz boat and placed into a tube furnace. Annealing steps were performed with varying parameters ranging from 1h

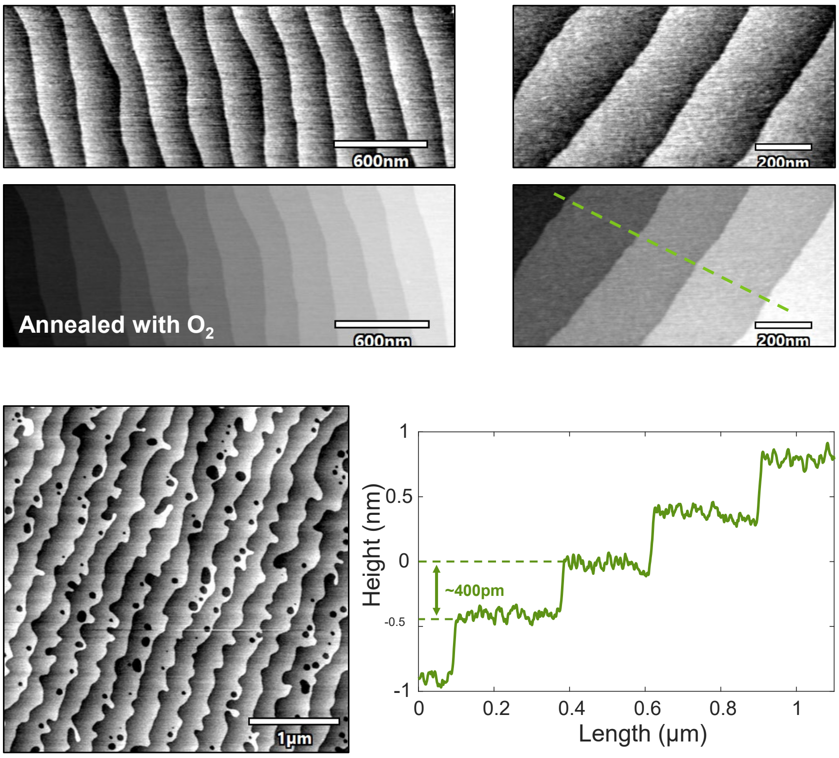

Figure 3.4: *DSO annealed with O_2. Top: AFM topography images of the DSO terrace structure after annealing. Nearly complete straight edges are observed. Bottom left: Topography image of an annealed DSO but with shorter annealing time, resulting in less straight edges. Bottom right: Height profile along the indicated green line showing the step height of around 400 pm.*

dwell time to 6h dwell time at maximum temperatures between 900°C and 1100°C. A constant O_2 flux of 18L/h was supplied for all tests and ramp rates of usually 10-15°C/min were used. As seen in Figure 3.4, resulting AFM images of the film showed well ordered and straight edges and height steps of 400pm are measured from the line profiles. The exact temperature did not play an important role (same results were obtained for all temperature ranges within 900°C-1100°C). As expected also the duration at the annealing temperature only played a secondary role. For very short annealing times resulting terraces with not perfectly straight edges are observed (see bottom left of Fig. 3.4), compared to dwell times of 2h or more for which straight edges are present. We therefore note that a minimum time is required to complete the reorganization of the surface layer, which will depend on the miscut angle which defines the widths of the steps and therefore the time needed to fully straighten the edges. While the achieved results look promising, single topographical measurements by AFM are not enough to judge the completeness of this step. It is unknown which termination is reached at the surface and if there remain regions with mixed termination (e.g. areas close to the steps, which are unattainable for the aspect ratio of the tip) [163].

Following the recipe from Kleibeuker et al., the annealed substrates are now treated with a

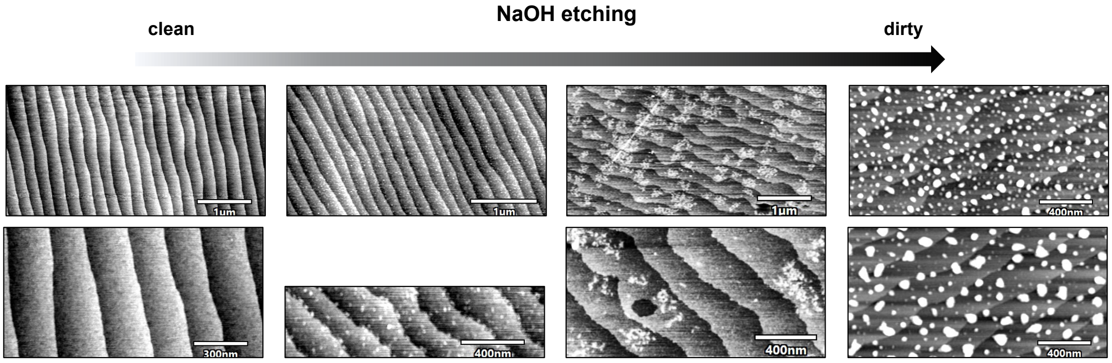

Figure 3.5: *Topography images of NaOH etched substrates with different levels of contamination. All substrates were annealed with O_2 prior to the etching. From left to right: The amount of particles increase depending on various modifications of the etching recipe and etching time.*

12M NaOH-DI solution (inside a sonicator) to selectively etch the Dy_2O_3 layers which should result in the formation of ScO_2-terminated surfaces. Durations between 2h to 6h were tested with overall similar outcome. The samples were afterwards rinsed with 3 consecutive beakers of DI water followed by rinsing in ethanol and dry blowing with a nitrogen-gun. Results with different degrees of contamination are achieved by this method as it can be seen in Figure 3.5. On the left side, a clean treated substrate is shown with nice and straight step edges. Moving to the right side more and more and bigger particles are observed on the surface of the steps, while the step edges are preserved underneath. A likely scenario for the appearance of the contaminants is that etched DyO particles are redeposited on the surface during the etching. This assumption is strengthened since modifications in the etching protocol led to a decrease in contamination. The employed modifications included a gradual decrease of the etching solution from 12M to 1M and a change in substrate position inside the etching solution from a horizontal towards a vertical position. Both methods aimed at reducing the redeposition of DyO particles, and resulted in a prevention of the (at least big) contaminants (although without a 100% success rate, most samples still showed small particles similar to the second image from the left in Fig. 3.5). Additionally, one should take care that the DSO surface never dries during the whole process as this greatly enhances the chances of redepositing particles.

Another tested modification of the recipe involved the quick etching of annealed DSO substrates with a HF-solution prior to the NaOH treatment. It is assumed that the aggressive non-selective HF etching would increase the roughness of the surface which in turn should lead to a faster NaOH etching time due to the increased surface area [165]. Therefore by reducing the time of the NaOH etching a reduced amount of redeposited particles is expected. In Figure 3.6, DSO substrates after the HF etching (30min sonication in DI water is followed by 30s in a buffered HF solution) and after successive NaOH etching (1h) are shown. After the Hf-etching, clearly a roughened surface is visible compared to the annealed surfaces and after the NaOH treatment, lesser particles are indeed observed. However the surface roughness of the steps is still highly increased. Potentially the short NaOH etching was not long enough

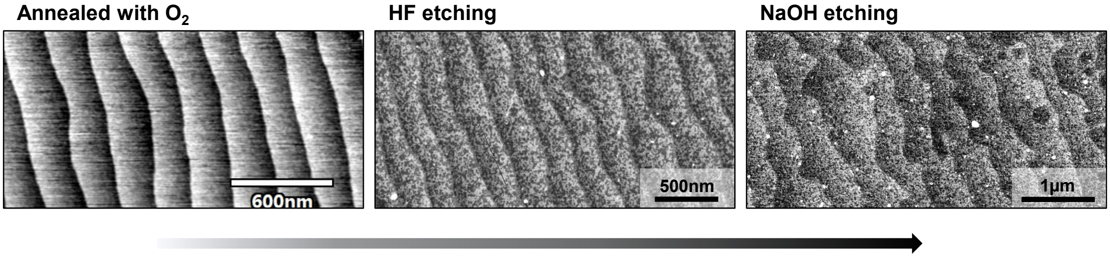

Figure 3.6: *Topography images of one DSO substrate during different stages of the Hf-modified etching recipe. An annealed DSO substrate (left) was etched for 30s in buffered HF-solution (center) and treated afterwards with the etching recipe using 12M NaOH for 1h (right).*

to full etch away the DyO layer which resulted in the enhanced roughness or a too long HF etching step resulted in too deep holes. Hf-treated substrates were not further tested however we want to note here that optimizing the etching-timings of the HF and NaOH steps might lead to an increased surface quality.

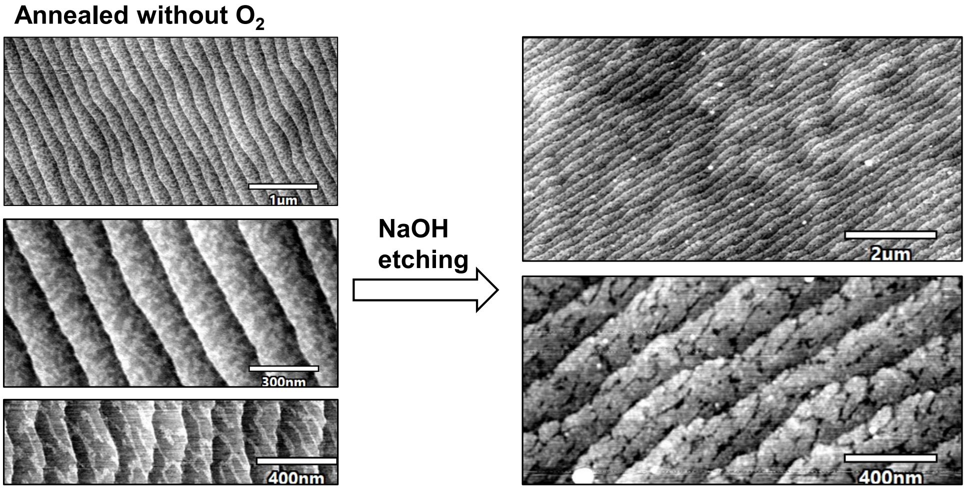

Figure 3.7: *DSO substrates annealed without oxygen before and after following NaOH etching. Left: AFM-topography images of the DSO substrates after annealing in ambient conditions. Right: Same DSO substrate after subsequent NaOH etching step.*

At last we investigated how DSO substrates annealed without or with limited oxygen flux evolved. In Figure 3.7 annealed substrates in ambient atmosphere are shown on the left. Clearly a mixed termination is visible in the two distinct height levels on the step surfaces. After etching (right side), fissured steps are observed, clearly indicating that only the DyO layers were etched in the previous mixed termination. These kind of substrates showed the lowest quality and the only one with clear indication of mixed termination which is why annealing without a sufficient flux of oxygen is not recommended.

3.1.3 SRO growth

After exploring different treatments for the DSO substrates, the different growth conditions for the SRO layer are investigated and how they are influenced by the substrate quality.

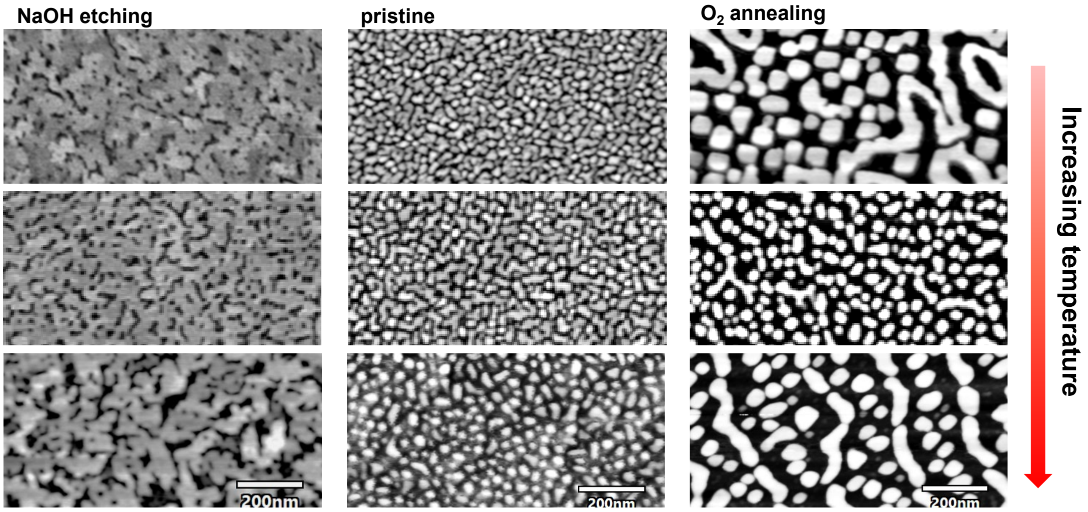

Figure 3.8: *SRO growth with different temperatures on different substrates. Left column: NaOH etched DSO substrates. Middle column: pristine DSO substrates. Right column: O_2 annealed DSO substrates. From top to bottom: Increasing deposition temperature from around 625°C to 675°C (43% to 47% heater power setpoints).*

Three different parameters were investigated in more details. First the influence of temperature on the SRO growth, second the influence of laser energy and third the influence of the deposition frequency. Before discussing the different experiments of varying parameters it is important to note that an exact analysis is hindered by the interdependence of PLD parameters for ideal growth conditions. To give an example, the temperature not only influences the mobility of the deposited material on the substrate which acts on the ability to reorganize for the preferred layer-by-layer growth, it also influences the volatility of the elements and can therefore influence the stoichiometry of the deposited material [155, 166]. The deposited stoichiometry itself however is depended on e.g. the oxygen pressure, the target to substrate distance as well as on the laser frequency [167]. Changing one parameter can thereby cause other parameters to shift for an ideal growth. Therefore, the following analysis should rather serve as a guideline, and investigate qualitative trends to improve the growth conditions as well as to identify which tuning of parameter is essential and for which a broader range of values is acceptable.

In Figure 3.8 the three columns represent the SRO growth onto different treated substrates. Left are the oxygen annealed + NaOH etched substrates, in the center pristine substrates are used and on the right side are substrates which are only annealed with O_2. First of all the growth on all substrates was not ideal, which is visible in the island formation of the O_2-annealed ones or in the trenches for the pristine and NaOH etched case. Especially the seen trenches in the O_2

annealed substrates could result from a badly terminated DSO surface. However, an overall trend is apparent when looking at the rows representing an increase in temperatures from top to bottom. Temperatures were tested from 43% to 47% power of the PLD heating system which corresponds to roughly 625°C to 675°C (see Fig. 2.4). For all cases a temperature stabilization time of approximately 1h was used. By increasing the temperature the dimensions of the trenches as well as the areas between the islands become larger and therefore a less uniform film is achieved. We therefore conclude to rather work with lower temperatures to limit the occurrence and dimensions of the trenches.

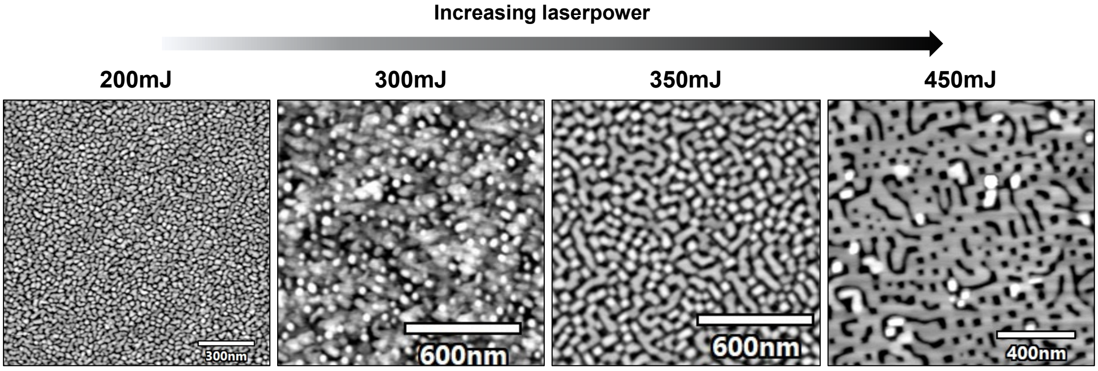

Figure 3.9: *Influence of the laser power on the SRO growth on pristine DSO substrates. From left to right: Increase of the used laser energy. Setpoints between 200mJ to 450mJ were tested.*

For testing the laser energy only pristine substrates were used for values between 200 mJ to 450 mJ (this value indicates the setpoint given to the PLD machine), which correspond to energy densities of 1.4 $\mathrm{J/cm^2}$ to 2.2 $\mathrm{J/cm^2}$, respectively. Resulting SRO growths are shown in Figure 3.9. For an increasing laser density an increase in the island size is visible. The 200 mJ deposition results in a grain like film with grain sizes of ~ 20nm. The AFM image of 300 mJ are of lesser quality and no grain sizes can be determined. For 350 mJ larger islands form with around 100 nm size and for films of 450 mJ we obtain a connected film with holes and small trenches. The growth with 450 mJ looks the most promising due to a connected film with flat surface, however the holes and defects still limit the follow up deposition of PZT layers.

Next, the laser deposition frequency investigated. Its influences on the SRO growth is shown in Figure 3.10. Again only pristine substrates are used and deposition frequencies from 1 Hz to 1 0Hz are tested. Starting from 1 Hz we observe the same trend as for the laser density. Lower deposition frequencies tend to form small grainy films whereas higher frequencies result in more connected and finally uniform films. The SRO film deposited with 10 Hz showed the best quality from all the so far tested recipes. No holes or defects are visible and the terrace structure of the underlying DSO substrate is reproduced, indicating an excellent layer-by-layer growth mode. We conclude, that higher frequencies lead to great improvement of the film conditions. We speculate that the higher frequencies prevent the formation of island growth especially during the first layers due to an increased growth speed and limited time for stabilization of defects while promoting a forced adaptation to the DSO lattice. However as

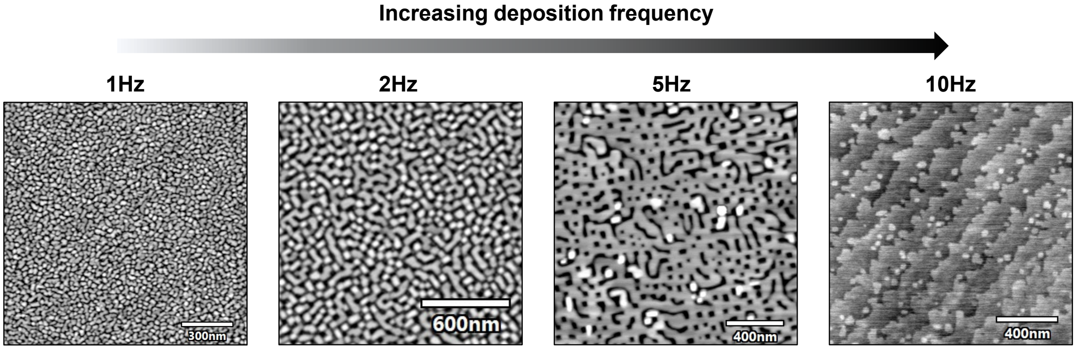

Figure 3.10: *Influence of the deposition frequency on the SRO growth on pristine DSO substrates. From left to right: Increase of the used laser frequencies. Frequencies between 1 Hz to 10 Hz were tested.*

Schraknepper et al. showed, exceeding the frequency of 10 Hz might shift the stoichiometry of the SRO film with resulting Ru-deficiency, which should be avoided.

A detailed look on the 10 Hz growth of Fig. 3.10 is shown in Figure 3.11 together with an image of the pristine DSO substrate used and an 3D image of the SRO layer representing the step structure. The used recipe is shown as well with all PLD-parameters. From the above tests, it can be concluded that for the used PLD Solmates-system, a higher frequency (10 Hz) as well as a limited temperature (≤625°C) and a minimum laser density of 2.0 J/cm^2 is optimal for good growth conditions of the SRO layer. It should be noted that there will exist other parameter combinations that will yield similar growths as it has been shown by various groups using e.g. low frequencies of 1-3 Hz [143]. However, despite the potential of even smoother surface topography and enhanced edge straightening, reachable by lower frequencies, the increased potential for island-growth are limiting an easy optimization.

After finding an optimal recipe for the SRO growth, we now discuss the influence of different (treated) substrates for the defect free growth. In Figure 3.12, 6 SRO growths are compared which all share the same SRO-recipe as given in Fig. 3.11. For these growths the deposition time for SRO layers was optimized to result in film of 20-25 nm. Different substrates are tested which include pristine DSO, DSO annealed with O_2 and 4 etched DSOs (all etched DSOs were previously annealed with O_2 as described in Fig. 3.4). The "etched (old)"-substrate was etched roughly 2 months before the SRO deposition, the "etched (old) + reetched" one was also 2 months old but was etched another time directly before the deposition. The "etched (new) #1 and #2" are freshly etched shortly before deposition. As seen before, the pristine DSO substrate resulted in a good SRO growth without defects even across larger areas. The "annealed with O_2" substrates gave a terrace like structure but with lots of holes and defects clearly worse than the pristine case and probably due to a mixed termination surface of the DSO. The "etched (old)" and "etched (old) + reetched" substrates both had lots of small particles on the surface, however both growths yielded excellent SRO films. The "etched (new) #1" had lots of bigger sized contaminants on the surface and as expected the resulting growth showed lots of defects

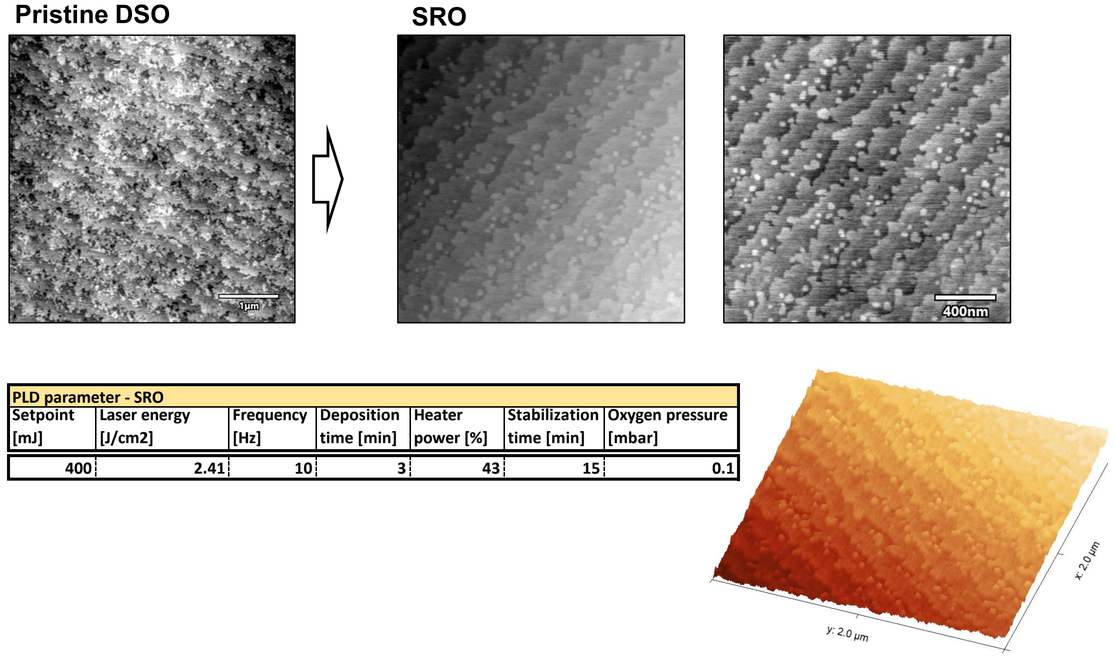

PLD parameter - SRO						
Setpoint [mJ]	Laser energy [J/cm2]	Frequency [Hz]	Deposition time [min]	Heater power [%]	Stabilization time [min]	Oxygen pressure [mbar]
400	2.41	10	3	43	15	0.1

Figure 3.11: *Optimized SRO growth on pristine DSO substrate. Left: Topography images of the pristine DSO substrate. Middle: Topography images of the optimized SRO growth. Bottom: Optimized SRO-recipe for the Solmates-PLD system and 3D visualization of the growth steps.*

and uneven steps. The "etched (new) #2" substrate however was much cleaner and therefore resulted again in a good growth of the SRO layer.

Based on these results we conclude that the surface treatment -opposed to some believes-only secondarily affects the SRO growth compared to the more important tuning of the PLD parameters. It is especially interesting that pristine as well as (nearly) perfectly etched substrates yield very similar depositions and that furthermore a minor amount of small particles on the DSO surface don't disturb the growth. Additionally, no degradation of the SRO growth is observed if the etching was done several months before the deposition. It is however advisable to check substrates before the growth to ensure that no excessive amount of particles got redeposited. Only the usage of annealing with oxygen or using substrates with big contaminants are not recommended as the resulting growths showed large number of defects in the SRO layers. We speculate that smaller particles are partially removed by the increased temperatures in the PLD chamber before deposition. Furthermore, since using pristine substrates resulted in similar growths, the following experiments were mainly carried out using the pristine DSOs, limiting the chances of contaminating the surface by treatments and making the whole PLD process simpler and more reliable.

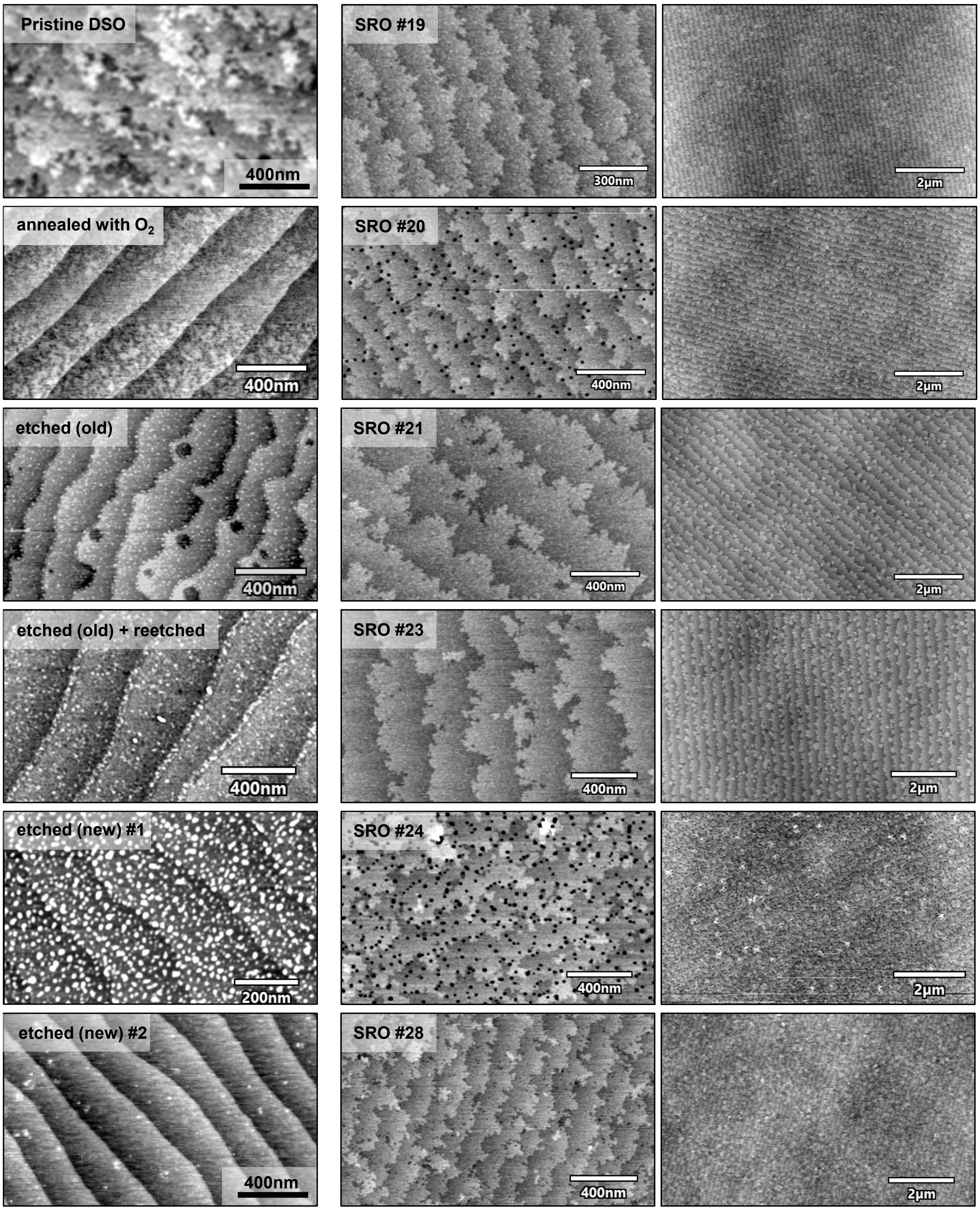

Figure 3.12: *Optimized SRO growth on differently treated DSO substrates. Topography images of the final SRO growths (detail image and overview image) using the optimized recipes are shown on the right side. From top to bottom: The different substrates: pristine DSO, annealed with O_2, "etched (old)", ""etched (old) + reetched", "etched (new)" and "etched (new) #2" are shown on the left side.*

3.2 PZT with SRO electrode - the search for vertical conduction

After successfully optimizing the SRO recipe the next step is to optimize the PZT layers on top. As discussed before, for the PZT layer we are looking to achieve a defect free film with an as smooth as possible surface. We expect to see the formation of an a-domain network due to the lattice strain from the DSO substrate. Furthermore, the aim is to achieve domain wall conduction for a-DWs as well as at 180°-DWs. a-DW conduction in strained PZT films has been reported in earlier works (see Section 1.4) while strong and stable strain-driven conduction in normally neutral 180°-DWs were first discovered within this work (while 180°-DW conduction in PZT films on STO substrates was observed previously by Guyonnet et al., their work showed lower DW conduction based on a different defect mediated mechanism [79]) and are in detail investigated in Chapter 4. Since the samples, in which first signs of 180°-DW conduction were observed, were fabricated around 8 years ago with a not longer existing PLD-system, this section aims to optimize the PZT growth to establish a reliable recipe to reproduce samples with 180°-DW conduction as well as to study the different process parameters and film characteristics necessary for the formation of the unusual conductive properties.

3.2.1 PZT growth optimization

For all following PZT growths shown (except if stated otherwise) the optimized SRO recipe from Figure 3.11 was used together with pristine DSO substrates. Based on various pre-tests, ferroelectric behaviour together with the formation of mainly out of plane polarized c-domains is achieved in nearly all samples even when holes and trenches are present, as seen in the TEM cross-section image and P-E loop of PZT #2 in Figure 3.13. Additionally the thicknesses of the layers (of all samples shown) were optimized to be around 20 nm/60 nm for the SRO/PZT stack (25 nm/59 nm are observed in Fig. 3.13 for PZT #2). The thickness of the SRO bottom electrode was optimized in order to guarantee high conductivity and to avoid the formation of islands and trenches observed for thinner SRO layers [168]. The PZT film thickness was chosen based previous works [94, 143], as simulations suggested a range of 50-70 nm for optimal DW conductivity (see also Chapter 1.4).

In Figure 3.14 the topography images of SRO/PZT films for three different parameter studies are shown. All images are scaled to approximately the same size to allow for comparison of the dimensions of the film's topography features. Here, first the topography images are studied to evaluate which growth conditions result in continuous films without holes and defects. In the next chapter 3.2.2, promising samples are tested for their electrical and ferroelectric behaviour. In the top row, the deposition frequency for the PZT growth is varied, in the middle row the temperature is increased and in the last row the process oxygen pressure is changed. The rest of the parameters were kept (mostly) the same to allow to differentiate between the effects of different parameters. The full list of all processing parameters for the shown samples are given in Appendix A.1.

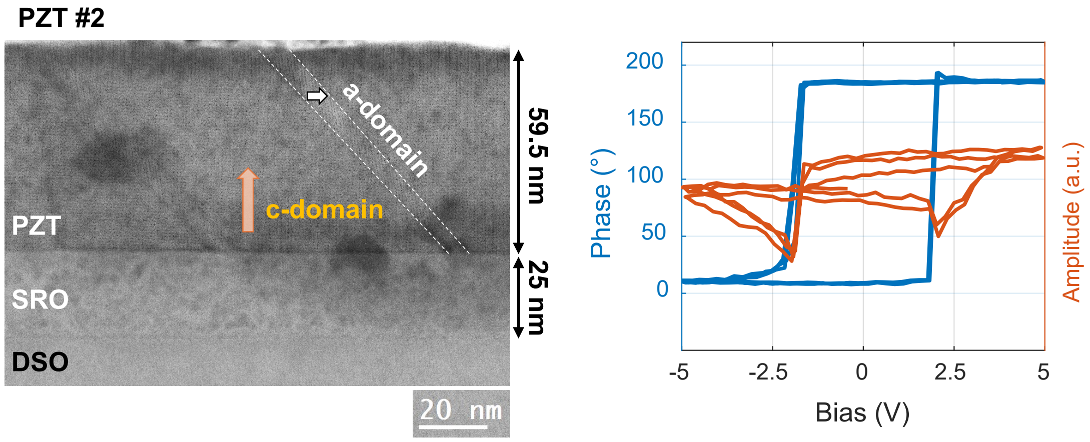

Figure 3.13: *STEM cross section image of PZT #2 on the left side and hysteresis loop of amplitude and phase of local piezo response probed by the AFM-tip on the surface of PZT #2 on the right side.*

For the frequency study all growths are done with 0.2mbar oxygen pressure and with 40% heater power. As seen in the first row for the lower frequencies (1Hz and 2Hz), defects and holes are present in the film topography. By increasing the the frequency (≥5Hz) the holes close and a continuous film is observed. It should be noted that the resulting "grain"-like structure results from a so called "wedding-cake" growth mode or Stranski Krastanov (SK) growth [169]. The Stranski Krastanov growth appears as a transition from layer-by-layer growth mode to the island growth mode. Especially in strained film, the strain energy of the single crystal layers can be reduced by the formation of islands and therefore promoting the transition to the SK mode. A magnified and high-resolution image of PZT #2 and PZT #20 are shown in Figure 3.15 in which the layered slices are observable. The surface roughness is slightly larger than observed on previous samples with pure layer-by-layer growth, however for films which show no apparent defects, the formation of a-domains (as seen in Fig. 3.15 for PZT #20) as well as the emergence of conductivity should not be influenced and therefore qualify for further investigations (see Section 3.2.2). Nevertheless, as shown, higher frequencies are beneficial for the growth of the PZT layers, due to limiting the evaporation of volatile cations like Pb as observed also in other works [170], and will be kept for the following growths.

The second row shows the change upon increasing the deposition temperature of the PZT growth (all growths are done with 10Hz and 0.2mbar). Although all samples are similar and no apparent defects are visible one aspect is interesting. The formation of a-domains is clearly more visible in the topographic images of PZT #20. As we will see later, other PZT samples form a-domains as well even through they are not readily visible in the topography images. If visible in topography, it means that the overall roughness of the wedding-cake structure is less than the height changes caused by the elastic a-domain formation. This is confirmed when looking at the overall roughness of the images, as sample PZT #5 and PZT #2 show values

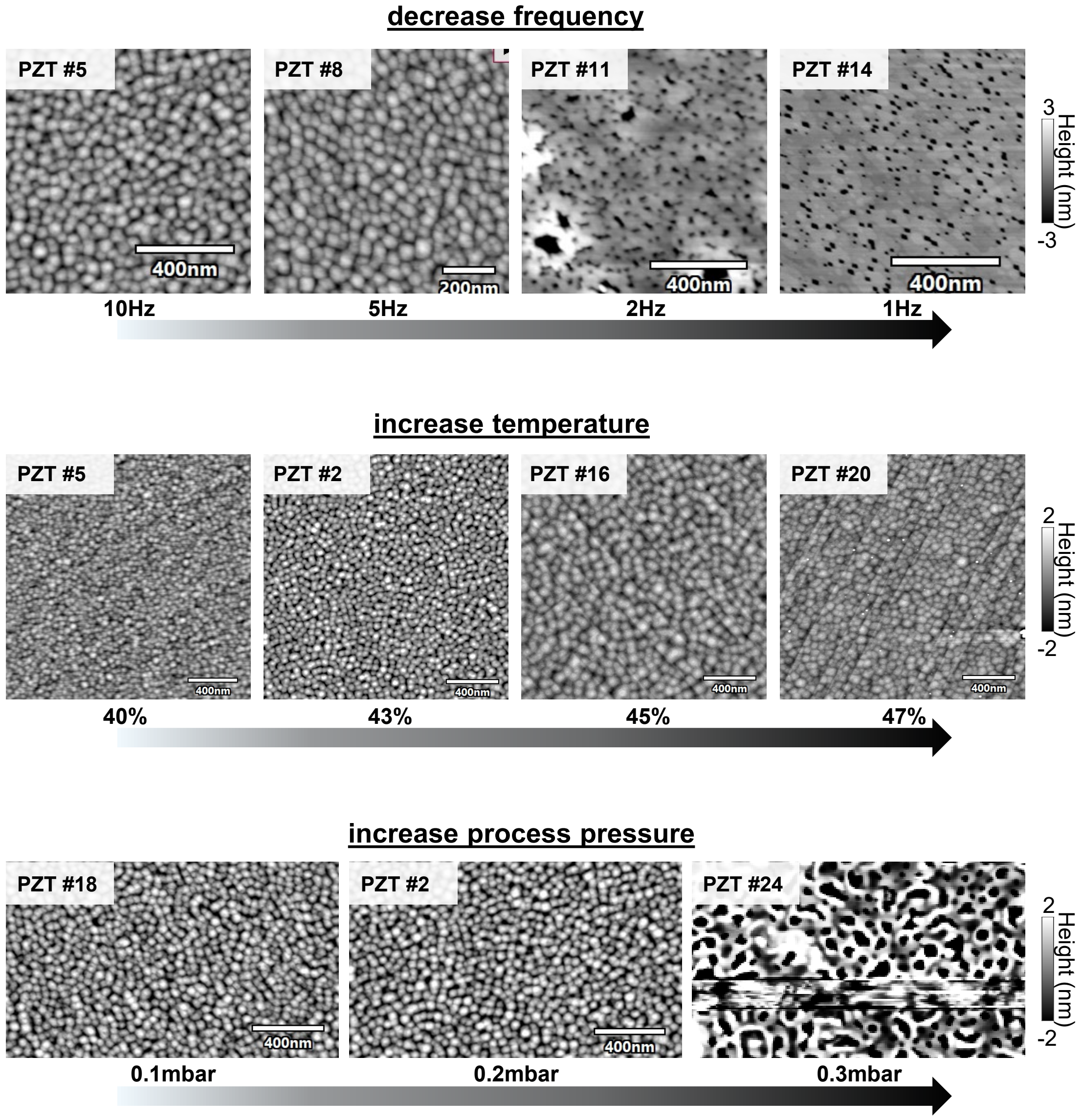

Figure 3.14: *Influence on different process parameters on the PZT growth. Only pristine DSO substrates are used and a 20-25 nm high-quality SRO layer using the optimized SRO recipe was grown prior to the PZT depositions. AFM topography images of the resulting pristine layers are shown. Top: Change in laser frequency going from 10 Hz to 1 Hz. Middle: Temperature increase from 40% to 47% (which corresponds to temperatures of 590°C to 675°C). Bottom: Increasing oxygen process pressure from 0.1 mbar to 0.3 mbar.*

of around 600 pm-800 pm RMS while PZT #16 and PZT #20 are as low as 480pm RMS. It is somewhat interesting that higher temperatures of 45% and more produce defect free films of higher quality. It was assumed that an increase over 600°C is disadvantageous for the PZT film growth due to the increased volatility of Pb cations for higher temperatures. However, as we can not be sure about the exact temperature of the growth (due to the missing temperature

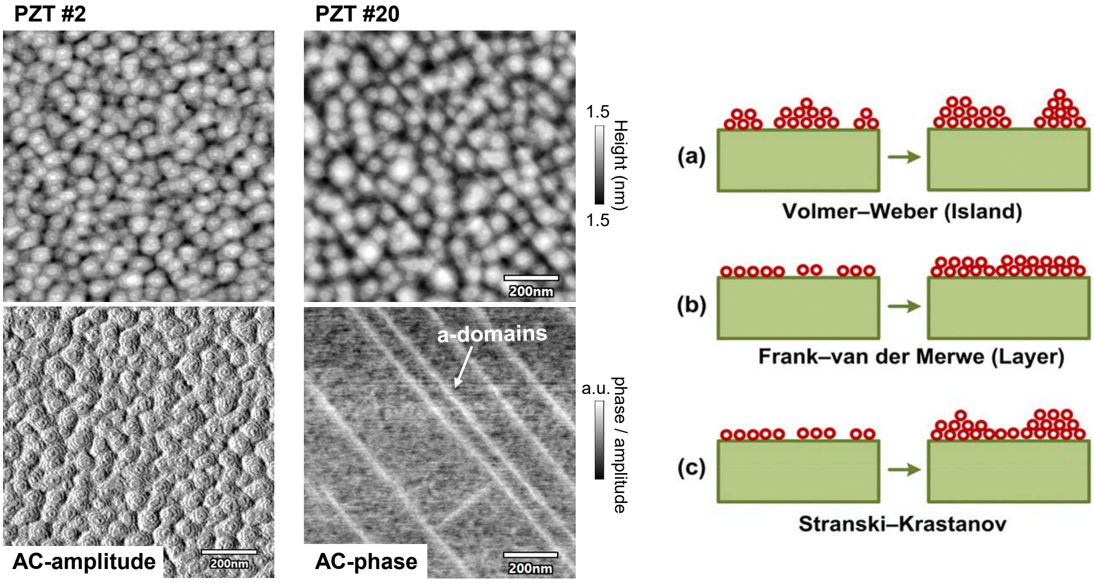

Figure 3.15: *High resolution topography (with AC-amplitude and AC-phase) image of PZT #2 and PZT #20 and schematic of the different epitaxial growth modes. Growth mode illustration adopted from [171].*

sensor) and excess Pb ions from the target (around 10% Pb excess) might help to compensate for the volatile ions, apparent temperatures of ≥650°C seem to result in better quality of the PZT films together with the used higher frequency of 10 Hz.

In the last row of Figure 3.14, three different process pressures are tested (with 10Hz frequency and 43% heater power). Clearly increasing the oxygen pressure above 0.2mbar dramatically destroys the film quality with large holes and non-uniform growth. For the lower pressures (0.1mbar and 0.2mbar) no apparent difference is detectable in topography. PZT #18 and PZT #2 will be interesting to compare for their conductive DW properties as the oxygen pressure during growth could influence the chemistry and availability of mobile charges. As these experiments were carried only shortly before submission of the thesis, the analysis of PZT #18 is subject of future work.

In conclusion, this study helped to narrow down the range of optimal parameters for sufficiently good continuous and flat PZT film growths on top of the SRO layers. Higher deposition frequencies together with rather higher temperatures and low process pressures yielded the best results. The wedding cake structure observed in nearly all cases might occur due to the relative high deposition frequency of ≥5Hz or is enhanced due to the non-treated substrates.

In the next subsection the promising PZT samples are investigated in more detail by piezoelectric force microscopy (PFM), conductive AFM (cAFM) and electrical characterization of the DWs to evaluate the ferroelectric behaviour, formation of the a-domains, switching behaviour and conductivity of DWs.

3.2.2 PZT sample characterizations - a-DW and 180°-DW conduction

In this subsection we will look into the samples PZT #2, PZT #5, PZT #8, PZT #16, and PZT #20 with a focus on conductive measurements of a-DWs and poled 180°-DWs.

First, PZT #5 and PZT #8 will be compared, which were grown with different frequencies (10Hz and 5Hz, respectively) both at 40% heater power. After that the 4 samples grown at different temperatures (PZT #5, PZT #2, PZT #16, and PZT #20) are compared.

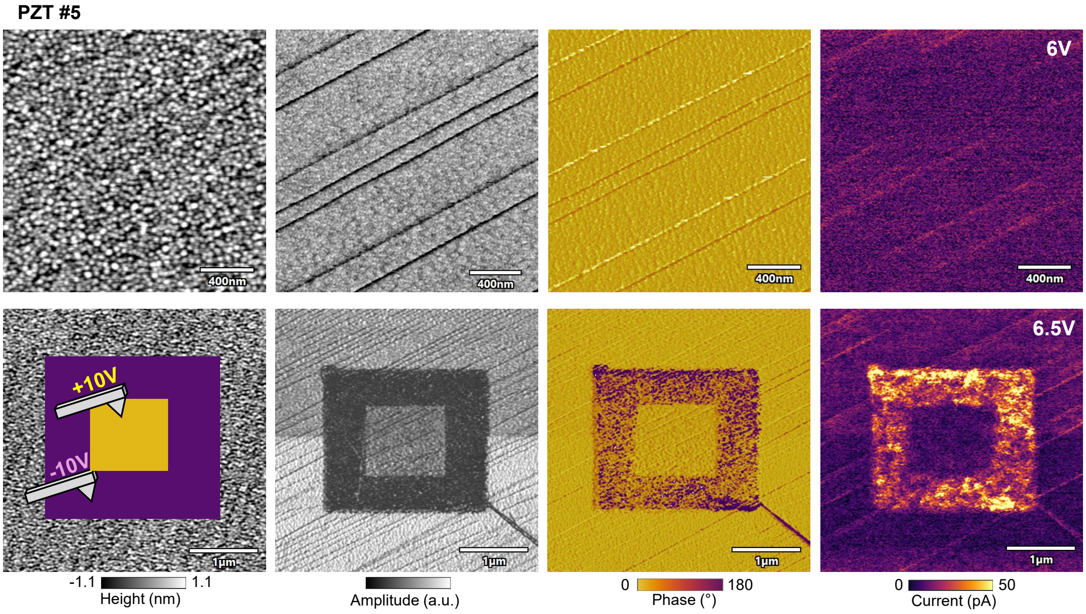

Figure 3.16: *AFM characterization of PZT #5. Top row: Topography, PFM and cAFM images of the pristine film. cAFM image acquired with 6 V sample bias. Bottom: Same type of AFM-images taken after a square in a square poling to observe the c-domain switching and create 180°-DWs. cAFM image taken with 6.5 V.*

In Figure 3.16, the sample PZT #5 is shown. In the top row, the pristine sample is imaged from left to right with topography, PFM-amplitude, PFM-phase and cAFM techniques. Long strip-like a-domains are visible in the amplitude image while the phase image shows an uniform polarization state of the c-domains. In cAFM nearly no contrast is visible with some slight hints of conduction along the a-domain boundaries for 6V. In the bottom row, a poling procedure was performed by first scanning with the AFM tip an area with +10V and subsequently a smaller area with -10V sample bias to create a square in a square poling. As seen in the PFM images, the poling procedure was suboptimal and not all c-domains switched. Following scans with cAFM with 6.5V bias showed an enhanced conductivity of the area but stays rather diffuse and not localized to the DWs. Since ±10V is the maximum of the AFM-controller with the Orca-tip holder, better results are expected if the poling could be enhanced (potentially by poling with higher biases). Nevertheless, the already high bias voltages used (6V and 6.5V) indicate suboptimal DW-conduction properties.

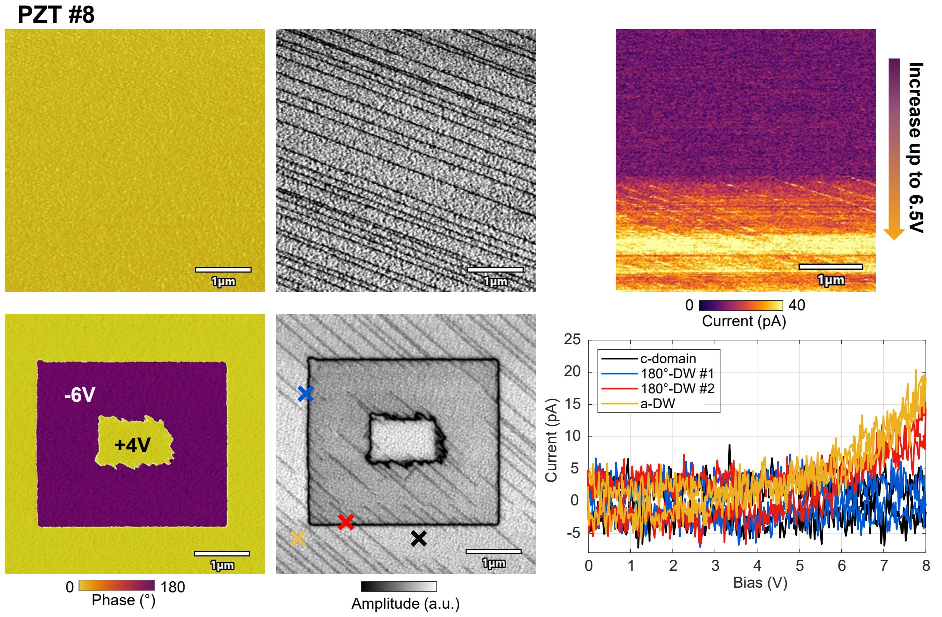

Figure 3.17: *AFM characterization of PZT #8. Left: PFM images before and after a square in a square poling are shown. Right top: cAFM image of the pristine PZT surface. The bias was increased during the scan from 0 V to 6.5 V. Bottom right: IV curves taken on different domain and DW types after the poling. Positions of the readout are marked in the PFM-amplitude image.*

Figure 3.17 shows the results obtained on PZT #8. Similar to PZT #5, long stripes of a-domains are recognizable from the PFM image and the c-domains are uniformly poled. A cAFM image with increasing voltage up to +6.5V bias showed rather non-localized conduction at higher voltages with some enhancement at the DWs. Similar square in a square polings were performed with -6V/+4V tip biases respectively. The resulting domain configuration showed a better switching of the c-domains with clear boundaries for the bigger square and some more diffuse switching for the smaller one. However, after the poling an unexpected distortion of the a-domain pattern is observed. Most of the long a-domains seem to be disrupted and start and end randomly in the c-domains, which could indicate that they are not properly formed and stabilized and hence most likely don't posses the needed charged a-DWs. For this sample, IV curves were recorded instead of an cAFM image. IV curves at different points on a c-domain (black), on an a-DW (yellow) and on two spots on the 180°-DW (blue and red) were recorded up to 8V. The current measurements showed no conduction within the resolution limit for the c-domain and one of the points on the 180°-DW and some low values of 15pA for the a-DW and the other 180°-DW spot. Overall, both samples, PZT #5 and PZT #8, are concluded to have rather poor non-DW associated conduction properties regardless of their deposition frequencies.

Next the temperature influence on the DW-conduction is studied. As seen from PZT #5 grown with 40% heater power, the DW-conduction was rather low and not localized. PZT #2 was

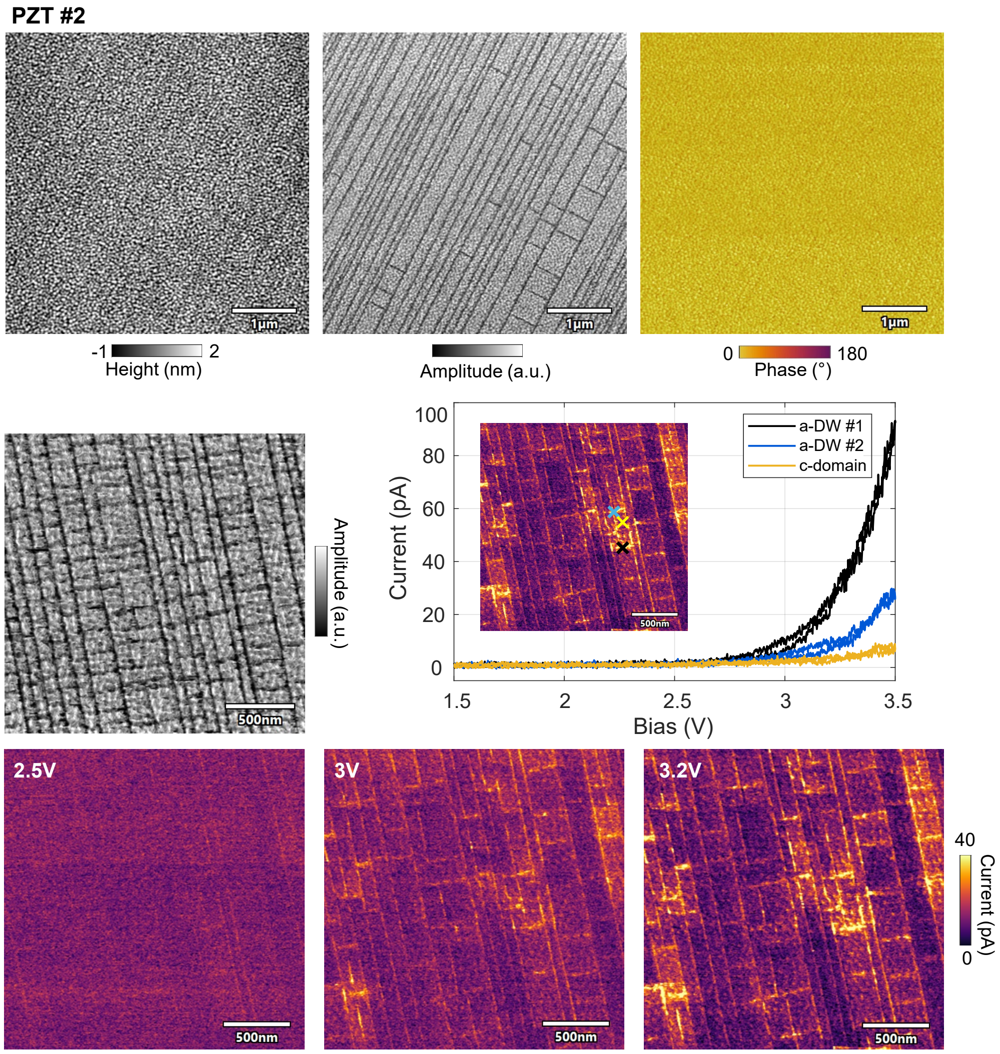

Figure 3.18: *AFM characterization of PZT #2. Top row: Topography and PFM images of the pristine sample. A cross-hatch pattern of a-domains is observed with some interconnecting perpendicular a-domains. Bottom: cAFM scans with different sample biases of 2.5 V, 3 V and 3.2 V, showing an increase of conductive response at the a-DWs. Center left: PFM amplitude image for the same area of the cAFM scans to related the conductive traces with presence of a-DWs. Center right: IV curves taken on a c-domain (yellow) and on two different a-DWs (black and blue) showing their conductive response up to 3.5 V.*

grown with 43% heater power and is shown in Figure 3.18. The a-domains predominately form in long stripes with some short interconnections, similar to the cross hatch pattern from previous works [94]. The uneven distribution of long strip-like domains and short perpendicular ones is a result of the slightly anisotropic epitaxial strain induced by the orthorhombic DSO substrate, which has two pseudocubic in-plane lattice parameters (see Section 1.4.1) [114]. Moreover, the population ratio of the a-domains is also influenced by the PLD growth conditions, the thickness of the film as well as annealing steps [172, 173, 143]. All c-domains are uniformly poled and cAFM scans with different sample bias voltage show discrete a-DW conduction starting from around 3V. Consecutive IV curves on a-DWs and on a c-domain show nearly insulating behaviour for the domain and clear enhanced conductivity at the a-DWs with values up to 100pA for 3.5V. An increase in short (perpendicular to the dominant stripe) a-domains is observed after continuous scanning by PFM or cAFM.

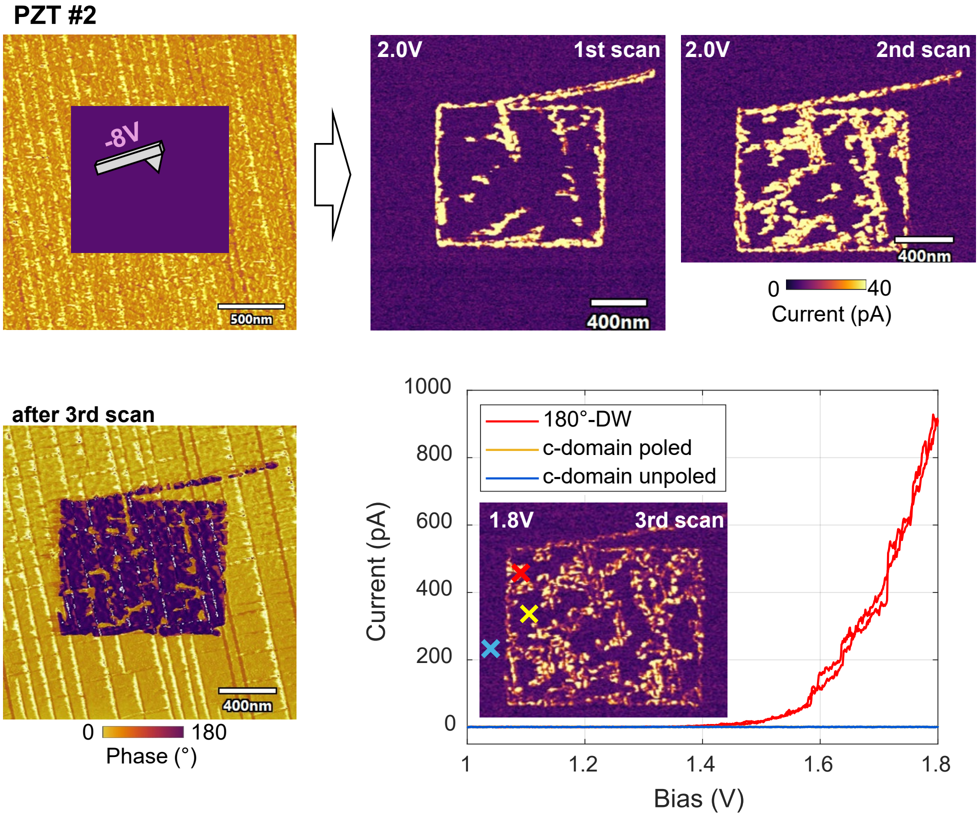

Figure 3.19: *180°-DW characteristics of PZT #2. Top: A 1 μm sized square is poled by application of a -8 V bias. Consecutive cAFM images taken with a 2 V bias show highly conductive traces following the border of the square together with some conductive regions in its center. In the second cAFM scan the amount of conductive traces inside the poled region is greatly enhanced. Bottom row: PFM phase image after the cAFM images. A partial backpoling of small yellow domains inside the poled purple square are observed, overlapping with the highly conductive channels observed in the cAFM image. IV curves recorded on one of the 180°-DWs and on insulating c-domains inside and outside the poled area.*

In Figure 3.19, the sample is poled by -8V and imaged by cAFM with 2V. Clear, and this time highly conductive lines corresponding to the outline of the poled area are seen. IV curves taken on a 180°-DW yield up to 1nA for only 1.8V compared to completely insulating c-domains inside and outside of the poled area independent of their polarization state. It is important to check both poled and unpoled c-domains, as it rules out polarization-driven resistive switching [174], and further strengthens the conclusion that the observed conductivity originates only from the 180°-DWs. However, by scanning the same area multiple times an enhancement of conductive lines inside the poled region is seen which is a result of a partially backpoling of the c-domains (proven by a followed PFM scan in which small yellow domains are seen inside the poled area, see Fig. 3.19).

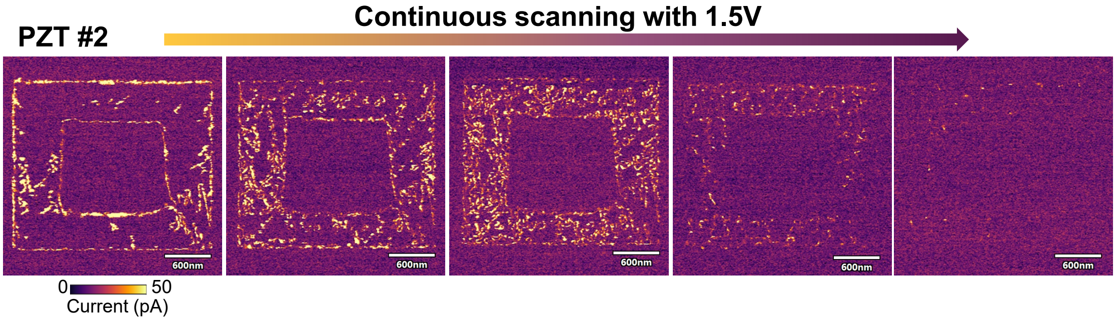

Figure 3.20: *Stability test of the conductive channels and c-domain poling in PZT #2. A square in a square poling was first performed followed by consecutive cAFM images of 1.5 V. 5 cAFM images of the series are shown including the 1st scan (left side) and last scan (right side). A continuous decrease of the conductive response together with an increased density of conductive traces for continues scanning is observed. In the last image nearly no conduction remained.*

Figure 3.20, studies this stability issue in more detail. A square in a square poling is performed and consecutive cAFM images are taken with a low voltage bias of 1.5V to reduce the effect of backswitching. Nevertheless, after around 10 scans (5 shown in the figure), no conductive response is measurable in that area and followed PFM images revealed the complete backswitching. As the coercive field was determined to be around 2V (see Fig. 3.13), continuous scanning with 1.5V is generally not be enough to promote the backswitching. However, the non-uniform electric field at the tip apex together with the effect of scanning and applied mechanical pressure might be enough to decrease the stability. Further experiments are needed to see if this sample can be used for device applications in which electric fields are more uniform due to the integration of electrodes.

The next sample, which is investigated in detail is PZT #16 grown with 45% laser power, see Figure 3.21. As seen in the topography image, some a-domains are visible as discussed before. cAFM images of the pristine area yield similar results as seen for PZT #2 in Fig. 3.18, with conduction at a-DWs starting from around 3V (not shown). Therefore directly the behaviour under poling and conduction of the 180°-DWs are checked. A 2µm square is poled with +4V sample bias. Under the application of bias, a reorganization of a-domains is observed with the formation of more interconnecting short domains. The cAFM images taken with 2.1V on the poled area show clean and conductive traces of the 180°-DW. IV-curves were probes at two different positions indicated as red and blue with readout voltages of 2.8V. At the red spot a very stable readout of around 8nA is observed for tens of consecutive pulses over 2 seconds. At the blue spot the observed conduction was higher, between 50nA to 120nA. The reason of the big changes in conduction readout could be some small movement or reorganization

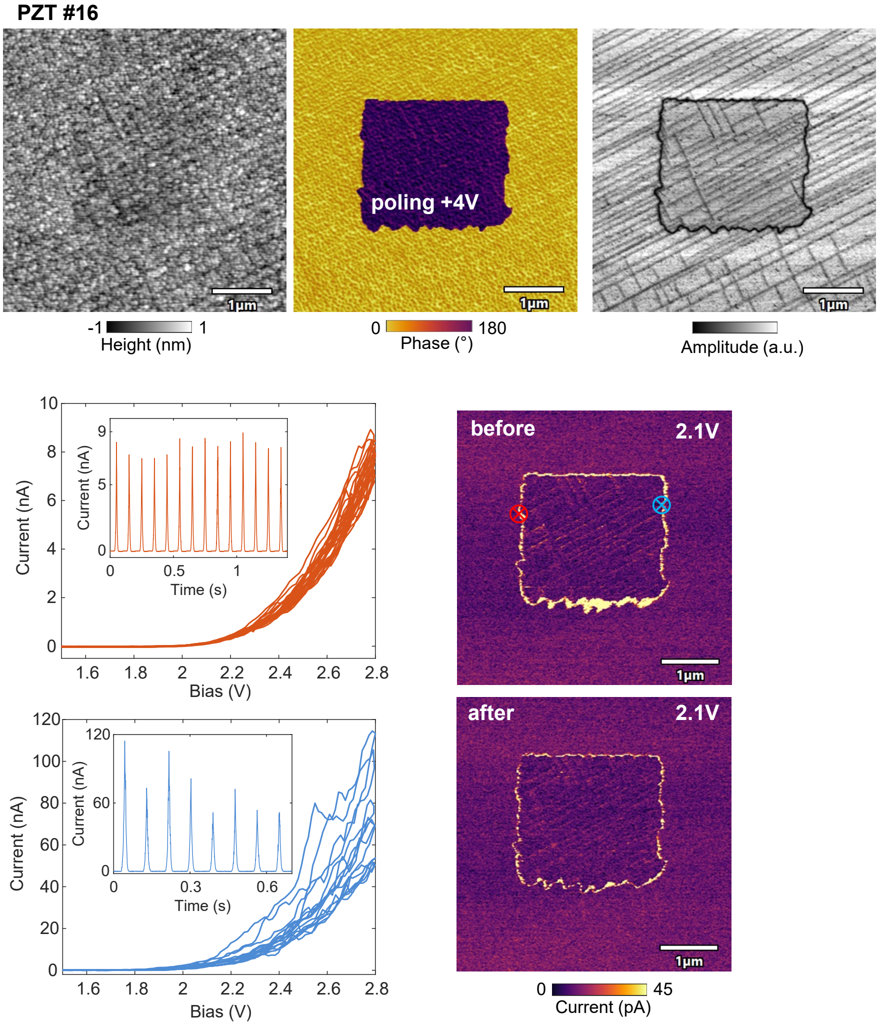

Figure 3.21: *AFM characterization of PZT #16. Top row: Topography, and PFM images after a poling, done by 4 V. PZT #16 is the only measured sample with pristine downwards polarized c-domains, identified by to the poling direction. A dense a-domain network is observed in the PFM-amplitude image. Bottom left: Multiple IV curves consecutively taken on two different spots on the 180°-DW (blue and red). Inserts show the current response in the time-domain. A very stable 8 nA conduction is seen for 180°-DW at the red spot, while at the blue spot higher current values (up to 120 nA) are recorded together with an increase in fluctuation from readout to readout. Bottom right side: cAFM images before and after the IV measurements show no change in position of the conductive channels indicating their stable character.*

of the 180°-DW, however the cAFM images from before and after the IV curves showed no visible change of the conductive path. Nevertheless, the persistence of 180°-DW conduction for tens of pulses shows the enhanced stability within this PZT sample compared to PZT #2. The difference of the conductivity with respect to different points on the 180°-DW is expected, as the conduction is known to be non-constant along the DW-length (detailed investigations are found in Section 4). The seen stability is most likely also attributed to the fact that the orientation of the pristine grown film is in the opposite direction compared to the previous samples (a positive bias is needed to switch the pristine c-domains compared to a negative bias for the other PZT samples). Based on the poling direction, the pristine c-domain orientation of sample PZT #16 can be determined to be downwards oriented. Since the current readout is done with positive voltages due to an asymmetry in the IV curves (no conduction is observed for negative voltages), the poled upwards oriented domains are aligned with the field direction of the readout voltage and prevent a partial backswitching.

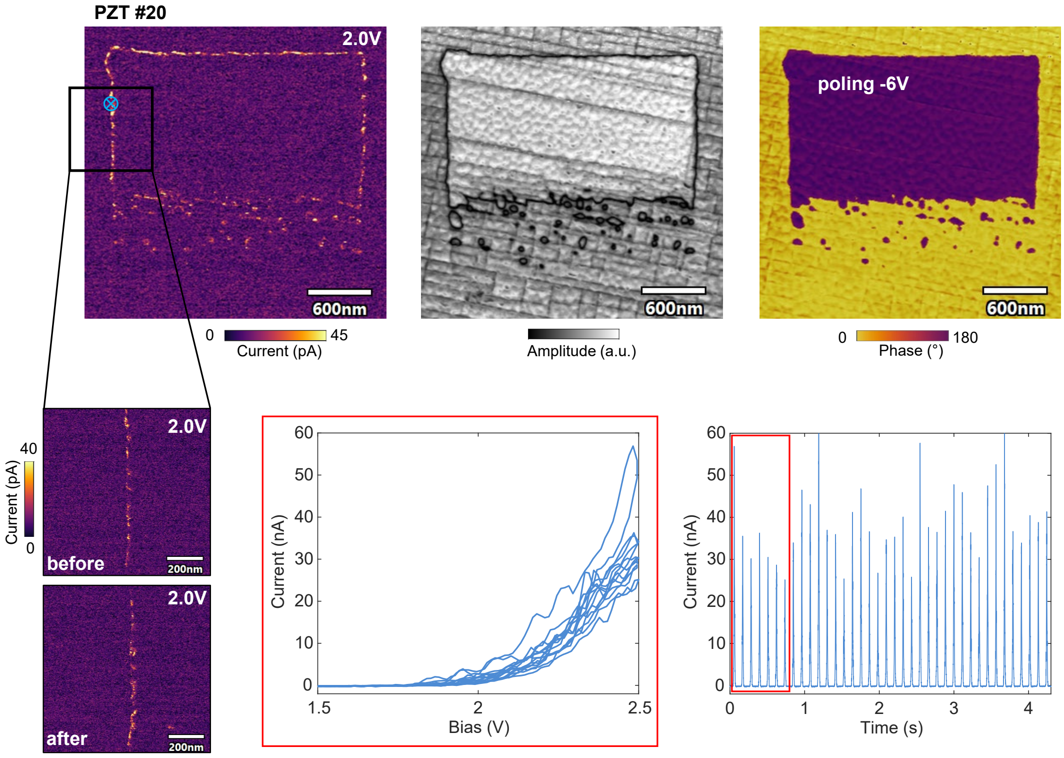

Figure 3.22: *AFM characterization of PZT #20. Top row: cAFM and PFM images of a poled originally square area by application of a -6 V sample bias. Already for the acquired PFM and cAFM a partial backswitching of the bottom part of the poled area is observed. Bottom row: Conduction readout of the 180°-DW at a spot indicated in the cAFM image. A total of 35 pulses are applied consecutively and the conduction is measured. A persistent conduction of tens of nanoampere is collected. The first 5 readouts are plotted as IV curves in the center. On the left side, the area where the conduction is measured on the 180°-DW is imaged before and after taking the IV curves by cAFM images at 2 V. No signs of deformation of the DW is observed.*

PZT #20 is the last sample of the temperature experiment with a growth temperature of 47% heater power. In Figure 3.22 the results are shown. In general, similar characteristics as to PZT #16 are seen, however the polarization direction was upwards oriented like in PZT #2, which required a negative bias to pole the pristine sample. This resulted in less stable polarized domain states as seen in the PFM images in which the bottom part started to backswitch. Despite this, probing IV curves yielded persistent current readout of around 30nA for 2.5V which was the highest in all samples. Before and after cAFM images confirmed, that the 180°-DW did not shift during the measurement of 4.5 seconds and that the current originated from the non-volatile DW.

In conclusion, the higher growth temperatures enhanced the DW conduction drastically from nearly non-existent for 40% to tens of nanoampere for reasonable voltage biases of ≤3 V. The increased temperature during growth is expected to change the defect density and result in higher number of mobile chargers and hence an increased conductive response. PZT #16 was the only sample with pristine downwards oriented c-domains and therefore showed the highest stability of written domains, potentially the most useful for further device applications.

3.2.3 PZT self-assembled nanoislands

Besides the samples studied above, other PZT samples were grown which showed non-continuous films but might potentially be useful nevertheless (process parameters are given in Appendix A.2). In Figure 3.23, some variations of self-assembled PZT nanoislands are shown, grown with different PLD-parameters. A change from a quasi-continuous film with high density of holes and trenches towards localized nanoislands is seen. PZT-NI #6 showed the most promise in regards to island sizes and island isolation.

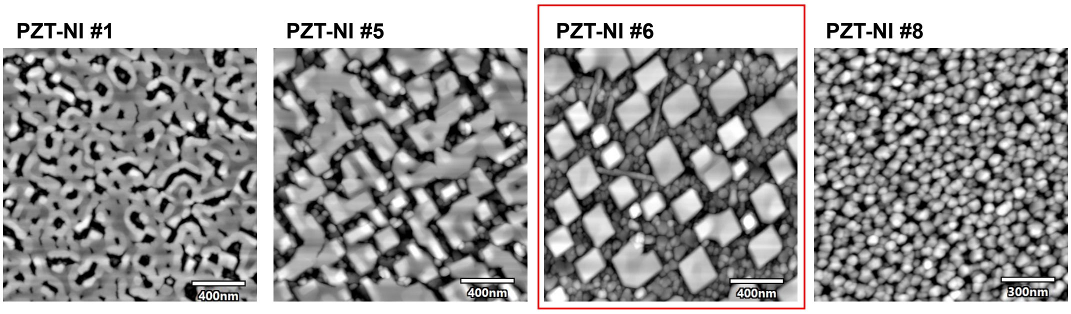

Figure 3.23: *Different formation of PZT nanoislands based on varying growth conditions. AFM topography images of the fabricated PZT nanoisland samples. For PZT-NI #1, the PZT film still shows a connectivity and no isolated islands. For PZT-NI #5 first isolated islands form with different sizes in irregular rectangular shapes. PZT-NI #6 shows the most well defined nearly square like nanoislands with persistent spacing between each islands. In PZT-NI #8, no real islands formation is observed and the "nanoislands" are small and densely packed.*

The nanoislands of PZT-NI #6 are 100 to 300 nm wide and around 30 nm high (this height might not be the total PZT film thickness as the surface layer is not determinable by AFM. Cross-section TEM experiments are needed to precisely evaluate the stack formation). First disregarded, later checks by PFM and cAFM revealed that each nanoisland forms uniformly poled switchable c-domains with excellent ferroelectric characteristics (sharp P-E loop with coercive field of roughly ±2.5 V), compare Fig. 3.24.

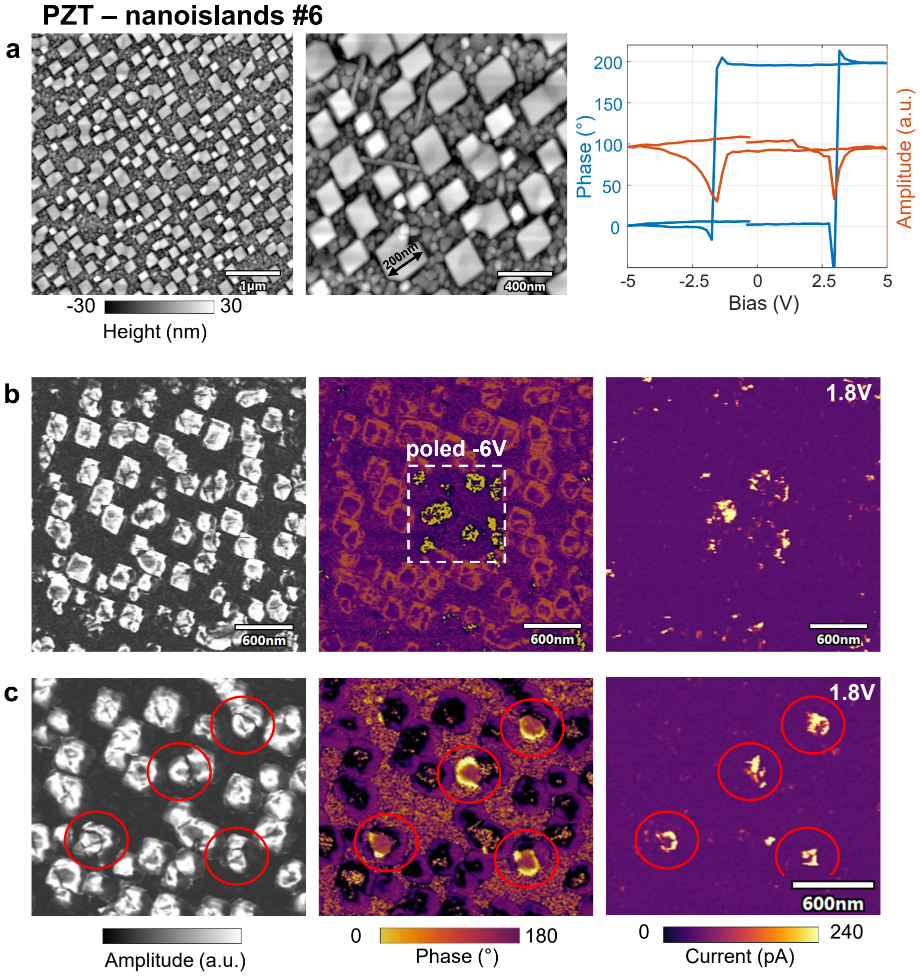

Figure 3.24: *AFM characterization of PZT-NI #6. a) topography large and small scale AFM image showing the overview of the nanoislands. Islands are formed as squares with sizes of 200 nm. Little variation between the nanoislands are seen and most of them exhibit the same shape and size. On the right side, a hysteresis loop of amplitude and phase of the local piezo response probed by the AFM-tip on one of the islands is shown, showing the excellent ferroelectric switching and a local coercive field of around 2.5 V. b) PFM and cAFM images of the nanoislands for which the center was poled by -6 V. The pristine nanoislands seem to form uniformly polarized nanosized c-domains. In cAFM a conductive response loosely matching the square "boundary" (indicated in white dashed lines) is observed. c) Local switching of individual nanodomains. PFM and cAFM images show the response after 4 nanodomains (marked by red circles) are locally switched by placing the AFM-tip onto them and applying a -6 V pulse for some hundreds of milliseconds. The subsequent cAFM image taken with 1.8 V shows a highly conductive response for the switched domains.*

Moreover the domains are switchable by either the same tip-scanning method used in Chapter 3.2.2 or by placing the tip steadily onto the nanoislands and applying a short (coercive field exceeding) voltage pulse. Both methods and correlating cAFM taken afterwards are shown in

Fig. 3.24 b) and c). In b), a square is poled by applying -6 V sample bias and the cAFM image was taken with 1.8 V. A clear conductive enhancement is shown for the poled area.
In c), the tip was placed at the nanoislands marked by the red circles. Voltage pulses of -6 V for several hundreds of milliseconds were applied and the cAFM image was taken with 1.8 V sample bias. Only the nanoislands which were switched by the tip showed an enhanced conductivity. Most likely the conduction results from 180°-DWs formed in the nanodomains however high resolution experiments are needed to verify and associate the observed conduction response to the existence of 180°-DWs.

The nanoisland sample PZT-NI #6 exhibit interesting properties due to the intrinsic small sizes of their nanodomains coupled with nanoampere-scale conduction responses when polarization is switched. Potential device ideas could exploit the nanometre size resisitve switching if the seen conduction can prove to be non-volatile. The seen nanoislands probably form due to an island growth, potentially already present for the SRO layer (compare islands growth in SRO layers in Chapter 3.1.3). However, more specific experiments need to be carried out to study the nanodomain formation, the formed conductive channels and their stability.

3.3 Summary

In summary, within this section, the growth conditions for highly tetragonal PZT films (Zr:Ti = 1:9) and $SrRuO_3$ bottom electrodes, onto $DyScO_3$ substrates for the employed Solmates PLD-system are investigated. Besides optimizing of the film properties, the formation of conductivity at 90°-DWs and 180°-DWs in the PZT films with respect to various process parameters is explored. First, it has been shown that pristine DSO substrates can be used for the growth of defect-free SRO/PZT layers without the need for pre-deposition treatments. The use of higher frequencies of 10 Hz proved to be ideal for the deposition of both the SRO and PZT films achieved by a predominantly layer-by-layer growth. The formation of expected a-domains was observed due to the lattice strain, induced by the DSO substrate. It was shown that the process temperature possessed a major role in the formation of enhanced and localized conduction at the domain walls. While changing the oxygen pressure during the controlled cooldown was not tested within this work, it is expected to also greatly influence the conductive properties and should be one of the key aspects of future work for tuning of the domain wall conductivity. Resulting PZT/SRO/DSO samples with conductive a-DWs and 180°-DWs could be fabricated and the non-volatile character of the conduction could be verified. Furthermore, PZT samples with self-assembled isolated nanoislands could be produced. Due to the intrinsic nanometer size of formed c-domains inside the nanoislands and observed highly conductive response of several nanoampere upon domain switching operations, these samples are potentially interesting. Further work needs to be carried out to carefully evaluate the properties of the seen conductivity. Despite the achieved reliable fabrication of samples with conductive domain walls, further AFM-measurements revealed issues with the stability of poled c-domains which directly influence the stability of the 180°-DW channels. These limitations need to be addressed and further optimized to enable the integration of the newly fabricated sample for stable and reliable device applications. Due to these issues, the detailed study of the unusual high conductivity at 180°-DWs and further device realizations presented in the next chapters, are performed on previously fabricated samples from the lab of Prof. Nava Setter, which showed the same unexpected conduction response at 180°-DWs while exhibiting a higher stability of the written domains.

Nevertheless, the presented studies of this chapter provide reliable growth recipes for high-quality SRO and PZT layers together with the verified formation of conductive domain walls for the Solmates PLD-system at EPFL. They further extend the insight into the interplay of the process parameters onto the tuning of the domain wall conductivity and lay a foundation for future work on the improvement of the stability and towards samples with in-plane conductive domain walls.

4 Conducting domain walls in strained PZT

In the previous chapter, the fabrication process of epitaxially grown PZT thin films was discussed and optimization steps were presented to promote the emergence of conductivity at the domain walls. In this chapter the domain walls, especially the artificially created 180°-DWs and their conductive properties are investigated. First, in Section 4.1 the formation of 180°-DWs by poling of c-domains is discussed and domain wall stability and tendency to align with the pristine a-domain network is studied. Next, the conductive properties of the normally neutral 180°-DWs are examined in detail which led to the observation of an unexpected, highly enhanced conductivity compared to previously reported results. In Section 4.2, the origin of the unusual conductivity is studied by temperature dependent measurements, different electrode materials, phase field simulations and TEM analysis. The combination of these studies showed that the normally neutral 180°-DWs are interconnected to the dense network of a-domains inside the film, which results in a distortion from their neutral structure and the emergence of charged segments. The content of this chapter is based on the work presented in [175, 152, 176]

4.1 Neutral 180°-DWs and their unusually high conductivity

As the properties of the a-domains in PZT-films and their DW-conductivity for carefully engineered strain conditions have been heavily investigated [94, 143], the focus of this chapter is put onto the other type of domain wall, which can be found in these PZT thin films. More precisely, 180°-DWs will be studied, which can be created by polarization switching of the out of plane c-domains. By applying an electric field, opposite to the c-domain polarization, above the coercive field, domain switching is promoted and 180°-DWs form at the boundaries of the switched and unswitched domains.

4.1.1 Domain wall formation and domain realignment

Polarization switching in ferroelectric tetragonal crystals along their c-axis present one of the most simplest cases. Ideally, no deformation to the crystal lattice is introduced in the system by partially switching of the domains as it presents a pure ferroelectric switching. Switched domains are therefore not detectable in a pure topographical analysis in contrast to ferroelastic domains, which result in changes of the PZT surface due to the 90° unit cell rotation at the boundary from the a-domain to the c-domain. The domain walls, which separate switched and unswitched c-domains in tetragonal PZT films are the prototype of neutral 180° (or Head to Tail) domain walls and are expected to form straight two dimensional vertical interfaces.

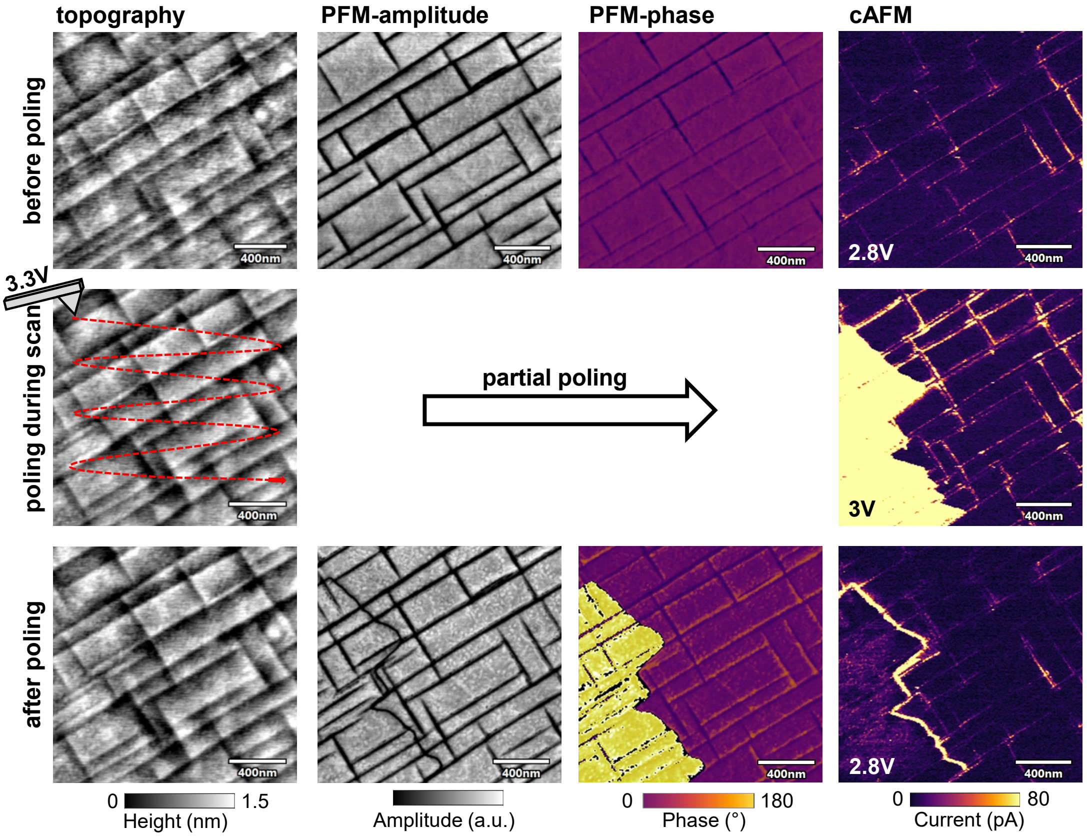

Figure 4.1: *Creation of conductive 180°-DWs by partially poling. Topography, PFM and cAFM images taken on the PZT surface. Top row: Imaging of the pristine PZT film. The weakly conducting a-DW network can be seen in the cAFM image taken at 2.8 V sample bias. Middle row: Bias voltage increase to 3.3 V during a cAFM scan leads to the partial poling of c-domains on the left side of the image. cAFM image shows high conductivity, resulting from the volatile switching currents. Bottom row: Imaging of the same area after the partial poling. The area, which was seen as highly conductive before is confirmed to be poled by 180°. At the botder of the two c-domains a 180°-DW is observable as a black line. cAFM image taken with 2.8 V shows conductive traces overlaping with the 180°-DW position.*

In Figure 4.1, the pristine properties of a PZT/SRO/DSO sample, similar to the ones fabricated in Chapter 3 and to the one investigated in previous work by Stolichnov et al. [94] are studied. The sample in Fig. 4.1 with layer thicknesses of around 60 nm for PZT and 20 nm for SRO, is examined with respect to its behaviour during and after a partial poling. In the top row the topography, PFM and cAFM images of a pristine area are shown. The cross-hatch pattern of a-domains in the PFM image, the uniformly polarized c-domains and the conductive traces of the a-DWs in the cAFM image are clearly visible. During the next cAFM scan (middle row) the voltage is slightly increased (from 2.8V to 3.3V) to overcome the coercive field voltage. Strong current signals (saturating the current sensor of 10nA) are picked up starting from the left side of the image in an arbitrary shape. Consecutive PFM scans (bottom row) reveal the partial switching of the left part of the image and the creation of a 180°-DW. As expected from 180°-DWs their presence is not visible in the topography image and can only be revealed by PFM imaging. The arbitrary shape of the poled region is explained by the fact that a voltage bias close to the coercive field value was chosen. Therefore and by taking into account a change in the contact resistance due to the AFM-tip scanning, only a part of the image was poled. To eliminate such effects a simple increase of the bias is enough to ensure a well defined poling area. Consecutive cAFM scans, now with again lower 2.5V bias show that most of the current signal from the previous cAFM scan inside the poled region is gone, leaving only a conductive line at the border to the pristine domain. By carefully comparing the cAFM and PFM images it is obvious that the newly formed conductive channel overlap with the created 180°-DW. The current signal, which was imaged during the poling step and which covered the whole area of the poled domain, is attributed to switching currents. These currents originate from the bound charges from the top and bottom surfaces of the domain. By switching the domain, the bound charges needs to be reversed and the carrier movements are detected as current spikes (or areas in case of a continuous scan). Their volatile behaviour is observed by the fact that consecutive cAFM scans show no conduction inside the poled regions. In contrast, the conductive channel formed at the c-domain boundary at the location of the 180°-DW seem to be persistent and is therefore not attributed to switching currents. Previous works showed that mobile defects such as oxygen vacancies can accumulate at neutral DWs such as 180°-DWs and give rise to low, thermally activated conduction (details in Chapter 1.2.1). However, the current values observed in Fig. 4.1, are orders of magnitude higher than for the simultaneously present partially charged a-domains or for other observed 180°-DWs in different PZT systems [79].

To further verify that the newly formed conductive channels are really associated with the 180°-DWs, extended experiments of domain wall movement by poling operations were performed. Figure 4.2 starts from the last polarization state seen in Fig. 4.1. This time the voltage bias is increased to 4V to ensure a well defined switching. First a smaller ~500nm large square (red dotted outline) is written in the top right area similar to the previous experiment. Consecutive cAFM and PFM scans show once again the appearance of a conductive line at the position of the 180°-DW. Next, another square is written inside the first one, but this time the writing bias is reversed to -3V (green outline). By this, the area is backswitched to its pristine polarization state. Based on the followed PFM and cAFM images, it is seen that also this operation creates 180°-DWs together with associated conductive channels independent of the writing bias polarity. In the last step, the response of the conductive channels upon moving the 180°-DW is investigated, compared to creation of new isolated DWs. By using a -3V bias and partially

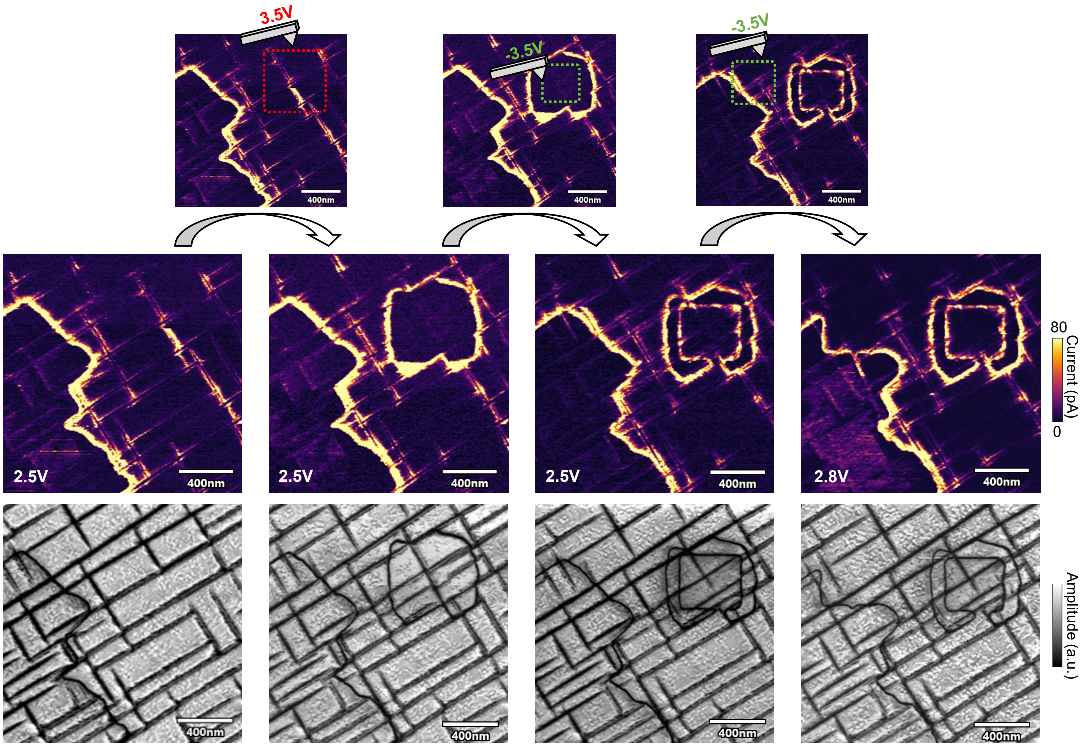

Figure 4.2: *180°-DW movement and the effect on the conductive channels. Starting point is the last cAFM image from the previous figure with an arbitrary 180°-DW formation on the left side. On the top the poling steps are depicted from one to the other image. In the center, cAFM images of the different stages are shown and on the bottom PFM images confirm the position of the DWs. From left to right: First, another square is poled in the top right corner with conductive boundaries. Second, a smaller square is backpoled inside the just poled domain again with conductive boundaries. In the last step the domain boundary on the left side is moved downwards. The conductive channel follows the new DW position seen in the PFM amplitude image.*

scanning from the top side onto the first written feature, a precise rearrangement of the existing 180°-DW as well as the conductive channel is observed to match the new defined outline. This type of movement control of 180°-DWs by electric fields is well know, however this study confirms the tight correlation of the conductive signal to the position of the domain wall together with the possibility of rearranging not only the DW itself but also the written conductive channels. It also verifies that the conduction is bound to the actual presence of the DW and not to the poling operation as a moving or removal of the domain wall leads to a complete vanishing of the conductive response.

Despite the excitement around the observation of the enhanced conductivity and the verified correlation to the 180°-DWs it also raised new questions, since the origin of this conduction was not expected. As mentioned earlier, polarization switching in tetragonal PZT is supposed to be a trivial case in which completely straight and neutral 180°-DWs form. At neutral domain

walls, there exist no polarization discontinuity which in comparison to charged domain walls has been shown to mediate a strong current response (see Chapter 1.2.1). The here observed conductive channels however show a strong current response in the nanoampere range and even orders of magnitude higher than that of charged 90°-DWs.
Interestingly, by careful analysis of the cAFM images and monitoring of the shape of the poled domains over time, a slight adaptation of the written 180°-domains to the underlying a-domain pattern is observed. Moreover, it seems like the 180°-DWs want to overlap with existing a-domains to form a supposedly more energetically favorable position. These observations promote a hypothesis to explain the conduction at normally neutral 180°-DWs through a dense a-domain assisted network. Following this idea, the observed conduction at 180°-DW would stems from a set of a-DWs, potentially small enough to not be resolvable by PFM. It has been shown that the a-DW conduction results from a bending from the neutral 45° angle, giving rise to a charged DW with potentially high conductivity. Further bending or interconnection to more a-DWs could explain the orders of magnitude enhanced conductivity found at the 180°-DWs.

To better understand the switched domain formation, the domain reorganisation and its interplay with a-domains, an experiment is conducted in which a square with different angles towards the cross hatch pattern of the a-domains is poled. In Figure 4.3 two square in a square polings were done (writing bias: +5V) with a 45°-angle (top row) and 0°-angle (bottom row). The 45°-poling created a multitude of small a-domains, visible in the PFM as well as the topography image. The new a-domains intersect longer stripes of previous c-domains and seem to form a dense connected network. Indeed looking at the conductive response in the cAFM image, one could argue that the observed conduction stems from the short zig-zag a-DWs at the boundary of the poled domains. Especially at the bottom boundary, a spread of conduction into the pristine area along the a-DWs is observed.

In comparison, the 0°-poling seems to have the opposite effect. Larger c-domains, than the ones usually found in the pristine film, are formed (top right) inside the poled area. Additionally, just based on the topography image, it would be impossible to judge, where the poling was performed. No zig-zag pattern of a-domains are created, indicating a less disruptive poling process. In a lot of places, the 180°-DW overlaps with existing a-domains (or a-domains got rearranged such that they overlap during the poling) as seen in the PFM image. Interestingly however, the conductive response along the 180°-DW seems to be independent of the different poling approaches. Strong conduction and straight channels are visible for both cases. Comparing the conduction values in the cAFM image, there is little reason to believe that one or the other poling type is in- or decreasing the overall conductivity. Therefore, even through the poling operation under an angle of 45° increases the formation of short a-domains, the conductivity seems to be a property of the 180°-DW. The reason for the increase in a-domains by poling, might originate from the fact that during poling when intersecting an existing a-domain, either the domains orientation or its in-plane polarization direction needs to be changed, to retain the polarization neutrality. Since a poling along the cross-hatch pattern intrinsically intersects with a lot less a-domains the amount of reorganisation needed

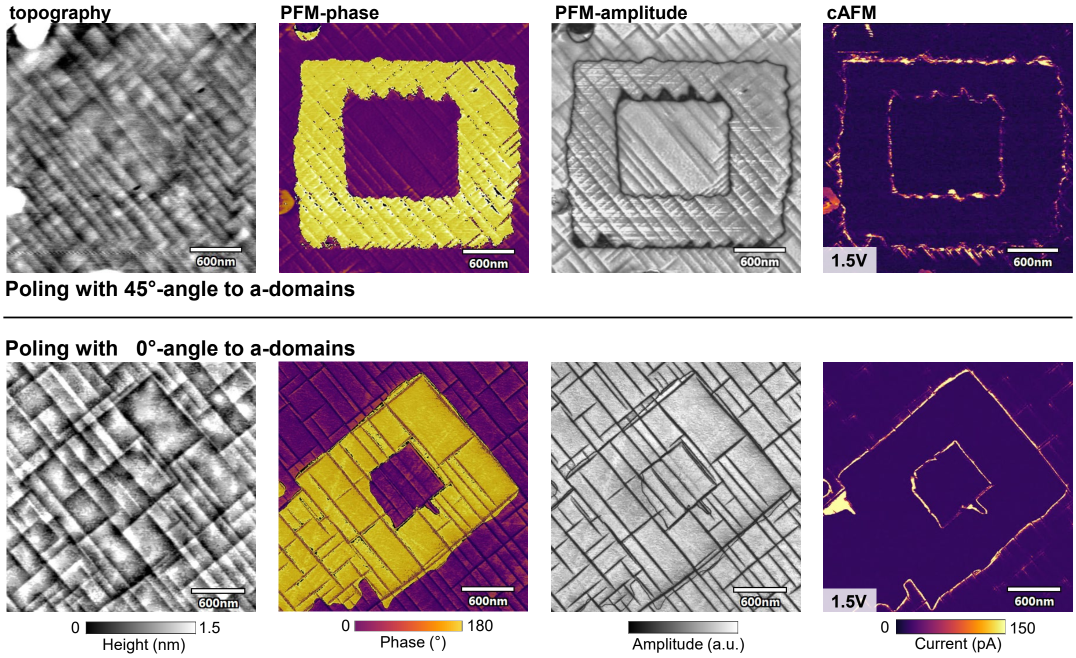

Figure 4.3: *Comparing the poling of c-domains under an angle of 45° to 0° towards the a-domains. Topography, PFM and cAFM images. Top row: Square in a square poling of c-domains done with a 45°-angle towards the a-domains. Bottom row: Square in a square poling of c-domains done with a 0°-angle towards the a-domains. A highly reduced creation of short a-domains is observed for the poling with a 0°-angle. Both cases show conductive outlines of the poled domains.*

is reduced which results in a less disruptive process.

To further explore the differences and interplay of 180°-DWs with a-DWs, high-resolution images are taken in the center of the 0°-poling area from Fig. 4.3. In Figure 4.4, the backpoled smaller square of the initial 0°-poling is shown in AFM, PFM and cAFM. From the combination of the topography image and PFM line-profile analysis it can be concluded that the bottom left part of the 180°-DW exist as an independent entity. As expected by 180°-DWs in the tetragonal crystal structure, virtually no signs of the 180°-DW is observed in the topography image. It should be noted that a sub-nanometer height resolution in these carefully acquired images is achieved, where single layers of the PZT-film can be identified. If the 180°-DW would be connected to any a-domains, they would result in measurable height changes. This is further proven by looking at the line-profile of the PFM-amplitude image. The a-domains are recognizable as relatively wide dips of the amplitude signal in contrast to the two sharp needle-like profiles of the 180°-DWs (marked with red circles). The fully symmetric profile of the 180°-DWs and their low width proves their isolated existence. The cAFM image confirms that also these segments of the 180°-DW, which have no interconnection to any a-domains show a enhanced conductive response. It should be noted here that a varying degree of conductivity along the DW path is observed.

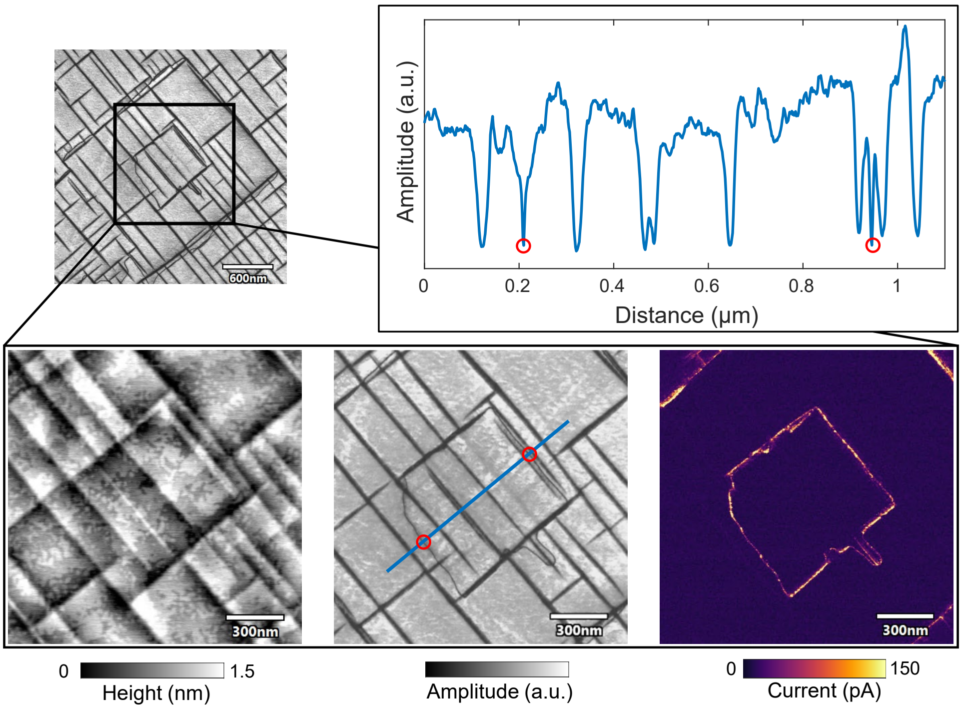

Figure 4.4: *A high-resolution view on closely spaced 180°-DWs and a-DWs. Topography, PFM and cAFM images of a 180°-DW. In this set of images, it is clear that the 180°-DW exists as a stand-alone object without any associated zigzag-shaped a-domains. The 180°-DW is readily seen in the PFM image (while no topography change is observed) with a curved shape and without any ferroelastic a-domains in its close proximity. This stand-alone 180°-DW section produces a conduction response clearly seen in the cAFM image. PFM cross-section profile further validates the pure 180°-nature of the DWs at the red dots, due to their ultra sharp profile in the amplitude signal compared to the wide a-domains.*

Another important aspect to confirm that the observed conduction is solely associated with the presence of 180°-DWs is to study the reversibility of the conductive channels. For this a square in a square poling was performed (Fig. 4.5) on a pristine area of the sample. From the PFM images the poled area is clearly visible as well as the 180°-DW, both in the PFM amplitude as well as the cAFM scan. Importantly, after repeatable scanning of the area with a negative bias of -4V, the poled regions are backswitched and any 180°-DW is removed. Together with it, the strong conductive channels also vanish, leaving no signs or footprints of the conduction behind. This confirms the reversible character of the written conductive 180°-DW channels, which is an important aspect for further device concepts and highlights the tight correlation of the conduction to the presence of the domain walls. It also hints towards an intrinsic conduction mechanism as defect assisted conductivity is prone to conductive footprints at the former location of erased DWs [93]. Further studies are conducted later within this section in Chapter 4.2, to better understand the origin of the DW conductivity, the DW structure inside the film and interplay with a-domains and type of accumulated charge carriers at the DW.

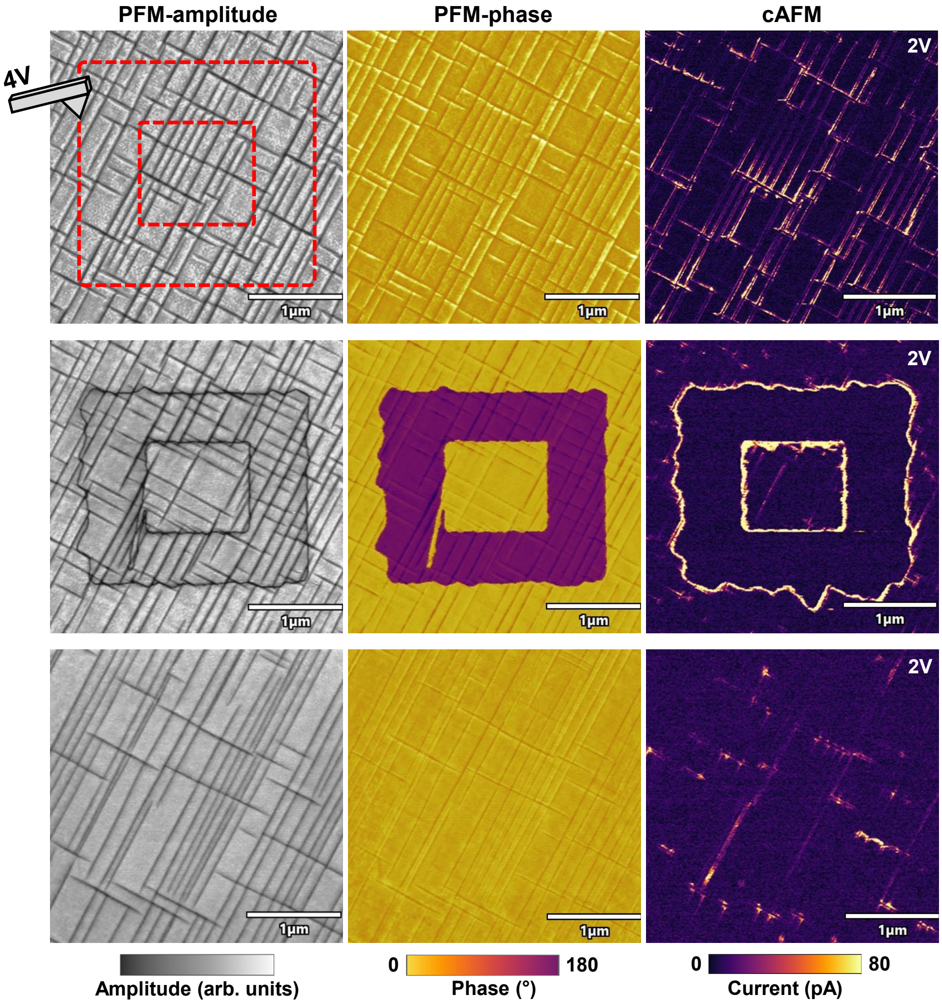

Figure 4.5: *Reversible conduction channels based on 180°-DWs. Series of PFM and cAFM images showing in the top row the pristine film, in the middle row the performed poling by a 4 V bias with the associated current channels at the position of the 180°-DWs and in the bottom row the images after the poled domain is subsequently removed. After removal of the 180°-DWs, the conductive channels are simultaneously erased.*

4.1.2 Stability of conduction and electrical properties

In the last subsection 4.1.1, an unexpected strong conductive response of artificially created 180°-DWs in strained PZT films were observed. Their formation and interaction with a-domains was studied. It could be confirmed that the new conductive channels are solely associated with 180°-DWs and that the conduction can not be explained by a network of the already known conductive a-DWs. In this subsection an in-depth look is taken at the electrical properties of the DW, especially the time and readout stability of the channels as well as the volatility of the conduction itself.

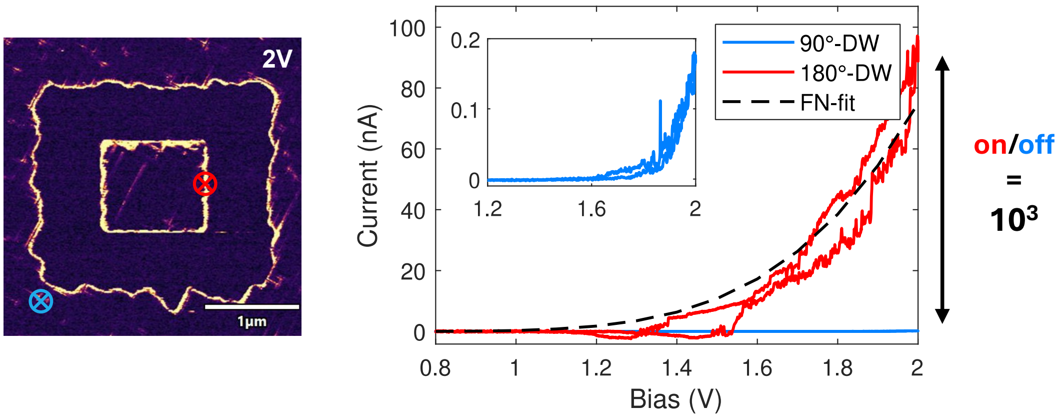

Figure 4.6: *I–V characteristics probed by the AFM-tip that contacts the surface at the positions indicated in blue for the a-DW and red for the 180°-DW together with the Fowler Nordheim-fit (black). A current difference of 3 orders of magnitude is observed.*

First, to quantify the conductivity of the 180°-DWs, IV-curves were recorded from 180°-DWs and a-DWs. The experiment was done on the domain walls from Figure 4.5. The IV-characteristics and the position of the AFM-tip location are shown in Figure 4.6. A 10^3 magnification of the conductivity is measured between the a-DW and the 180°-DW, reaching 100nA for a 2V bias. Secondly, the essential features of the conduction behavior, including its polarity dependence (no conduction readout for negative voltage bias) and non-linear I–V characteristics, are consistent with the transport limited model described by electron tunneling injection through the AFM-tip/PZT interface [177]. The Fowler-Nordheim (FN) formalism provides an adequate description of this mechanism, which is supported by the FN-fit of the I–V curve (black dotted line) in Fig. 4.6. For the fit, the classic FN formula, which describes tunneling through the triangular potential barrier Φ as a function of the applied electric field F is used:

$$I = S\frac{e^3 m_{tip}}{8\pi h m_{PZT}\Phi} \times F^2 \exp\left(-\frac{8\pi\sqrt{2m_{PZT}}}{3he}\frac{\Phi^{3/2}}{F}\right), \tag{4.1}$$

in which m_{tip} and m_{PZT} are the electron effective tunneling masses for the tip and PZT. S, e, and h are the effective tunneling area, electron charge and Plank constant, respectively. In order to convert the applied voltage V to the electric field F, a model of a spherical tip of radius R [178] is used, which yields a convenient approximation applicable within the relevant length scale: $F = V/R$. The fit in Fig. 4.6 was obtained for the potential barrier $\Phi = 0.8$ eV, $m_{tip} = m_e$, $m_{PZT} = 3m_e$ (with m_e the free electron mass), effective tip radius of 2 nm and S = 10 nm [79].

Next, the time stability of the 180°-DWs are probed. 180° switched c-domains in tetragonal PZT show an excellent domain non-volatility, due to minimal competing strain effects between

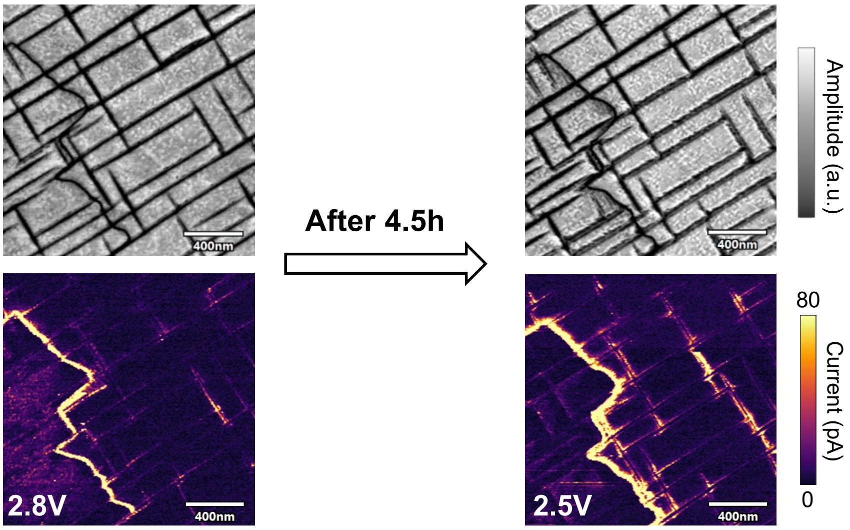

Figure 4.7: *Time stability of the 180°-conductive channels. An artificially poled domain is imaged by PFM and cAFM directly after its creation and after 4.5h, without noticable change in the DW structure or conductive response.*

the purely ferroelectric regions. However, it is not clear a priori if the conduction properties exhibit the same time stability. In Figure 4.7, the poled region from Figure 4.1, is imaged again 4.5h after its creation. Multiple scans (PFM as well as cAFM) were performed during this period. It is obvious that the conductive paths from the 180°-DWs still exist. An excellent positional as well as conductive stability of the written channels is observed highlighting their non-volatile nature. Subsequent tests showed that the conductivity remained stable even for days after their creation, persisting as long as the DW exists with no measurable decrease of its conductivity.

Another important aspect to test is the readout stability of the current channels. In Figure 4.8, multiple IV curves are taken on a 180°-DWs segment. The current readout of the domain wall is stable over multiple consecutive readouts and symmetric for the forward and backward bias (triangular pulses are used from 0 V to 2 V). This property is interesting as it has been shown, that 71°-DWs in BFO systems posses dynamic conduction properties [122, 83]. In contrast to the observed stable behaviour at the 180°-DW in PZT, the conduction at the BFO domain walls increases with the number of consecutive pulses and a hysteresis windows opens between the forward and backward bias curves (compare Fig. 4.8). Different mechanism, seem to play a role in the DW-conduction of the PZT and BFO system. It was argued that a local Joule-heating effect is increasing the conduction at the BFO-DWs. Other works, reported slight domain changes which could give rise to the modified conduction readout. Possible other effects could involve the successive accumulation of oxygen vacancies, which are a known responsible mediator of the conduction in BFO-systems [93, 97]. The stable readout properties of the PZT however, indicate a transport mechanism (mostly) independent from extrinsic defect effects. Furthermore, the consecutive current readout is not decreasing the conductivity

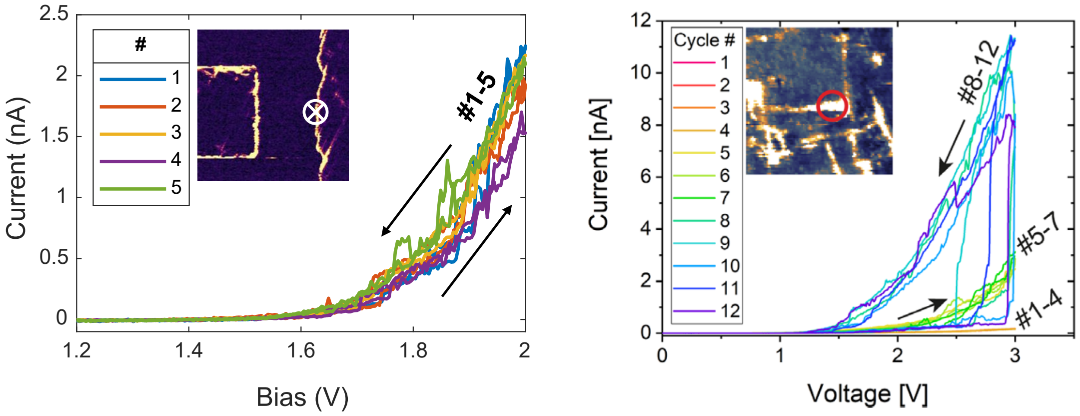

Figure 4.8: *Comparison of the readout stability of conductive DWs in PZT and BFO. Left: Artificially created 180°-DW in PZT probed by 5 triangular voltage pulses (0 V to 2 V). Right: Pristine DWs in BFO probed by 10 consecutive voltage pulses. While the IV-curves perfectly overlap for the PZT DWs, the BFO DWs show an increase in conductivity for ongoing current readouts. IV curves on BFO are adopted from* [122]

measured through the DW nor displacing the DW to an extend that the conduction would significantly drops. This confirms that the measured conduction is not associated with the volatile polarization switching currents. Because in the case of polarization switching currents, the measured conduction would be associated with a displacement of the DW and would drastically decrease once the DW is pushed far enough away due to the repeated voltage pulses.

Overall in this section, it has been shown that the enhanced conductivity found at 180°-DWs can be up to 3 orders of magnitude higher than the one measured at the pristine a-DWs. It could be concluded that the current channels are directly associated with the presence of 180°-DWs and that the unusual high conductivity is not explainable by the sole presence of the slightly charged a-DWs. Moreover, the 180°-DW conduction showed to be robust and stable in the time domain as well as under readout operations. The conductive channels are reconfigurable under applied electric biases and completely removable once the 180°-DW is erased, rendering them interesting for potential new DW-based nanodevices.

4.2 Conduction origin and properties - the everlasting question

In the previous Section the formation of normally neutral conductive 180°-DWs is observed and the properties of the associated conductive channels is studied. However, the nanoscopic origin of the conductivity is still unknown as the model for neutral DWs can not explain the unusual high conductance with a defect-based transport mechanism. Compared to the work on defect-mediated conduction at neutral DWs in PZT films by Guyonnet et al. [79], orders of magnitude higher conductivity is seen in the presented sample. Furthermore, other hints like the excellent stability of the 180°-DW conduction point towards an intrinsic current transport mechanism. It is known that nanoscopic wrinkles can emerge at neutral walls and that the overall assumption of completely straight 180°-DWs is often distorted in real scenarios due to boundary conditions [92], leading to enhanced and unexpected conductivity like observed for the partially charged a-domains in strained PZT samples [179]. Therefore, to better understand the underlying mechanism of the conduction but also the formation and structure of the -thought to be- straight 180°-DW and its interplay with strained a-domains, a series of experiments are conducted and presented in this section. Specifically, temperature dependent conduction measurements are performed together with cryogenic poling experiments as well as phase-field simulations and TEM cross-section analysis of 180°-DWs were carried out.

4.2.1 Temperature dependent conduction measurements

Most of AFM experiments are carried out in an environment-controlled chamber, as explained in Section 2.1, which also offers a temperature control from room temperature (RT ~ 30°C) up to 250°C. The temperature control within the small volume of the AFM chamber enables functional measurements (PFM as well as cAFM and electrical measurements) at reasonable speeds for different temperatures. It allows to create and probe the conduction of domain walls for different temperatures which gives an insights into the thermal dependency of the conduction mechanism and interface barriers.

Two tests were performed, one by simply creating a poled region and consecutively probe the area by cAFM at different temperatures to measure the conductance of the 180°-DWs. In a more sophisticated test the 180°-DWs were confined under an electrode and the resistivity of the capacitor device is measured for different temperatures.

In the first experiment a roundish domain was created by applying a bias of 6V for 1s to the AFM tip which is brought into contact with the sample. In Figure 4.9a, the cAFM images taken on that region with a 1.7V sample bias are shown for the different temperatures with the same color scale for the current values. The created domain is roughly 500 nm in diameter and the 180°-DW ring shows good contrast for the first cAFM image at RT (35°C). By successively heating the sample to 100°C, a decrease of conductivity is seen until the conductive outline of the domain nearly vanishes. After a followed cooling down, the conductivity can be restored as seen in the last images labeled "4" and "5" for 60°C and 35°C, respectively. A quantitative analysis is shown in Figure 4.9b and c. The DW section, which is indicated in the insert of Fig. 4.9b was measured by a line profile with a 15-point average. The resulting profiles for the temperatures are given in b and plotted for their peak maximum over the temperature in c. A clear decrease in conduction is observed for increasing temperatures and importantly after the temperature is decreased the conduction values are be restored to their old values. This proven reversible characteristic is important to highlight and together with the cAFM images confirm that the observed property is a result of the DW conductivity and not due

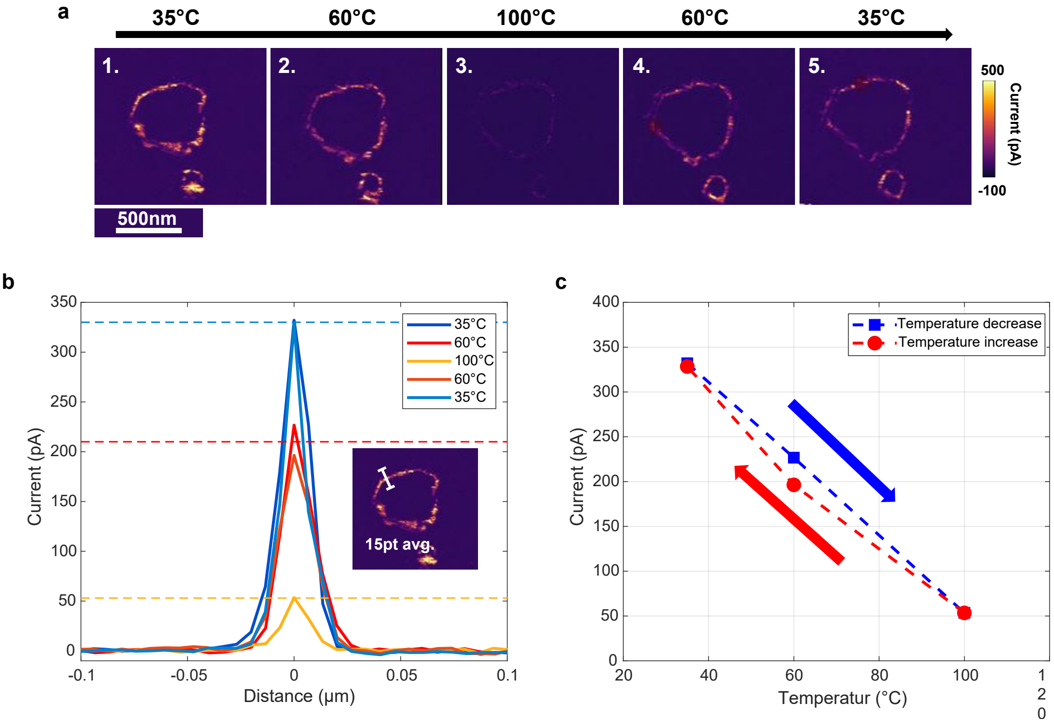

Figure 4.9: *Temperature dependent measurements of the 180°-DW conductance within the temperature range of 35-100°C. A ~700 nm big domain has been created by poling of c-domains. a) cAFM scans with 1.7 V sample bias have been taken at different temperatures of 35°C, 60°C and 100°C during the heating up and equally at the same temperatures during the controlled cooldown. All cAFM images are scaled the same to allow for an easy visual evaluation. b) A 15 point average on a segment of the 180°-DW is taken and the resulting current profiles for the 5 different temperatures are plotted. c) Maximum current values are plotted over the temperature. Red indicates the heating up and blue the cooling down. A clear non-thermally tendency is observed as well as a recovery of the suppressed conduction after cooling down.*

to structural changes. A possible explanation for the conduction decrease could be a non-thermally activated "metallic-like" conduction mechanism (as it has been shown also in other DW-systems [119, 76]). However, it is important to note that not only the DW itself is probed but rather the whole system of bottom interface, conduction through the DW and top interface.

To get more insight into the temperature dependence of the conduction mechanism the second experiment is performed by injecting 180°-DWs inside the inter-electrode area of a capacitor device. By doing so, the tip-PZT surface interface is exchanged with the top electrode-DW interface, providing a way to observe changes in the conductive response resulting from the top interface. Moreover, the highly localized electric fields at the tip apex are substituted with more uniform electric fields applied through the electrode. As it will be explained later in detail in Chapter 5 and 6, the confinement of DWs inside an electrode area is not as trivial as it seems. Nevertheless using high resistive platinum electrodes, a deterministic poling of domains under the electrode is achieved, and 180°-DWs can be injected and stabilized inside the capacitor devices (for details please see Section 6).

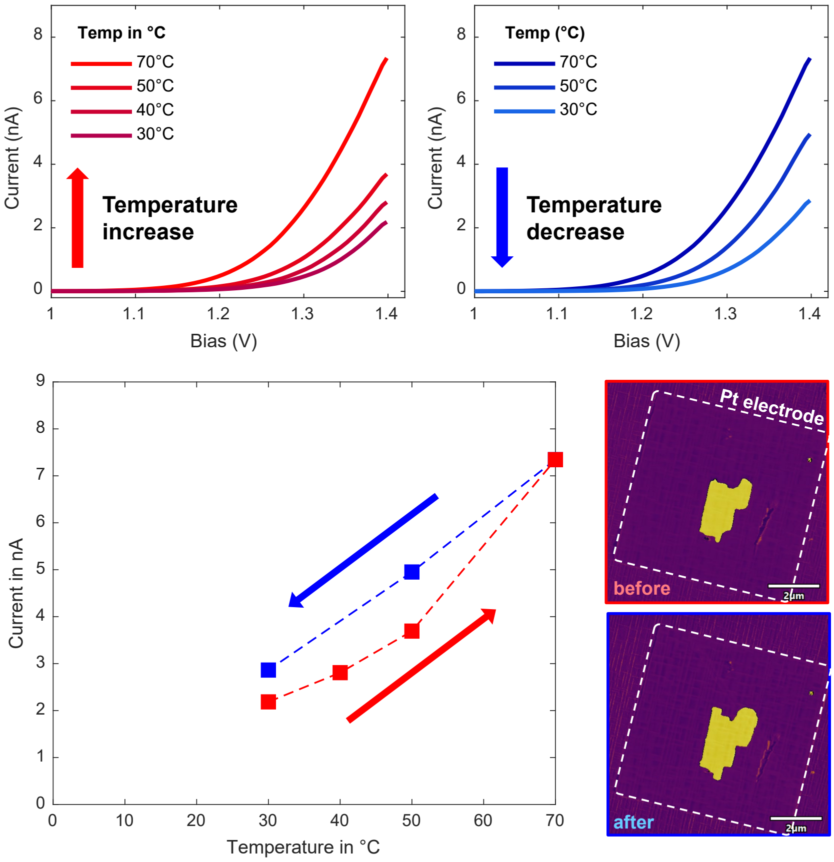

Figure 4.10: *Temperature dependent measurements of the 180°-DW conductance within the temperature range of 30-70°C using a high-R Pt-electrode. A high-resistive platinum electrode is used to confine 180°-DWs inside a capacitor device (details on the electrode and the confinement of DWs in Chapter 6). Top row: IV curves taken at different temperatures during the heating up and cooling down with the tip placed in the center of the device. Bottom: Maximum current values, which were read from the capacitor device are plotted over the temperature at which they were recorded. A clear thermally activate behaviour is observed. PFM images before and after the test confirm the stability of the written domain inside the capacitor.*

In Figure 4.10a and b, IV curves for the temperature increase and decrease are plotted respectively. Initially a maximum current of 2nA is observed for the 1.4V applied bias. By increasing the temperature from 30°C to 70°C the current at 1.4V is increased to 7nA. A reversible change is observed for the temperature decrease with decreasing current values. The maximum current values are plotted over the temperature values in Fig. 4.10c and PFM images of the polarized domain before and after the heating cycle are shown (both taken at 30°C). A slight increase in domain size is observed after cooling down to RT. The difference in the current values for the temperature increase and decrease seen in Fig. 4.10c could result from a combination of the change in domain size or from not fully stabilized temperature values. The waiting time in between setting of the new temperature and recording of the IV curves was set to 5min. The maximum temperature was capped at 70°C because similar experiments showed strong distortions of the polarized domains under the electrode if temperatures above 80°C were exceeded. Nevertheless the trend as well as the reversibility is clearly seen and interestingly of opposite character than for the experiment in Fig. 4.9. This time a positive thermal activated behaviour is observed for the current characteristic.

Since the main difference between the experiments was the top electrode contact (tip vs. high resistive Pt-electrode) some conclusions can be drawn for the interface contact. Due to the carbon contamination typically observed within scanning electron microscopy (SEM) chambers, where the electrodes were deposited, and the electron beam induced deposition (EBID) technique itself, used to create them, defects and carbon contaminants are introduced not only in the electrode material but also at the electrode PZT interface. Consequently, the formation of a Schottky barrier is expected. The clear positive temperature dependence further strengthens this assumption and suggests that the Schottky barrier dominates the current transport. In contrast, for the tip-PZT interface case, a temperature independent Fowler-Nordheim tunneling is assumed to occur at the tip apex due to the highly increased nonlinear electric field (see Fig. 4.6). The resulting negative temperature dependence observed in this case would therefore mainly be attributed to the intrinsic current transport along the DW.

The results also highlight another important aspect which needs to be considered when investigating the conductive properties of DWs. When probing the DW, in reality the whole DW-system is investigated and the experimental setup needs to be carefully designed to study intrinsic contributions of the DW itself. Contact interfaces can easily dominate the measured characteristics and change depending on the exact type of measurement as seen above. Classical experiments to evaluate the intrinsic properties, like 4-point probe measurement on single DWs are difficult to realize and advanced setups need to be invented to study such properties as demonstrated e.g. in Hall-effect measurements in DWs in $YbMnO_3$ [98].

4.2.2 Cryogenic AFM experiments down to 4K

In this subsection, investigations are done to evaluate if and how conductivity at 180°-DWs is preserved at cryogenic temperatures. In DW-systems, which are based on defect mediated conduction, a strong decay of conductivity is observed when cryogenic temperatures are approached. As shown in previous works on strain deformed a-domains in PZT films [94], for some DWs, conductivity is preserved even at 4 K, indicating a non-defect mediated transport as extrinsic ionic conduction and movement of defects is frozen.

In the following the results of AFM-based measurements at 42 K and 4 K in an ultra-high vacuum (UHV) are shown. The chamber of the Cryo-SPM, manufactured by Omicron Nanotechnology (currently Scienta Omicron) operates at ≤10^{-9} mbar pressure. Conductive diamond coated probes similar to the ones for RT measurements were used to allow for continuous and comparable measurements. All results shown are done with the same probe during one session which lasted several days in which the temperature of the UHV chamber was kept at 4K. Small temperature changes e.g. going from 4 K to 42 K were performed by a small heating element near the sample which provided fast and local temperature changes.

Prior to the poling experiments, in Figure 4.11 pristine areas were characterized at 4 K and 42 K, which revealed a conduction pattern coinciding with the narrow a-domains, similar to the RT-data in Section 4.1 and to previously published results [94]. cAFM maps were acquired with a sample bias of 5.4 V and 6 V for the 42 K and 4 K experiments respectively and the IV curves taken on a-DWs at 4 K showed conduction of tens of picoampere for 5 V bias.

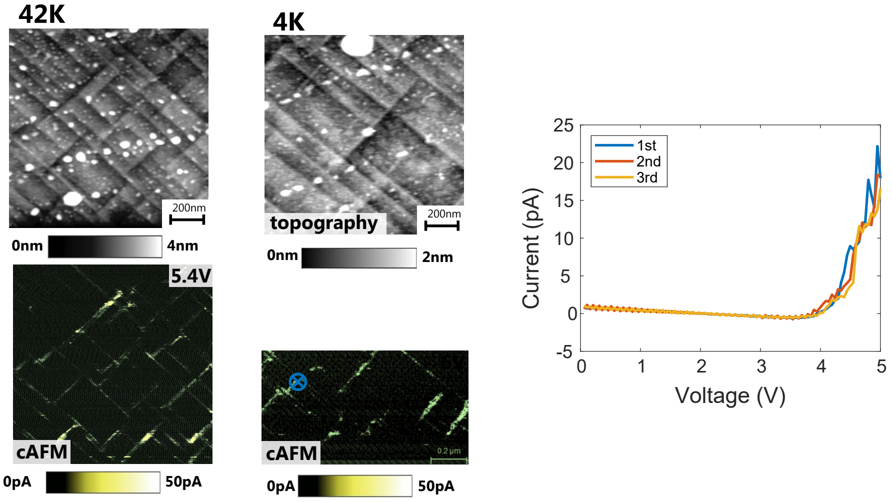

Figure 4.11: *Pristine a-DW conduction at cryogenic temperatures. Left: Topography and cAFM images at 42 K. The sample bias was 5.4 V and current traces of several tens of pA were observed. Center: Topography and cAFM images at 4 K. The sample bias was 6 V and similar current values were observed in comparison to a). Right: IV curves measured on pristine a-DWs at 4 K. Tens of pA conduction is maintained even at very low temperatures.*

Because of the UHV environment and the cryogenic temperatures, the voltages required for polarization switching and conduction measurements were higher compared to those used for the RT-measurements shown in Fig. 4.6 and 4.5. Specifically, the polarization switching required a sample bias of 7 V while the a-DW conduction was detectable only above 5 V. For reliable poling a sample bias of 9 V was used, which resulted in relative uniform square-like poled regions at 4 K (Fig. 4.12, upper panel) and 42 K (Fig. 4.12, middle panel). As a side effect of using higher poling voltages, particle deposition on the PZT surface inside the scanned areas was observed (see Figure 4.13), accompanied with a partial blurring of the cAFM images. Due to the complex resulting conductive patterns, all further analysis were therefore

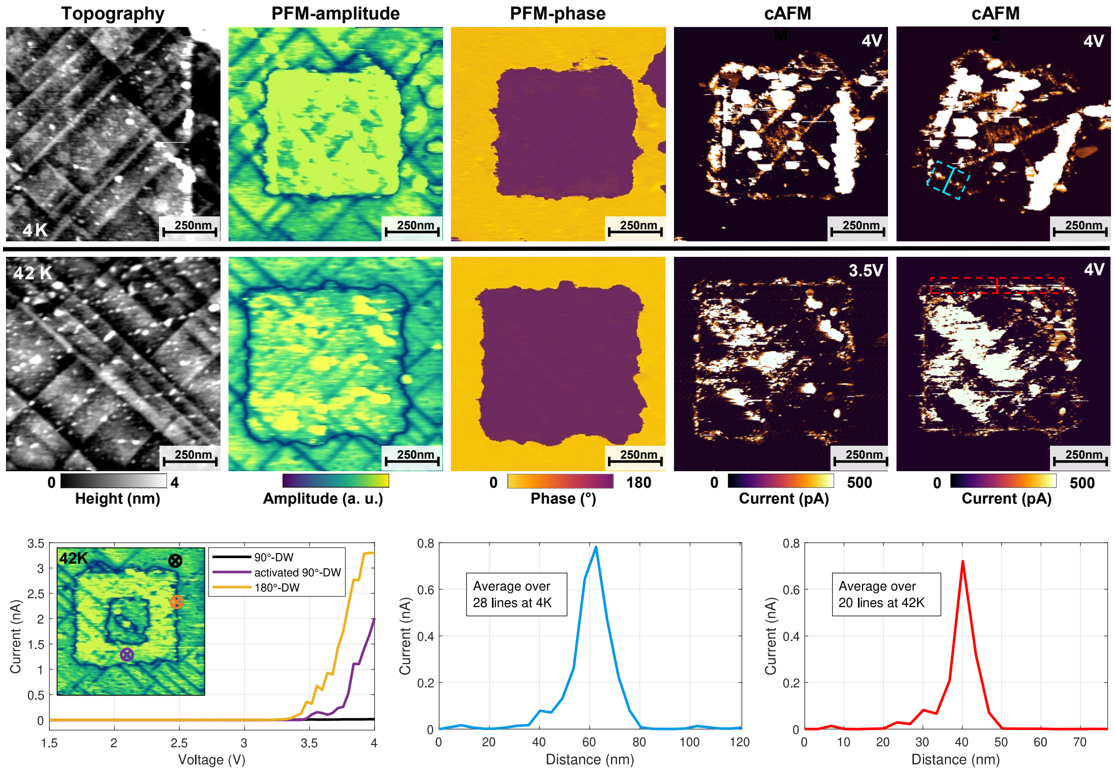

Figure 4.12: *Top row: Topography, PFM and cAFM images of poled regions at 4 K. Middle row: Same images as in the top row at 42 K. In the PFM-phase images the clear 180° contrast between pristine (yellow) and poled (purple) domains is visible. The 180°-DWs (black square outlines), show strong conductivity as confirmed by the cAFM images. This conduction is detectable under varying imaging parameters like scanning angle or voltage bias both at 4 K and 42 K. In all cAFM images, in addition to 180°-DWs, an enhanced conduction of the a-DWs inside the poled regions is observed. Bottom row: Single-spot I–V characteristics at 42 K of a pristine 90°-DW outside the poled region (black), the enhanced 90°-DW conduction inside (purple) and the strong 180°-DW response (orange). The insert indicates the positions where the I–V curves where taken with the tip as a top electrode. Averaged cross-section profiles at 4 K and 42 K collected on the marked areas in the cAFM images show similar maximum current around 800 pA for both temperatures.*

focused on zones free of the distorting artifacts. Moreover, within the poled regions, zones with high density of a-domains tend to appear as extended regions of high conduction. In all cAFM images in 4.12 one readily identifies a strong nA-range conductive response of newly created 180°-DWs. These conductive traces persist through sequential scans with varying scanning angle or changing bias. I–V curves measured up to 4 V on individual a- and 180°-DWs illustrate the typical current response observed at 42 K (bottom row of Fig. 4.12). Analysis of the data acquired at 42 K and 4 K using the same measurement protocol and the same probe revealed their remarkable similarity. Direct comparison of the conduction traces of 180°-DWs measured at 4 K and 42 K with the same sample bias of 4 V show strikingly close quantitative characteristics. Current values - approaching 0.8 nA - have been obtained for

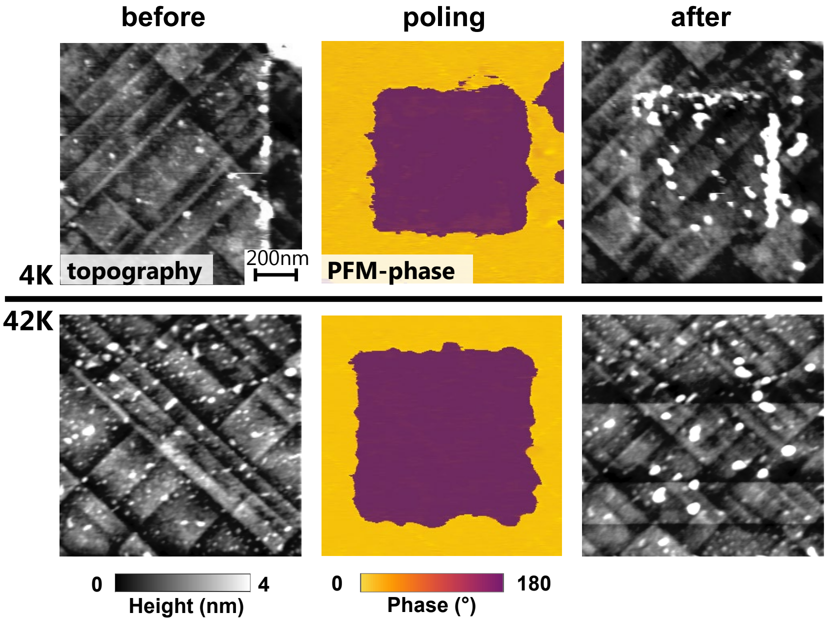

Figure 4.13: *Creation of surface particles after poling with high electric fields. Before and after topography images together with the PFM phase image of the performed poling. The effect of using a high electric-field for poling is observed in the formation of surface particles. These particles remained even after scanning in contact mode. By using lower electric field, fewer particles could be produced but at the same time, the uniformity of the poling is reduced.*

both temperatures by averaging the conduction data over a 180°-DW segment, chosen in a way to minimize any possible interference with the conductive a-DWs. It was possible to control and modify the conductive channels, produced at the cryogenic temperatures, by external biases identical to the RT-measurements and similar probe/PZT interface limited I–V characteristics (polarity dependence and non-linearity) were observed. The conductive traces could be completely erased without leaving conductive footprints by removing the switched domains through backpoling with a sample bias of ≤-5 V.

The results of cryogenic scanning probe microscopy provide a valuable insight into the physical origin of the observed 180°-DW conduction. In particular, together with the previous temperature and stability experiments they imply an intrinsic nature associated with the domain walls' electronic properties rather than an extrinsic defect-driven mechanism. The formation of a 2D electron or hole gas, characterized by its metallic-like conduction is consistent with the non thermally-activated conduction observed at the 180°-DWs, which supports remarkably high current levels down to 4K. With at least 1 nA at 4 V measured by a scanning diamond probe in a cryogenic environment, it illustrates the potential for DW-applications in a wide temperature range.

4.2.3 Phase-field simulations - unrevealing the complex domain interactions

To gain further insights into the origin of the 180°-DW conductivity and especially into the interplay between the a- and c-domain boundaries, quantitative phase-field simulations of the poling dynamics were performed in collaboration with partners from the MANIC consortium (simulations were carried out by Yuri Tikhonov and Igor Lukyanchuk from the University of Picardie).

For the simulations, a PZT film, strained by the substrate with a tensile strain of $u_m = 0.35\%$ is modeled. The pristine state is prepared from the paraelectric phase by field-cooling. Interaction of free carriers with the charged domain walls is accounted for by the introduction of the Thomas-Fermi-Debye-Hückel screening term into the electrostatic Poisson equation. The carriers' concentration is accounted for by the screening length δ. Further details can be found in the published paper [175].

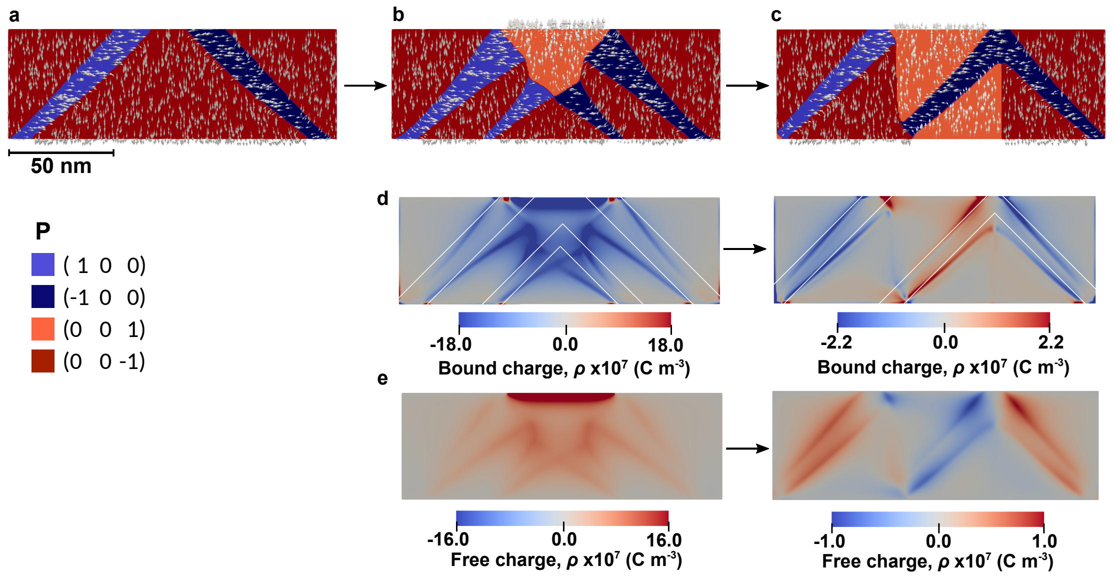

Figure 4.14: *a) Distribution of polarization and domains in pristine PZT prior to poling. b) The initial poling stage: after the tip contacts the uniformly poled PZT, a new c-domain forms in a near-surface region producing additional a-domain stripes propagating towards the bottom interface. c) Further evolution of the system leads to an alignment of the 180°-DW with the crystal axis. Relaxed state of the system after the tip removal. d) Bound charges concentrated near the bent 90°-DWs for the poling stages b) and c), respectively. The white lines show the charge-neutral direction of the domain walls. e) Free conductive charges distribution that screens the bound charges for the same stages of poling.*

Quantitative 2D cross-section simulations of a 50 nm thick PZT sample are carried out and shown in Figure 4.14. When the tip bias is applied to the pristine sample(a), an inversely-polarized domain forms at the near-surface region b). Afterwards, it propagates further inside the film until it reaches the substrate surface and straightens the 180°-DWs c). During the dynamical formation of this new poled domain, additional a-domain stripes are created at the boundaries of the growing c-domain. Once formed, they propagate rapidly and form stripes to the film surface with a nearly 45° inclination, as required by electrostatic compatibility conditions. Interestingly, at lower tip voltages the poled c-domains do not reach the final state but get pinned during the process, accompanied by the formation of terminal a-domain shoots, of octopus-like shapes, see Fig. 4.14 b).

These poling dynamics give a hint for understanding the conductive traces at the poled region boundaries. Importantly, the boundary between poled and pristine regions, which looks from the surface as a single 180°-DW (as observed in Fig. 4.4), has in fact a more complex internal structure. As shown in Fig. 4.14 b) and c), it is associated with conducting a-DWs, which either emerge from the separation boundary at the surface or nucleate from the 180°-DW inside the sample and propagate downwards to the bottom electrode. These in-plane domains can be nested and further connect with other conducting a-DWs in the depth of the film. This simulation suggests that the conductivity of the 180°-DW mimic the conductivity of the associated a-DWs, which emerge at the poled region boundaries.

Fig. 4.14 d) and e), present details of the bound and free charge distribution along the domain walls during the poling process and after the tip removal, respectively. The charge-neutral 45° orientation is indicated by white lines. Fig. 4.14 d) shows the distribution of the bound charge in the vicinity of the domain walls. Fig. 4.14 e) shows the distribution of the free charges, which accumulate due to screening of the bound charge-induced electrostatic potential. A much higher charge density is observed in the case of the pinned polarization domain (Fig. 4.14 b)) which did not propagate through the film completely. It is assumed that variations of free charges and hence measurable conduction will arise along the 180°-DW due to the changing interplay of c-domain boundary and a-domains inside the film. The changing interplay of c- and a-domains boundaries inside the film might also cause a locally different conductivity along the in-plane direction of the DW when probed from the surface. Such cases are in line with experimental observations of varying conduction along the 180°-DWs in cAFM scans, see Chapter 4.1.

Since the previous quantitative simulations, which indicate the strong interplay of c- and a-domain boundaries were only performed in 2D, they paint a simplified picture of the whole complexity. New quantitative 3D simulations are performed to evaluate the real contribution of the nested domain network inside the film for the conductive properties seen at the surface. In Figure 4.15, the results of the new simulations are shown. A 60 nm thick PZT film is modeled with constrained lateral dimensions of 250 x 250 nm. The domain configuration of the relaxed thin film before poling is shown in Fig. 4.15 a) together with the uniform surface bound charges at the positions of a-DWs (Fig. 4.15 c)) (with blue traces corresponding to positive bound charges and yellow traces to negative ones). The state after the poling of a circular upwards oriented domain area with radius of 100nm and successful relaxation is shown in Fig. 4.15 b). The associated picture of bound charges also changes and traces now contour both a- and 180°-domain walls as shown in Fig. 4.15 d). It is worth to note here that bound charge distribution is now non-uniform along the domain walls as discussed before and seen in cAFM experiments.

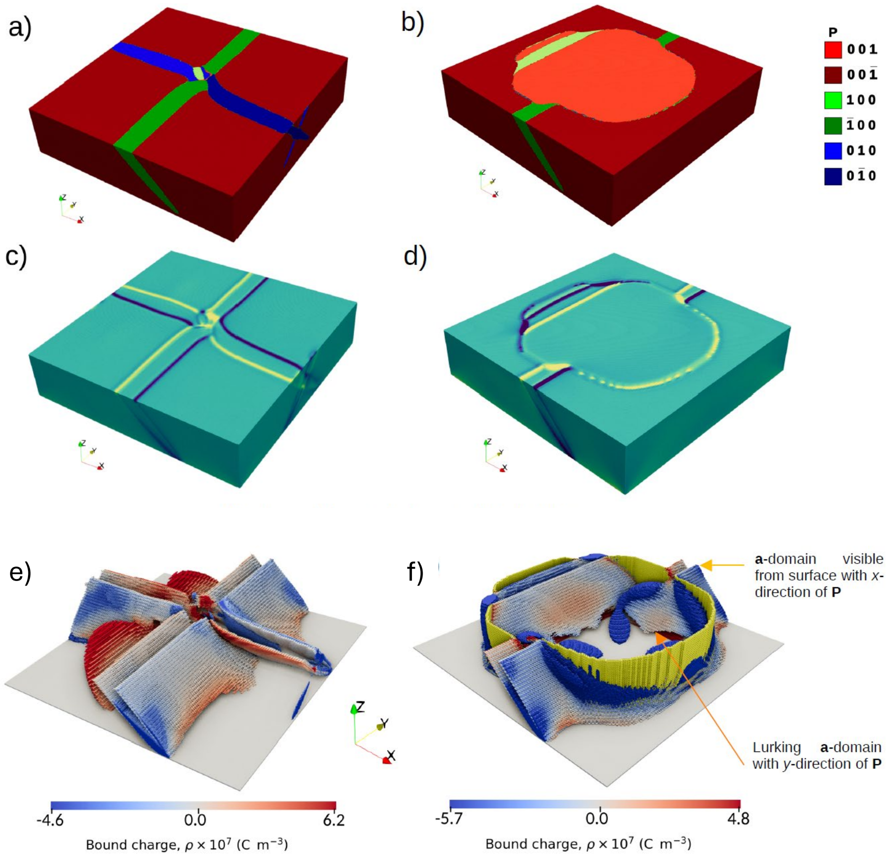

Figure 4.15: *Quantitative 3D Phase-field simulations of domain wall interactions. The geometric dimension of the film are 250x250x60 nm. a)-d) Surface view of PZT thin film. a) Domains in pristine state after initial relaxation. b) Domains in the state after application of electrical field in radius of 100 nm and relaxation. c) Positive and negative bound charges distribution at the surface before poling. d) Bound charge distribution at the surface after poling. e)-f) Both panels represent the internal structure of domain walls of the same PZT thin film region before and after poling. Grey surfaces are walls of a-domains. The yellow surface is 180°-domain wall. Blue and red corresponds to distribution of bound charge. e) Pristine state before poling. f) State after poling in the region with radius of 100 nm and the following relaxation.*

To better understand the behaviour of conductive domain walls the internal structure of the domains in the volume of the thin film is studied. In Fig. 4.15 e) and f) the bulk of the domains is removed and only the domain walls as the surfaces of the domains together with the bound charges are shown. a-DWs are shown in grey whereas 180°-DWs, which are only present in Fig. 4.15 f), are colored in yellow. Negative bound charges appear blue while positive bound charges appear red. In Fig. 4.15 e), medium level of bound charges are formed, predominantly at the bottom of the slightly charged a-DWs. Interestingly, there exist a-domains which lurk in the bulk of the film and do not propagate fully to the top surface, which carry an increased amount of bound charges (seen as enhanced red areas). The situation drastically change after the poling when 180°-DWs interact with the a-DWs. Predominantly, enhanced dark blue areas are seen in Fig. 4.15 f), representing new highly increased areas of negative bound charges. They tend to accumulate at the intersections between the two types of DWs and extend into the bulk. The high bound charge areas are expected to arise from charged surfaces within the film, at which the complex interactions of the 6 differently oriented domains can not stabilize into complete neutral domain boundaries. The apparent difference between negative and positive bound charges suggest the predominant formation of Tail-to-Tail DWs.

As bound charges need to be screened by free carriers it is expected that hole carriers accumulate at the blue regions of negative bound charges, which favors the formation of a 2D hole gas (opposed to the previous expected 2D electron gas). A 2D hole gas would explain the observed properties of an intrinsic conduction and further support the AFM measurements at cryogenic temperatures. Since the free carriers are bound to the extended volumetric regions of domain wall interactions the conductivity issue transforms into a problem of percolation of free charges from the top to the bottom of the film. 3 dimensional current paths crossing different types of DWs and intersections are supposed to appear, which can be rearranged by electric field induced reorganization of the DW-interplay and positioning. Due to the strong interplay of the 180°-DW and a-DW needed for the exceptional conductivity to arise, simulations suggest that a dense interconnected pattern of a-domains is a requirement for the observed conduction. This finding is supported by results from Chapter 3 in which a reduced conductivity is observed in samples with mainly elongated stripe like and less dense and interconnected a-domains (see sample PZT #5 and PZT #8 in Section 3.2.2).

4.2.4 STEM - an insight beyond the surface

In order to verify the predicted simulation results experimentally, atomic scale scanning transmission electron microscopy (STEM) studies were carried out. STEM enables an insight beyond the PZT surface, to study the domain configurations and structure of the domain boundaries with atomic resolution inside the film. One downside is the two dimensional character of the imaging, which prevents the exploration of the 3D structure of the interconnected domains. Nevertheless, as we will see in the following section, the insights gained by the STEM analysis through imaging of the in-depth structure of 180°-DWs, provide valuable insights into their charge state and their interplay with a-domains. The STEM experiments and lamella preparation were carried out at the Universidad de Zaragoza by Panagiotis Koutsogiannis, José A. Pardo and César Magén.

In Figure 4.16 a), AFM images of the PZT sample, which will be investigated by STEM are shown. This sample showed very similar characteristics as the one studied in detail in Section 4.1. Highly conductive 180°-DWs are seen and for voltage biases of 2.2 V and more also a-DW conduction can be observed. The only noticeable difference is the pristine polarization direction of the c-domains, which in this sample is upwards oriented compared to the previous seen downwards oriented. Therefore, the poling of c-domains needs to be done with a negative voltage bias applied to the bottom electrode. For the poled areas in Fig. 4.16 a) and c), -5V

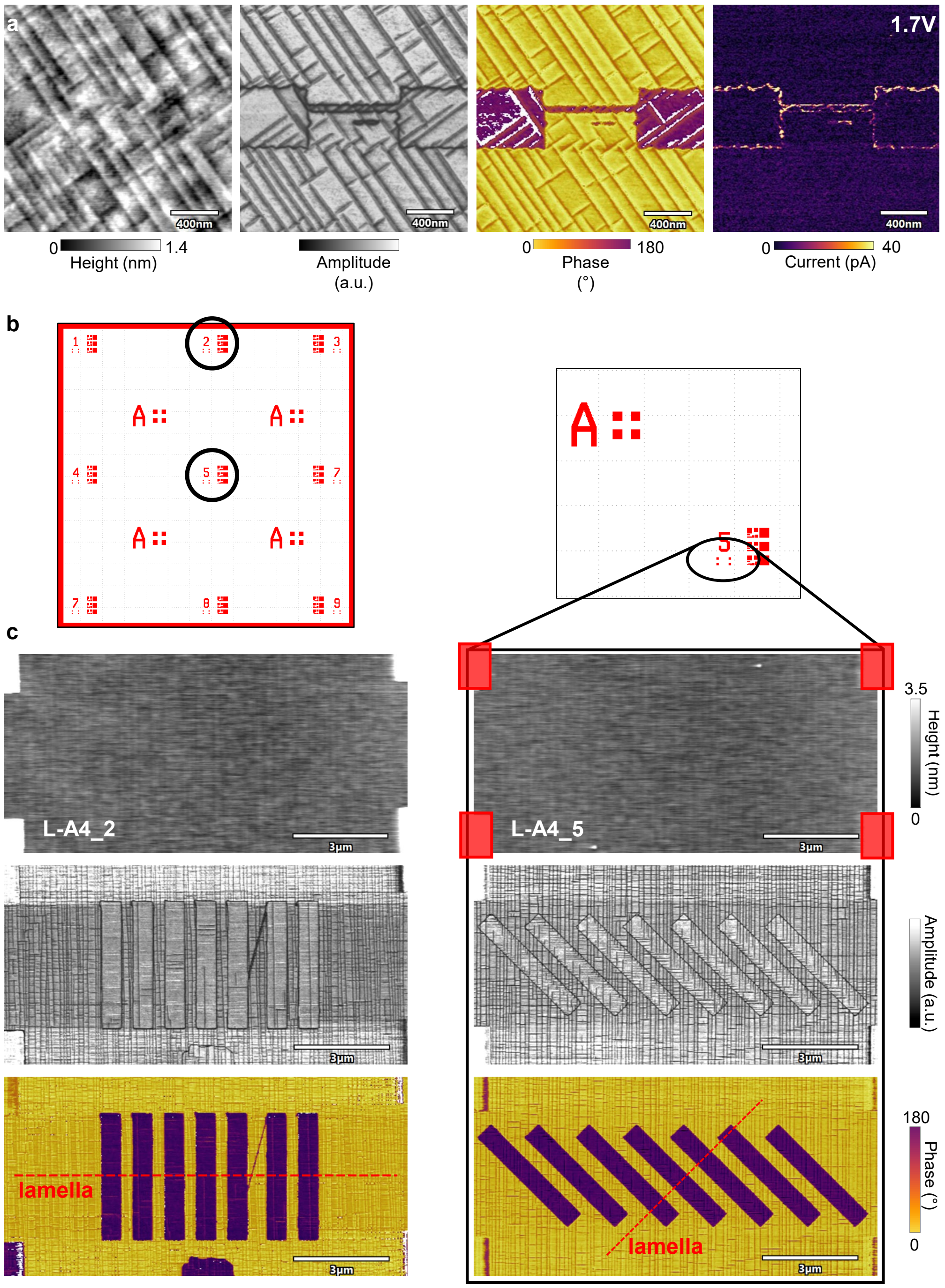

Figure 4.16: *PZT characterization and poling pattern for STEM experiments. a) Topography, PFM-amplitude, PFM-phase and cAFM images of the PZT sample studied in the STEM experiments. Formations of conductive 180°-DWs are seen upon poling with a sample bias of -5 V. b) Layout of the markers used to pole the PZT film and cut the lamella. c) Topography and PFM images of the final poling used for the STEM experiments. Red dashed line in the phase images indicate the position of the lamella preparations.*

are used. In Figure 4.16 b), the layout of the markers are shown which were deposited to be able to find back the poled areas when preparing the lamellas. Areas of 10x4 µm are marked in which strip like domains are poled. The lamellas are cut along the [100] direction for "L-A4-2" and [110] direction for "L-A4-5", which result in regions of alternating up- and downwards polarized domains, see Fig. 4.16. Details on the lamella preparation, the STEM instrument and different acquired images as well as the associated image analysis are given in Section 2.3 c).

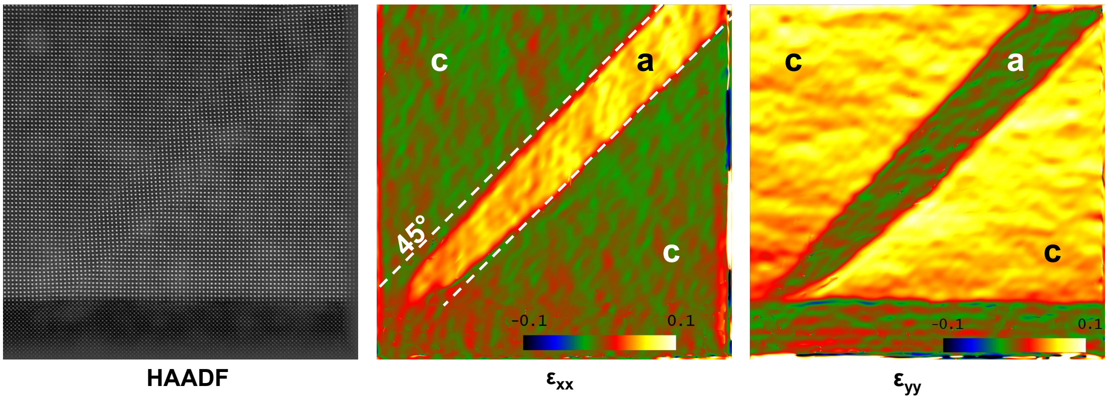

Figure 4.17: *STEM image of bended a-domain. Left: HAADF high-resolution image of a pristine a-domain. Center and right: GPA ϵ_{xx} and ϵ_{yy} deformation maps. Neutral 45° angle is marked as white dashed line.*

In Figure 4.17, a HAADF image of a pristine a-domain is shown together with the corresponding GPA ϵ_{xx} and ϵ_{yy} deformation maps. Clearly visible, the strained a-domains distort from the neutral 45° angle at the bottom SRO interface, confirming the expected results from simulations and previous works [94]. The thickness of the SRO and PZT layers for this PZT sample, were found to be 22.5 nm and 66.9 nm, respectively.

Figure 4.18 now shows a more interesting section of the PZT film. The overview image is a low-magnification ADF image, in which the a-domain as well as a 180°-DW are clearly visible. The 180°-DW can be identified in the ADF image as a bright line from the top to bottom surface due to local strain. The polarization of the left- (green, upwards) and right-side (purple, downwards) domains were confirmed through a polar analysis of the high-resolution ABF image taken on a 180°-DW segment, seen in Fig. 4.18 b). Already visible in the overview image is the strong distortion of the 180°-DW with respect to the out of plane [001]-direction. The DW bends to the left side until it hits the a-domain. It penetrates horizontally through the in-plane domain and continues to form a mostly vertical connection to the bottom surface after exiting the left side of the a-domain. Even more interesting is the atomic scale structure of the 180°-DW, revealed by the polar analysis. Charged segments are clearly distinguishable, marked as orange and blue areas, which form local Tail-to-Tail (T-T) and Head-to-Head (H-H) DW segments respectively (compare also the schematic in Fig. 4.18 c)). Such a structure of a normally straight 180°-DW is not expected and believed to arise due to its position and interplay with the a-domain and bottom interface.

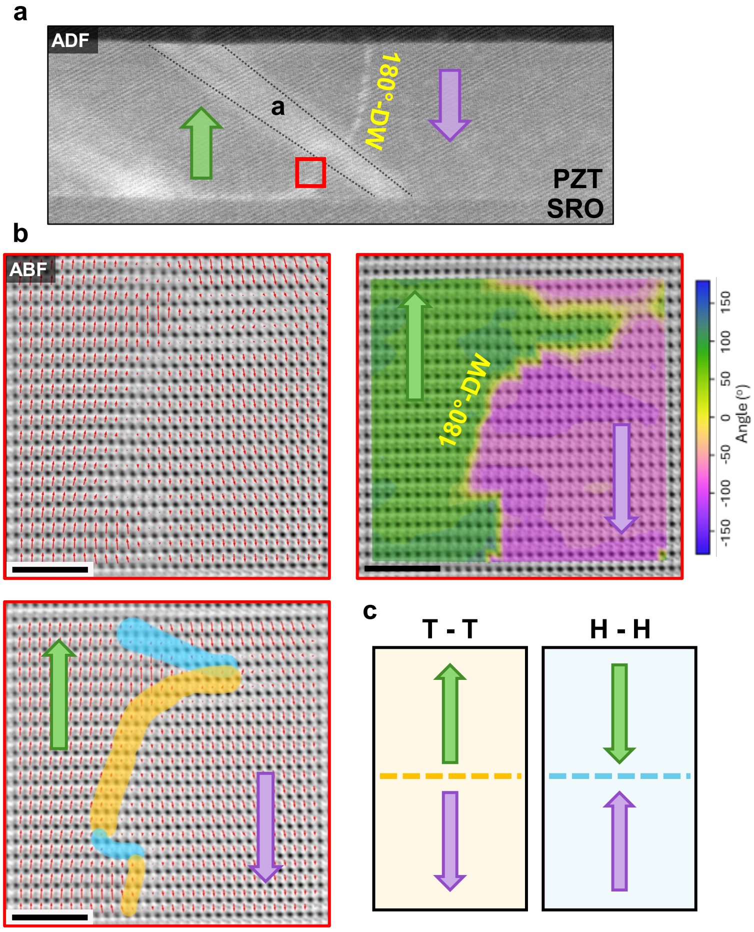

Figure 4.18: *STEM images of a twisted DW. a) STEM-ADF image of a nominally 180° DW. b) STEM-ABF image of the DW collected from the region marked in a), with the oxygen atomic displacement plot overlaid. The highlighted yellow and blue regions at the DW indicate region with tail-to-tail and head-to-head DWs, respectively. The angle of the polarization vector indicates the disturbance and non-uniformity at the vicinity of the DW. c) Schematic of the Tail-to-Tail and Head-to-Head DW types with the used color code.*

Other parts of the lamella are investigated and different 180°-DW formations are found. In Figure 4.19 a region of the PZT film is imaged in which three a-domains and two 180°-DWs are present. Detailed analysis by high-resolution HAADF and polar analysis of the atomic-ionic shift are shown in Fig. 4.19 b) and c), which correspond to the marked areas in blue and orange in the overview, respectively. Similar to Fig. 4.18, a section of the 180°-DW is analysed in the orange region. However this time the 180°-DW segment is mostly straight with no local twists or distortions. Only a slight bending of around 4° towards the poled domain is observed which indicates its weakly charged state. In the blue area the focus is put onto the interaction of the 180°-DW at the bottom interface. An inclination of the 180°-DW of around 45° towards the out of plane direction is seen approximately 10nm above the SRO interface. This inclination generates a T-T DW segment and is observed for nearly all 180°-DWs. A possible explanation of this unexpected inclination is, that the twist occurs at positions of former a-domains of the pristine regions, which are destroyed during the poling process. Due to the charged nature of a-domains (especially at the bottom interface, see Fig. 4.17), mobile defects (which are naturally present in all oxides) will get attracted towards these regions. If the polarization switching of c-domains is then causing a reorganization with partial erasure of the a-domains which has been seen in the simulation results and in the results of Section 4.1, the remaining increased density of defects at this position might lead to a stabilization of the unexpected inclination angle and the T-T DWs. It should be noted that such areas of increased bound charges at the bottom interface are seen in the simulation results in Fig. 4.15.

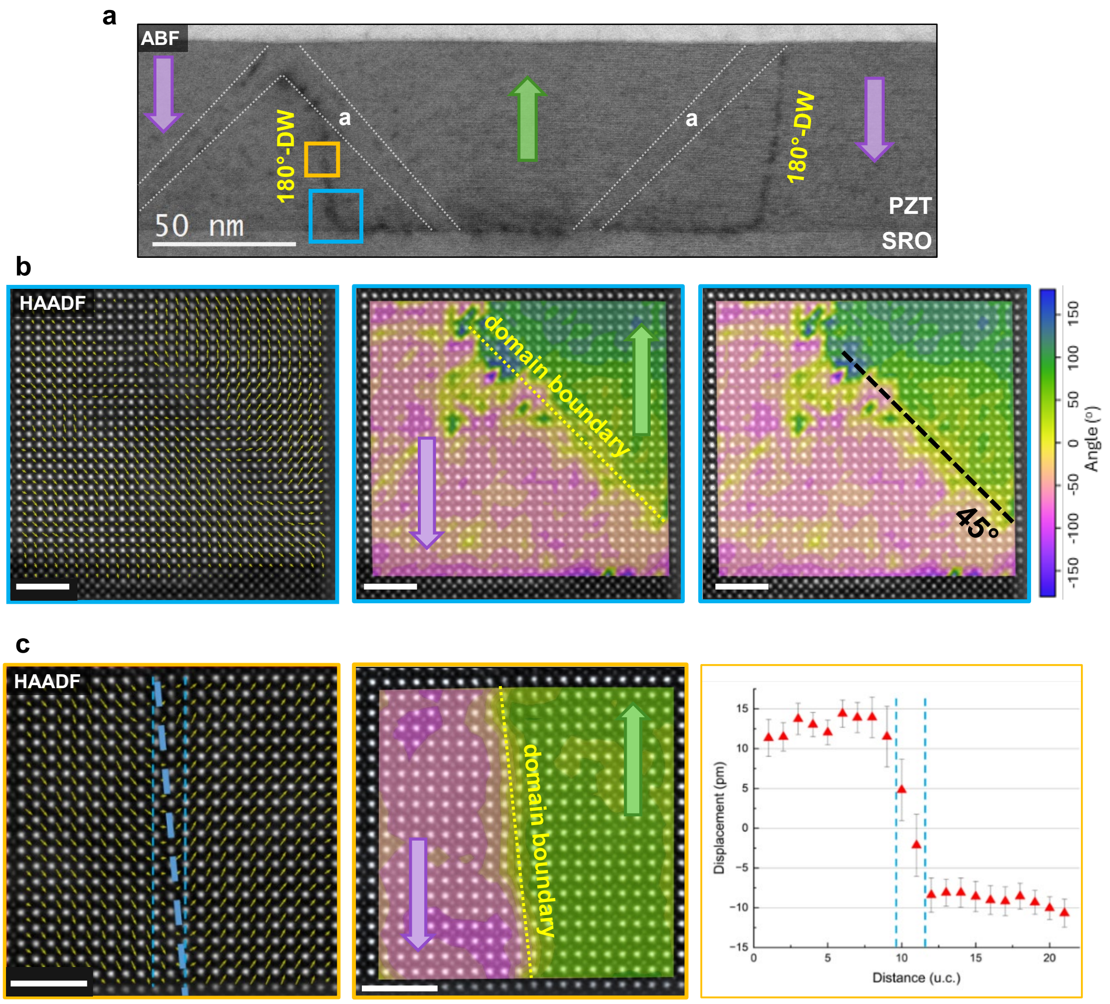

Figure 4.19: *a) Low-magnification ABF image of a 150 nm poled region (green arrow) with adjacent 180°-DWs (visible as black lines). b), c) Two regions imaged with high-resolution HAADF, measuring the polar shift of Ti atoms. Polar analysis is carried out and colored in the polar plots on the right side. b) A 45°-angle of the 180°-DW forming at the bottom interface with the SRO is revealed (blue square). c) A relatively straight part of the 180°-DW is observed in the center of the film (orange square).*

Another instance of a T-T DW formation is shown in Figure 4.20. It shows the same region as seen in the left side of Figure 4.19. The appearance of the T-T segment at the bottom interface has been discussed above but another segment in the center of the film also creates a T-T formation. This time the charged DW is induced due to the interaction of the c-domain switching happening between the left and the right side of the a-domain. The need of the a-domain to remain in its strain induced structure together with the forced polar discontinuities at the domain boundaries lead to a the formation of the charged T-T DW segment.

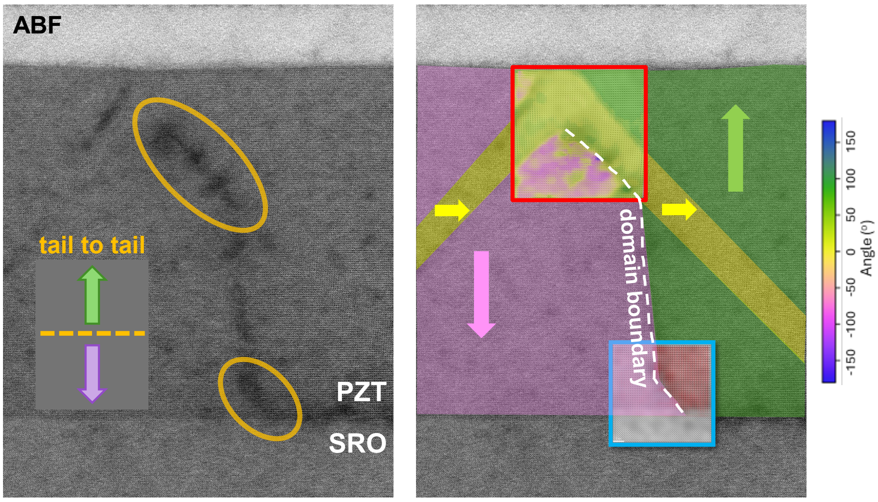

Figure 4.20: *STEM images of the nominally 180° DW interacting with an a-domain. Left: STEM- ABF image shows the nominally 180°-DW under investigation. It starts at the surface of the PZT at the intersection between two a-domains and follows the a-DW on the right side up to about 40 nm from the SRO electrode. Then the DW twists and follows a trajectory along [001] up to about 10 nm from the SRO electrode where is twists again along [011] until it reaches the SRO electrode. STEM-HAADF images with a plot of polarization vectors in the vicinity of the nominally 180°-DW are shown on the right side inside the red and blue squares (overlapping the colored ABF image). The polarization discontinuity with Tail-to-Tail formation is highlighted in the orange circles on the left side.*

The local chemistry of the 180°-DW was examined in Figure 4.21, using STEM-EELS line scans. The beam was scanned between the pristine (blue) and poled ferroelectric c-domain (green) with a pixel size of about half unit cell, passing through regions of a 180°-DW (orange) that exhibit polar discontinuities. No evidence of oxygen vacancies or other charging agents were found in the spectra collected from the Ti-L edge and O-K edge, as shown in Fig. 4.21 (center plot), due to no substantial modifications observed in the edges. On the contrary, the orange spectra of the 180°-DW position collected at the low-loss region, as shown in Fig. 4.21 (right plot), exhibit a notable increase in the peak at 22 eV. The peak at 22 eV can be assigned to the energy of the volume plasmon $\hbar\omega_p$ [180]. The increase of the intensity of the volume plasmon at the position of the domain boundary might be attributed to the existence of free charges in the DW. However, the lack of sufficient data and the absence of previous work on the topic prohibit us from drawing conclusive results.

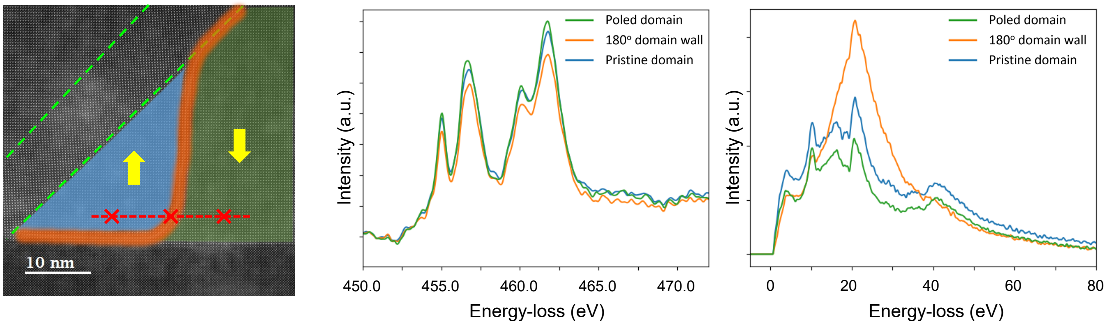

Figure 4.21: *STEM-EELS line scans collected from the region highlighted with red arrows in the HAADF image shown on the right, reveal the local chemistry of the domain wall between pristine and poled ferroelectric domains in the tetragonal PZT thin films. The DW is marked in orange separating the pristine and poled domain highlighted in green and blue, respectively. No evidence of oxygen vacancies or other charging agents were found in the Ti L edge spectra (center plot). A notable increase in the peak intensity at 22 eV is observed in the low-loss spectrum (right plot).*

To conclude this subsection of STEM experiments, it has been experimentally shown that the internal structure of normally neutral and straight 180°-DWs are heavily distorted in the presented strained PZT sample. While some areas of the 180°-DW are just slightly deviating from its neutral [001]-axis, interactions with a-domains as well as the bottom interface promote the formation of charged segments predominantly in the form of T-T DWs. The competing interplay of strained and dense a-domains together with the formation of the poled c-domains often result in unavoidable charged surfaces, which are not isolated to the 180°-DW but rather form at their interaction regions. These experimental results as well as the unusual twist of 180°-DWs at the bottom interface match with the predictions of the simulations in Section 4.2.3. Furthermore the same type of charged walls, the Tail-to-Tail DWs, which were predicted, are found by the STEM studies. It is also easy to imagine that the observed formations of charged surfaces will greatly differ, depending on the exact position of the DWs, and be enhanced wherever an enhanced density of a-domains is present, very similar to the results seen in the surface images by cAFM. The EELS experiment also shows the missing oxygen vacancies at the DW, in accordance with the expected non-defect mediated conduction mechanism. Nevertheless it should be noted here that no signs of lurking a-domains, which only partially exist in the film without connecting the top and bottom interface, have been detected in the STEM studies nor the existence of proposed 3D percolation channels for carriers could be studied.

4.3 Summary

In summary, in this chapter the first observations of highly conductive normally neutral 180°-DWs in strained PZT samples are presented. Exhibiting a three orders of magnitude enhanced conductivity compared to previously studied a-DWs, the 180°-DWs moreover showed excellent time and positional stability, due to their ferroelectric nature. Their ability to be moved, erased or created at will by electric stimuli together with the proved non-volatile and highly enhanced conductivity makes them extremely attractive for DW-based nanoelectronic devices. The assumed standard a/c-domain structure with straight walls for PZT thin films is challenged by the found intrinsic conduction mechanism and the assumed formation of a complex 3D entanglement of the domains. Phase field simulations suggest that the complex interconnected behaviour of the ferroelectric 180°-DWs with the ferroelastic a-domains lead to the appearance of a large amount of negative bound charges, which mediate a three-dimensional percolation-based current transport along different DW-interfaces.

Atomic-scale STEM analysis of the domain wall structure and domain formation under poling could experimentally verify these findings and show that the previously -believed to be-straight structure of the 180°-DWs is distorted and charged surfaces arise, which predominantly form as Tail-to-Tail boundaries. The observed charged segments of the 180°-DWs are found to form at the interaction points with a-domains, as predicted by the phase-field simulations. Moreover, the intrinsic carrier transport mechanism, which is considered based on temperature dependent conduction measurements and the observation of the formation of conductive 180°-DWs at cryogenic temperatures, is matched by the results of the simulation as well as the STEM experiments.

5 Memristive devices based on 180°-DWs

In this chapter, it will be explore how first prototype devices can be build based on the newly discovered conductive 180°-DWs in PZT films. First, Cr/Au electrodes are introduced which enable a stable contact to the 180°-DWs. Basic binary memory devices are formed for the resulting capacitor devices with promising on/off ratios. To further expand the field of application relevant devices, a higher control over the domain wall creation and positioning is needed for sophisticated devices. For this new electrode materials are investigated. Graphene flakes as well as patterned graphene monolayers demonstrate to be suitable candidates for a stochastic-driven but repeatable control over the domain wall nucleation. Importantly, by employing graphene electrodes, the domain expansion is limited such that domain wall can be confined and stabilized inside the capacitor area. First experimental demonstrations of memristive devices based on the modulated domain wall density in PZT are presented. A gradual change of the resistive states based on the number and amplitude of poling pulses is shown. The content of this chapter is based on the work presented in [175, 181]

5.1 Contacting DWs for device applications - Cr/Au

In this section, the fabrication of Cr/Au electrodes is briefly discussed and followed by the characterization of their electrical properties when connected with different kind of DWs. It will be shown how the electrode-DW contact can be formed and how it improves the stability of the electrical readout of the DWs. Possible stable configurations will be explored by which these contacts can be created and what limitations are observed when using pure metal evaporated electrodes together with 180°-DW in highly ordered tetragonal PZT film. Finally some basic binary memory devices are presented based on a vertical capacitor geometry.

5.1.1 Fabrication and electrical characterization

The process flow for the fabrication of the nanosized Cr/Au contacts with the most important steps, is shown in Fig.5.1.

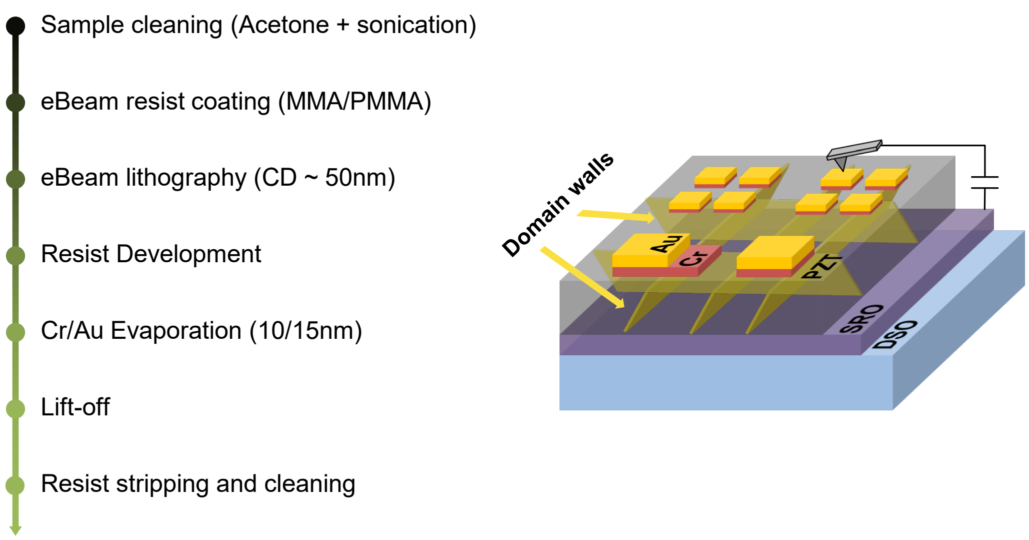

Figure 5.1: *Left: Most important steps of the process flow to fabricate the nanosized Cr/Au electrodes. Right: Schematic of the final structure with Cr/Au electrodes contacting the domain walls.*

The first step to enable a good interface with the surface of the film and to electrically contact the DWs, is to meticulously clean the sample. A combination of acetone immersion plus sonication for 5min is used followed by light scrubbing of the sample surface using a lens tissue and finished with a quick rinse in ethanol and drying with a nitrogen-gun. The more standard cleaning step of oxygen plasma cleaning is intentionally skipped since the reactive oxygen plasma could interact with the oxide surface of the PZT-film and alter its properties. After the cleaning an electron beam (ebeam) lithography step is performed to achieve device geometries smaller than 1 µm. After the eBeam resist is developed and the pattern is checked with an scanning electron microscope (SEM), the metal layers are evaporated. After the evaporation a lift-off process is used to release the metal structures. The decision to use a lift-off method was taken due to its less aggressive interaction with the PZT surface compared to wet etching processes with harsh chemicals, potentially altering the oxide surface or the DW properties. The last step involves wet resist stripping and cleaning of the sample to remove all excess resist residues.

In Figure 5.2 (upper part) the layout of the design for the different electrodes is shown. Different dimensions of square electrodes from 50 nm to 1 µm are designed together with reference marks for identification and navigation within the AFM-system. The lower part of Figure 5.2 shows an SEM image of the smallest electrode design of 50 nm after the eBeam lithography step (no metal deposited, contrast between eBeam resist and PZT surface) on a test sample (the underlying grain structure of the test PZT-sample can be observed). The targeted 50 nm are exceeded as shown, with openings of around 85 nm. Since the dimensions of the smallest electrodes were chosen to match the crosshatch pattern distance (distance between

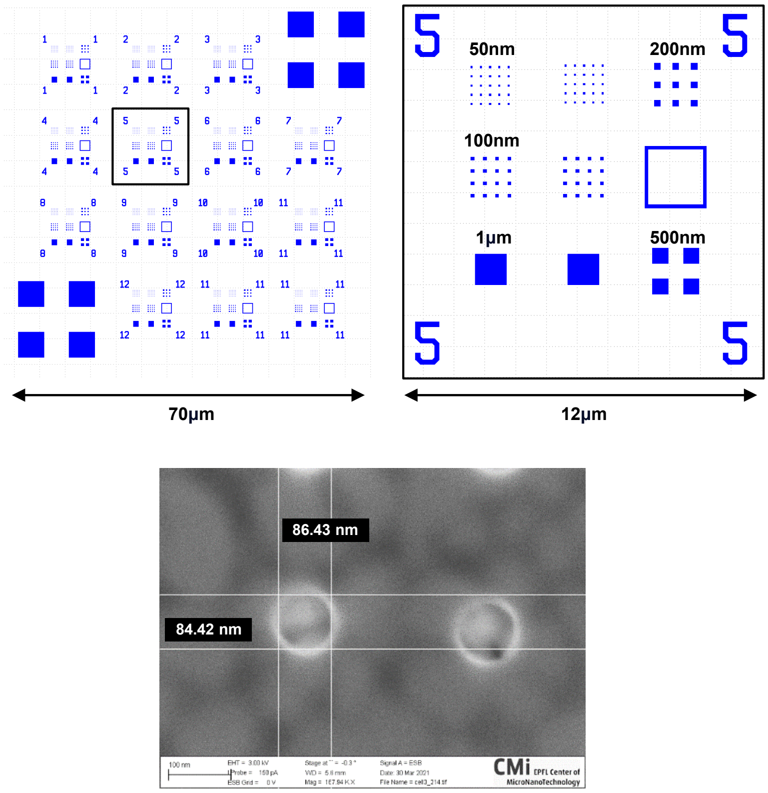

Figure 5.2: *Cr/Au electrode design layout and resulting eBeam pattern. Top: Design layout for the Cr/Au electrodes with a variety of different sizes from 50 nm to 5 µm as well as markers to identify the right area within the AFM-microscope. Bottom: SEM image of the eBeam pattern after development on a PZT test sample. The shown circular features are the 50 nm electrodes from the initial design.*

a-domains normally between 100-300 nm), this slight variation was acceptable and the eBeam parameters were not further optimised.

Figure 5.3 shows AFM topography scans of the 50 nm, 100 nm and 200 nm electrodes after the full fabrication and cleaning steps. For the smallest sizes (50 nm), most of the patterned 5x5 layouts only showed a subset of the 25 electrodes, which most likely occurred because of adhesion problems and the rather harsh sonication cleaning step after the deposition. For the 100 nm and 200 nm layouts adhesion was better and most patterns came out as expected. The final diameter of all design was between 20-30 nm wider than targeted, which was expected after investigating the SEM image of the eBeam lithography step in Fig. 5.2. Another aspect visible from the 3D images is that the electrodes with sizes smaller than 230 nm appeared roundish on the surface which could be problematic for future precise nanometric PFM investigations. The 230 nm electrodes (and all bigger layouts) showed nice flat surfaces with only minor tilted side walls.

Next, the contact to single a-DWs is studied by using the small electrodes of 120 nm size. Their

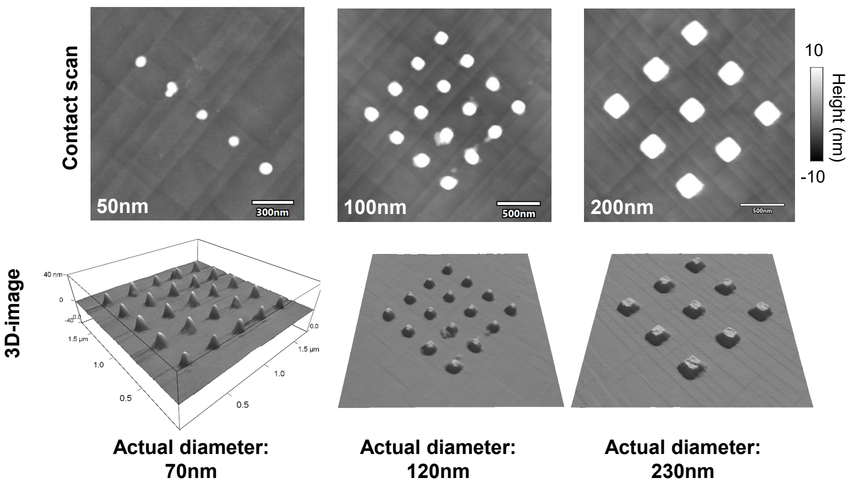

Figure 5.3: *AFM topography images of the resulting Cr/Au electrodes. From left to right: The resulting electrodes for the 50 nm, 100 nm and 200 nm designs. Bottom shows the 3D image of the topography image of the electrodes respectively. For all design an increase in size of about 20 nm is observed.*

size nicely matched the dimensions of the crosshatch pattern in a way that some electrodes contact single DWs, two DWs if they fall onto a DW junction or no DWs if they are placed onto a c-domain. The kind of contact is readily visualized by PFM scans as shown in Fig. 5.4. After the PFM images, a cAFM scan was performed to visualize, which electrodes form a good contact with the a-DWs. Interestingly, only one electrode appeared to be strongly connected (seen in a strong signal in the cAFM map) with most of the electrodes only showing medium

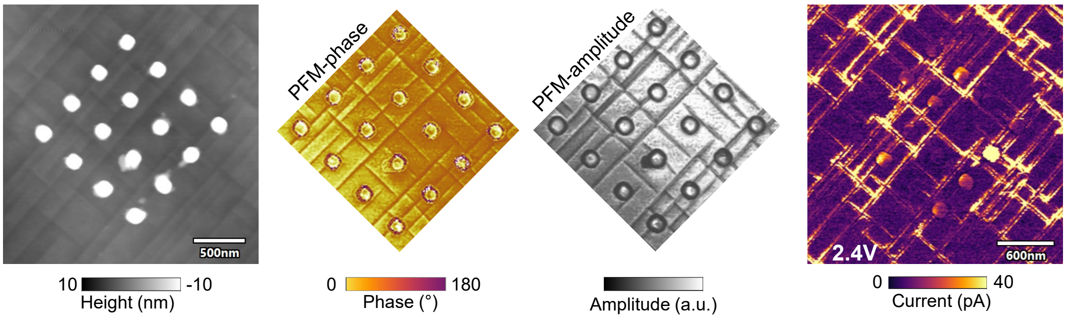

Figure 5.4: *PFM and cAFM characterization of 100 nm Cr/Au electrodes. From left to right: Topography, PFM phase and amplitude and cAFM image of the 100 nm electrodes. From the phase image we see that the whole area is in the pristine unpoled state with no 180°-DWs present. The a-DWs show their know conductive behaviour in the cAFM map, taken with a bias of 2.4V. Some of the electrodes, when scanned in cAFM, show a conductive response, indicating that they formed a contact to the a-DWs. However, most of the electrodes show either no conduction or only very little.*

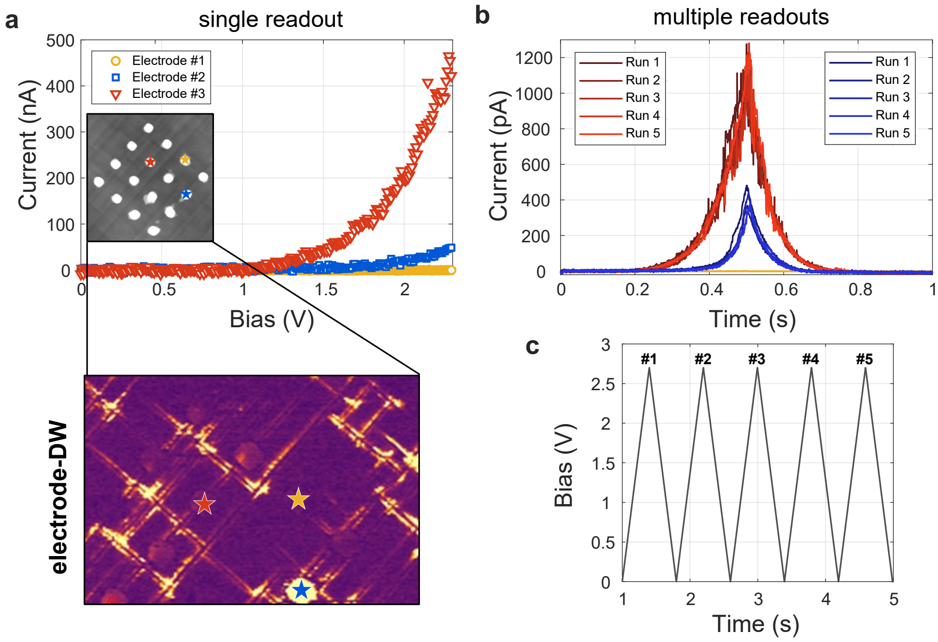

Figure 5.5: *Characterization of the Cr/Au electrode - DW contact. a) Single IV-curves taken with the tip placed onto the marked electrodes. Interestingly the blue electrode showed the highest response in the cAFM image but provided only a slight conduction of around 50 pA. The red electrode yielded a current of 450 pA which matches the values of a single DW readout with the tip. The yellow electrode did not show up in the cAFM image and the IV curves also shows no current indicating that no connection between a-DW and electrode is formed. b) Characteristics of multiple readouts with the Cr/Au electrodes shown in the time domain. The same electrodes are used as in a). Importantly, the multiple IV curves nearly perfectly overalp with each other highlighting the stable readout of the DW conduction with the electrodes and the enhaned signal to noise ratio compare to readouts by the tip. c) Pulse waveform used for the measurements in b).*

conduction while the DWs are nicely visualized. Certainly, cAFM scans can be influenced by the tip contact and potential problems with residual resists, debris at the tip etc. could alter the appearance of the conduction of the electrodes in the images. Therefore the next study investigated the electrical connection by IV curves.

In Figure 5.5, IV curves are taken on the 3 marked electrodes as well as on 3 positions directly on a-DWs. First, single IV curves are shown taken with the tip placed onto the 3 different electrodes (red, blue and yellow). Each electrode show significantly different characteristics with the red electrode being the most conductive with around 200pA for 2V while the blue only exhibited 20pA for 2V and the yellow seemed to be not connected at all. Based on the PFM and cAFM image the blue was expected to be the most conductive as it seems to be connected to two a-DWs while the red one is only connected to one a-DW. This difference could be attributed to the non-uniformity of the a-DW conduction along their length as observed throughout the cAFM scans or due to an non-ideal interface between the metal and the PZT surface. By comparing the IV characteristics of the red electrode to previously measured IV curves on single a-DWs 4.1, a good match of the current values (200pA for 2V) is observed despite the different shape of the IV curve due to a different conduction mechanisms at the interface and the different materials. It is therefore concluded that an ideal contact of that red electrode with exactly one a-DW is achieved.

In the right column, multiple IV curves are taken and plotted on top of each other in the time domain (the bias profile is shown in the bottom right). IV curves from the same electrode nicely overlap on top of each other showing the stable readout characteristics and proofing the non-volatility of the DW-conduction. It also confirms that it is possible to create stable and well defined access to the DW-current. In comparison the similar IV measurements are shown in the lower row where a-DWs are contacted by the AFM tip. The red spot is taken on top of an a-DW junction and the blue and yellow points are taken on a single DW segment. The first observation is, that the current starts rising at a higher voltage value due to an additional barrier from the tip-surface interface, secondly as seen in the time domain, the current readout shows significant variability between consecutive readout cycles due to the non-uniform electric field at the tip apex and the variable contact. Despite the tendency that the DW-junction (red) seems to be more conductive than the single DW segments, it is concluded that it is difficult to precisely measure the conductance of the DWs by a AFM-tip due to the huge variability.

5.1.2 180°-DW contact for first device applications

After verifying that the weakly conducting a-DWs can be well contacted with reliable readouts, the more interesting approach of creating and connecting 180°-DWs to the electrodes was pursued. By achieving a stable connection of an artificially written conducting 180°-DW with the nanometer sized electrodes, a conductive path should be formed between the top and bottom electrode which would lead to a huge resistive change of the device. If it is possible to control the creation and erasure of the DW-connection the reliable switching of the device between its high- and low resistive state and thus creating a binary memory device is achieved.

Due to existing problems with the adhesion and limitations with PFM imaging of DW-segments under the non-uniform area of the smaller electrodes, the middle sized electrodes with areas of 230-280 nm were used for these experiments. Previous measurements showed that a decent PFM-amplitude contrast could be achieved to visualize the DWs under the electrode. First experiments were carried out in which the tip was placed on top of the electrode, and short voltage (down to 50 µs) pulses of +5 V were applied to partially switch the c-domains under the electrode. However it turned out that even for the shortest dwell times of the poling pulses, the c-domain area under the electrode would switch completely. Simultaneously, the DW is pushed outside of the electrode area without forming a stable connection with the electrode.

Therefore another method was tested, for which a c-domain outside but in close proximity of the electrode is poled by a AFM tip. Through a step by step expansion of the poled region

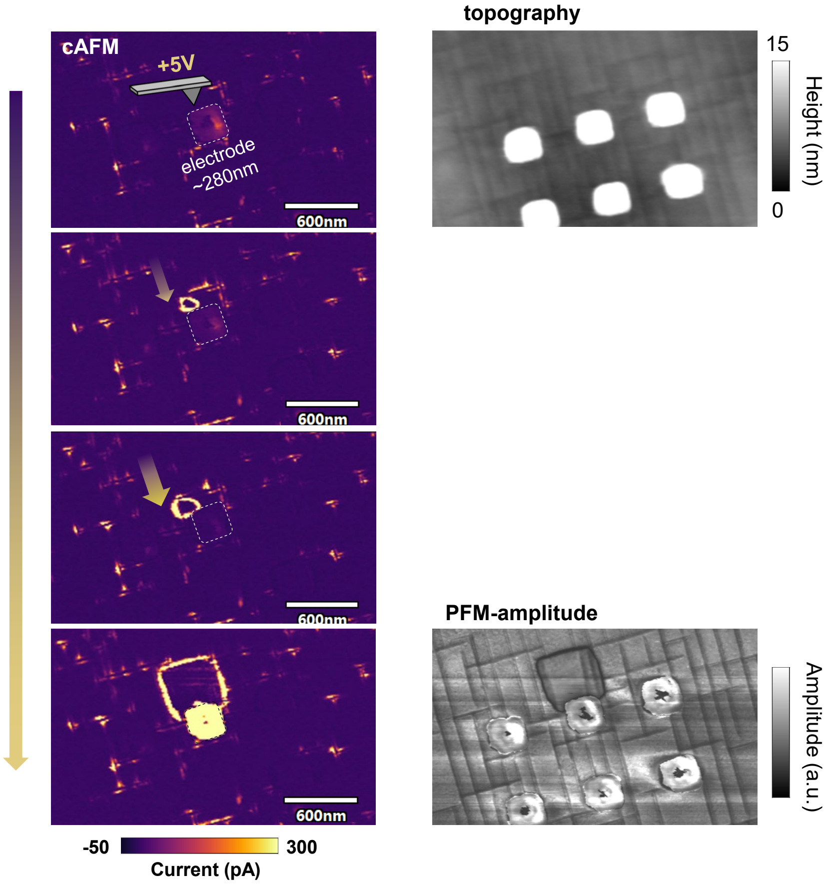

Figure 5.6: *Contacting Cr/Au electrodes by 180°-DWs. Left side: Series of cAFM images showing the progressive increase of the poled domain size with its associated 180°-DW until it forms contact with the Cr/Au electrode. In the first image the schematic of the tip indicates the location where the domain is nucleated by a +5V/0.4s pulse. In the next image a poled tiny domain can be deducted based on the appeared conductive ring representing the 180°-DW. The Dw is further pushed to the electrode by 5V/0.4s pulses until it adapts the shape of the electrode without the formation of a connection. For the last cAFM image in the row, a 5V/5s pulse is applied to greatly extend the poled domain and enable the DW to form a connection with the now highly conductive electrode. Right side: top image shows the topography of that area and the Cr/Au electrodes of around 300 nm size. Bottom image shows a PFM amplitude image after the final cAFM image is taken. The black outline of the poled domain represents the 180°-DW, touching the border of the electrode.*

diameter by applying consecutive poling pulses, the 180°-DW can be pushed towards the electrode border and eventually form a stable connection with it. In Figure 5.6 a cAFM sequence of this method is shown. Starting from the pristine state (top image) in which the 2̃80 nm electrode is only slightly conductive (due to some connected a-DWs) and no poled domains nor 180°-DWs are present. Next, a tiny domain is poled and subsequently further expanded by consecutive +5 V/0.4s voltage pulses. In the 3rd image, the 180°-DW

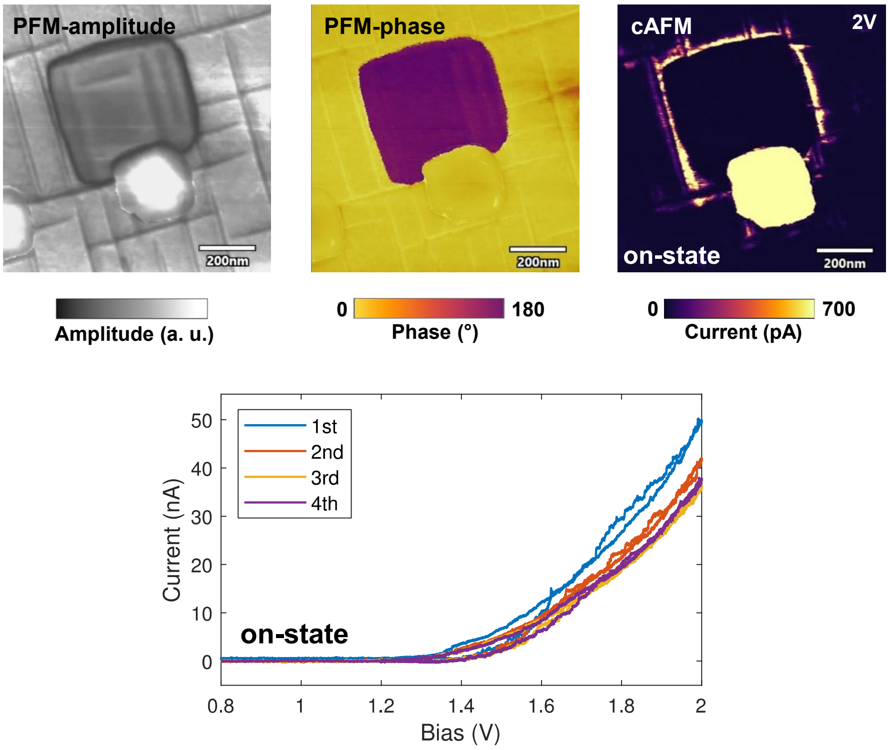

Figure 5.7: *Low-voltage readout of single 180°-DW devices using sub-micron electrodes. PFM-amplitude (left), PFM-phase (center) and cAFM (rigth) scans show the capacitor device connected with a single 180°-DW. cAFM maps were taken with a sample bias of 2 V. On-state of the device, the 180°-DW is pushed inside the capacitor area ensuring a stable conduction path between the top and bottom electrode. Consecutive I–V curves are performed (bottom) by placing the AFM-tip onto the electrode. Stable and low-noise current values of 40–50 nA were achieved for <2 V over multiple readouts.*

starts adapting to the electrode shape, but does not form the necessary connection (seen in the still non-conductive electrode area in cAFM). Only after further increasing and pushing with longer pulse duration of 5s, the DW contacts the electrode, which immediately becomes highly conductive. The DW now bridges the top Cr/Au electrode with the biased bottom SRO electrode, which puts the capacitor device in a low-resistive state (LRS).

The formed DW-electrode device is now studied in more detail in Figure 5.7. Interestingly, the 180°-DW does not penetrate under the electrode area but rather follows its boundary as seen in the PFM images. IV curves are recorded by placing the AFM-tip on top of the electrode and applying a triangular voltage pulse from 0V to 2V and back to 0V. A nearly noise free current of around 40nA is observed which does not change upon consecutive readouts. Although the exact overlapping length of the DW with the electrode border can not be determined due to limitations in the resolution of the PFM images, the IV curves verify the achieved non-volatile connection and the LRS.
In Figure 5.8, another set of IV curves are taken on different positions on the electrode by the

AFM tip. The resulting curves (shown in the time domain) show a nice overlap onto each other which confirms the uniformity of the contact and shows no distance dependence of the readout position to the DW.

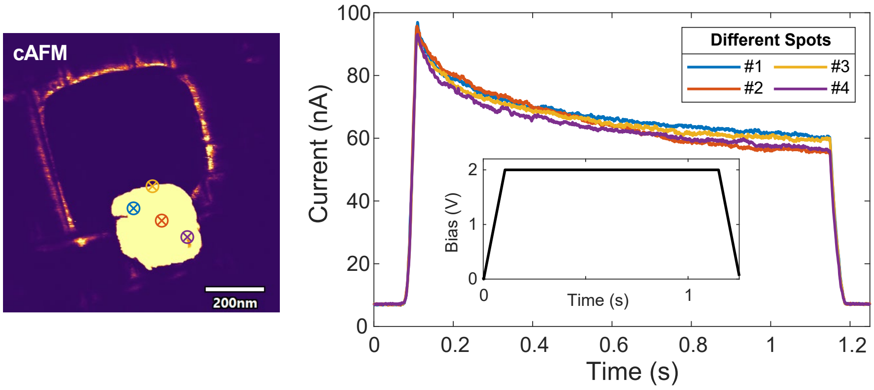

Figure 5.8: *DC-current readout from different spots on the electrode. IV curves are taken by the AFM tip with the bias waveform depicted in the insert (2V/1s, DC) on different points on the electrode. No change of the acquired current curves are observed for the 4 spots.*

After creating the LRS by the described method of domain expansion, the resistive switching of the prototype device is explored. Starting from the on-state two ways of off-switching of the device are shown in Figure 5.9. Similar to the IV readout, the AFM-tip is placed onto the electrode and a voltage pulse greater than the coercive field is applied. In the first test, the poled domain is expanded by applying a positive voltage pulse onto the electrode. The domain expands beyond the electrode area until the DW is completely pushed outside of the electrode boundary and the device area is uniformly poled upwards (purple). The DW-electrode connection is interrupted and the device is put back to its HRS. Analogously, by applying a negative bias, the poled domain starts to shrink and the DW is pushed away from the electrode boundary until the c-domain under the electrode is switched back completely (yellow). For both HRS-cases, IV curves are recorded and plotted in the right column with off-currents of around 20-30pA for 2V. By comparing both cases it can be exclude that the on-state current originates from polarization field dependent resisitive switching but rather solely depends on the DW-mediated current and the formed DW-electrode contact. The change of the resistivity results in an on/off ratio of the demonstrated memory device of around 10^3.

Because it was not possible to position the DW directly under the electrode, more experiments were performed to evaluate the stability of the DW-electrode contact and hence the device characteristics. In Figure 5.10 time dependent measurements are performed. In the upper part the pulse scheme readout of the DW conductance with the AFM tip on the DW (yellow dots) is compared with the readout through the electrode (red dots). Similar to the case of the a-DW contact in Fig. 5.5, the readout by contacting the 180°-DW with the tip showed huge variability between 19 nA to 50 nA while the conduction recorded through the electrode showed a smooth curve with a low scattering rate of ≤4%. For the pulsed readout through the electrode we do observe a sharp decay in the beginning for the first ~5 pulses followed by a

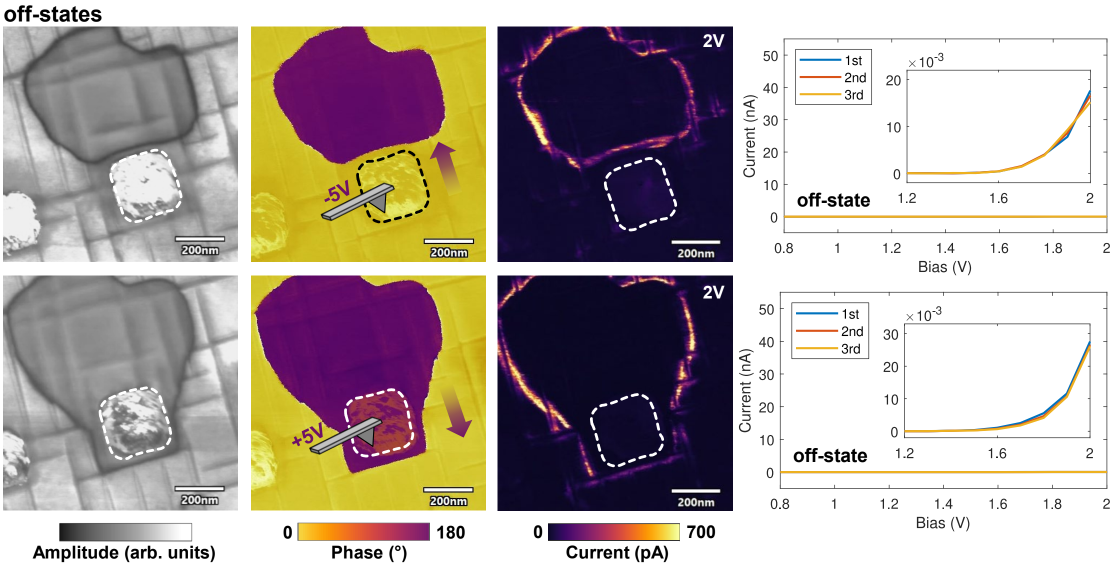

Figure 5.9: *Different off-states of the Cr/Au DW-device. PFM-amplitude (left column), PFM-phase (center) and cAFM (rigth) scans show the capacitor device (outlined by dotted line) uniformly poled without a connected domain wall (off-state). cAFM maps were taken with a sample bias of 2 V. After applying to the top electrode a positive voltage pulse exceeding the coercive field value, the 180°-DW is pushed away from the device, breaking the conduction path and inducing the high-resistance state. On the right side, consecutive I–V scans are performed through the electrode showing low sub-20 pA currents. By using a voltage pulse of opposite polarity (negative), the poled region can be extended to fully cover the electrode area (with no domain wall touching the electrode). This results in similar I–V characteristics with only tens of pA currents.*

saturation of the conductance level. Another comparison is done by looking at the difference between a pulsed (red) and DC (blue) readout through the electrode. Interestingly the resulting curves nearly fully match each other both in the absolute conductance level as well as in the decay and saturation behaviour. The decay can be attributed to electrostatic decharging of the capacitor device as well as to charge trapping effects. In the lower part of Figure 5.10 repeated pulsed readout schemes are performed. Each cycle consists out of 10 pulses for a total of 1.5 s. Six such cycles are applied consecutively with some tens of seconds between each run. The superb stability of the readout characteristics is observed in the current curves as each consecutive run matches the other. The previously observed decay from 120 nA for the first 4-5 pulses is followed by a saturation of around 60 nA for the 2 V readout pulses.

The excellent stability as well as the big on/off ratio of three orders of magnitude achieved for this DW-memory device with below 300 nm electrode diameter showcases the feasibility to use stable 180°-DWs for nanoelectronic devices. The proposed device operated with low voltages below 5 V and only employed electrical stimuli. Furthermore the contacting allowed for cleaner readout and characterisation of the DW-current compared to readout schemes with an AFM-tip.

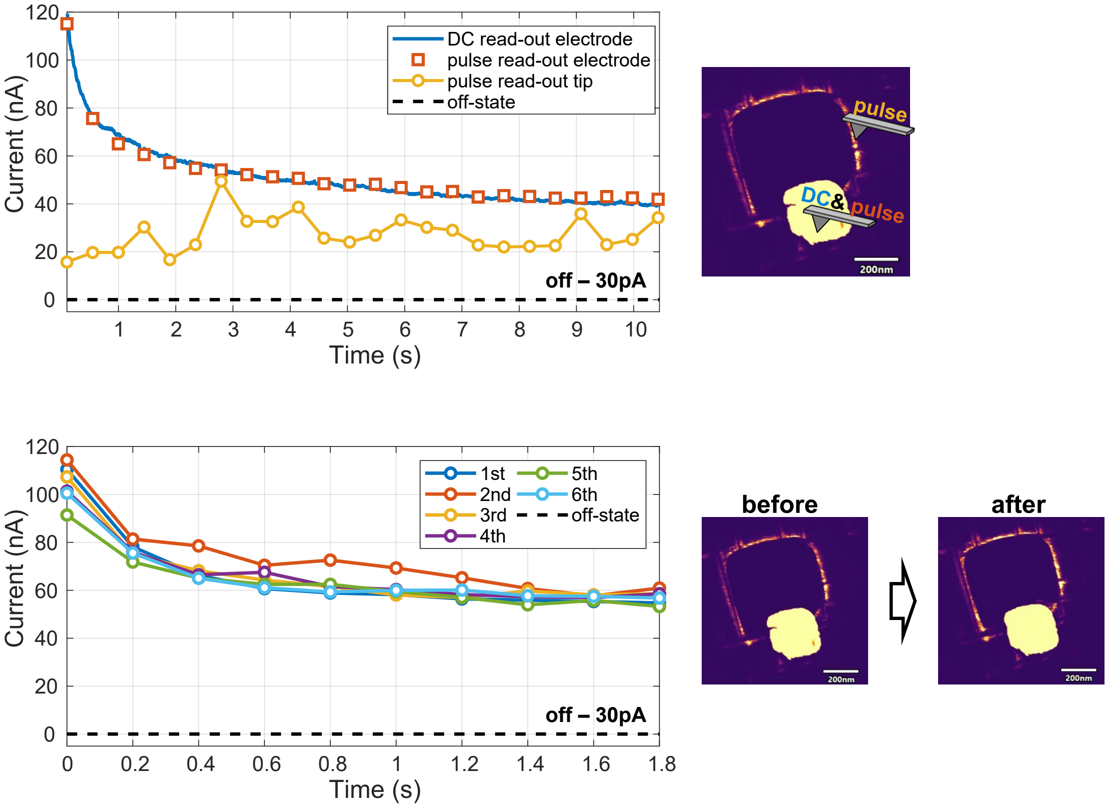

Figure 5.10: *Top: Comparison between different readout methods. Yellow dotted line indicates a pulse readout by placing the tip directly on the 180°-DW. The red dotted line shows the same readout scheme with the tip sitting on the electrode. Blue solid line indicates a readout through the electrode but with a constant 2 V DC readout. Bottom: Consecutive pulse train measurements performed on an on-state device. Each pulse train consists of 10 triangular voltage pulses of 2V/200ms. The black line for both plots indicates the off-state conductance level of 30 pA.*

To further push the concept of DW-mediated resistance switching and to achieve advanced functionalities within DW-based devices, a better degree of control over the DW position is needed. Especially the ability to position the DW directly under the electrode is desirable since it would allow for quantitative measurement of the DW conductivity per length scale. The presented conduction measurements so far, especially Fig. 5.7 and Fig. 5.10, can only qualitatively show the high current values achievable by contacting the 180°-DWs. Due to the fact that the 180°-DW adapts the shape of the electrode and only partially overlaps with its boarder it is impossible for us to evaluate the exact length of the DW-segment which is actively contributing to the current transport.

Experiments, in which more effort was done to try to position the DW directly under the electrode are shown in Figure 5.11. The same method of domain expansion is used as described above. In this experiment we observed a partial switching of the c-domain under the electrode area as seen in the middle row image with clear contrast of the 180°-DW under the electrode.

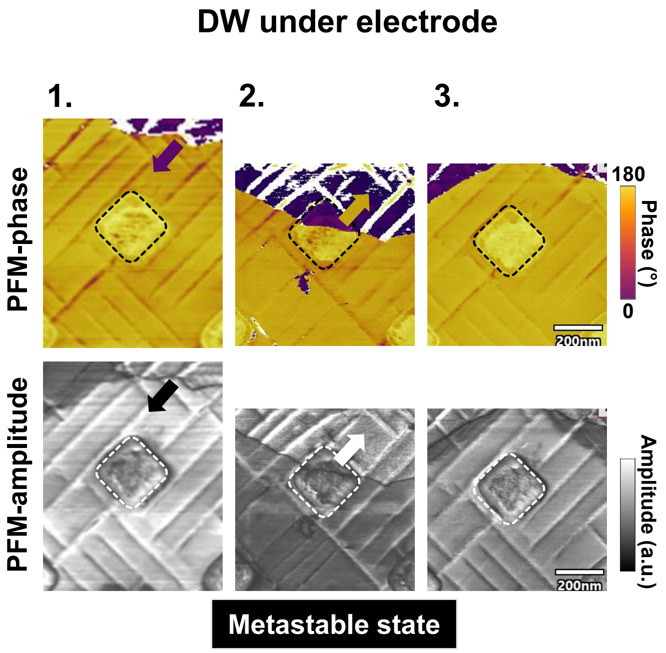

Figure 5.11: *Stabilizing a 180°-DW under the Cr/Au electrode. PFM images of the 3 stages of a metastable partially switched Cr/Au electrode are shown. In 1. the DW located in the top right corner is pushed towards the electrode. In 2. the DW is located exactly under the electrode. In 3. directly after the PFM take from 2, the DW is pushed away from the electrode area. The state of 2. showed to be metastable. While it was possible to create it, consecutive PFM or IV curves resulted in a collapse of the state leading to the DW being pushed away. No control or ability to position the DW under the electrode area is achieved by using Cr/Au electrodes.*

Unfortunately, this configuration was unstable and collapsed by either fully switching or backswitching of the area under the electrode (the case for backswitching to the downward polarized state is shown in the right column), if probed by electrical stimuli like consecutive PFM imaging or IV-measurements. Due to the good contact created by using metal evaporation and the high conductivity of the pure metal electrodes, the electric field when applied to the top electrode immediately expands to the full contact area. Because the PZT films exhibit excellent sharp switching characteristics due to its ideal ferroelectric properties, tetragonal crystal structure and low-defect density growth conditions, an near instant switching of the whole c-domains underneath the electrode is observed when applying voltage biases to the capacitor.

5.2 Memristive properties using 2D-graphene flakes and monolayer devices

As seen in the last chapter, using standard electrode materials (for example the employed Cr/Au contacts) in combination with high quality epitaxial PZT films provided poor control over the domain nucleation and expansion and therefore over the domain wall position. While the near instant switching of c-domains is beneficial for a lot of applications for fast and precise control of the polarization directions, for DW-based devices the intermediate, half-poled or mixed domain states are preferred since they lead to the formation of domain walls. The stability of the mixed domain states is often limited due to the energy-unfavourable formation of charged DWs which give rise to the conductive channels which are to be exploited. Secondly, their reliable and repetitive creation is often difficult to achieve. As discussed in Chapter 1.2.2, different approaches have been proposed to control the formation and positioning of the DWs, however most of them involved irreversible changes in either the active material or the electric field guiding electrodes.

In this chapter we want to focus on a type of electrode which combines two important aspects: first the formation of high-quality contact between electrode material and the DW-channels with low resistivity to enable high current readout for low voltage operations and second a mechanism for a stochastic yet controllable stabilization of a mixed domain configuration. Graphene (Gr) electrodes have been demonstrated to be efficiently integrated with ferroelectric materials, leading to a sharper ferroelectric switching [182] as well as increased memory performances of ferroelectric field effect transistors and ferroelectric tunnel junctions[183, 184] by interfacial effects and stochastic out of plain domain switching. Gr-electrodes have also been used in domain-wall based LNO devices to promote a partial domain switching as discussed in Section 1.3. Together with its unique chemical stability and impermeability for oxygen improved performances in polarization stability and aging are expected.

PZT samples with conductive 180°-DWs that were investigated in previous Chapters 4 and 5.1 were used to realize two types of Gr-electrode capacitor devices: 1. multi-layer (ML) graphene flake devices and 2. patterned single-layer (SL) graphene devices.

5.2.1 Graphene flakes

The multi-layer Gr top electrodes are deposited by scotch-tape exfoliation forming simple parallel-plate capacitors. For that graphene bulk crystals, synthesized by HQ Graphene, were used. By carefully applying scotch tape to the graphene crystal surface and then peeling it off repeatedly to mechanically exfoliate the material, multi-layer flakes are obtained. The exfoliated flakes were then transferred to the PZT sample. In Figure 5.12, optical microscope images of the randomly deposited flakes are shown. A pre-screening was performed to find thin flakes with flat surface and limited size. Through the optical image suitable nearly transparent flakes (e.g. in the top left image of Fig. 5.12) were identified.

Piezoelectric Force Microscopy (PFM) imaging on top of the graphene flake electrodes enabled direct monitoring of the polarization domain state inside the capacitor as seen in Figure 5.13. The phase and amplitude loops of local piezoelectric response measured on Flake #1 yield a coercive field of ±2.5V. For extensive measurements where the mechanical and electrical robustness is essential, flakes with thicknesses between 10-12nm and an area of some μm^2 are

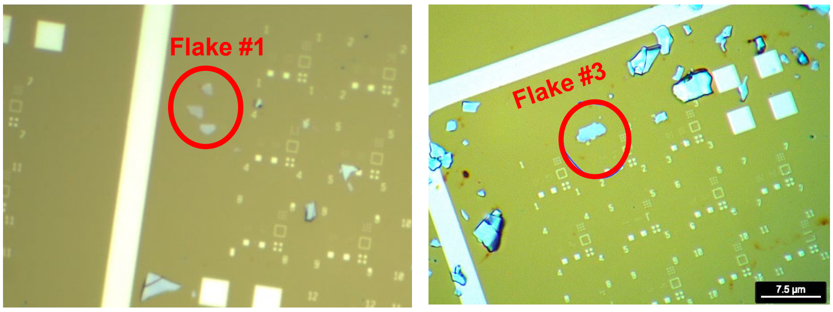

Figure 5.12: *Optical microscope image of transferred Gr-flakes. The optical microscope is used to identify suitable graphene flakes with the right properties. Flake #1 and Flake #3 which are studied in detail are marked in the images.*

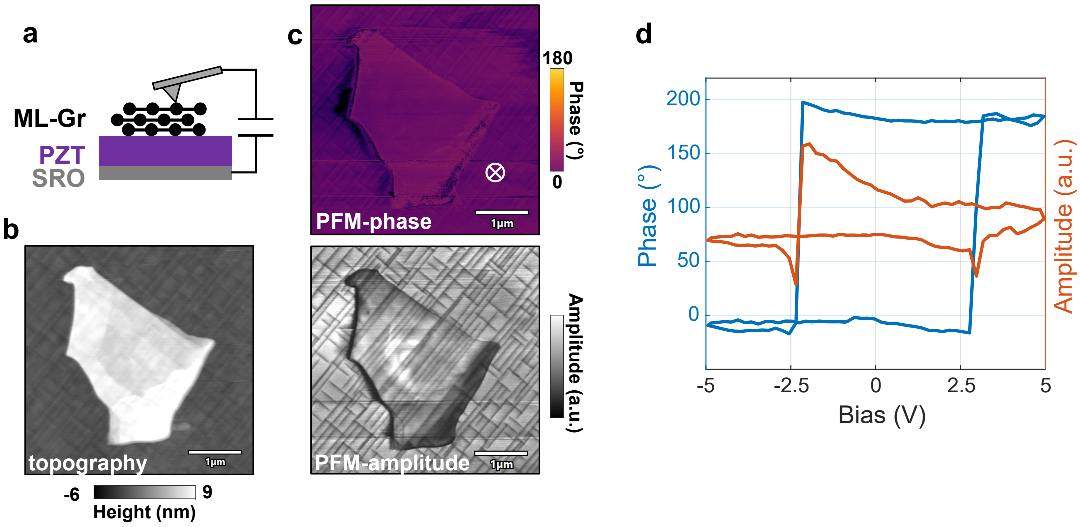

Figure 5.13: *Multi-layer graphene flake capacitor characterized by scanning probe microscopy. a) Schematic of the device geometry for probing local piezo response and device operation. b) AFM topography image of the graphene device indicating its nearly complete flat surface. c) Phase and amplitude map of local piezoelectric response. The homogeneous phase color (purple) attests to the uniform downward-oriented polarization of c-domains. The amplitude image shows that the visualization of domain walls through the electrode is feasible. d) Hysteresis loop of amplitude and phase of local piezo response probed through the graphene electrode by the AFM-tip.*

chosen. Figure 5.14 shows three ML-Gr capacitors which are investigated for further electrical measurements. PFM images of the pristine devices are displayed along the topographic images showing the uniformly downwards (purple color) polarized domain structure with intersecting a-domains. The three flakes are all around 10nm in height as shown by the line profiles and a reasonably uniform surface is observed (only flake #3 overlapped with a previously deposited

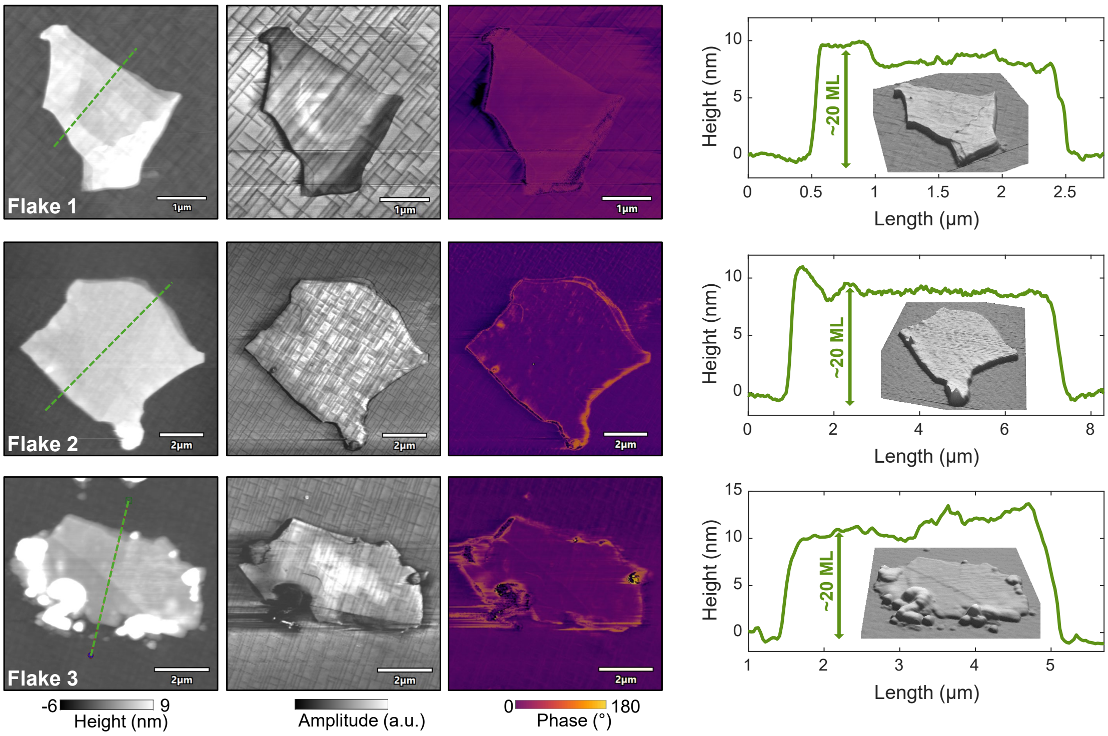

Figure 5.14: *Overview of the three investigated graphene multi-layer devices. From top to bottom: Flake 1-3 each with an AFM-topography image, PFM images of the pristine device state and a height profile alone the green lines respectively.*

marker. The "2" can be recognized in the topography image). Because of the used hard and stiff diamond coated tips, careful settings for the contact scan parameters were chosen. Deflection setpoints of maximum 0.1V (still ensuring decent contact force for PFM imaging) were used together with high gain factors and slow scanning rates. Despite these precautions, some

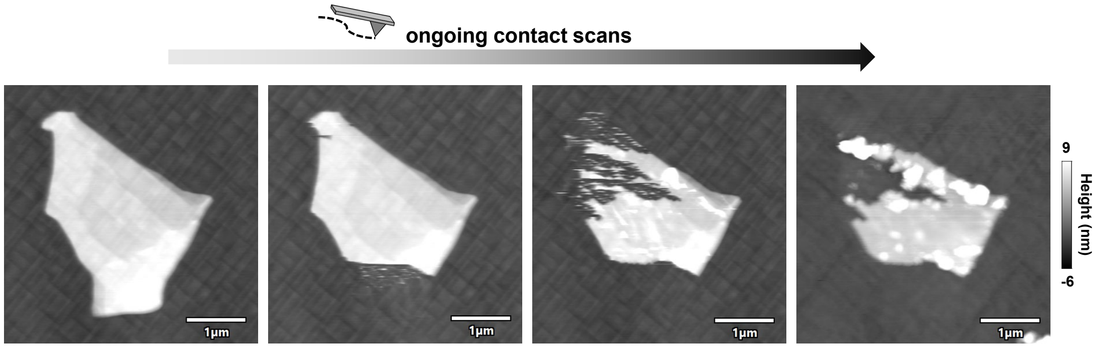

Figure 5.15: *Partial removal of the graphene device by consecutive contact scans. From left to right: First contact image taken on the graphene electrode. After some scans, the bottom part is removed. Further scanning completely cuts into the whole area of the device until it is destroyed.*

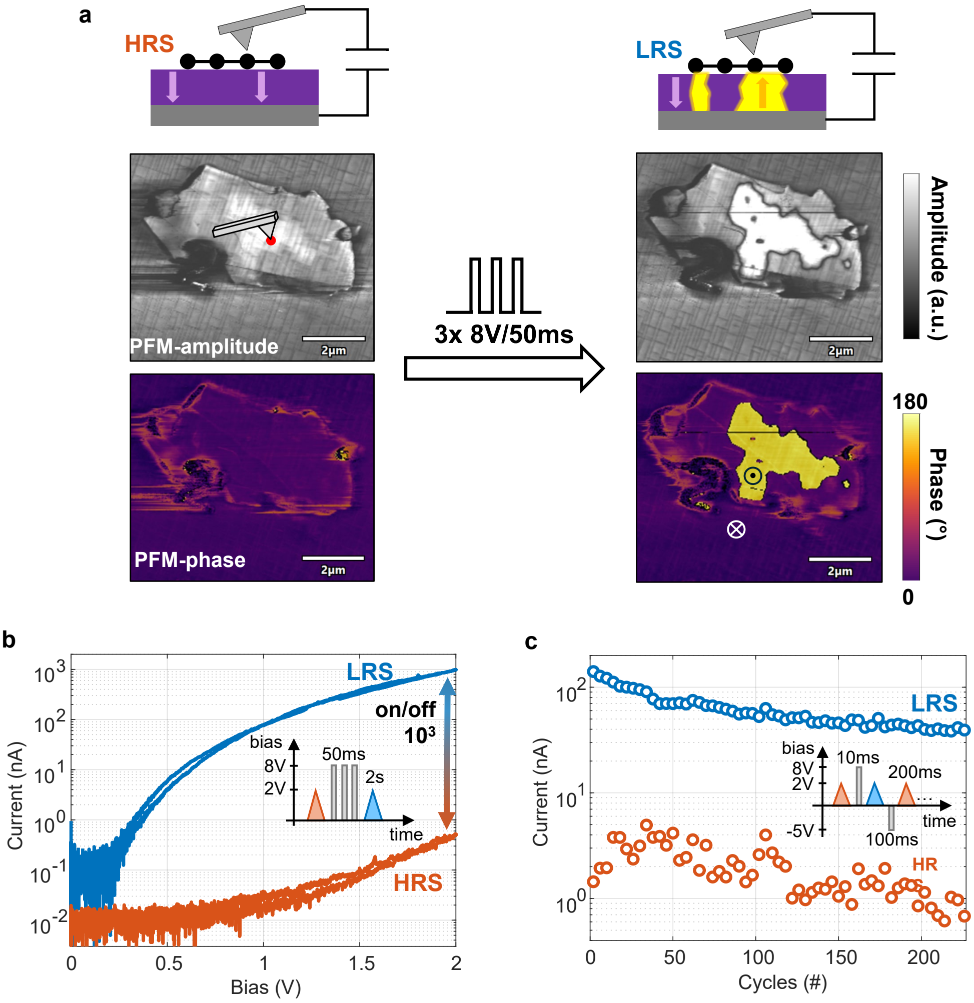

Figure 5.16: *Graphene-flake device characteristics. a) Schematic and PFM-phase images of the off-state (HRS) and on-state (LRS) of the device before and after the application of three poling pulses (8V/50ms). b) IV-characteristics of the off-state and on-state related to the device states in a) with an on/off ratio of 10^3. c) Endurance test of the device. Cycling between the LRS and the HRS is performed by application of alternating positive (+8V/10ms) and negative (-5V/100ms) pulses. Current readout is performed after each operations (2V/200ms) for up to 220 cycles.*

devices were damaged due to the repeated scanning as seen in the topographic image series in Figure 5.15. The images show intermediate steps of the partial removing of the Gr-flake. A total of 15 scans were taken on the flake before partially got removed. Another problem associated with repeated scanning and the partial removal of material (and potential residual particles introduced by the scotch tape transfer) occurred when switching between PFM imaging and electrical measurements (by placing the AFM tip onto the Gr-flake). By switching between the different modes contaminants can be picked up by the tip and successive operations are then influenced by a different contact resistance of the tip. A worse PFM signal or reduced electrical readout occurred. Due to these problems, for most of the presented results the PFM analysis are decoupled from the electrical measurements to ensure comparability and repeatability especially for the electrical measurements.

In the first test procedure shown in Figure 5.16 a, after an initial poling operation (3x 8V/50ms) on the Gr-flake, a mixed domain configuration is created by partially poling of the c-domains and thus injecting 180°-DWs inside the Gr capacitor device area. Consecutively acquired IV curves show that domain-wall based conduction up to 1µA for 2V are reached, which are plotted together with IV curves for the off-state in Fig. 5.16b. An on/off ratio up to 10^3 is observed.

Endurance tests, in which the device is cycled between the low-resistive state (LRS) and the high-resistive state (HRS) by alternating positive and negative pulses are shown in Fig 5.16c. A persisting difference by a factor of >10, with a slight trend of current decrease by 50% after 100 cycles in the LRS is observed.

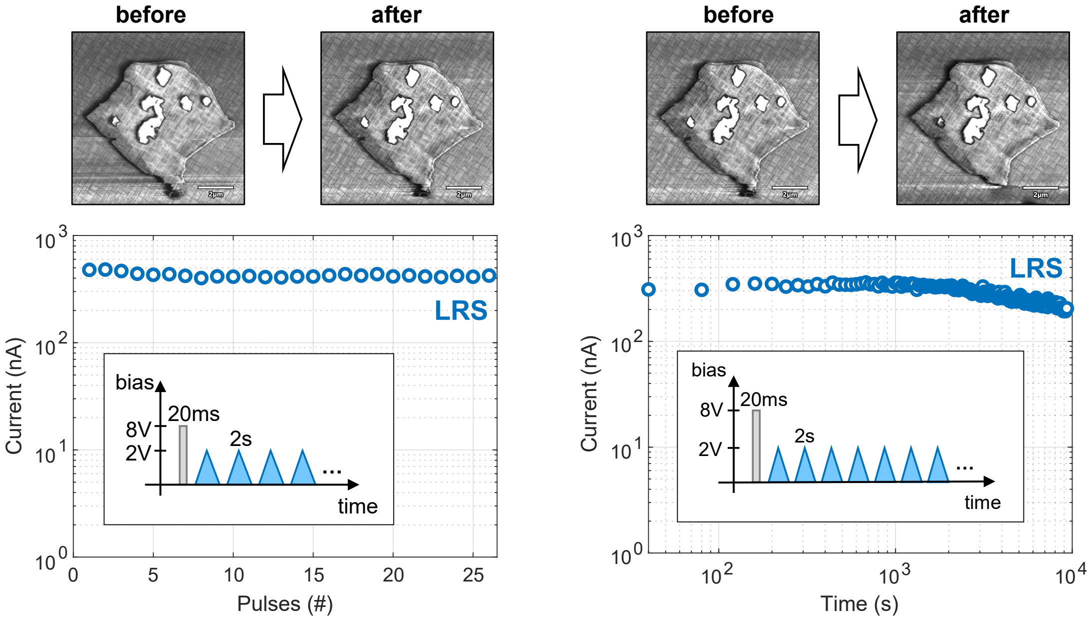

Figure 5.17: *Retention characteristics of the graphene-flake device. a) Short time retention test. The device is brought into a multi-domain state by a 8V/20ms pulse and is consecutively probed by 26 readout pulses (2V/2s). Inserts show the virtually unchanged domain configuration before and after the test. b) Long time retention test. After the test in a) the device is further probed up to* 10^4 *seconds. PFM images of the domain state before and after the test are shown in the insert.*

The stability of the current output under repeated pulsed readout is checked by retention tests shown in Figure 5.17 in which the LRS is recorded over a short (26 pulses ≙ 5min) and long (nearly 3h) timespan by 2V/2s pulses. An excellent shot-term stability is observed with a slight decrease in the conduction level for the long time measurement after around 50 min. PFM images of the domain configuration taken before and after the test confirm the stability of the written domain pattern and validates the non-volatile DW conduction as opposed to the alternative scenario of transient current spikes associated with DW movement.

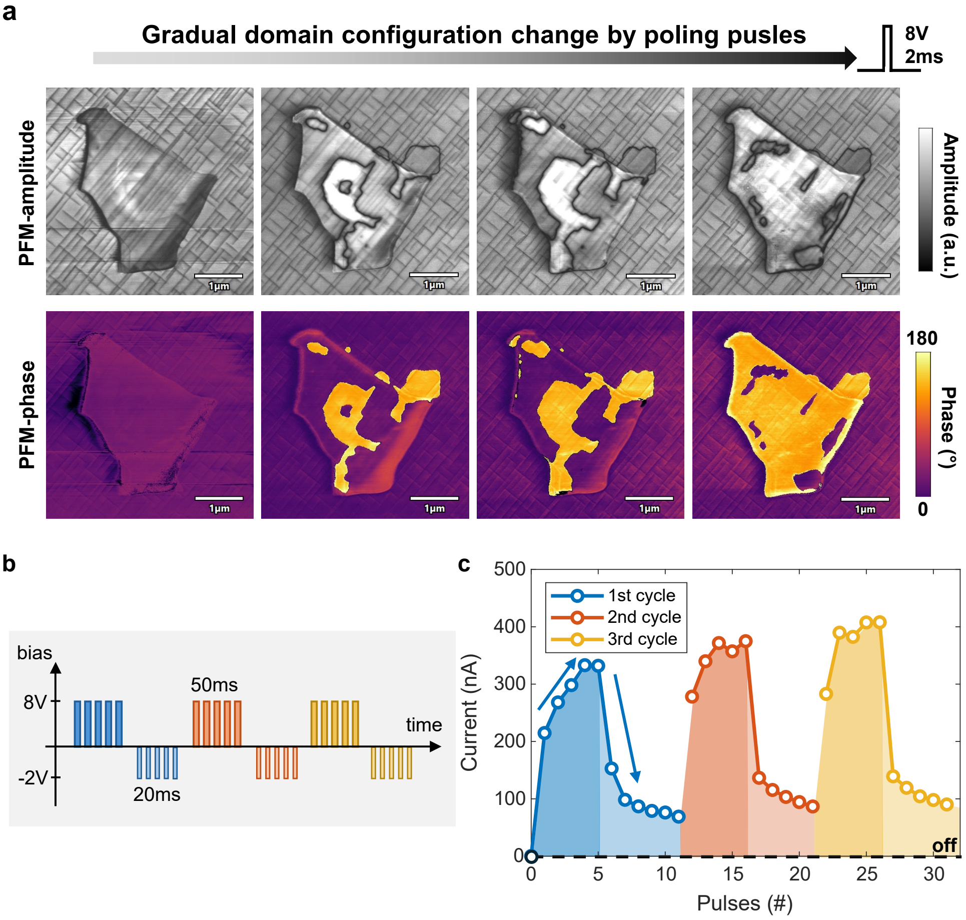

Figure 5.18: *Persisting multi-state conduction in partially switched graphene/PZT capacitors. a) Series of PFM images showing partial domain reversal by sequential poling pulses (8V/2ms) with one pulse in between images. Starting from the pristine state without any poled domain, the first pulse brings the device in a multi-domain state and following pulses result in gradual domain changes. b) Poling scheme for the experiment in c). Alternating positive (5x 8V/50ms) and negative (5x -2V/20ms) pulses are applied to gradually change the domain configuration under the Gr-electrode. c) Readout with 2V/200ms pulses after each poling pulse shown in b). A gradual increase of the current up to hundreds of nanoampere can be observed for positive pulses and a sharp transition towards the HRS for negative pulses.*

In order to explore the potential for multi-state memristive operations of the graphene devices we gradually altered the domain configuration with a sequence of poling pulses. In Figure 5.18, PFM images of the successive poling steps are recorded after each 8V/2ms pulse. Initially in the fully downwards polarized state (purple), the first poling pulse create switched domains (yellow) at different locations. Successive pulses enlarge these domains until they close holes and merge together. Separate electrical measurements are performed to test the conductive response at different poling stages. As it can be seen in Figure 5.18b and c, after the application of the first poling pulse the conduction rises to 200nA, which corresponds to a mixed-domain state, successive pulses increase the conductivity further up to 350nA. After the 5 positive pulses 5 pulses of negative polarity are applied to consecutively reduce the conductivity again and bring the device state back closer to its pristine HRS state (it is noteworthy that the device did not fully reset after only 5 repoling pulses and a remaining conduction of around 70nA is observed). The response to the repoling pulses is non-linear: a sharp decrease for the first pulse is followed by a gradual decrease in conduction. This behaviour occurs since most of the poled c-domains are already switched back within 1 or 2 pulses whereas it takes longer to fully switch back all domains inside the device area. Figure 5.18c shows that the operation of gradual tuning of the domain wall conduction is reproducible. Three identical cycles of poling/repoling schemes can be replicated with a similar gradual increase and decrease of current (red and yellow sections).

5.2.2 Monolayer Graphene

The memristive properties observed for the prototype PZT capacitors with graphene-flake top electrodes indicate their potential for advanced multi-resistive state devices. The next step is to go from randomly exfoliated Gr-flakes to technologically favourable pattern-able single layer graphene sheets. Single layer graphene sheets offer the ultimate thinnest electrode material while still maintaining the excellent in-plane conductivity and high-quality contact. We will see in this chapter which switching dynamics and electrical characteristics are observed for the single-layer Gr-devices and how they compare to the results of the multi-layer flakes devices.

For the SL-Gr-devices, 10x10 mm monolayer graphene sheets on a polymer substrate were purchased from Graphenea (“Easy Transfer: Monolayer Graphene on Polymer Film“). The SL-sheets were transferred according to the manual by first releasing of the Gr-layer from the polymer substrate in deionized water. Second, transferring the Gr-layer onto the PZT chip by "fishing" from below. And last, by removing of the protective sacrificial layer on top of the Gr by dipping the sample in hot acetone (50°C) for 1h followed by standard cleaning steps (isopropanol + N_2-gun).

The reason to use commercially available "Easy-Transfer" solution was the nearly defect free high quality film obtained with this method. In Figure 5.19, SEM images of two different Gr-monolayers onto PZT samples are shown after the final transfer. Left, a Gr-monolayer is shown which was released by an in-house metal etching process from Cu tape in CMi. On the right side the transferred "Easy-Transfer" monolayer from Graphenea. Directly visible is the high defect density for the "in-house" graphene. The dark lines indicate either ruptures or residual contaminants from the Cu etching. Lighter grey lines correspond to the grain boundaries of the Gr-film, which are inherently present in all chemical vapor deposition (CVD) grown graphene films. The lighter grey roundish areas correspond to nucleation sides at which the formation of the second layer started. They also naturally occur in these kind of

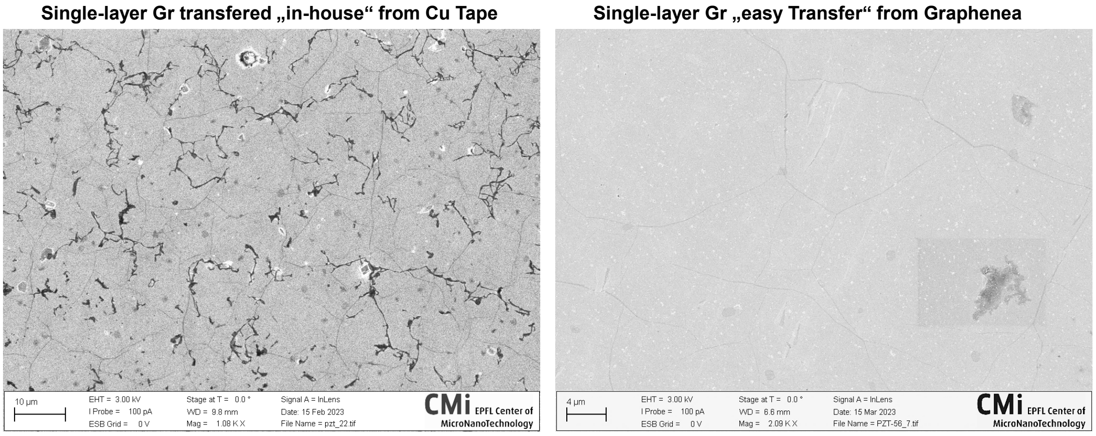

Figure 5.19: *Comparison of the quality of different transferred graphene monolayers on PZT samples by SEM images. Left: SEM image of a single-layer graphene transferred onto a PZT-test sample. The Gr film was released by a Cu-etching step with an in-house developed process at CMi. Right: SEM image of a single-layer graphene purchased and transferred by the instructions from Graphenea. The Gr-film is released by an immersion in deionized water without the need for an etching step.*

films and present no problem in terms of quality of the film. As seen on the right side, the "Easy-Transfer" film appears to show nearly no defects while only the light grey grain boundaries and nucleation centers are similarly present. The small white dots probably represent residuals from the etched protective film. It should be noted that the field of view for the right side is only a quarter of the area of the left side. Nevertheless, it is obvious that the transfer of the Graphenea film yielded a much higher quality film with highly reduced defects. The "in-house" graphene film seems to exhibit a decent quality in terms of grain size (around 10 µm), but the etching process needs to be optimized before large scale sheets can be used.

Patterning was done by electron beam lithography followed by careful oxygen plasma etching. In Figure 5.20 the effect of oxygen plasma directly on the PZT surface is shown. Particles with sizes of 100 nm appear over the whole sample, potentially due to chemical reactions with the oxide surface. To limit this degrading effect a smart design for patterning the Gr-electrodes was developed. Devices with different dimension between 5-10 µm in length and 0.1µm to 2µm in width were fabricated. In the SEM image in Figure 5.21a, the patterned Gr-layer is shown in the darker grey color. The devices were patterned inside a roughly 30x30µm square such that the O_2 plasma was only applied within the limited area. Outside, the graphene layer plus the MMA/PMMA resist coating protected the PZT surface. In Figure 5.21b, AFM topography images of the same area are shown and in c one of the devices is imaged in detail together with a profile measuring the height of the graphene layer to be around 0.5 nm, which roughly equals the theoretical monolayer height of 0.34 nm. The homogeneous Van der Waals interface as well as roughness on the surface of the graphene as well as of the PZT surface itself make more precise thickness measurements difficult. However an enhanced roughness is seen on the graphene surface compared to the PZT surface which could hint to some small

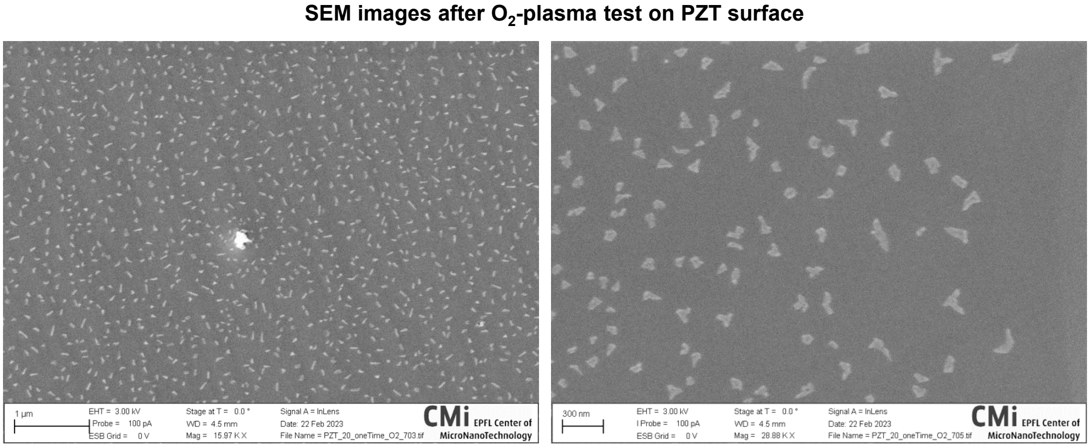

Figure 5.20: *SEM images of the surface of a PZT sample after a O_2-plasma treatment. Even through a "low"-recipe was used, a dense particle formation is observed on the surface of the oxide.*

scale defects of the Gr-film or in the Van der Waals interface.

Due to the fragility of the fabricated isolated graphene monolayers, experimental studies that combined PFM and conduction analysis were challenging. In particular, repeated through-electrode PFM imaging could damage the graphene monolayer and impede reliable conduction measurements similar to what was observed for the Gr-flakes in Figure 5.15. To address these complications, separate Gr monolayer capacitors were used for PFM analysis while others were reserved for evaluating the memristive performances.

Figure 5.22a, shows the gradual domain configuration change upon consecutive repoling pulses (-2V/0.5ms) of a SL-Gr device starting from the fully poled state. Similar to the measurements of Figure 5.18 on the Gr-flake, a confinement of the domain walls was possible as well as changing the polarisation completely. In Figure 5.22b the electrical response to the gradual domain configuration change is shown. The current values were probed by 1.5V/200ms readout pulses in between the 2V/0.5ms poling pulses. As expected the conduction values first increase until a mixed state with maximum density of conducting 180°-DWs is reached. Upon further poling the merging domains start to reduce the domain wall density and decrease the overall conduction of the device until it reaches its HRS for which it is fully poled. This shows the possibility to gradually tune the resistive state by applying a set of identical pulses, without reversing the polarity while covering a large conductivity range from 2.1nA (HRS) to 60nA (LRS).

The time dependent conduction response under DC readout, shown in Figure 5.23a illustrates the multi-state memristor performance. In this measurement, a 1.5V DC readout voltage was combined with a series of poling pulses produced every 3s in a way to gradually switch the polarization. Each poling pulse provoked a conduction increase. The time dependence of the current for each step is characterized by an initial steep decrease of 200-400 pA followed by a

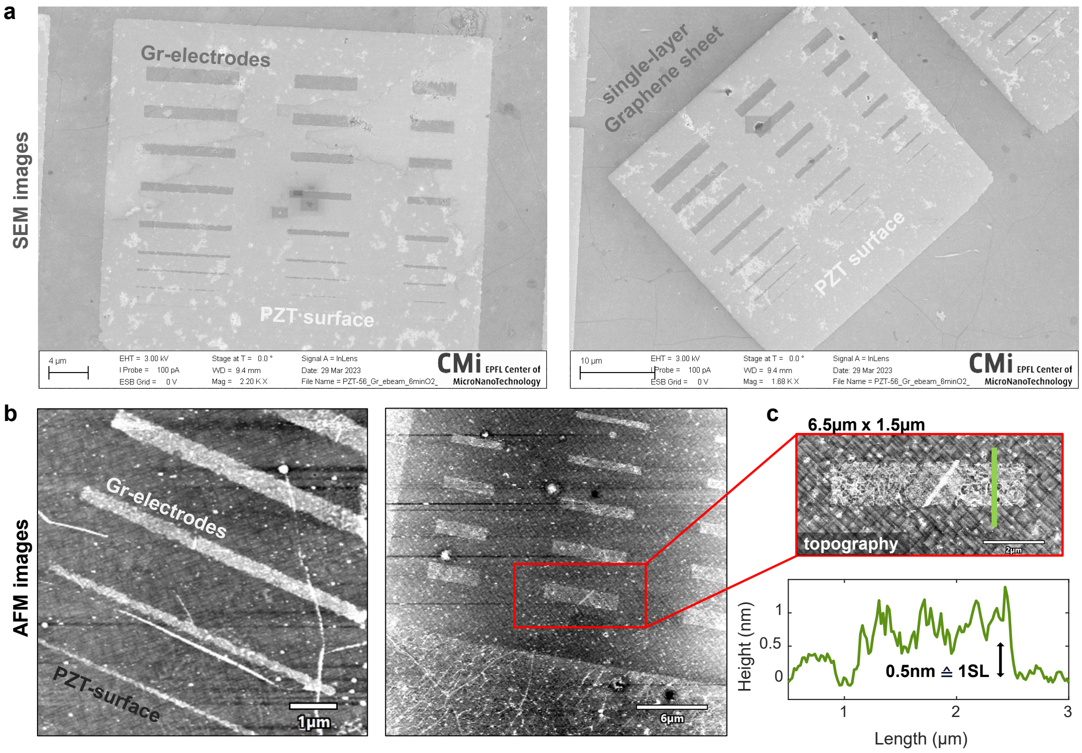

Figure 5.21: *Patterned graphene monolayer devices. a) SEM images of the patterned design. Dark grey color indicates the Gr-layer while light grey color indidcates the bare PZT surface. b) AFM topography images of some monolayer Gr-devices. In the AFM images, the Gr-layer is white or light grey while the PZT surface appears darker. c) Zoomed-in AFM image of a single Gr-electrode with a height profile indicating the monolayer nature of the graphene.*

saturation region. The stabilized currents detected after each poling steps are well separated by a gap of 100-150pA. To demonstrate a broader range of accessible conduction states we performed pulse number modulation schemes by applying series of poling pulses with varying amplitude. In Figure 5.23b, the amplitudes of the pulse trains are increased from 2V to 10V (with constant 1ms dwell time), and for each run the response to the 20 pulses are recorded. After each set the device is rest to its HRS. A steeper conduction increase is observed for higher amplitude values, with the trend being particularly clear for the first 3 pulses. In contrast to Figure 5.22b, in which pulses of the same polarity were applied until the conduction began to decrease, in Figure 5.23c we started from the LRS and applied pulses of the opposite polarity. Because the reset pulses return the polarization to its preferential direction, a sharp decrease is observed for the first pulses independently of their amplitude (similar to the experiment in Fig. 5.18), followed by a slow gradual decrease. For pulses with higher amplitudes (≤-3V) the first pulses are sufficient for a nearly complete reset of the HRS.

After evaluating the device performance, a more detailed look is given to the switching behaviour of the device. For this, a SL-Gr-device is driven from its repoled state into the poled

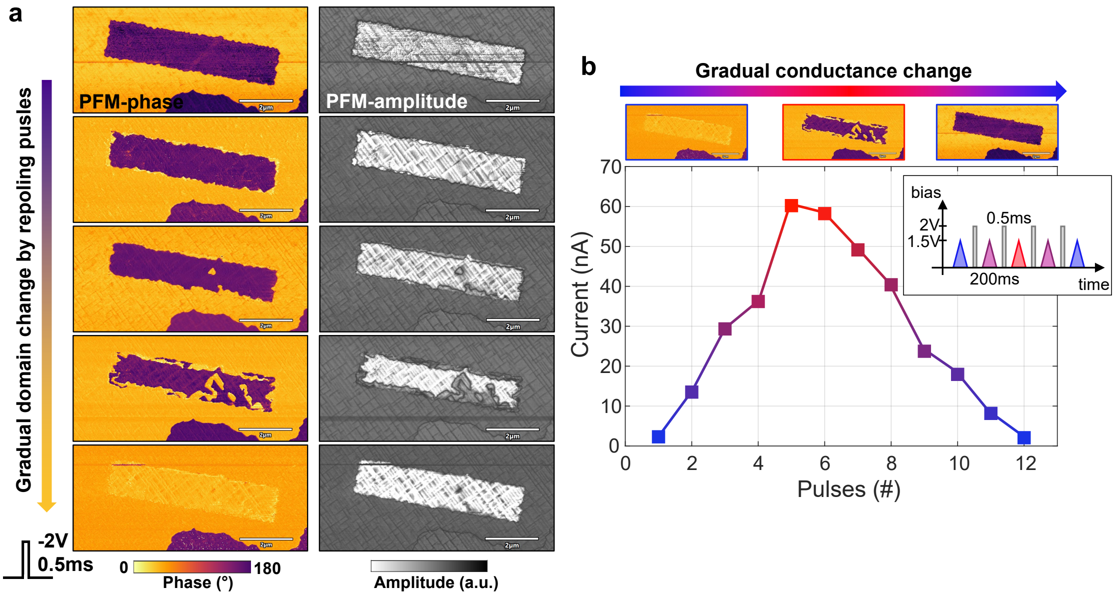

Figure 5.22: *Gradual domain switching in a single-layer graphene capacitor. a) PFM images of different poling states of the SL-Gr device created by -2V/0.5ms repoling pulses. The device is switched completely from its fully poled to pristine state. b) Current measurements depending on the number of applied 2V/0.5ms poling pulses. Current is recorded with 1.5V/200ms readout pulses. An increase in conductance is followed by a symmetric decrease. The maximum current corresponds to the mixed domain configuration with a maximum density of domain walls.*

state and back to its repoled state by application of 6V/1ms poling pulses and -4V/1ms repoling pulses. The PFM images of the intermediate device states during this cycling are shown in Figure 5.24. For these experiments no conduction is measured but a detailed look is given to the evolution of the domain configuration during the poling/repoling. As seen in Fig. 5.24b and highlighted in c, by applying the first 6V/1ms pulse, 5 small domains are nucleated. The next pulse increases the size of the poled domains while the one after that not only further increases the existing domains but start to merge them together. Finally the whole domain is poled (full device area is purple).

For the repoling operation, (as supported by the electrical measurements in Fig. 5.23c), a faster more abrupt backswitching is observed, which is why only one intermediate state is observed for the chosen repoling pulse parameters. In Figure 5.24d, the starting nucleation spots for the repoling domains are marked. Interestingly the nearly perfectly match to the 5 spots observed for the initial poling.

It is therefore concluded that the same areas serve as the starting points from which the first domains are either poled or repoled, followed by domain expansion and domain merging until the polarization state is completely reversed. This scenario is also plausible with regards to the Gr-electrode properties. It was speculated that defects in the Gr-sheet or in the Van der Waals interface between the Gr-layer and the PZT surface result in localized areas of better contact

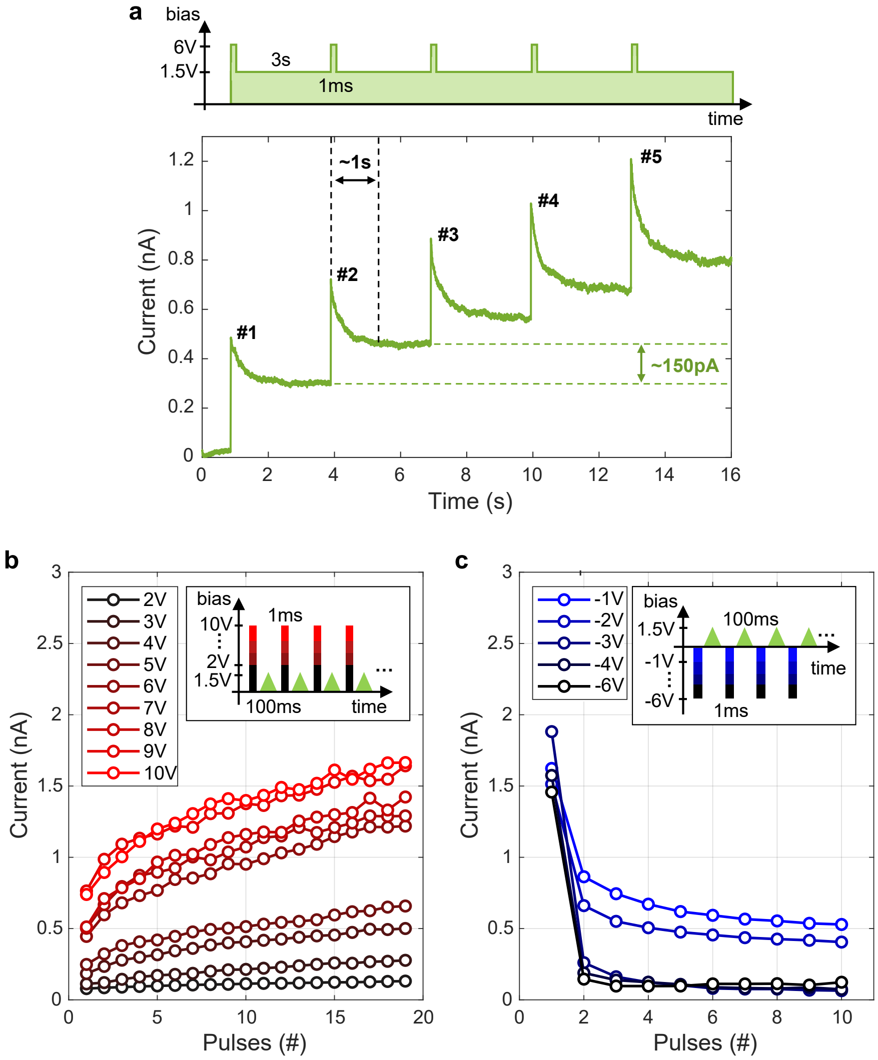

Figure 5.23: *Single-layer graphene device characteristics. a) Stability of addressed gradual resistance levels. The resistivity is tuned by 6V/1ms pulses, while the conductance is simultaneously read out by a constant 1.5V/3s DC bias. A initial conduction decrease is followed by a saturation of each level, creating distinct resistive states. b) Tunability of the conductance profile. For a pulse number modulation (PNM) scheme, the amplitude was varied for each set from 2 V to 10 V. An increase in the slope of the conduction increase is seen for higher pulse amplitudes. c) Tunability of the conductance decrease. Similar to the increase, for the decrease of conductance a PNM scheme is used with amplitudes from -1 V to -6 V. For amplitudes ≤-3 V, the conductance is nearly instantly reduced to the HRS level which equals a complete backswitching.*

with a faster polarization switching. Furthermore, the domain expansion and hence the domain walls encounter pinning effects which need repeated poling/repoling operations to fully overcome this barrier to switch the whole device. The resulting stabilized mixed domain configurations and their gradual tunability are exploited in the presented device concepts

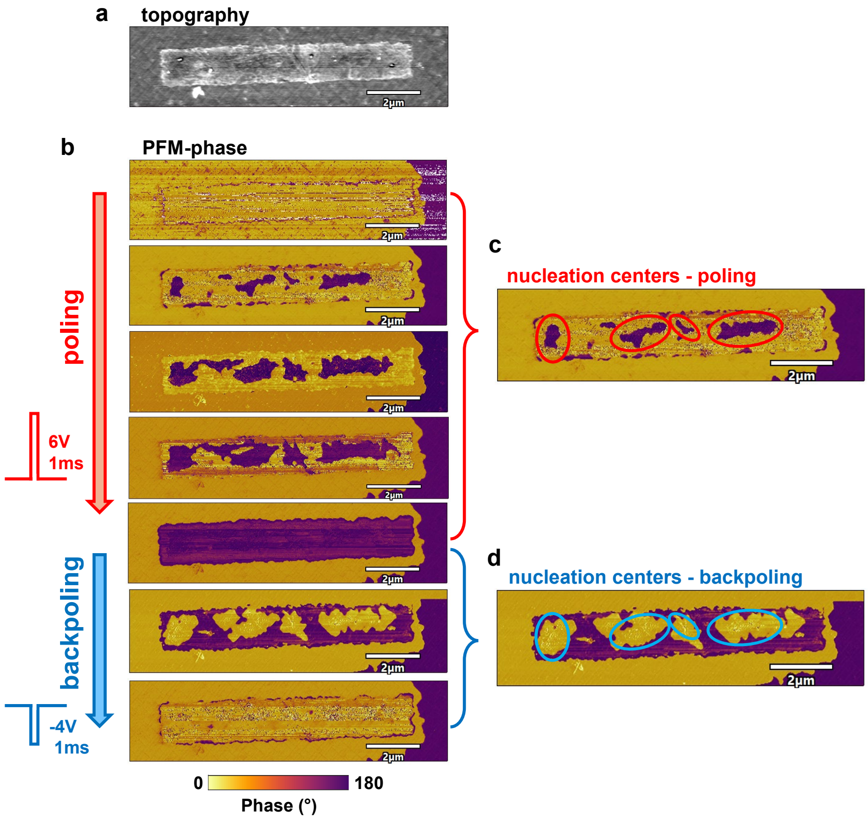

Figure 5.24: *Domain nucleation in single-layer graphene devices. a) Topography image of the investigated graphene device. b) Series of PFM images starting from the pristine unpoled state. By applying 6V/1ms pulses, a number of small domains nucleate randomly under the electrode area. Consecutive pulses lead to a expansion of the existing domains until they start to merge and finally result in a fully poled device state. From here, backpoling pulses (-4V/1ms) are applied to trigger nucleation centers for the backswitching domains. Lesser pulses are needed to switch back the device to its initial state. c) Nucleation centers for the poling operation are marked in red, referring to the positions at which the first domains start to switch. d) Nucleation centers for the backpoling operation are marked in blue. Interestingly the same areas are marked as in c), confirming that the nucleation always start at from the same positions independently of the poling direction.*

which are based on the density modulation of conductive domain walls.
Additionally, even through the resulting domain configurations differ from electrode to electrode, within one device the preferred nucleation centers stay the same (as shown in Fig. 5.24), which should result in an enhanced address- and repeatability of the achieved resistive states.

5.3 Summary

In conclusion, in the first part of the chapter Cr/Au evaporated electrodes are presented showing to be able to contact both a-DWs and 180°-DWs. The enhanced stability of the conduction readout is confirmed when using the metal electrodes compared to the AFM-tip, due to the enhanced homogeneous contact and current driving electric field. Basic binary memory devices are demonstrated by pushing an artificially created 180°-DW towards the electrode area forming a contact at its border and connecting the top and bottom electrode of the capacitor devices. Three orders of magnitude on/off ratios are demonstrated together with the controlled creation and breaking of the DW-contact by electric fields. Stable readouts confirm the non-volatility of the formed conducting DW channels. However, the precise control of a stable DW position under the electrode is unattainable by this approach.

In the second part of this chapter, by integrating a different electrode material, specifically graphene multi- and single-layers, these limitations can be overcome. The intrinsic properties of graphene sheets, their high in-plane conductivity with excellent contact to the oxide surface, paired with naturally formed defects in the van der Waals interface provided both high on-state currents and limiting domain growth of the c-domains. The limiting domain growth results in the formation of stable mixed-domain configurations which are associated with the presence of 180°-DWs inside the capacitor. The confined DWs mediate current readouts between 10-100nA/μm^2 for low voltages of 2V or less while maintaining a reproducible high resistance off-state. Upon application of consecutive poling pulses, the observed change in the multi-domain state lead to a gradual change of the device's resistive states. Therefore multi-resistive states and memristive functionalities are accessible for the fabricated Gr/PZT/SRO devices, with proven non-volatile characteristics. PFM imaging allowed to visualize the different multi-domain states and link them to the change in conductance. Furthermore, the detailed PFM-analysis of the changing domain states during cycling from the repoled to the poled and back to the repoled state showed the persistent nature of nucleation centers, which are the starting points for the switching domains. Such controlled reproducible formations of domain configurations are believed to result in an enhanced ability to repeatable address the different conductance states.

6 High-resistive Platinum - a pathway to advanced domain wall control

In this chapter a different approach to control and confine domain walls is explored. Compared to graphene electrodes, introduced in Chapter 5.2, which enabled the formation of stable multi-domain configurations in a stochastic manner, the here discussed high-resistive platinum electrodes present a pathway for a deterministic control of the nucleation centers of polarization domains, their growth direction and speed as well as the final position of their boundaries. In the beginning of the chapter the fabrication of the high-resistive platinum electrodes are discussed with regards to their shape and surface topology, which influence the domain dynamics under poling. Then, a controlled domain-by-domain switching concept is used to build a prototype memristive device with stable multi-resistive states. A linear and symmetric conductance increase and decrease is achieved due to the distinct addressability of single domains and a quantitative dependency between the conductance increase to the total domain wall length is established. In the second part of this chapter, the established functionalities of the high-resistive electrodes are used together with another observed unique property of this type of electrodes. A distance dependent current readout between the position of the domain wall and the readout point is exploited to demonstrate a novel proximity-sensitive memristor concept. Compared to the previously presented device, which uses a modulation of the domain wall density to control the conductance, this device concept relies solely on one nanometer sized domain wall segment which can be precisely positioned inside a one dimensional electrode design. The content of this chapter is based on the work presented in [176].

The sought-after advanced functionality of multi-resisitve state switching, can be achieved within the realm of DW-based ferroelectric systems in two established ways: either by changing the conductivity of single domain walls or by controlling of the domain wall density. The previous established graphene/PZT interface in Section 5.2 used the latter case by enabling the formation of multi-domain configurations within the capacitor device area, which led to the confinement of a set of domain walls. Manipulation of the domain wall density could be achieved by altering the domain configuration by electrical pulses applied through the graphene electrode. While a step-wise tuning of the resistivity could be demonstrated, the resulting formation and modification of the multi-domain pattern was not actively controllable.

As discussed in Section 1.2.2, Section 1.3 and seen in the observations of Chapter 5, the reliable control over the domain wall dynamics presents a persisting challenge and limits advanced device concepts for both branches, single-DWs as well as DW-density tuning. Most proposed approaches are hindered by a direct and irreversible change (mechanical, chemical, etc.) in either the electrode or inter-electrode area. Advancements in reliable control with flexibility over the resulting domain pattern and domain dynamics are needed for the envisioned reconfigurable DW-devices and circuits. One pathway to an agile domain control, which will be discussed and implemented in this chapter was introduced by McGilly et al. [116, 117] through the use of high resistive electrodes.

High-resistive electrodes can be created by electron beam induced deposition (EBID), by breaking of a metal-containing organic precursor gas. In this work, platinum was used as the metal and the electrodes were deposited by a FEI Nova 600 NanoLab FIB tool. To break the precursor gas either an electron or a focused ion beam (FIB) can be used. The standard electron beam parameters are 5 kV and 1.6 nA and while for the FIB 50pA and 30kV are used. Individual pattern could be drawn and consecutively written by either of the beams by breaking of the organic Pt-rich organic precursor $((CH_3)_3CH_3C_5H_4Pt)$. During the deposition carbon-rich organic defects are incorporated inside the electrode, which results in their high resistivity. In this work EBID-electrodes down to sizes of 100 nm were deposited, however a

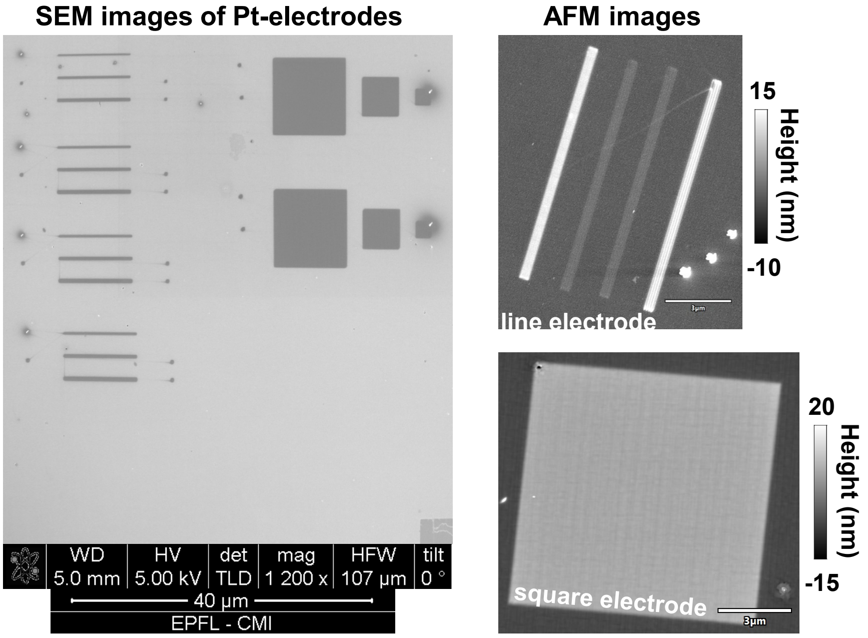

Figure 6.1: Left: SEM images directly after deposition of the high resistive platinum electrodes. Next to the line and square electrodes deposition artifacts can be observed due to the finite speed of the mirror controlling the electron beam. Right: AFM topography images of 4 line electrodes with different thicknesses and a 10x10 µm square electrode. The underlying height changes cause by the a-domains can be seen at the electrode surface.

resolution limit of single dots and lines as small as 2 nm are reported [185].
Figure 6.1 shows a SEM overview image on the left of some differently shaped patterned high-resistive platinum (high-R Pt) electrodes together with with some higher resolution AFM images on the right side of line electrodes with different thicknesses and a larger square electrode of 10x10 µm size.

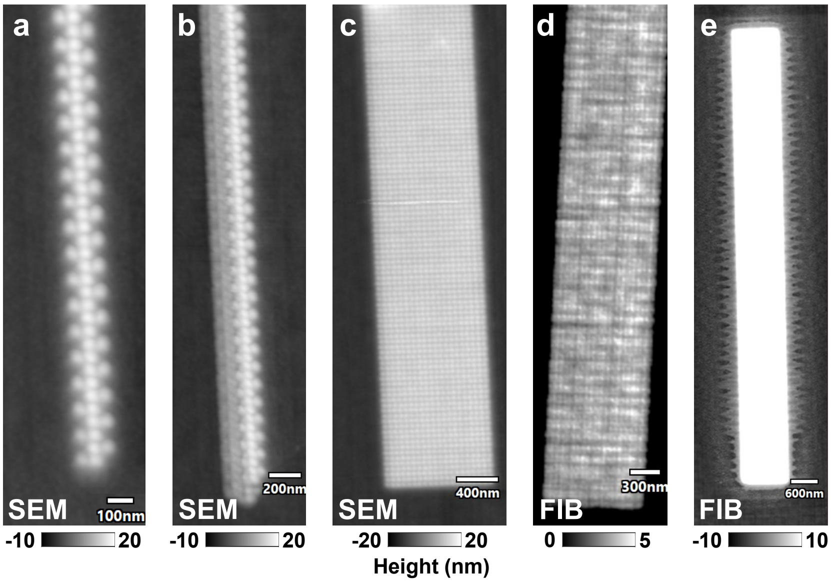

Figure 6.2: *Various designs of the deposited high-R Pt electrodes. Different deposition parameters were tested, especially the stitching value, resulting in electrodes with different structures and surface topography. a)-c) are deposited using the electron beam while d) and e) are fabricated by the FIB. a) A dot-like structure which is only loosely connected. b) A similar dot-like pattern which is more connected. c) Rectangular electrode, which shows high density of small dots creating a valley-like surface. d) Similar surface as seen in c) but with denser and smaller dots. e) Line electrode with thin spike-like side structures attached to it.*

In Figure 6.2, the effect of different parameters of the deposition pattern and the difference between electron beam and FIB are shown. The designs in d) and e) are written by the FIB which often resulted in associated thinner electrode structures at the side of the design as seen in e). The surface topology depended heavily on the overlap parameter of the pixels. A value of 60% and more was used to result in smooth surfaces while lower values resulted in an increase of a dot-like or valley-like pattern (compare Fig. 6.2 a)-d)). Furthermore, by playing with the stitching parameter the connectivity between the created dots could be modulated and high local thickness differences of the electrode could be achieved.

The high-R electrodes possess a sheet resistance that is more than three orders of magnitude higher than that of conventional electrodes of the same thickness [186, 187]. The elevated resistance limits the speed of charge movement, resulting in a voltage gradient across the high-R electrode when subject to sufficiently short voltage pulses [116]. Therefore, by tuning the amplitude and dwell time of poling pulses, the propagation of the domain walls can be

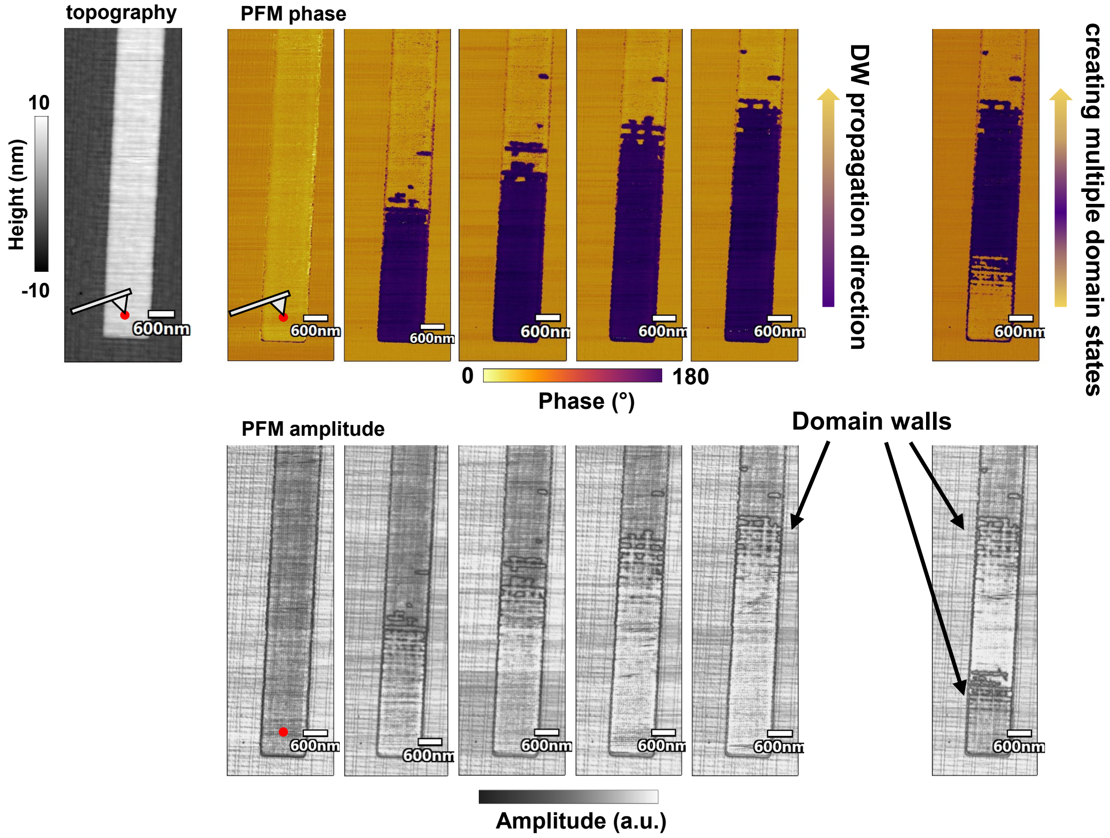

Figure 6.3: *Progressively advancing of a DW front inside a high-R Pt electrode. Left side shows a AFM-topography image of the high-R Pt electrode and the position where the tip applied the voltage. A sequence of PFM images is shown demonstrating the progressive propagation of the DW front pushed by application of consecutive poling pulses (-8V/50ms) applied at the bottom of the electrode. One pulse is applied between each image. On the right side, after the DW has propagated for around 6µm, a voltage pulse of opposite polarity (8V/6ms) is used to inject a second DW front. Importantly for this electrode design with valley-like surface structure is the formation of a fractured DW front as the DW movement and the domain poling does not happen in a smooth continuous way.*

controlled enabling position-sensitive operations. This concept is shown in Figure 6.3, for which the electrode d) from Fig. 6.2 is used. The tip was placed on top of the bottom part of the electrode and a short 50 ms voltage pulse of -8 V was applied. Consecutive PFM images are shown after each additional poling pulse. 180°-DWs can be identified as the dark lines in the amplitude images at the evolving domain boundaries. Furthermore, by locally reversing the polarization, the bottom part can be switched back without interfering with the first DW-front resulting in the injection of a second DW-front. A subset of domain boundaries can therefore be written inside the electrode as demonstrated. These first experiments show the general feasibility of the concept of controlled positioning and moving of domain walls underneath an electrode for a high quality epitaxial PZT film compared to the near instant whole domain switching using Cr/Au electrodes or the stochastic formation of multi-domain states with graphene electrodes.

However, in the employed electrode design, we observe the formation of a non-uniform DW-front, which seems to propagate by nucleation of adjacent stripes or smaller domains. This behaviour can be understood by looking at the topography image of the electrode. The formation of small dots can be identified which are a result of the process parameters and a non-ideal stitching or overlap of the patterned pixels. This results in an uneven valley-like topography. Since the thickness of the electrode mediates its resistivity the result is a locally changing electric field. Therefore, the domain boundary does not propagate with a single smooth front but rather evolves in a step-like nucleation of the following valleys. While these switching dynamics are interesting in itself and present another way of the electrode and its shape to tune the dynamics of the propagating domain wall, for the rest of this chapter, electrodes with an optimized flat surface are used. A smooth topography of the high-R Pt electrodes results in a uniform growth of the domain boundary with continuous domain walls as will be seen in the upcoming sections.

6.1 Memristor with deterministic domain-by-domain switching

In this section, square high-R Pt electrodes with sizes 5x5 μm and 7x7 μm are used which were deposited by the EBID technique using an electron beam. A 5x5 μm square electrode acting as a capacitor device, with optimized patterning parameters for a smooth topography is shown in Figure 6.4. Fig. 6.4 a) and b) show a AFM topography image and the associated surface values captured from the indicated red square. A RMS value of 324 pm is measured for the topography roughness on the electrode surface, which is similar to the roughness of the PZT surface itself. In c) and d), the 3D-image of the AFM data show the smooth surface visually and a line profile evaluates the thickness of the electrode to be around 12 nm. These thickness values were chosen based on previous studies, which showed that with this value the resistivity of the electrodes matches well with easily accessible poling dwell times in the millisecond regime [116].

In Figure 6.5 a), PFM images on the square electrode are taken showing that the domain(-wall) configuration and polarization state of the capacitor can be visualized through the electrode. Images before and after the switching of a small circular domain in the center are shown, which was created by placing the AFM-tip onto the electrode and applying a short 1 ms voltage pulse of 5 V. The domain forms directly under the tip location who acts as a nanometric contact, which shows the position-sensitive control over the switching dynamics. By creating a switched domain, simultaneously a 180°-DW ring is injected in the device, bridging the inter-electrode gap. The resulting conductance change of the device from its original high-resistive state (HRS) to its low-resistive state (LRS) can be observed in Figure 6.5 b), in which IV curves from before (red) and after (blue) the poling pulse are recorded. In the pristine HRS without any 180°-domain wall, a current lower than the noise level of around 5 pA for 1.5 V is measured. After the poling pulse, the injected domain wall mediates a current transport providing a

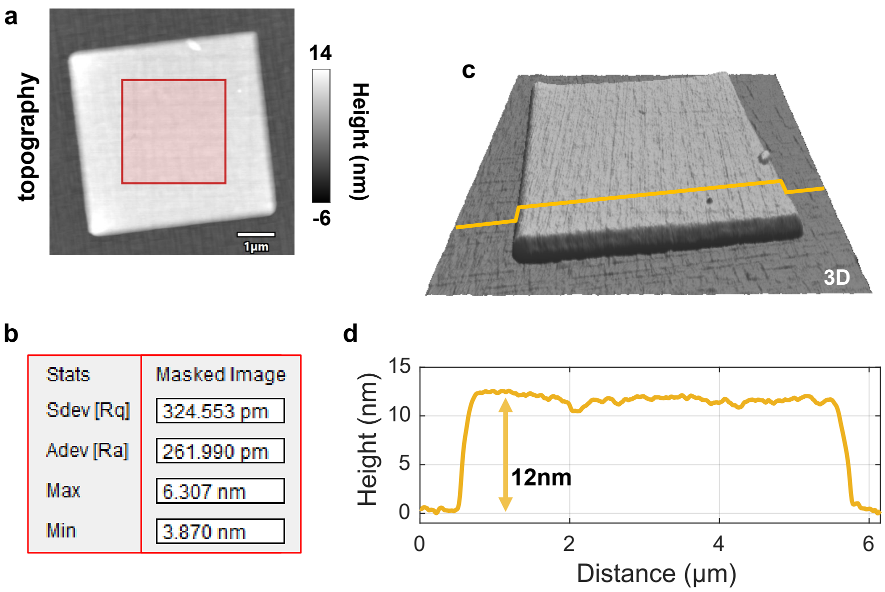

Stats	Masked Image
Sdev [Rq]	324.553 pm
Adev [Ra]	261.990 pm
Max	6.307 nm
Min	3.870 nm

Figure 6.4: *a) AFM-topography image of the 5x5 µm high-R Pt device. b) Associated roughness values for the indicated area on the electrode in a). c) 3D representation based on the AFM image, visualizing the smooth topography. d) Height profile along the yellow line indicated in c) showing an electrode height of 12 nm.*

readout of ~3 nA for 1.5 V which results in an on/off ratio of at least 3 orders of magnitude. The on/off switching as well as the current readout are performed from the same location in the center of the electrode (green dot) with the advantage of immediate successive write and readout operations. It is important to note that it is still possible to access significantly high current values for low-voltage operations when applying electrodes with high resistivity. The formed capacitor devices with limited domain switching operations readily demonstrate the achieved memory functionality.

To check the stability of the conductance readout as well as the domain configuration, retention tests are performed in which a created LRS of a high-R Pt device is probed with consecutive readout pulses. In Figure 6.6 a), a retention test is shown for which a singular domain is poled in the center of the device, similar to the experiments of Fig. 6.5. The circular domain was poled by a 6V/1ms pulse and the readout was done by 2V/2ms pulses. A total of 1120 pulses are recorded consecutively without a degradation of the LRS. PFM images before (directly after the creation of the switched domain) and after the readout pulses show only a very small deformation of the circular domain. The reason for the small variation can be explained by mainly two reasons. The amplitude of the readout pulses are close to the coercive field value of our PZT, which could lead to some small expansion of the domain. Furthermore, as seen in Chapter 4, even when using only subcoercive voltages, slight rearrangements of recently poled c-domain were observed to adapt to more energy efficient positions often overlapping with the underlying a-domain network. This was explained with 3D-phase field simulations which showed the formation of charged domain boundaries inside the film. Reorientation

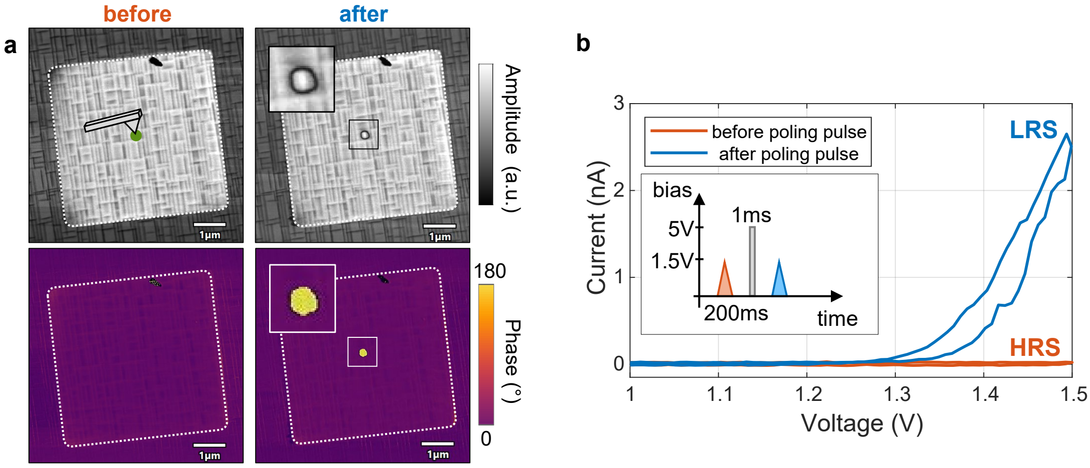

Figure 6.5: *a) PFM images of a high-R Pt electrode before and after a 5V/1ms poling pulse applied at the center of the device by the AFM tip. A round polarized domain is observed after the poling together with a ring-like 180°-DW. b) IV characteristics recorded by the AFM-tip at the same position before and after the poling. Without any 180°-DW, the conductance of the device is below the noise level of 5 pA (HRS). After the injection of the 180°-DW the conduction is increase to around 3 nA (LRS).*

of those boundaries to align with a-domains are expected such that electrostatic preferred configurations with reduced energy cost of the charge domain walls are formed.

Nevertheless, by observing only minor changes in the domain configuration while maintaining the stable current readout, it is concluded that the application of the 2V/2ms pulses do not destroy the written features nor alter their conductive properties.

To demonstrate, how a real domain distortion changes the conductive state, an experiment with different readout pulses is shown in Figure 6.6 b). Here, 4 small domains are poled in a rectangular layout, all with equal distance to the readout point in the center of the electrode. This time, instead of the 2V/2ms pulses, 1.5V/200ms pulses are used. The observed current values are not constant in this experiment but start to increase first, followed by a saturation. By comparing the PFM images from before, in the middle and after the experiment the reason for the change in conductance is revealed. The written domain configuration is massively altered and merging domains resulted in only two big switched regions. While no new domains are nucleated at the point of the tip position (center of the device), the already written domains showed an enhanced tendency for domain expansion even for subcoercive pulses. The resulting change of the domain structure hence alters the overall measured conductance. However, the main difference here are the long readout times of 200 ms, as it is know that the electric field evolves over time in these electrodes, a limiting of the dwell time directly confines the area for which domain can be nucleated. Therefore, working with high-R electrodes, the combination of amplitude and dwell time needs to be carefully adjusted together with the working thickness of the electrodes to ensure the stability and confinement of the written domain walls.

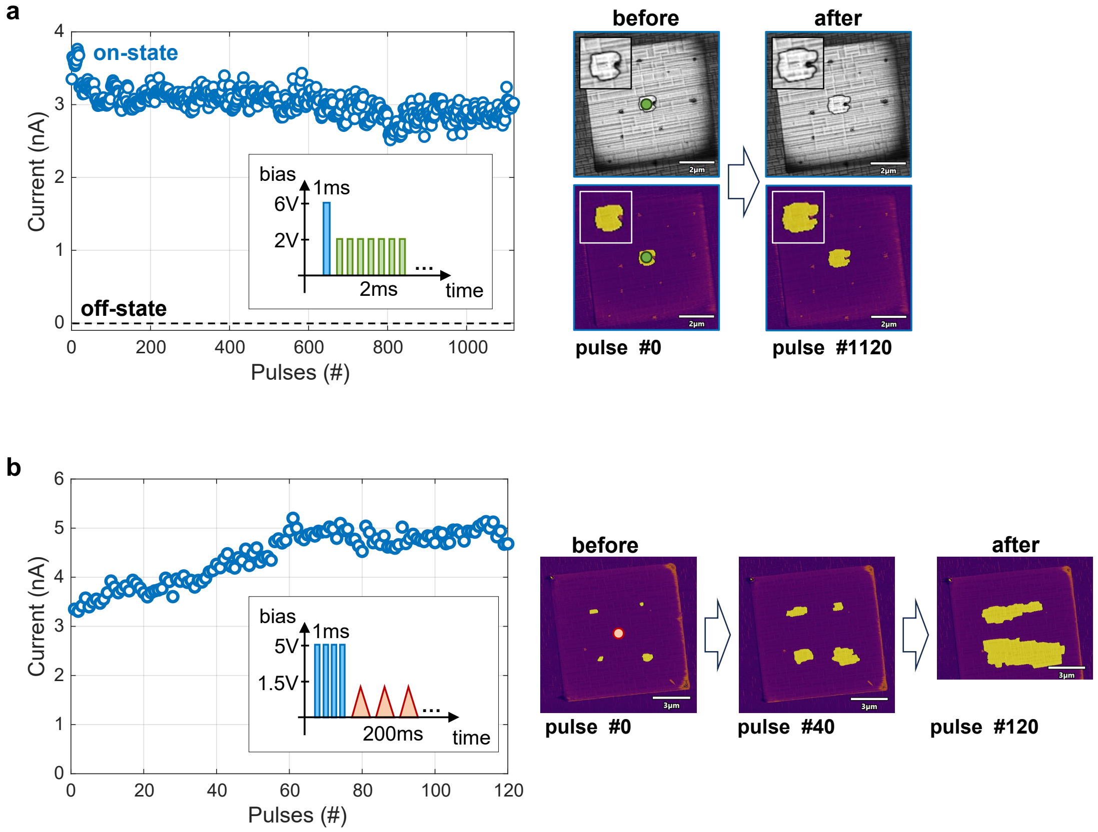

Figure 6.6: *Retention tests of the LRS depending on the type of readout pulses. a) Retention test of the LRS with short readout pulses. A circular domain is poled first and imaged by PFM, then 1120 1.5V/2ms readout pulses are applied at the center and the current response is recorded. A PFM image is taken after the test to confirm the stability of the circular poled domain. b) Retention test of the LRS with long readout pulses. 4 small domains are poled before the retention test around the readout point. 120 readout pulses (1.5V/200ms) are recorded. PFM images before during and after the test show the increasing distortion of the previously written 4 features during the readout.*

In the endurance tests shown in Figure 6.7, the other type of stability is tested. By repeatably cycling the device between its LRS and HRS, the fatigue, domain reproducibility and current stability is tested. For this, a circular domain is alternately created and erased with readout pulses before and after each operation. The first test is performed in Fig. 6.7 a) with 100 cycles after which a PFM image is taken to evaluate if the same poling pulses result in the same domain formation. The PFM images show a nearly perfect match between the result before the first cycling and the one after 100 cycles. The stability is verified by the excellent current stability at 4 nA.

Subsequent tests are performed after the PFM image of cycle #100 was taken. The cycling was continued another 640 times, resulting in a total number of 740 cycles, shown in Fig. 6.7 b). The overall LRS level is robustly stable and followed PFM images after cycle #740 showed that

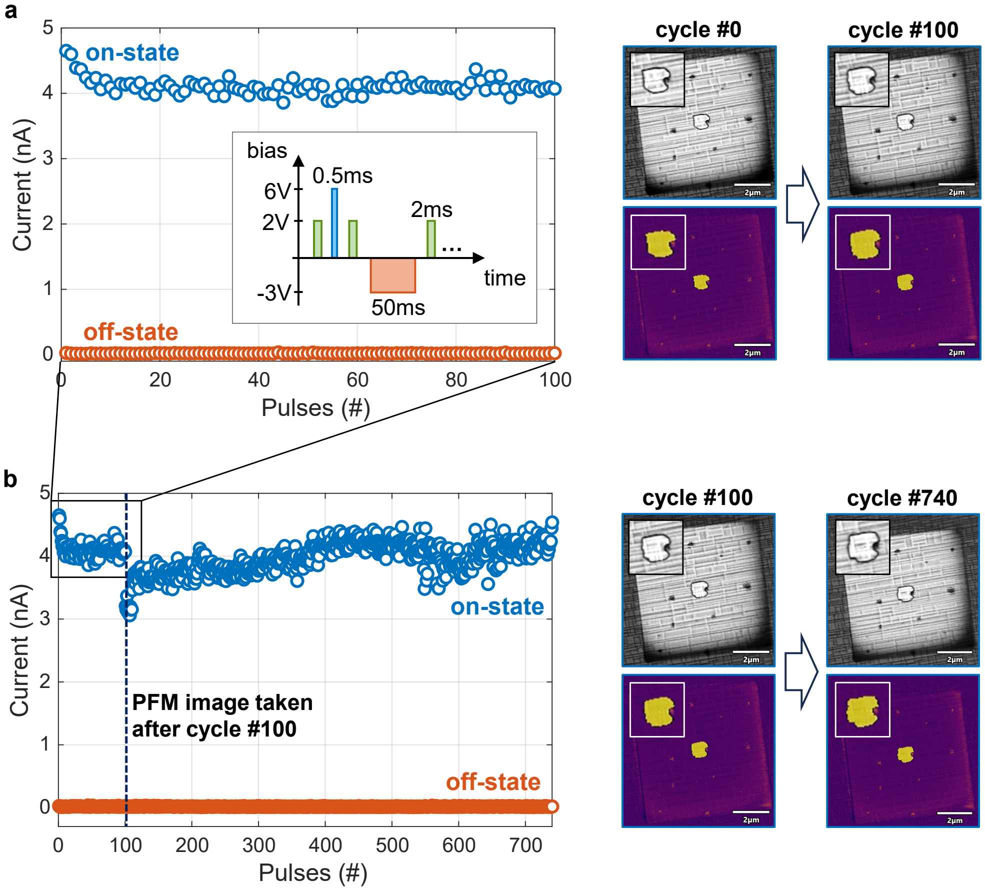

Figure 6.7: *Short and long endurance tests. a) Endurance test by alternating injection and erasure of a polarized circular domain in the center of the device. After each operation the conductance state of the device is recorded by 1.5V/2ms pulses with the AFM tip in the center of the domain. PFM images before and after are taken to monitor potential degradation for the poling process. b) Continuation of the test in a) for a total of 740 pulses. The sharp decrease in current seen results from the taken PFM image after 100 pulses. The contact scanning induced a change in the contact resistance leading to a lower current readout. After around 10 cycles the current readout was recovered and stayed nearly constant for the rest of the test. PFM image taken after the test confirmed the persistent stability of the written domain by the cycling operation.*

the created domain exhibits the same outline as before. The sharp drop to 3 nA after exactly 100 cycles, which quickly is recovered is due to the acquiring of the PFM image after the first test round. A slightly modified contact resistance between the tip and the electrode is expected to cause the change in current readout, probably resulting from a minor contamination at the tip-apex during the contact scanning of the PFM image. This observation illustrates the known sensitive interaction of the AFM-tip to surface which can easily influence the electrical measurements.

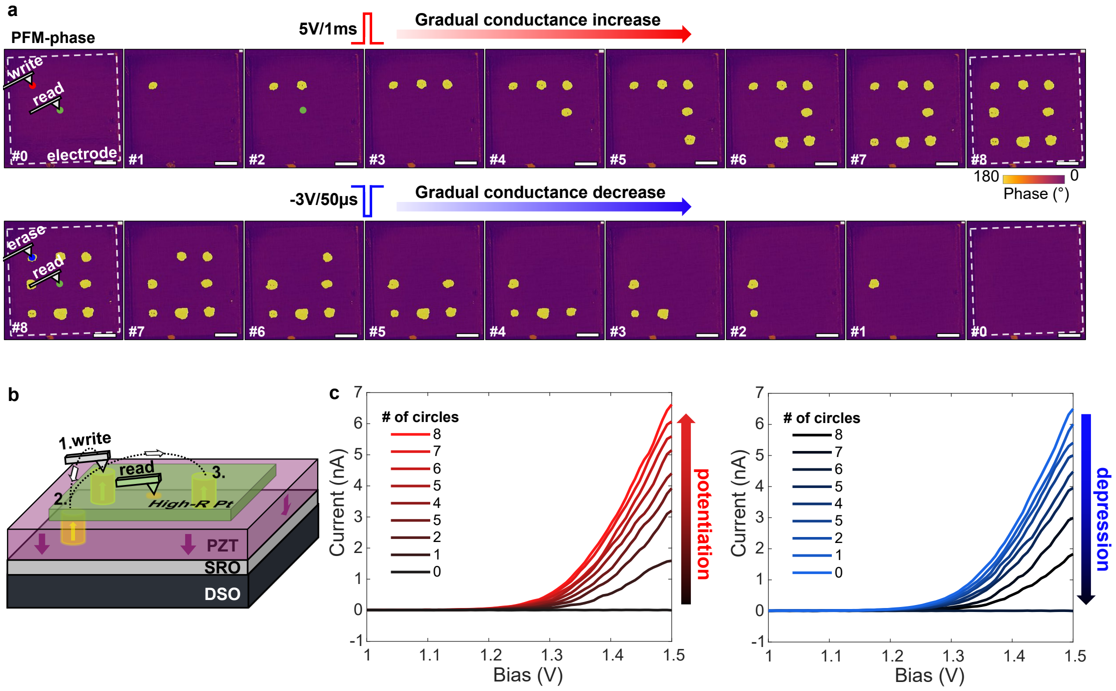

Figure 6.8: *Working principle of the domain-by-domain switchable memristor. a) PFM-images of each device state after the consecutive domain-by-domain poling operations. Top row shows the step-by-step increase in poled domains (yellow) by application of positive pulses (5V/1ms). Bottom row shows the step-by step turning off of individual domains by negative pulses (-3V/50µs). b) Device schematic with poling and readout operation. c) IV curves taken from the readout point at the center of the device for each device state corresponding to the number of poled domains under the electrode. Left side for the increase in domains with an increasing current readout and right side with a reducing current for the step-by-step erasure of domains.*

These above observed characteristics pave the way for more advanced multi-resistive level device concepts, relying on repeatedly creating and erasing of domain walls, which deterministically change the conductive channels in the device. In Figure 6.8 b), the working principle of the device is illustrated. By varying the tip position on the high-R Pt electrode and the application of short (5V/1ms) voltage pulses an independent set of domains can be written in the device at different locations while the current readout is performed from a non-changing position in the center of the electrode. In Figure 6.8 a), PFM images taken after each poling operation are shown, revealing the step-by-step creation of new domains (top row). Notably, the application of the consecutive poling pulses at different positions do not result in a collapse nor significant change of the shape or position of the existing domains due to the well confined electric poling field. By measuring the conductance of the device after each stage through IV curves (see Fig. 6.8 c)) taken from the center of the device (green dot), we observe a gradual increase of the conductivity up to a maximum of 7 nA for 8 injected domain wall rings. Even more importantly it was possible to selectively turn off the switched domains again by adjusting the width and amplitude of the backpoling pulses (-3V/50µs). By placing the tip at the poled domain locations, a sequential deactivation of single domains was realized (Fig. 6.8 a), bottom row). Consequently, by erasing the domain walls associated with the poled domains the conductivity of the device is step-wise decreased.

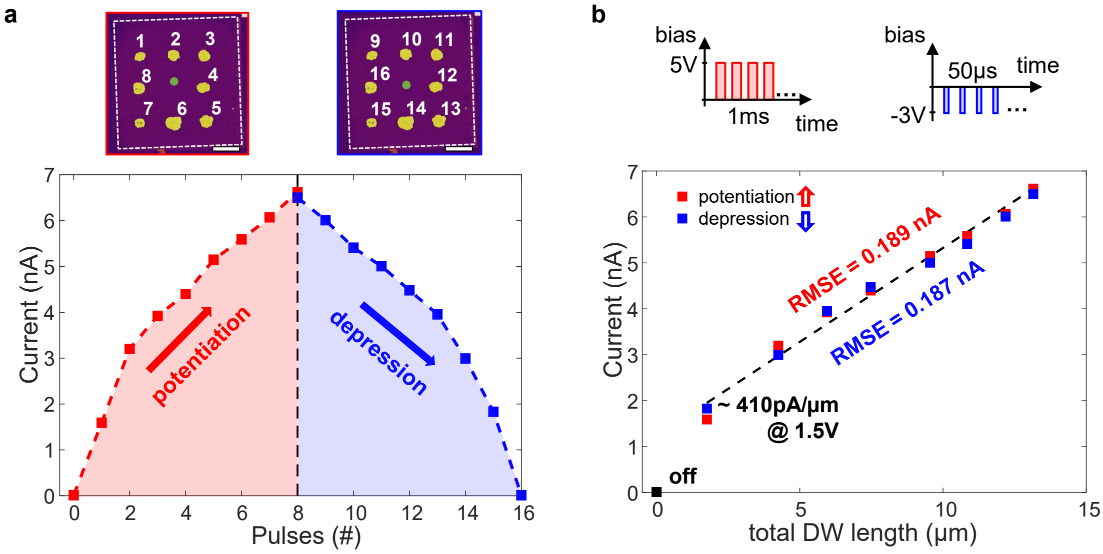

__Figure 6.9:__ Symmetry in linearity of the resistive change of the high-R Pt device. a) Change of conductivity for each of the 9 levels (8 poled domains + off state) acquired by IV curves taken from the center (green dot) of the device. The red curve indicates the increase in conduction when more domains are poled and the blue curve corresponds to the case when domains are switched off and the conductance decreases. A high degree of symmetry between the potentiation and depression curves is apparent. b) Plot of the conduction values over the total domain wall length (DW-length acquired by calculating the accumulated domain circumference at each state). A linear behaviour is observed with a slope value of 410 pA/µm and supported by the RMSE values of 0.189nA and 0.187nA for the increase and decrease respectively.

The maximum current values for the 1. 5V readout pulses from Fig. 6.8 c) are plotted in Figure 6.9 a) over the amount of pulses used (which represents the number of switched domains). A highly symmetric structure of the increase and decrease of the conduction, respectively the resistive state of the device is observed. This symmetry is achieved due to the controlled nucleation and annihilation of selected domains. In Figure 6.9 b), the same current values are now plotted over the total DW-length for the associated domain state. The DW length was calculated by accumulation of the measured circumference of each domain. The now plotted conduction values not only exhibit the observed excellent symmetry but also show a high linearity of the current increase and decrease depending on the total DW-length. A slope of around 410pA/µm at 1.5 V bias is calculated. It has to be noted here that even through a possible gradual increase is implied, so far only step-like increases or decreases are demonstrated by switching of single domains. A complete gradual change of the conductance by manipulating the DW-length by fractions of µm needs to be verified in future experiments.

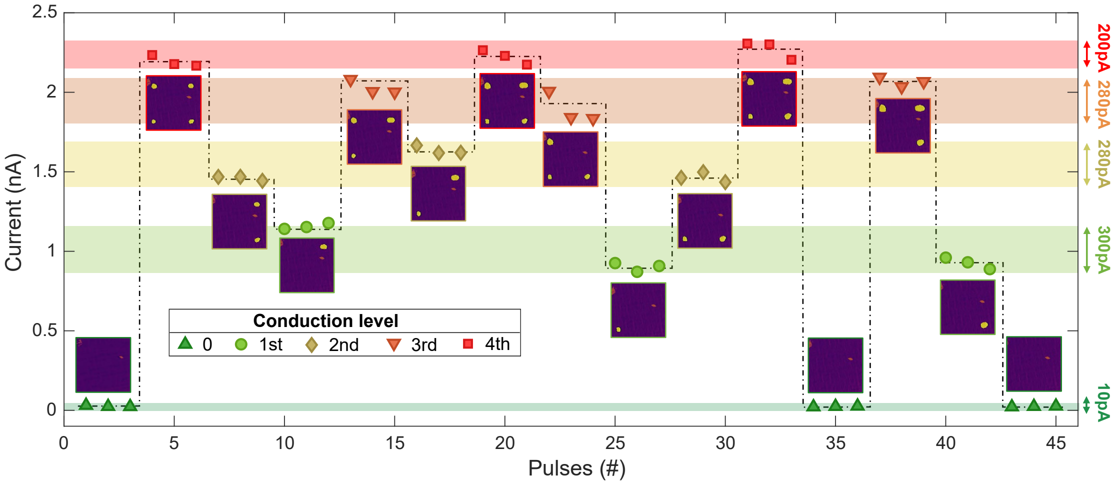

Figure 6.10: *Independent addressing of 4 conduction levels in a random sequence. Each conduction level is addressed 3 times, the parameters of the poling/depoling pulses were 5V/0.5ms and -2.5V/80µs respectively. For each level 3 readout pulses are recorded before switching to the next level and PFM images are taken after each operation to confirm the correlation between conduction state and domain configuration.*

To further show the versatility and robustness of the approach, an experiment was performed to deterministically address each conduction level independently of the previous state and in a repeatable manner. For the data in Figure 6.10 we used a device similar to the one from Figure 6.8 with a 7x7 µm surface area. In Figure 6.10, starting from the off-state with mono-domain configuration and a current readout lower than the noise level (≤ 5pA), we cycle between different domain configurations ranging from 0 to 4 poled domains (see PFM-phase inserts at each conduction level), arranged in a square around the readout point (center of the device). An irregular sequence is performed in which each conduction level is addressed 3 times. After applying the poling (5V/1ms) or repoling pulses (-2.5V/80µs) needed to reach the new state, the conduction is read form the center with 3 consecutive pulses (1.5V/100ms).

It was possible to address each resistive state repeatably, meaning that after cycling through different configurations, it is possible to restore the conduction value within a margin of 200-300 pA. The reason we observe a slight change in conduction values within one level is mainly due to the variation of conductance of created domain walls based on their location. For example, for the case of 1 poled domain (in the square layout), which corresponds to the first conduction level, there are 4 possible configurations (top-left, top-right, bottom-left and bottom-right). 3 of them are addressed in Figure 6.10 with the first one (top-right) showing slightly higher conductance than the two other cases (bottom-left and bottom-right). This could originate from different defect densities and specific domain wall configurations at each location as well as on slight variations in total DW-circumferences and distance differences to the center. Another point is that the non-optimized longer voltage pulses are used to read out the current. Shorter (in terms of dwell time) readout pulses, as discussed within Fig. 6.6, yield a better stability of the already written domains.

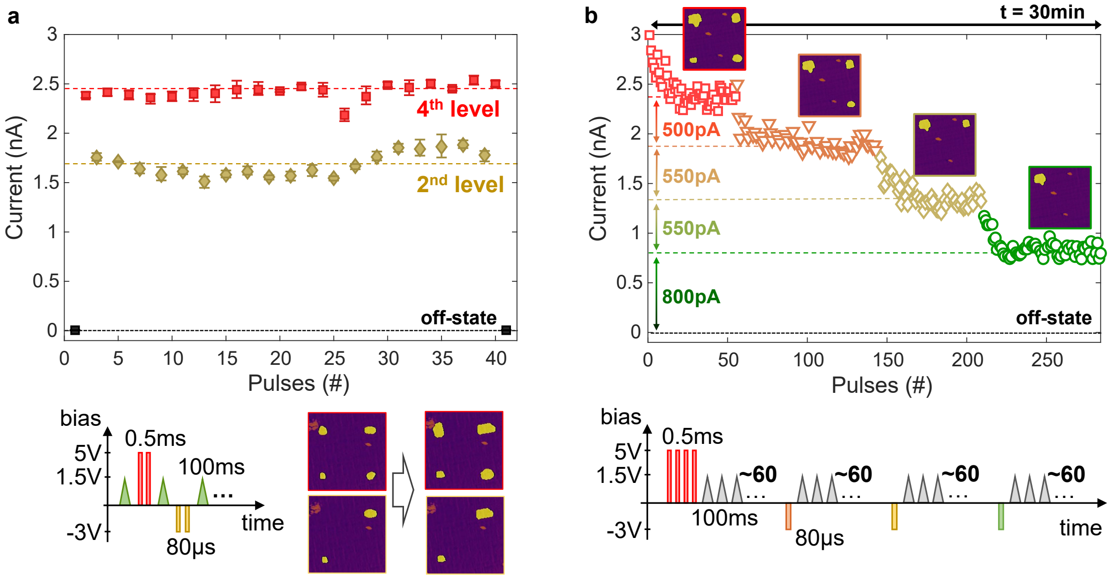

Figure 6.11: a) Multi-level endurance test by cycling between the 4th and 2nd conduction level of the memristive device by the alternating application of two poling (5V/0.5ms) and depoling pulses (-3V/80µs). Current values are recorded by 1.5V/100ms pulses after each operation. PFM images before and after the test (inserts) confirm the stability of the written domain patterns. b) Retention characteristics of the 4 conduction levels, probed by consecutive application of around 60 pulses (1.5V/100ms). After a stabilization phase for around 5 pulses (~1s) the conduction remains stable and each level is well separated by at least 500 pA. PFM inserts show the domain configuration of each state.

In Figure 6.11 a), the multi-level endurance is tested by cycling between the conduction level corresponding to 2 and 4 poled domains. Between each readout pulse two poling (5V/0.5ms) or repoling (-3V/80µs) pulses are applied respectively. For up to 40 times, the domains were cycled and showed reasonable stability. For the 2nd level we observe an increase of around 100 pA after 28 cycles, but the overall conduction stayed within a range of ±140 pA, which illustrates that repetitive cycling is not only possible for the switching of one domain between the on and off state as seen in Figure 6.7, but also within different multi-resistive states. Before and after images of the 2nd and 4th state shows a slight increase of the poled domains after the cycling. This slight degradation could probably be improved, again by application of shorter readout pulses to increase the stability of the observed current values and the stability of the written domains.

To complement the stability study, Figure 6.11 b) shows the retention of the 4 resistive levels used in Figure 6.10. For each level, around 60 readout pulses (1.5V/100ms) are recorded. Between each 5 pulses we introduced a waiting time of several seconds to simultaneously test for a longer time-stability. Each level was therefore probed for a total time of 2-3 min and the total experiment lasted for around 30 min (taking into account the time to switch levels and to acquire the PFM images for each state). We observe that each level shows a slight current decrease for the first 3-5 pulses (for around 1 s) of 500 pA and stabilizes afterwards. The stabilized discrete levels show a wide enough margin between each other to be distinguishable (difference between each level ≥500 pA) together with a scattering within the stabilized levels of ≤300 pA. This characteristic illustrates the non-volatile behaviour of each addressable conduction state with high robustness over repetitive readouts and longer timescales. It is important to note that here the scattering within one level is different than the variations seen in Figure 6.10. Here, we are probing the stability of one configuration which belongs to one conduction level (e.g. for level 1, only the configuration with the top left poled domain is probed), whereas in Figure 6.10, the predominant change in conduction values arise from cycling between different configurations belonging to one conduction level.

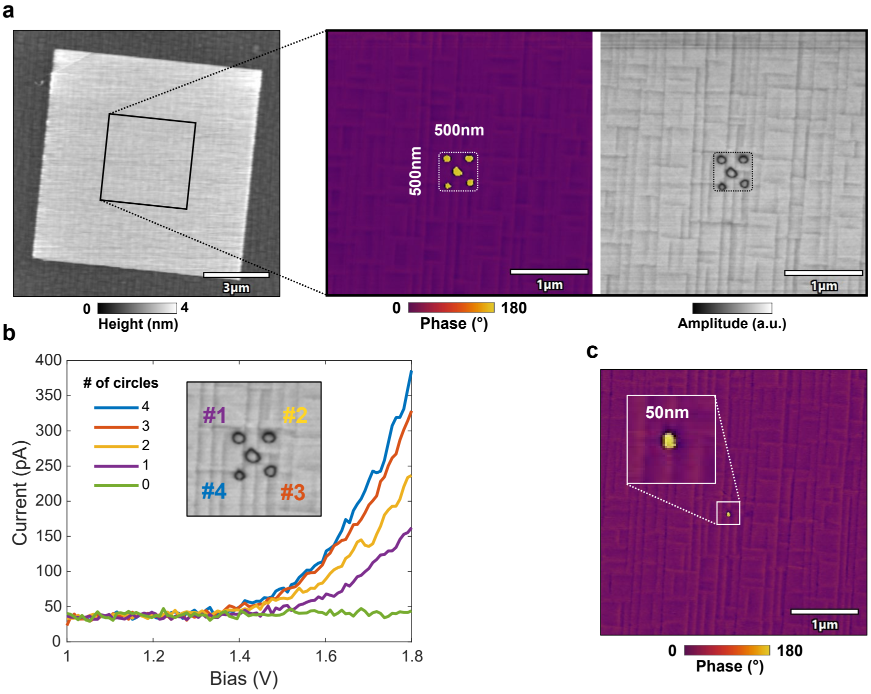

Figure 6.12: *Thin high-R Pt electrode for advanced scalability. a) Topography AFM images of a thin (6 nm) high-R Pt electrode. Magnified PFM images show the center of the electrode after creating 5 circular domains in square pattern with dimensions of ≤500 nm by 5V/1ms pulses. b) IV curves recorded after each poling of the nanodomains. c) PFM image of the smallest controlled nanodomain nucleation achieved within this electrode by a 5V/0.5ms pulse. The domain size is as small as 50 nm in diameter.*

Possible scalable approaches are explored in Figure 6.12. For these experiments, a thinner 6 nm thick high-R Pt electrode is fabricated. By adjusting the poling pulse parameters to 5V/1ms, 5 circular domains could be written inside a sub 0.25 µm^2 area, see Fig. 6.12 a). Concurrent IV measurements at the center showed a similar current increase as it was observed for the larger domains. In Fig. 6.12 b), the IV curves for the first 4 poled nanodomains are shown together with the off state. The PFM image was taken after all measurements were done demonstrating that throughout the consecutive poling operations and current readouts, the written pattern remained stable without any signs of domain collapsing. The achieved reduction in size of the stable switched domains is enabled by the increased resistivity of the thinner electrode, which leads to an enhanced confinement of the electric field. The calculated conductance increase per total DW-length for the data in Fig. 6.12 b) results in a slope of around 310pA/µm for 1.8 V, comparable to the values for the thicker electrode with 410pA/µm for 1.5V in Fig. 6.9. The decrease can be explained by the increased intrinsic resistivity, which reduces the measurable current. Figure 6.12 c), shows the minimum achieved domain size on this electrode by application of a 5V/0.5ms pulse, measuring only 50 nm in diameter. Despite the potential for future scaling of device concepts using thin high-R Pt electrodes these results further demonstrate the advanced controllability over the domain switching with achieved precision of sub 100 nm domain nucleation under a micrometer sized continuous electrode. Such dimensions are normally only accessible by a tip-induced switching in which the 5-20 nm wide tip apex functions as a nanometric contact.

In this section, a domain-wall memristor featuring multiple randomly accessible and well-discriminated conduction states based on the position-controlled injection of individual sub-micron polarization domains is demonstrated. The non-volatile multi-resistive states can be addressed repeatedly by selective domain-by-domain switching within the simple parallel-plate capacitor geometry. Furthermore the scalability of the approach of tuning the total DW-length through a deterministic control of the DW density is demonstrated by going to thinner electrodes with an increased confinement of the applied electric field. Besides the extensive investigations of domain dynamics, domain stability and dependency on the DW-mediated current transport within the high-R Pt devices, the here studied memristor is only one possible approach and should foremost highlight the advancements in DW-control due to the time-evolving switching dynamics. Especially different types of electrode designs as presented in Fig. 6.2, with varying topography and induced non-uniform electric fields are believed to present interesting paths for realization of new device ideas. As an example, the poling operations performed in Fig. 6.3, show the formation of a fractured domain wall front. Such entities should show an increased current response compared to a single smooth domain wall segment due to the increased DW-length.

6.2 Position sensitive domain wall memristor

In the last section, a memristive device was presented that operated on the precise nucleation and annihilation of sub-micron sized domains to change the resistivity based on the modulated DW-length inside the device area. Besides the novelty in controlling individual domains to deterministically address the step-wise resistance states, the fundamental principle by which the conductivity is tuned remains a DW-population or DW-total length variation. Such device concepts will always need to balance between device size, number of accessible resistive-states and total current output. The other pathway normally involves the change of conductivity of a single domain wall, which mainly is done by manipulating its charge state. However most of the proposed techniques yield only volatile resistance changes. In this section a different approach is discussed and a novel position-sensitive domain wall memristor is demonstrated.

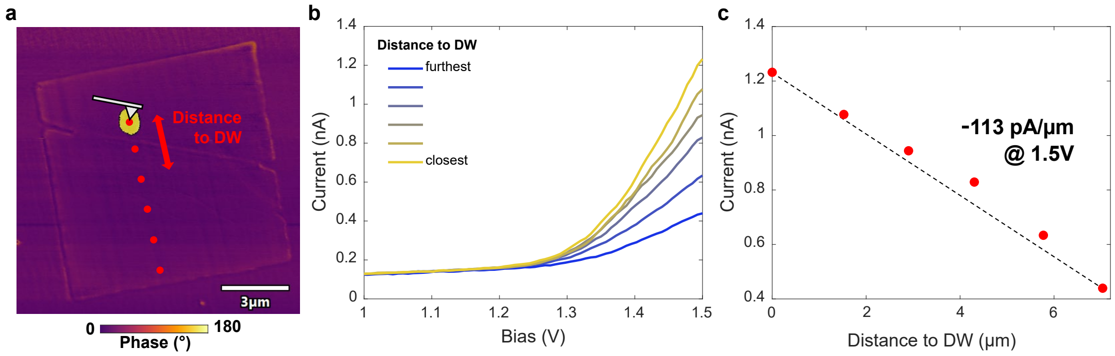

Figure 6.13: *Distant dependent current readout using high-R Pt electrodes. a) PFM image of a high-R Pt electrode. A circular domain (yellow) was poled on the top left side. Red dots indicate the AFM-tip positions at which IV curves were taken to readout the current. b) IV curves of the points indicated in a). A decrease in current is observed for the readout points further away from the poled domains. c) Maximum current values from b) plotted over their distance to the 180°-DW position. The black dotted line shows a slope gradient of -113 pA/μm.*

The fundamental property by which the later introduced device works is the distance dependent conduction measurement based on the position of the domain wall and the readout position of the tip contacting the electrode. Differently to the demonstrated devices with Cr/Au or graphene electrodes for which the same current values are collected for different tip positions on the electrode (compare Fig. 5.8), here a linear dependence on the measured current to the distance is observed. In Figure 6.13 a), a small circular domain is poled inside a high-R Pt device. IV curves up to 1.5 V are collected with an increasing distance to the center of the domain and hence to the domain wall. A decrease in the observed current values is seen in Fig. 6.13 b). For Figure 6.13 c), the maximum values of the IV curves at 1.5 V are plotted over the measured distance between the domain center to the position of tip. A linear fit (black dotted line) is plotted together with the data points exhibiting a negative slope of -113 pA/μm. This observation is attributed to the finite resistance of the electrode which acts like a resistor with constant resistivity but linear dependence of its length. This property of the high-R Pt electrode is the reason why the readout points for all measurements in Section 6.1 were chosen to be exactly in the center and with nearly equal distances to the injected and erased domain walls. What was initially believed to be a major disadvantage resulting in non-linear and varying current values if not properly matched with the readout point, is now used as the driving functionality in the new device concept.

To enable a better functionality and reproducibility, instead of the square electrode layout, a one dimensional line electrode is used with a width of 300 nm and a length of 10 μm. This design choice enables the confinement of the DW propagation in one direction and also reduces the device dimensions. In Figure 6.14 the domain dynamics of the line electrodes are shown.

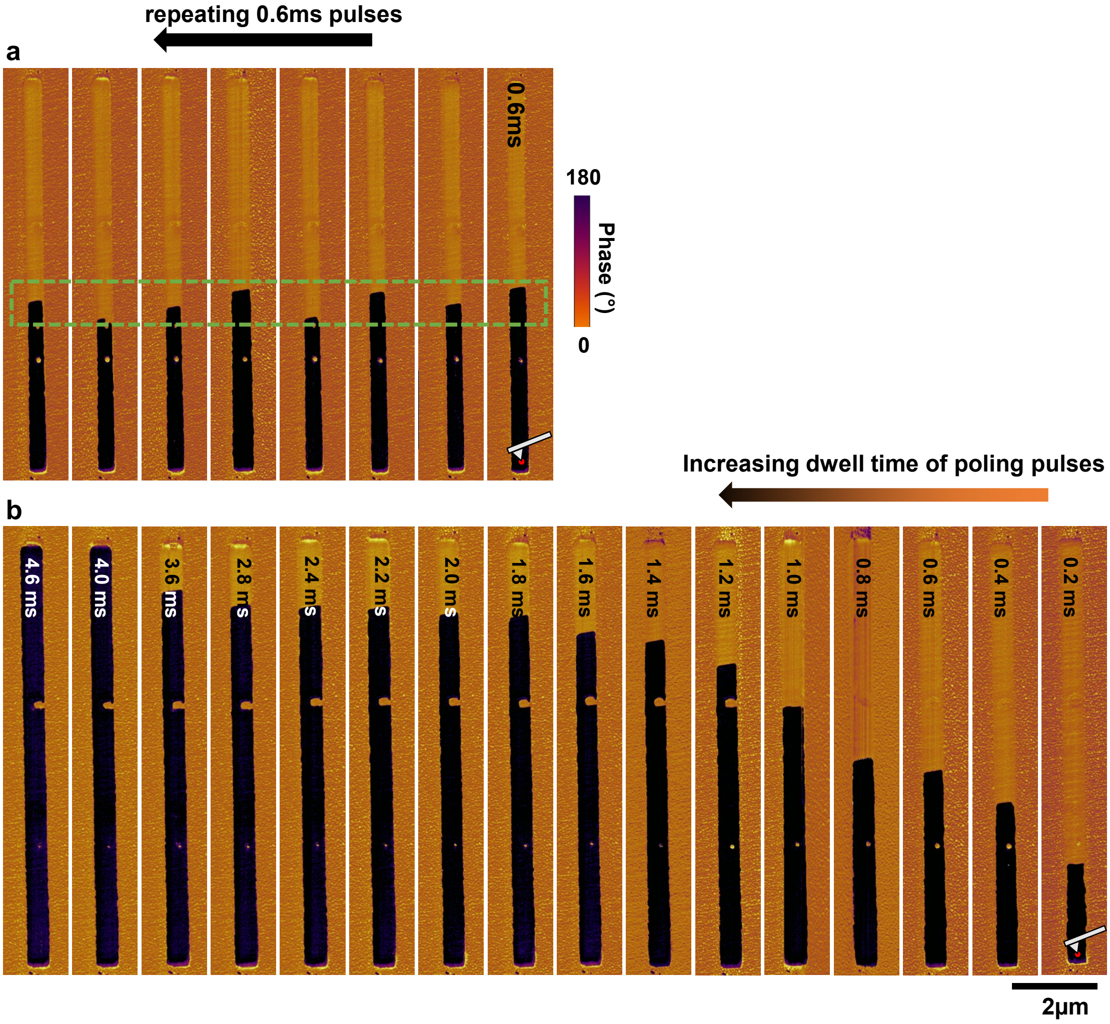

Figure 6.14: *a) PFM images of the repeated application of a 0.6ms poling pulse at the bottom of the line electrode. For each new image and before the next poling pulse the domain is repoled to start from its pristine state. The final position of the DW in each image shows the distribution and effective resolution by which the DW can be repeatably positioned. b) Domain wall propagation study depending on the dwell time of the poling pulse. PFM images show the final position of the domain for the different dwell times. In between the images the domain is reset. A nearly linear increase in domain propagation is seen for values up to 1.8 ms after which the final position seems to stagnate until a long enough time of 4 ms and more are enough to fully switch the domain under the electrode.*

In Fig. 6.14 a), similar to the first measurements in Fig. 6.3, the tip is placed at the bottom of the line electrode and a 6V/0.6ms pulse is applied. In between each PFM-phase image the device is brought back to its pristine state by the application of a -5V/100ms repoling pulse. The PFM images show the repeated domain growth for identical poling pulses. A variation in the final position of the domain is observed and the total area in which the final positions were found is indicated by the green rectangular. This area corresponds to the achievable precision by which the DW can be positioned. Obviously, these variations are not ideal and need further optimization to be able to reliably position the DW in a more narrow range.

In Figure 6.14 b), a similar experiment is performed, but this time the pulse duration is gradually increased from 0.2 ms to 4.6 ms. Longer pulse durations show to induce an increasing DW displacement with durations of 4m s and more being sufficient to fully pole the line electrode. For values between 0.2 ms and 1.8 ms a more or less linear increase of the DW position is observed, followed by a saturation region (1.8 ms to 3.6 ms) and an abrupt jump to the fully poled state for dwell times of more than 4 ms. It should be noted here that a slight non-linear tendency was expected based on the results of McGilly et al. [116], but an increased non-continuous step-like dependency is observed. The resulting differences might be explained by domain wall pinning effects due to the underlying existing ferroelastic network, which could locally restrict the free motion of the DW front.

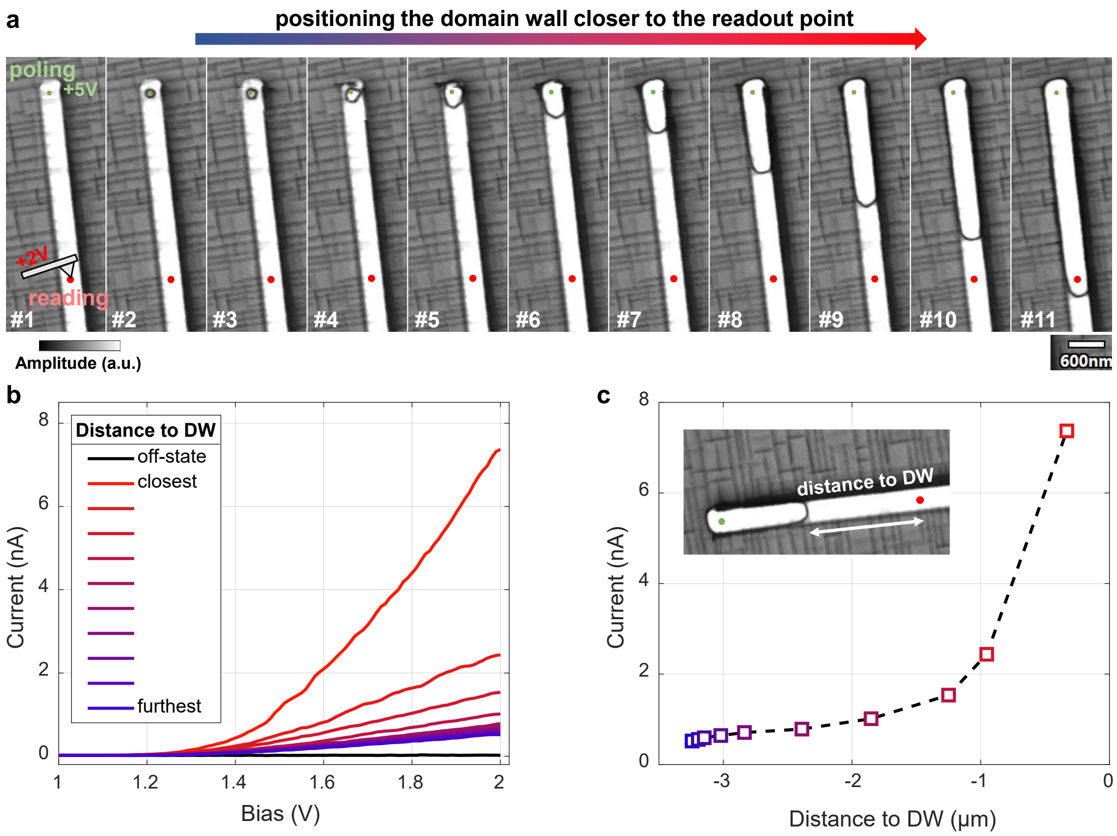

Figure 6.15: *Working principle of the proximity-sensitive memristor. a) PFM images of the successive increasing poled domain size and associated progressive position of the DW achieved by application of 5V pulses from the green position at the top of the line electrode. The current is read with 2V from the point labeled in red. b) IV curves for the shown 11 device states with different DW positions. c) Plot of the maximum current values from b) over the distance of the DW-front to the readout point. A non-linear current increase is observed for shorter distances.*

The device operation based on the two previously explored effects (distance dependent conduction readout and DW positioning through electric fields) is shown in Figure 6.15. In Fig. 6.15 a), the tip is positioned at the top part of the electrode to apply consecutive poling pulses. In between each poling pulse, the current is readout form the other side (roughly in the center of the long line electrode) at a distance of approximately 3.5 µm to the nucleation center. The PFM amplitude images show the gradual propagation of the DW with decreasing distance to the readout point. The recorded IV curves for each state of the device are shown in Fig. 6.15 b). The maximum value is plotted over the measured distance to the DW in Figure 6.15 c). A non-linear conduction increase is observed for a closer positioning of the DW. Maximum current values of over 7 nA are recorded for the state at which the DW is nearly perfectly placed under the readout point. It is important to highlight here that the predominant resistance change is solely mediated by the moving domain wall segment of roughly 300 nm width. No additional domain walls are injected into the device to tune the resistivity nor is the conductivity of the domain wall segment itself changed.

To further characterize the device, and verify the observed current characteristics a second experiment was done. In Figure 6.16 an intermediate domain state was created by pushing the DW roughly 3 µm away from the bottom nucleation center. Now instead of controlling the domain wall, the tip is moved to different positions on the line electrode and the DW is kept stationary. An interesting current profile is obtained by moving the tip from the bottom of the line electrode from which the domain nucleation started to the center of the line electrode. The blue segment indicates the positions of the tip for which the DW is behind the readout point (which equals a state in which a poling pulse is applied which pushed the DW further than the readout point) while the red area indicates the region for which the tip is behind the DW (this case is similar to the previously presented experiment in Fig. 6.15), and the green dot indicates the position at which the tip is placed directly on the DW. As expected and observed in Fig. 6.15, when the DW is in front of the readout point a non-linear current curve is obtained for an increasing distance. However, if the DW is behind the tip-position the current dependency with increasing distance appears to be linear. This behaviour is believed to originate from border effects. Inside the blue region additional to the main contribution of the free moving DW segment, the DW overlaps with the border of the electrode. As seen previously with Cr/Au electrodes (see Section 5.1), DWs positioned at the border of the electrode area can remain partially in contact and mediate a current transport. This effect is expected to cause the shift from the non-linear dependency to a linear dependency of the current readout, as additional surrounding DW segments contribute to the overall measured current. More studies are needed to explore this effect in detail. Nevertheless it also provides us with two regimes to work with, depending on where the readout point is located and where the domain wall is positioned. Overall while the experiments with a moving tip do not reflect an actual working operation of the device it helps to clarify two things. First, the discussed two regimes available to tune the resistivity of the device are observed. Second, since the red region of Fig. 6.16 and the experiment in Fig. 6.15 show the same current characteristics, it can be concluded that the only origin for the resistive tuning is the position of the DW, while the

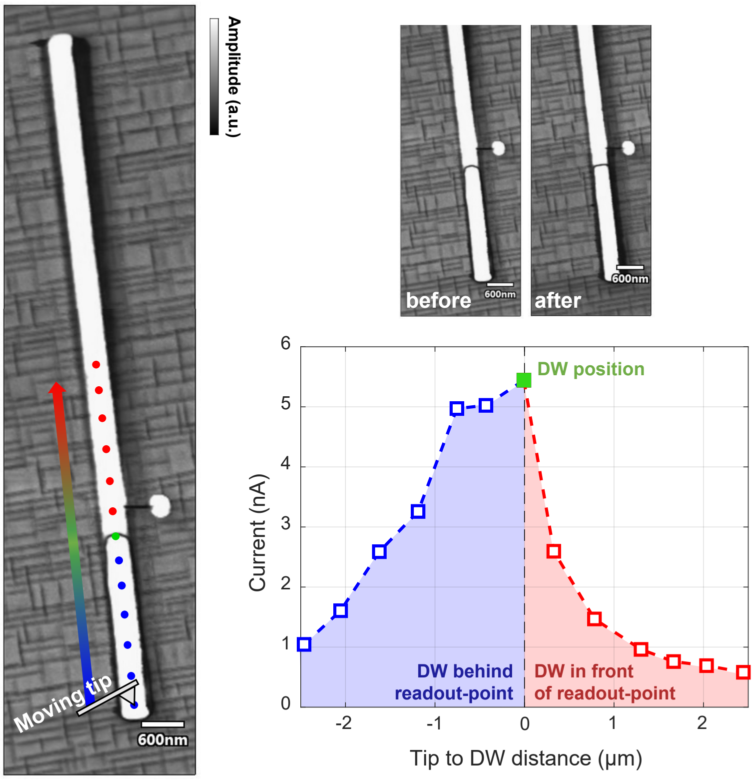

Figure 6.16: *Two resistive switching regimes of the line memristor. In this experiment the device was brought into an intermediate position characterized by a DW positioned in the bottom half of the device. IV curves are taken on different positions along the electrode to map the different current responses depending on the readout position. Left: PFM amplitude image of the investigated device state. Blue points represent the positions of the readout for which the DW is behind the readout position, while red points correspond to the positions for which the DW is in front of the readout point. The green dot represents the readout of current directly on top of the DW. Right: Plot of the maximum current value of the IV curves with regard to their distance to the DW. Two regimes can be identified. Inside the blue region, the conductance change is linear while for the red region a nonlinear dependency is observed. PFM images before and after the 13 IV readouts are shown above the plot, verifying the stable position of the DW.*

conductivity of the DW-segment remains stable even when being moved and repositioned by electric fields of micrometer distances.

The proposed concept of a distance-dependent current modification demonstrates another pathway of a resistive switching using only a single nanometer size DW segment with robust and stable conductive properties. Furthermore, the device concept links the resistivity readout to the time-evolving DW position. In the here first presented prototype only stationary device states are studied, but readily demonstrate the potential to be used for dynamic time-sensitive operations. Examples could include to work with spiking signals and use the evolving position of DWs to trigger at spatially resolved readout point.

6.3 Summary

In summary, Chapter 6 introduces high-resistive platinum electrodes for an advanced control over the domain wall nucleation position and propagation. Different designs of the electrode and their surface are presented for capacitor devices and their influence on the switching dynamics and the creation of domain walls is discussed. The precise confinement of switched domains inside the capacitor is demonstrated together with extensive studies on the stability of the created domain configurations as well as for the resulting current output characteristics. Based on these results a domain wall based memristor device is build in which an individual addressability of switched domains leads to a step-wise tunability of the device's resistance states. A nearly perfect symmetry of the conductance increase and decrease is observed mediated by the controlled injection of 180°-DWs. The conductivity could be linked to scale linearly with the the total DW-length confined inside the capacitor. Reproducible addressing of the gradual conductance states is demonstrated together with their non-volatility.

In the second part of the chapter, a novel way of tuning the device conductance is presented in which a single nanometric DW-segment is precisely positioned within a one dimensional line electrode. Based on the observed property of the high-resistive electrodes to posses a distance dependent current readout, a device is demonstrates which uses the controlled distance between a created 180°-DW and a fixed readout point to gradually tune its resistivity. Two regimes, a linear and a non-linear regime, could be identified, based on if the domain wall is positioned in front or behind the readout point, respectively. Further comparisons of the experiments validated the stable nature of the conductance of the DW-segment when moved inside the electrode.

Overall, the presented work in this chapter demonstrates the advanced control over the domain walls by using high-R Pt electrodes and leads to two implementations of memristive functionalities based on fundamentally different device concepts. Future work and device ideas are expected to build upon the presented fundamental studies of the interaction of the time-evolving domain wall positions and distance dependent current readout schemes to fully exploit the reconfigurability of the non-volatile conductive domain wall channels.

7 Conclusions and future perspectives

In this final chapter, the main achievements presented in this manuscript are summarized and the most significant contributions are discussed within the current state of the research field. To conclude this work, potential perspectives and future directions are discussed, based on the foundation laid by this thesis to advance the field of domain wall nanoelectronics.

7.1 Main achievements and future perspectives

For this final chapter the four main results are summarized shortly and then put into perspective and discussed with regards to the current state of the research field and future directions.

1. **Guidelines and recipes for tuning domain wall conductivity in PLD-growths**
   The growth conditions for highly tetragonal PZT films (Zr:Ti = 1:9), with a $SrRuO_3$ bottom electrode, onto $DyScO_3$ substrates for the Solmates PLD-system at EPFL were investigated. The studies resulted in reliable growth recipes for SRO/PZT films on pristine DSO substrates possessing both conductive pristine a-DWs as well as artificially created conductive 180°-DWs. It was shown that the process temperature possessed a major role in the formation of the enhanced and localized conduction at the domain wall. Furthermore, the growth of PZT samples with self-assembled isolated nanoislands were achieved showing nanometer sized c-domains paired with a strong conductive response of several nanoamperes upon domain switching operations.

   Together with the known influence of the oxygen pressure during growth on the conductivity of domain walls, in this work also the temperature influence is studied. As it was shown, the decreasing temperature during growth of the PZT layers resulted in a decrease of DW-conduction potentially mediated by a change of the charge carrier providing oxygen vacancies. However, also the missing formation of interconnected charged a-domains seen in low-temperature samples could further influence the missing conductivity of the 180°-DWs. Further studies on the new samples, combined with

STEM experiments could reveal if and how the domain wall structure itself is influenced on the process parameters. Future perspectives involve the realization of in-plane conductivity in PZT films. Proposed pathways involve the integration of a thin isolating SRO layer and STEM resolved atomic characterizations of the domain walls to identify how their structure differs from samples with SRO bottom electrodes. If such samples can be realized, it would enable to not only study the in-plane behaviour of the conductive channels, their interconnectivity and networking behaviour, but also offers new ways to investigate the intrinsic properties of the conduction through e.g. advanced Hall-effect measurements. However, the experimentally observed and simulated non-uniformity of 180°-DWs and the varying dependency of the conduction along the domain wall could impose fundamental limitations for the reliable observation of in-plane conductivity.

2. **First observation of charged 180°-DWs in PZT thin film and their conduction origins**
   Within this work the first observations of highly conductive 180°-DWs in epitaxial PZT thin films are presented. While previous reported results on weakly conducting 180°-DWs in PZT were known, the in this work in detailed studied 180°-DWs could be proven to exhibit a fundamentally different conduction mechanism. Compared to a defect mediated conduction present at domain walls in PZT films grown on STO substrates, the here observed conductivity of 180°-DWs in PZT films grown on DSO substrates could be demonstrated to result from charged DW-interfaces mediating an intrinsic conduction mechanism. Based on phase-field simulations and STEM-experiments, it could be shown that "thought-to-be straight" 180°-DWs deviate from their neutral structure due to their interaction with the ferroelastic a-domain network. The arising charged domain boundaries created at the interaction points of the two domain wall types form experimentally observed Tail-to-Tail DWs, promoting the appearance of a 2D hole-gas. This result is supported by the non-thermally activated conduction properties of the 180°-DWs observed at cryogenic temperatures. The charged DW-interfaces are stabilized due to their interaction with the stable ferroelastic a-domains network, resulting in the formation of highly conductive and non-volatile channels. The conductive channels are solely linked to the the presence of the 180°-DWs and the intrinsic transport mechanism provides an agile reconfiguration of the conductive properties based on domain manipulation by electric fields.

   Within the field of domain wall electronics, different kinds of DW interfaces have been extensively studied in various material systems. Conductive charged DWs as well as conductive neutral DWs have been observed and their associated conduction mechanism have been explored. High conduction values have so far solely been reported for charged DWs, which either needed to be created by cumbersome poling operations in carefully oriented crystal structures or formed only transiently with volatile conduction characteristics.
   The here presented work on normally neutral 180°-DWs, explores the possibility to combine the high conductivity found in charged DWs with the easy and readily available switchability of stable ferroelectric 180° domain switching. The properties of high con-

ductivity, non-volatility and easy manipulation by electric fields observed at these walls make them attractive for reconfigurable DW-based device application. Future work could involve quantitative studies on the carrier type and densities of the 180°-DWs by sophisticated Hall-effect measurements to verify the proposed hole-type conduction. Together with growth studies e.g. on different substrates with varying lattice constants, the direct influence of the a-domain network, its density or the degree of the charge state of the a-DW onto the conductivity of the artificially created 180°-DWs could be further studied to deepen the understanding of the observed domain interplay.

3. **Memristive functionalities based on graphene enabled multi-domain switching**
   Based on the explored properties of the highly conductive and non-volatile 180°-DWs, memristive functionalities are realized in capacitor-type memory devices. After first unsuccessful attempts of confining the created 180°-DWs under a pure metal electrode, the integration of graphene proved to overcome the limitation of sharp and near instant full domain switching in high-quality epitaxial PZT films under an electrode area. The intrinsic properties of graphene sheets, their high in-plane conductivity with excellent contact to the oxide surface, paired with naturally formed defects in the van der Waals interface provided both high on-state currents between 10-100 nA/μm^2 and limiting domain growth of the c-domains. The resulting multi-domain states showed stable non-volatile characteristics and were tunable upon application of consecutive pulses resulting in a step-wise change of the device's resistive states. PFM imaging allowed to visualize the different multi-domain states and link them to the change in conductance.

   Proposed DW-memristor concepts based on the tuning of the domain wall density have so far suffered from either low readout current of the single contributing DWs leading to large device sizes, reduced stability of artificially created charged DWs offering high resistive changes or were limited in controlling the formation of DWs and repeatable addressing of multiple resistive states. The proposed concept of integrating graphene electrodes together with the strain-stabilized formation of the highly conductive domain walls in PZT offer a way to overcome these limitations. The challenge arises from the conflicting demands for the sharp polarization reversal in an epitaxial layer with high-quality interface (i) together with stable intermediate multi-domain configurations needed for stabilized and confined DWs (ii). The requirement (i) implies very fast switching occurring within a narrow voltage range, where the multi-domain patterns form only transiently while the system evolves toward complete switching, which is in conflict with the requirement (ii). The graphene electrode solves these issue by providing both a defect-mediated growth limitation for the switching domains by the natural occurring defects in graphene films while simultaneously maintaining the high quality interface needed for low-voltage switching and high current readouts. Moreover, since the locally defined nucleation centers, for which the domain switching starts, are persistent, the repeatable addressing of the resistive levels and symmetry of conduction increase and decrease is enhanced due to the reproducible formation of the same mixed-domain configurations.

4. **Deterministic domain control for advanced memristive DW-based device concepts** Additionally, besides the realization of memristive functionality with graphene-based capacitors, due to a stochastic switching, a deterministic poling of individual domains with limited domain growth and confinement of the 180°-DWs is realized. By using high-R Pt electrodes, a time evolving electric field is exploited to control the speed and final position of 180°-DWs. Resulting domain configurations exhibited excellent stability characteristics leading to a controllable change of the resistive levels of the capacitor devices. A high degree of symmetry and linearity of the conductance increase and decrease are reported due to the precise and controlled switching of individual domains. Furthermore, the concept of controlled propagation of domain walls together with the unique distance dependent conduction properties provided by high-resistive electrodes is exploited to build the first proximity-sensitive domain wall memristor. Based on the controlled positioning of the conductive domain wall within a 1D line electrode with respect to the readout point, the resistivity can be modulated in a precise and highly gradual way. Furthermore the concept utilizes only a single movable 300 nm wide DW-segment to control the resistivity with conduction values up to several nanoampere for low-voltage operations compared to the limited scalability for devices relying on a DW-density tuning.

   Most of the research in the field of domain wall electronics in recent years has been focused on the investigation of the intrinsic conduction properties and the possibility to tune the conductivity of the domain walls. While such initial studies are of great importance for the fields and are further needed to offer competitive systems for memristive devices and neuromorphic elements in terms of accessible current output, stability or CMOS compatibility, future work also needs to explore and exploit the unique advantages offered by domain walls. One way is to use single DWs as the functional elements for ultimate scalability. Other directions could investigate on the reconfigurability of the DW-channels, as most concepts to date only use simple inject/erase operations instead of agile interconnections formed by DWs. These perspectives will be fueled by work dedicated into the advancements of an enhanced and flexible control over the position and nucleation of single-DWs. As presented in the thesis, one way could be to implement time-dependent domain expansion schemes introduced by high-R Pt electrodes to offer flexibility in the final DW position, inaccessible by standard electrode material and device concepts.

7.2 Concluding remarks

The exploration of novel neuromorphic computation hardware is fueled by the accelerating demand in computation speed, energy consumption and the growing prevalence of AI-applications. Within this field ferroelectric materials have shown to be competitive systems for building novel nanoelectronic devices like artificial neurons/synapses or memristive elements.

In this thesis, ferroelectric domain walls are investigated, which offer a wealth of unique properties and advantages to realize the sought after brain-like functionalities. Their intrinsically nanometric size coupled with the emergence of functional properties like enhanced conductivity and flexibility offer a platform for reconfigurable conductive channels. The ability to tune the conductance of these channels and to control and reconfigure them by will through electric stimuli holds great potential if their conductive properties can be further enhanced and reliable device concepts overcome the existing compatibility issues with the CMOS-technology.

A PLD process parameters

A.1 SRO/PZT films

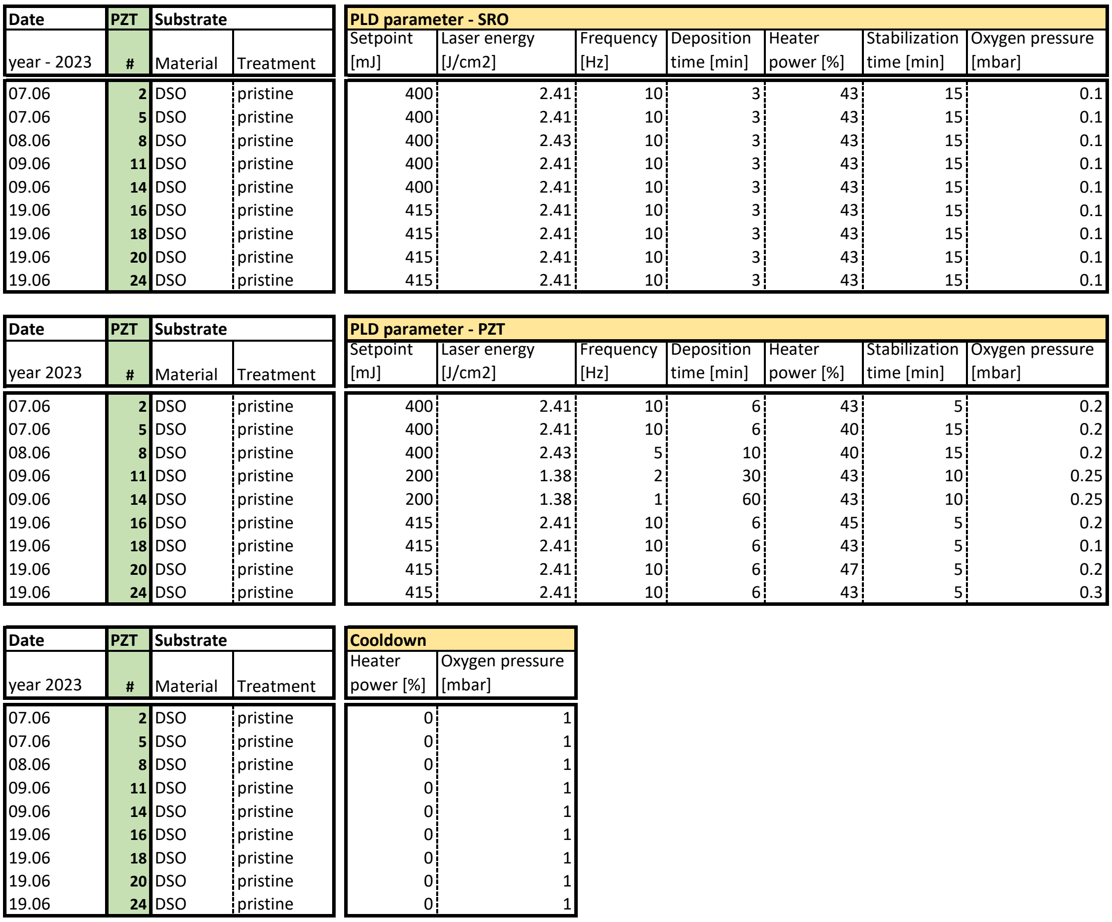

Date	PZT	Substrate		PLD parameter - SRO						
year - 2023	#	Material	Treatment	Setpoint [mJ]	Laser energy [J/cm2]	Frequency [Hz]	Deposition time [min]	Heater power [%]	Stabilization time [min]	Oxygen pressure [mbar]
07.06	2	DSO	pristine	400	2.41	10	3	43	15	0.1
07.06	5	DSO	pristine	400	2.41	10	3	43	15	0.1
08.06	8	DSO	pristine	400	2.43	10	3	43	15	0.1
09.06	11	DSO	pristine	400	2.41	10	3	43	15	0.1
09.06	14	DSO	pristine	400	2.41	10	3	43	15	0.1
19.06	16	DSO	pristine	415	2.41	10	3	43	15	0.1
19.06	18	DSO	pristine	415	2.41	10	3	43	15	0.1
19.06	20	DSO	pristine	415	2.41	10	3	43	15	0.1
19.06	24	DSO	pristine	415	2.41	10	3	43	15	0.1

Date	PZT	Substrate		PLD parameter - PZT						
year 2023	#	Material	Treatment	Setpoint [mJ]	Laser energy [J/cm2]	Frequency [Hz]	Deposition time [min]	Heater power [%]	Stabilization time [min]	Oxygen pressure [mbar]
07.06	2	DSO	pristine	400	2.41	10	6	43	5	0.2
07.06	5	DSO	pristine	400	2.41	10	6	40	15	0.2
08.06	8	DSO	pristine	400	2.43	5	10	40	15	0.2
09.06	11	DSO	pristine	200	1.38	2	30	43	10	0.25
09.06	14	DSO	pristine	200	1.38	1	60	43	10	0.25
19.06	16	DSO	pristine	415	2.41	10	6	45	5	0.2
19.06	18	DSO	pristine	415	2.41	10	6	43	5	0.1
19.06	20	DSO	pristine	415	2.41	10	6	47	5	0.2
19.06	24	DSO	pristine	415	2.41	10	6	43	5	0.3

Date	PZT	Substrate		Cooldown	
year 2023	#	Material	Treatment	Heater power [%]	Oxygen pressure [mbar]
07.06	2	DSO	pristine	0	1
07.06	5	DSO	pristine	0	1
08.06	8	DSO	pristine	0	1
09.06	11	DSO	pristine	0	1
09.06	14	DSO	pristine	0	1
19.06	16	DSO	pristine	0	1
19.06	18	DSO	pristine	0	1
19.06	20	DSO	pristine	0	1
19.06	24	DSO	pristine	0	1

Figure A.1: *PLD process parameter for the SRO and PZT layers of PZT samples with continuous surfaces presented in this work.*

A.2 PZT nanoislands

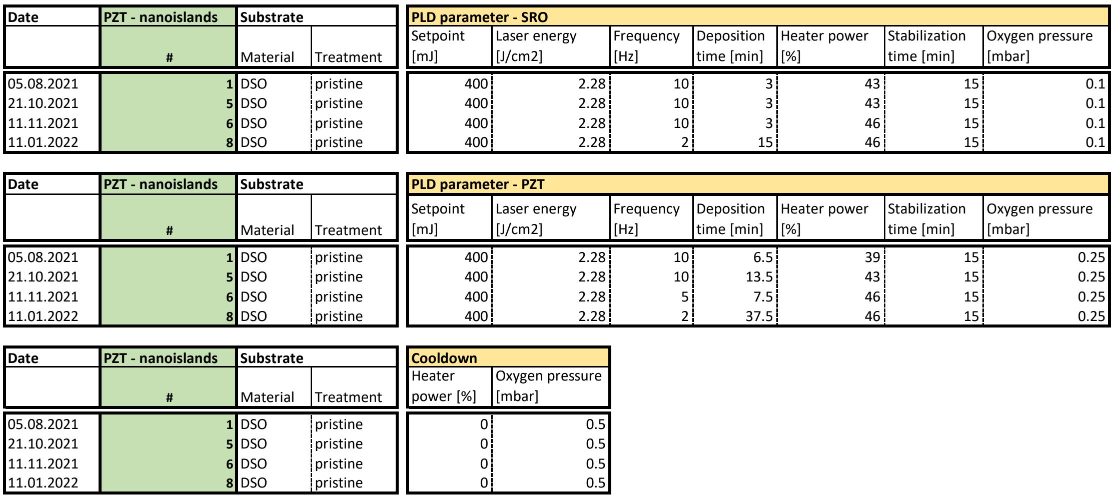

Date	PZT - nanoislands #	Substrate Material	Substrate Treatment	PLD parameter - SRO Setpoint [mJ]	Laser energy [J/cm2]	Frequency [Hz]	Deposition time [min]	Heater power [%]	Stabilization time [min]	Oxygen pressure [mbar]
05.08.2021	1	DSO	pristine	400	2.28	10	3	43	15	0.1
21.10.2021	5	DSO	pristine	400	2.28	10	3	43	15	0.1
11.11.2021	6	DSO	pristine	400	2.28	10	3	46	15	0.1
11.01.2022	8	DSO	pristine	400	2.28	2	15	46	15	0.1

Date	PZT - nanoislands #	Substrate Material	Substrate Treatment	PLD parameter - PZT Setpoint [mJ]	Laser energy [J/cm2]	Frequency [Hz]	Deposition time [min]	Heater power [%]	Stabilization time [min]	Oxygen pressure [mbar]
05.08.2021	1	DSO	pristine	400	2.28	10	6.5	39	15	0.25
21.10.2021	5	DSO	pristine	400	2.28	10	13.5	43	15	0.25
11.11.2021	6	DSO	pristine	400	2.28	5	7.5	46	15	0.25
11.01.2022	8	DSO	pristine	400	2.28	2	37.5	46	15	0.25

Date	PZT - nanoislands #	Substrate Material	Substrate Treatment	Cooldown Heater power [%]	Oxygen pressure [mbar]
05.08.2021	1	DSO	pristine	0	0.5
21.10.2021	5	DSO	pristine	0	0.5
11.11.2021	6	DSO	pristine	0	0.5
11.01.2022	8	DSO	pristine	0	0.5

Figure A.2: *PLD process parameter for the SRO and PZT layers for the nanoisland samples presented in this work.*

Bibliography

[1] William Shockley. “The path to the conception of the junction transistor”. In: *IEEE Transactions on Electron Devices* 23.7 (1976), pp. 597–620.

[2] MM Irvine. “Early digital computers at bell telephone laboratories”. In: *IEEE Annals of the History of Computing* 23.3 (2001), pp. 22–42.

[3] Gordon E Moore. “Cramming more components onto integrated circuits”. In: *Proceedings of the IEEE* 86.1 (1998), pp. 82–85.

[4] Sayeef Salahuddin, Kai Ni, and Suman Datta. “The era of hyper-scaling in electronics”. In: *Nature electronics* 1.8 (2018), pp. 442–450.

[5] David J Frank. “Power-constrained CMOS scaling limits”. In: *IBM Journal of Research and Development* 46.2.3 (2002), pp. 235–244.

[6] Tim Berners-Lee, Robert Cailliau, Jean-François Groff, and Bernd Pollermann. “World-Wide Web: the information universe”. In: *Internet Research* 2.1 (1992), pp. 52–58.

[7] Andrew Trotman and Jinglan Zhang. “Future web growth and its consequences for web search architectures”. In: *arXiv preprint arXiv:1307.1179* (2013).

[8] Vijay Sivaraman, Hassan Habibi Gharakheili, Clinton Fernandes, Narelle Clark, and Tanya Karliychuk. “Smart IoT devices in the home: Security and privacy implications”. In: *IEEE Technology and Society Magazine* 37.2 (2018), pp. 71–79.

[9] James Manyika, Michael Chui, Peter Bisson, Jonathan Woetzel, Richard Dobbs, Jacques Bughin, and Dan Aharon. “The Internet of Things: Mapping the value beyond the hype”. In: (2015).

[10] Adrian M Ionescu. “Energy efficient computing and sensing in the Zettabyte era: From silicon to the cloud”. In: *2017 IEEE International Electron Devices Meeting (IEDM)*. IEEE. 2017, pp. 1–2.

[11] Anders SG Andrae and Tomas Edler. “On global electricity usage of communication technology: trends to 2030”. In: *Challenges* 6.1 (2015), pp. 117–157.

[12] Noelia Hernández, Ignacio Parra, Héctor Corrales, Rubén Izquierdo, Augusto Luis Ballardini, Carlota Salinas, and Iván Garcıa. “WiFiNet: WiFi-based indoor localisation using CNNs”. In: *Expert Systems with Applications* 177 (2021), p. 114906.

[13] Pranav Rajpurkar, Emma Chen, Oishi Banerjee, and Eric J Topol. “AI in health and medicine”. In: *Nature medicine* 28.1 (2022), pp. 31–38.

[14] Yogesh K Dwivedi, Anuj Sharma, Nripendra P Rana, Mihalis Giannakis, Pooja Goel, and Vincent Dutot. “Evolution of artificial intelligence research in Technological Forecasting and Social Change: Research topics, trends, and future directions”. In: *Technological Forecasting and Social Change* 192 (2023), p. 122579.

[15] Liu Yufeia, Salmiza Salehb, Huang Jiahuic, and Syed Mohamad Syed. “Review of the application of artificial intelligence in education”. In: *Integration (Amsterdam)* 12.8 (2020), pp. 1–15.

[16] Caiming Zhang and Yang Lu. “Study on artificial intelligence: The state of the art and future prospects”. In: *Journal of Industrial Information Integration* 23 (2021), p. 100224.

[17] Joshua Taylor, Vina El Ardeliya, and Julia Wolfson. “Exploration of Artificial Intelligence in Creative Fields: Generative Art, Music, and Design”. In: *International Journal of Cyber and IT Service Management* 4.1 (2024), pp. 39–45.

[18] Shahin Atakishiyev, Mohammad Salameh, Hengshuai Yao, and Randy Goebel. “Explainable artificial intelligence for autonomous driving: A comprehensive overview and field guide for future research directions”. In: *arXiv preprint arXiv:2112.11561* (2021).

[19] Yupeng Chang, Xu Wang, Jindong Wang, Yuan Wu, Linyi Yang, Kaijie Zhu, Hao Chen, Xiaoyuan Yi, Cunxiang Wang, Yidong Wang, et al. “A survey on evaluation of large language models”. In: *ACM Transactions on Intelligent Systems and Technology* 15.3 (2024), pp. 1–45.

[20] Adnan Mehonic and Anthony J Kenyon. “Brain-inspired computing needs a master plan”. In: *Nature* 604.7905 (2022), pp. 255–260.

[21] David Patterson, Joseph Gonzalez, Quoc Le, Chen Liang, Lluis-Miquel Munguia, Daniel Rothchild, David So, Maud Texier, and Jeff Dean. “Carbon emissions and large neural network training”. In: *arXiv preprint arXiv:2104.10350* (2021).

[22] Xingqi Zou, Sheng Xu, Xiaoming Chen, Liang Yan, and Yinhe Han. “Breaking the von Neumann bottleneck: architecture-level processing-in-memory technology”. In: *Science China Information Sciences* 64.6 (2021), p. 160404.

[23] Danijela Marković, Alice Mizrahi, Damien Querlioz, and Julie Grollier. “Physics for neuromorphic computing”. In: *Nature Reviews Physics* 2.9 (2020), pp. 499–510.

[24] Kaushik Roy, Akhilesh Jaiswal, and Priyadarshini Panda. “Towards spike-based machine intelligence with neuromorphic computing”. In: *Nature* 575.7784 (2019), pp. 607–617.

[25] Sadegh Kamaei Bahmaei. *Energy-Efficient Electronic Functions Based on the Co-integration of 2D and Ferroelectric Materials.* Tech. rep. EPFL, 2023.

[26] Catherine D Schuman, Shruti R Kulkarni, Maryam Parsa, J Parker Mitchell, Bill Kay, et al. “Opportunities for neuromorphic computing algorithms and applications”. In: *Nature Computational Science* 2.1 (2022), pp. 10–19.

[27] Carver Mead. “Neuromorphic electronic systems”. In: *Proceedings of the IEEE* 78.10 (1990), pp. 1629–1636.

[28] Steve B Furber, Francesco Galluppi, Steve Temple, and Luis A Plana. “The spinnaker project”. In: *Proceedings of the IEEE* 102.5 (2014), pp. 652–665.

[29] Johannes Schemmel, Daniel Brüderle, Andreas Grübl, Matthias Hock, Karlheinz Meier, and Sebastian Millner. “A wafer-scale neuromorphic hardware system for large-scale neural modeling”. In: *2010 ieee international symposium on circuits and systems (iscas)*. IEEE. 2010, pp. 1947–1950.

[30] Paul A Merolla, John V Arthur, Rodrigo Alvarez-Icaza, Andrew S Cassidy, Jun Sawada, Filipp Akopyan, Bryan L Jackson, Nabil Imam, Chen Guo, Yutaka Nakamura, et al. “A million spiking-neuron integrated circuit with a scalable communication network and interface”. In: *Science* 345.6197 (2014), pp. 668–673.

[31] Mike Davies, Narayan Srinivasa, Tsung-Han Lin, Gautham Chinya, Yongqiang Cao, Sri Harsha Choday, Georgios Dimou, Prasad Joshi, Nabil Imam, Shweta Jain, et al. “Loihi: A neuromorphic manycore processor with on-chip learning”. In: *Ieee Micro* 38.1 (2018), pp. 82–99.

[32] Giacomo Indiveri, Bernabé Linares-Barranco, Tara Julia Hamilton, André van Schaik, Ralph Etienne-Cummings, Tobi Delbruck, Shih-Chii Liu, Piotr Dudek, Philipp Häfliger, Sylvie Renaud, et al. “Neuromorphic silicon neuron circuits”. In: *Frontiers in neuroscience* 5 (2011), p. 73.

[33] S Oh, H Hwang, and IK Yoo. “Ferroelectric materials for neuromorphic computing”. In: *Apl Materials* 7.9 (2019).

[34] Vinod K Sangwan and Mark C Hersam. “Neuromorphic nanoelectronic materials”. In: *Nature nanotechnology* 15.7 (2020), pp. 517–528.

[35] Min-Kyu Kim, Youngjun Park, Ik-Jyae Kim, and Jang-Sik Lee. “Emerging materials for neuromorphic devices and systems”. In: *Iscience* 23.12 (2020).

[36] SR Nandakumar, Shruti R Kulkarni, Anakha V Babu, and Bipin Rajendran. “Building brain-inspired computing systems: Examining the role of nanoscale devices”. In: *IEEE Nanotechnology Magazine* 12.3 (2018), pp. 19–35.

[37] Joseph S Najem, Graham J Taylor, Ryan J Weiss, Md Sakib Hasan, Garrett Rose, Catherine D Schuman, Alex Belianinov, C Patrick Collier, and Stephen A Sarles. “Memristive ion channel-doped biomembranes as synaptic mimics”. In: *ACS nano* 12.5 (2018), pp. 4702–4711.

[38] Raisul Islam, Haitong Li, Pai-Yu Chen, Weier Wan, Hong-Yu Chen, Bin Gao, Huaqiang Wu, Shimeng Yu, Krishna Saraswat, and HS Philip Wong. "Device and materials requirements for neuromorphic computing". In: *Journal of Physics D: Applied Physics* 52.11 (2019), p. 113001.

[39] Tae-Jun Ko, Hao Li, Sohrab Alex Mofid, Changhyeon Yoo, Emmanuel Okogbue, Sang Sub Han, Mashiyat Sumaiya Shawkat, Adithi Krishnaprasad, Molla Manjurul Islam, Durjoy Dev, et al. "Two-dimensional near-atom-thickness materials for emerging neuromorphic devices and applications". In: *IScience* 23.11 (2020).

[40] Leon Chua. "Memristor-the missing circuit element". In: *IEEE Transactions on circuit theory* 18.5 (1971), pp. 507–519.

[41] Sung Hyun Jo, Ting Chang, Idongesit Ebong, Bhavitavya B Bhadviya, Pinaki Mazumder, and Wei Lu. "Nanoscale memristor device as synapse in neuromorphic systems". In: *Nano letters* 10.4 (2010), pp. 1297–1301.

[42] Yibo Li, Zhongrui Wang, Rivu Midya, Qiangfei Xia, and J Joshua Yang. "Review of memristor devices in neuromorphic computing: materials sciences and device challenges". In: *Journal of Physics D: Applied Physics* 51.50 (2018), p. 503002.

[43] Han Bao, Houji Zhou, Jiancong Li, Huaizhi Pei, Jing Tian, Ling Yang, Shengguang Ren, Shaoqin Tong, Yi Li, Yuhui He, et al. "Toward memristive in-memory computing: principles and applications". In: *Frontiers of Optoelectronics* 15.1 (2022), p. 23.

[44] Dragan Damjanovic, Paul Muralt, and Nava Setter. "Ferroelectric sensors". In: *IEEE sensors journal* 1.3 (2001), pp. 191–206.

[45] P Muralt. "Ferroelectric thin films for micro-sensors and actuators: a review". In: *Journal of micromechanics and microengineering* 10.2 (2000), p. 136.

[46] James F Scott and Carlos A Paz de Araujo. "Ferroelectric memories". In: *Science* 246.4936 (1989), pp. 1400–1405.

[47] T Mikolajick, U Schroeder, and S Slesazeck. "The past, the present, and the future of ferroelectric memories". In: *IEEE Transactions on Electron Devices* 67.4 (2020), pp. 1434–1443.

[48] Junjun Li, Jason Claude, Luis Enrique Norena-Franco, Sang Il Seok, and Qing Wang. "Electrical energy storage in ferroelectric polymer nanocomposites containing surface-functionalized BaTiO3 nanoparticles". In: *Chemistry of Materials* 20.20 (2008), pp. 6304–6306.

[49] Michael Hoffmann, Franz Paul Gustav Fengler, Benjamin Max, Uwe Schroeder, Stefan Slesazeck, and Thomas Mikolajick. "Negative capacitance for electrostatic supercapacitors". In: *Advanced Energy Materials* 9.40 (2019), p. 1901154.

[50] Joseph Valasek. "Piezo-electric and allied phenomena in Rochelle salt". In: *Physical review* 17.4 (1921), p. 475.

[51] Yuhuan Xu. *Ferroelectric materials and their applications*. Elsevier, 2013.

[52] Carlotta Gastaldi. *Exploring negative capacitance and neuromorphic devices based on CMOS-compatible ferroelectric HfO2*. Tech. rep. EPFL, 2022.

[53] Karin M Rabe, Charles H Ahn, and Jean-Marc Triscone. *Physics of ferroelectrics: a modern perspective*. Vol. 105. Springer Science & Business Media, 2007.

[54] EL Pradeesh, S Udhayakumar, MG Vasundhara, and GK Kalavathi. “A review on piezoelectric energy harvesting”. In: *Microsystem Technologies* 28.8 (2022), pp. 1797–1830.

[55] Gene H Haertling. “Ferroelectric ceramics: history and technology”. In: *Journal of the American Ceramic Society* 82.4 (1999), pp. 797–818.

[56] N Izyumskaya, Ya Alivov, and H Morkoç. “Oxides, oxides, and more oxides: high-κ oxides, ferroelectrics, ferromagnetics, and multiferroics”. In: *Critical Reviews in Solid State and Materials Sciences* 34.3-4 (2009), pp. 89–179.

[57] Zuo-Guang Ye. *Handbook of advanced dielectric, piezoelectric and ferroelectric materials: Synthesis, properties and applications*. Elsevier, 2008.

[58] TS Böscke, J Müller, D Bräuhaus, U Schröder, and UJAPL Böttger. “Ferroelectricity in hafnium oxide thin films”. In: *Applied Physics Letters* 99.10 (2011).

[59] Jill Guyonnet and Jill Guyonnet. “Domain walls in ferroelectric materials”. In: *Ferroelectric Domain Walls: Statics, Dynamics, and Functionalities Revealed by Atomic Force Microscopy* (2014), pp. 7–24.

[60] Alexander Kirillovich Tagantsev, L Eric Cross, and Jan Fousek. *Domains in ferroic crystals and thin films*. Vol. 13. Springer, 2010.

[61] Kullaiah Byrappa and Tadashi Ohachi. *Crystal growth technology*. Elsevier, 2003.

[62] N Setter, D Damjanovic, L Eng, G Fox, Spartak Gevorgian, S Hong, A Kingon, H Kohlstedt, NY Park, GB Stephenson, et al. “Ferroelectric thin films: Review of materials, properties, and applications”. In: *Journal of applied physics* 100.5 (2006).

[63] Donald M Evans, Vincent Garcia, Dennis Meier, and Manuel Bibes. “Domains and domain walls in multiferroics”. In: *Physical Sciences Reviews* 5.9 (2020).

[64] Martin F Sarott, Ursina Bucheli, Adrian Lochmann, Manfred Fiebig, and Morgan Trassin. “Controlling the polarization in ferroelectric PZT films via the epitaxial growth conditions”. In: *Advanced Functional Materials* 33.28 (2023), p. 2214849.

[65] V Nagarajan, A Roytburd, A Stanishevsky, S Prasertchoung, T Zhao, L-Q Chen, J Melngailis, O Auciello, and R Ramesh. “Dynamics of ferroelastic domains in ferroelectric thin films”. In: *Nature materials* 2.1 (2003), pp. 43–47.

[66] Florin Zavaliche, P Shafer, R Ramesh, MP Cruz, RR Das, DM Kim, and CB Eom. “Polarization switching in epitaxial BiFeO3 films”. In: *Applied physics letters* 87.25 (2005).

[67] GF Nataf, Mael Guennou, JM Gregg, D Meier, J Hlinka, EKH Salje, and Jens Kreisel. “Domain-wall engineering and topological defects in ferroelectric and ferroelastic materials”. In: *Nature Reviews Physics* 2.11 (2020), pp. 634–648.

[68] J Mannhar and A Herrnberger. “The interface is still the device”. In: *Nat. Mater* 11.2 (2012), p. 91.

[69] Herbert Kroemer. “Nobel Lecture: Quasielectric fields and band offsets: teaching electrons new tricks”. In: *Reviews of modern physics* 73.3 (2001), p. 783.

[70] Pavlo Zubko, Stefano Gariglio, Marc Gabay, Philippe Ghosez, and Jean-Marc Triscone. “Interface physics in complex oxide heterostructures”. In: *Annu. Rev. Condens. Matter Phys.* 2.1 (2011), pp. 141–165.

[71] CW Bark, DA Felker, Yong Wang, Y Zhang, HW Jang, CM Folkman, JW Park, SH Baek, H Zhou, DD Fong, et al. “Tailoring a two-dimensional electron gas at the LaAlO3/SrTiO3 (001) interface by epitaxial strain”. In: *Proceedings of the National Academy of Sciences* 108.12 (2011), pp. 4720–4724.

[72] Jan Seidel, Lane W Martin, Qili He, Q Zhan, Y-H Chu, A Rother, ME Hawkridge, Peter Maksymovych, P Yu, Martin Gajek, et al. “Conduction at domain walls in oxide multiferroics”. In: *Nature materials* 8.3 (2009), pp. 229–234.

[73] Dennis Meier and Sverre M Selbach. “Ferroelectric domain walls for nanotechnology”. In: *Nature Reviews Materials* 7.3 (2022), pp. 157–173.

[74] Gustau Catalan, J Seidel, Ramamoorthy Ramesh, and James F Scott. “Domain wall nanoelectronics”. In: *Reviews of Modern Physics* 84.1 (2012), p. 119.

[75] BM Vul, GM Guro, and II Ivanchik. “Encountering domains in ferroelectrics”. In: *Ferroelectrics* 6.1 (1973), pp. 29–31.

[76] Tomas Sluka, Alexander K Tagantsev, Petr Bednyakov, and Nava Setter. “Free-electron gas at charged domain walls in insulating BaTiO3”. In: *Nature communications* 4.1 (2013), p. 1808.

[77] Mathias Schröder, Alexander Haußmann, Andreas Thiessen, Elisabeth Soergel, Theo Woike, and Lukas M Eng. “Conducting domain walls in lithium niobate single crystals”. In: *Advanced functional materials* 22.18 (2012), pp. 3936–3944.

[78] Christoph S Werner, Simon J Herr, Karsten Buse, Boris Sturman, Elisabeth Soergel, Cina Razzaghi, and Ingo Breunig. “Large and accessible conductivity of charged domain walls in lithium niobate”. In: *Scientific Reports* 7.1 (2017), p. 9862.

[79] Jill Guyonnet, Iaroslav Gaponenko, Stefano Gariglio, and Patrycja Paruch. “Conduction at domain walls in insulating Pb (Zr _{0.2} Ti _{0.8}) O _3 thin films”. In: *arXiv preprint arXiv:1205.0164* (2012).

[80] Peter Maksymovych, Anna N Morozovska, Pu Yu, Eugene A Eliseev, Ying-Hao Chu, Ramamoorthy Ramesh, Arthur P Baddorf, and Sergei V Kalinin. “Tunable metallic conductance in ferroelectric nanodomains”. In: *Nano letters* 12.1 (2012), pp. 209–213.

[81] Saeedeh Farokhipoor and Beatriz Noheda. “Conduction through 71 domain walls in BiFeO 3 thin films”. In: *Physical Review Letters* 107.12 (2011), p. 127601.

[82] Yi Zhang, Haidong Lu, Xingxu Yan, Xiaoxing Cheng, Lin Xie, Toshihiro Aoki, Linze Li, Colin Heikes, Shu Ping Lau, Darrell G Schlom, et al. "Intrinsic conductance of domain walls in BiFeO3". In: *Advanced Materials* 31.36 (2019), p. 1902099.

[83] Peter Maksymovych, Jan Seidel, Ying Hao Chu, Pingping Wu, Arthur P Baddorf, Long-Qing Chen, Sergei V Kalinin, and Ramamoorthy Ramesh. "Dynamic conductivity of ferroelectric domain walls in BiFeO3". In: *Nano letters* 11.5 (2011), pp. 1906–1912.

[84] Dennis Meier, Jan Seidel, Andres Cano, Kris Delaney, Yu Kumagai, Maxim Mostovoy, Nicola A Spaldin, Ramamoorthy Ramesh, and Manfred Fiebig. "Anisotropic conductance at improper ferroelectric domain walls". In: *Nature materials* 11.4 (2012), pp. 284–288.

[85] Yi Du, XL Wang, DP Chen, SX Dou, ZX Cheng, M Higgins, G Wallace, and JY Wang. "Domain wall conductivity in oxygen deficient multiferroic YMnO3 single crystals". In: *Applied Physics Letters* 99.25 (2011).

[86] Weida Wu, Yoichi Horibe, Nara Lee, S-W Cheong, and JR Guest. "Conduction of topologically protected charged ferroelectric domain walls". In: *Physical review letters* 108.7 (2012), p. 077203.

[87] Raymond GP McQuaid, Michael P Campbell, Roger W Whatmore, Amit Kumar, and J Marty Gregg. "Injection and controlled motion of conducting domain walls in improper ferroelectric Cu-Cl boracite". In: *Nature Communications* 8.1 (2017), p. 15105.

[88] Somnath Ghara, Korbinian Geirhos, Lukas Kuerten, Peter Lunkenheimer, Vladimir Tsurkan, Manfred Fiebig, and Istvan Kézsmárki. "Giant conductivity of mobile non-oxide domain walls". In: *Nature Communications* 12.1 (2021), p. 3975.

[89] Petr S Bednyakov, Boris I Sturman, Tomas Sluka, Alexander K Tagantsev, and Petr V Yudin. "Physics and applications of charged domain walls". In: *npj Computational Materials* 4.1 (2018), p. 65.

[90] Mingfeng Chen, Jing Wang, Ruixue Zhu, Yuanwei Sun, Qinghua Zhang, Ji Ma, Yue Wang, Lin Gu, Peng Gao, Jing Ma, et al. "Stabilization of ferroelastic charged domain walls in self-assembled BiFeO3 nanoislands". In: *Journal of Applied Physics* 128.12 (2020).

[91] Didrik Rene Småbråten, Theodor Secanell Holstad, Donald M Evans, Z Yan, Edith Bourret, Dennis Meier, and Sverre Magnus Selbach. "Domain wall mobility and roughening in doped ferroelectric hexagonal manganites". In: *Physical Review Research* 2.3 (2020), p. 033159.

[92] Chun-Lin Jia, Knut W Urban, Marin Alexe, Dietrich Hesse, and Ionela Vrejoiu. "Direct observation of continuous electric dipole rotation in flux-closure domains in ferroelectric Pb (Zr, Ti) O3". In: *Science* 331.6023 (2011), pp. 1420–1423.

[93] I Stolichnov, M Iwanowska, E Colla, B Ziegler, I Gaponenko, P Paruch, Mark Huijben, G Rijnders, and N Setter. "Persistent conductive footprints of 109 domain walls in bismuth ferrite films". In: *Applied Physics Letters* 104.13 (2014).

[94] Igor Stolichnov, Ludwig Feigl, Leo J McGilly, Tomas Sluka, Xian-Kui Wei, Enrico Colla, Arnaud Crassous, Konstantin Shapovalov, Petr Yudin, Alexander K Tagantsev, et al. "Bent ferroelectric domain walls as reconfigurable metallic-like channels". In: *Nano Letters* 15.12 (2015), pp. 8049–8055.

[95] Arnaud Crassous, Tomas Sluka, Alexander K Tagantsev, and Nava Setter. "Polarization charge as a reconfigurable quasi-dopant in ferroelectric thin films". In: *Nature nanotechnology* 10.7 (2015), pp. 614–618.

[96] S Farokhipoor and B Noheda. "Local conductivity and the role of vacancies around twin walls of (001)- BiFeO3 thin films". In: *Journal of Applied Physics* 112.5 (2012).

[97] Jan Seidel, Petro Maksymovych, Y Batra, A Katan, S-Y Yang, Qiwei He, Arthur P Baddorf, Sergei V Kalinin, C-H Yang, J-C Yang, et al. "Domain wall conductivity in La-doped BiFeO 3". In: *Physical review letters* 105.19 (2010), p. 197603.

[98] MP Campbell, JPV McConville, RGP McQuaid, D Prabhakaran, A Kumar, and JM Gregg. "Hall effect in charged conducting ferroelectric domain walls". In: *Nature Communications* 7.1 (2016), p. 13764.

[99] Patrick W Turner, James PV McConville, Shane J McCartan, Michael H Campbell, Jakob Schaab, Ray GP McQuaid, Amit Kumar, and J Marty Gregg. "Large carrier mobilities in ErMnO3 conducting domain walls revealed by quantitative hall-effect measurements". In: *Nano letters* 18.10 (2018), pp. 6381–6386.

[100] Henrik Beccard, Elke Beyreuther, Benjamin Kirbus, Samuel D Seddon, Michael Rüsing, and Lukas M Eng. "Hall mobilities and sheet carrier densities in a single Li Nb O 3 conductive ferroelectric domain wall". In: *Physical Review Applied* 20.6 (2023), p. 064043.

[101] Haidong Lu, Yueze Tan, James PV McConville, Zahra Ahmadi, Bo Wang, Michele Conroy, Kalani Moore, Ursel Bangert, Jeffrey E Shield, Long-Qing Chen, et al. "Electrical tunability of domain wall conductivity in LiNbO3 thin films". In: *Advanced Materials* 31.48 (2019), p. 1902890.

[102] Ahmet Suna, Conor Joseph McCluskey, Jesi Rit Maguire, Kristina Mary Holsgrove, Amit Kumar, Raymond Gerard Peter McQuaid, and John Marty Gregg. "Tuning Local Conductance to Enable Demonstrator Ferroelectric Domain Wall Diodes and Logic Gates". In: *Advanced Physics Research* 2.5 (2023), p. 2200095.

[103] Pankaj Sharma, Anna N Morozovska, Eugene A Eliseev, Qi Zhang, Daniel Sando, Nagarajan Valanoor, and Jan Seidel. "Specific Conductivity of a Ferroelectric Domain Wall". In: *ACS Applied Electronic Materials* 4.6 (2022), pp. 2739–2746.

[104] Dongfang Chen, Xiaojun Tan, Bowen Shen, and Jun Jiang. "Erasable Domain Wall Current-Dominated Resistive Switching in BiFeO3 Devices with an Oxide–Metal Interface". In: *ACS Applied Materials & Interfaces* 15.20 (2023), pp. 25041–25048.

[105] Pankaj Sharma, Daniel Sando, Qi Zhang, Xiaoxing Cheng, Sergey Prosandeev, Ralph Bulanadi, Sergei Prokhorenko, Laurent Bellaiche, Long-Qing Chen, Valanoor Nagarajan, et al. "Conformational domain wall switch". In: *Advanced Functional Materials* 29.18 (2019), p. 1807523.

[106] JR Whyte, RGP McQuaid, Chris M Ashcroft, JF Einsle, Carlota Canalias, Alexei Gruverman, and JM Gregg. "Sequential injection of domain walls into ferroelectrics at different bias voltages: Paving the way for "domain wall memristors"". In: *Journal of Applied Physics* 116.6 (2014).

[107] Jonathan R Whyte, Raymond GP McQuaid, Pankaj Sharma, Carlota Canalias, James F Scott, Alexei Gruverman, and J Marty Gregg. "Ferroelectric domain wall injection". In: *Advanced Materials* 26.2 (2014), pp. 293–298.

[108] Leo J McGilly, Ludwig Feigl, and Nava Setter. "Dynamics of ferroelectric 180 domain walls at engineered pinning centers". In: *Applied Physics Letters* 111.2 (2017).

[109] Leo J McGilly, Cosmin S Sandu, Ludwig Feigl, Dragan Damjanovic, and Nava Setter. "Nanoscale defect engineering and the resulting effects on domain wall dynamics in ferroelectric thin films". In: *Advanced Functional Materials* 27.15 (2017), p. 1605196.

[110] JR Whyte and JM Gregg. "A diode for ferroelectric domain-wall motion". In: *Nature Communications* 6.1 (2015), p. 7361.

[111] JH Franken, HJM Swagten, and Bert Koopmans. "Shift registers based on magnetic domain wall ratchets with perpendicular anisotropy". In: *Nature nanotechnology* 7.8 (2012), pp. 499–503.

[112] Haidong Lu, Bo Wang, Tao Li, Alexey Lipatov, Hyungwoo Lee, Anil Rajapitamahuni, Ruijuan Xu, Xia Hong, Saeedeh Farokhipoor, Lane W Martin, et al. "Nanodomain engineering in ferroelectric capacitors with graphene electrodes". In: *Nano letters* 16.10 (2016), pp. 6460–6466.

[113] Raymond GP McQuaid, Michael P Campbell, Roger W Whatmore, Amit Kumar, and J Marty Gregg. "Injection and controlled motion of conducting domain walls in improper ferroelectric Cu-Cl boracite". In: *Nature Communications* 8.1 (2017), p. 15105.

[114] Guoliang Yuan, Houbing Huang, Chen Li, Di Liu, Zhihao Cheng, and Di Wu. "Ferroelastic-Domain-Assisted Mechanical Switching of Ferroelectric Domains in Pb (Zr, Ti) O3 Thin Films". In: *Advanced Electronic Materials* 6.7 (2020), p. 2000300.

[115] Stuart SP Parkin, Masamitsu Hayashi, and Luc Thomas. "Magnetic domain-wall racetrack memory". In: *science* 320.5873 (2008), pp. 190–194.

[116] LJ McGilly, P Yudin, L Feigl, AK Tagantsev, and N Setter. "Controlling domain wall motion in ferroelectric thin films". In: *Nature nanotechnology* 10.2 (2015), pp. 145–150.

[117] LJ McGilly, L Feigl, T Sluka, P Yudin, AK Tagantsev, and N Setter. "Velocity control of 180 domain walls in ferroelectric thin films by electrode modification". In: *Nano letters* 16.1 (2016), pp. 68–73.

[118] Pankaj Sharma, Qi Zhang, Daniel Sando, Chi Hou Lei, Yunya Liu, Jiangyu Li, Valanoor Nagarajan, and Jan Seidel. “Nonvolatile ferroelectric domain wall memory”. In: *Science advances* 3.6 (2017), e1700512.

[119] Wenda Yang, Guo Tian, Hua Fan, Yue Zhao, Hongying Chen, Luyong Zhang, Yadong Wang, Zhen Fan, Zhipeng Hou, Deyang Chen, et al. “Nonvolatile ferroelectric-domain-wall memory embedded in a complex topological domain structure”. In: *Advanced Materials* 34.10 (2022), p. 2107711.

[120] Jing Wang, Jing Ma, Houbing Huang, Ji Ma, Hasnain Mehdi Jafri, Yuanyuan Fan, Huayu Yang, Yue Wang, Mingfeng Chen, Di Liu, et al. “Ferroelectric domain-wall logic units”. In: *Nature communications* 13.1 (2022), p. 3255.

[121] Ahmet Suna, OE Baxter, JPV McConville, Amit Kumar, RGP McQuaid, and JM Gregg. “Conducting ferroelectric domain walls emulating aspects of neurological behavior”. In: *Applied Physics Letters* 121.22 (2022).

[122] Jan L Rieck, Davide Cipollini, Mart Salverda, Cynthia P Quinteros, Lambert RB Schomaker, and Beatriz Noheda. “Ferroelastic domain walls in BiFeO3 as memristive networks”. In: *Advanced Intelligent Systems* 5.1 (2023), p. 2200292.

[123] Mantas Lukoševičius and Herbert Jaeger. “Reservoir computing approaches to recurrent neural network training”. In: *Computer science review* 3.3 (2009), pp. 127–149.

[124] An Quan Jiang, Wen Ping Geng, Peng Lv, Jia-wang Hong, Jun Jiang, Chao Wang, Xiao Jie Chai, Jian Wei Lian, Yan Zhang, Rong Huang, et al. “Ferroelectric domain wall memory with embedded selector realized in LiNbO3 single crystals integrated on Si wafers”. In: *Nature Materials* 19.11 (2020), pp. 1188–1194.

[125] Jie Sun, Yiming Li, Yangjun Ou, Qianwei Huang, Xiaozhou Liao, Zibin Chen, Xiaojie Chai, Xiao Zhuang, Wendi Zhang, Chao Wang, et al. “In-Memory Computing of Multi-level Ferroelectric Domain Wall Diodes at LiNbO3 Interfaces”. In: *Advanced Functional Materials* 32.49 (2022), p. 2207418.

[126] Jun Jiang, Xiaojie Chai, Chao Wang, and Anquan Jiang. “High temperature ferroelectric domain wall memory”. In: *Journal of Alloys and Compounds* 856 (2021), p. 158155.

[127] Jesi R Maguire, Conor J McCluskey, Kristina M Holsgrove, Ahmet Suna, Amit Kumar, Raymond GP McQuaid, and J Marty Gregg. “Ferroelectric Domain Wall p-n Junctions”. In: *Nano Letters* 23.22 (2023), pp. 10360–10366.

[128] Zhongran Liu, Han Wang, Ming Li, Lingling Tao, Tula R Paudel, Hongyang Yu, Yuxuan Wang, Siyuan Hong, Meng Zhang, Zhaohui Ren, et al. “In-plane charged domain walls with memristive behaviour in a ferroelectric film”. In: *Nature* 613.7945 (2023), pp. 656–661.

[129] Linze Li, Jason Britson, Jacob R Jokisaari, Yi Zhang, Carolina Adamo, Alexander Melville, Darrell G Schlom, Long-Qing Chen, and Xiaoqing Pan. “Giant resistive switching via control of ferroelectric charged domain walls”. In: *Advanced Materials* 28.31 (2016), pp. 6574–6580.

[130] P Chaudhary, Haidong Lu, A Lipatov, Z Ahmadi, JPV McConville, A Sokolov, JE Shield, A Sinitskii, JM Gregg, and Alexei Gruverman. “Low-voltage domain-wall LiNbO3 memristors”. In: *Nano Letters* 20.8 (2020), pp. 5873–5878.

[131] James PV McConville, Haidong Lu, Bo Wang, Yueze Tan, Charlotte Cochard, Michele Conroy, Kalani Moore, Alan Harvey, Ursel Bangert, Long-Qing Chen, et al. “Ferroelectric domain wall memristor”. In: *Advanced functional materials* 30.28 (2020), p. 2000109.

[132] LE Cross and RE Newnham. “History of ferroelectrics”. In: *Ceramics and civilization* 3 (1987), pp. 289–305.

[133] Gen Shirane, Kazuo Suzuki, and Akitsu Takeda. “Phase transitions in solid solutions of PbZrO3 and PbTiO3 (II) X-ray study”. In: *Journal of the Physical Society of Japan* 7.1 (1952), pp. 12–18.

[134] Manjusha Eledath and Maneesh Chandran. “Status review of the science and technology of PZT/diamond heterostructures and their applications”. In: *Journal of Materials Research* 36.23 (2021), pp. 4725–4745.

[135] B Noheda, DE Cox, G Shirane, JA Gonzalo, LE Cross, and SE Park. “A monoclinic ferroelectric phase in the Pb (Zr 1- x Ti x) O 3 solid solution”. In: *Applied physics letters* 74.14 (1999), pp. 2059–2061.

[136] N Zhang, H Yokota, Anthony Michael Glazer, Z Ren, DA Keen, Dean Samuel Keeble, Pam A Thomas, and Z-G Ye. “The missing boundary in the phase diagram of PbZr1-xTixO3”. In: *Nature communications* 5.1 (2014), p. 5231.

[137] B Jaffe, W Cook, and H Jaffe. “Piezoelectric Ceramics London: Academic”. In: (1971).

[138] Ching-Chang Chung. “Microstructural evolution in lead zirconate titanate (PZT) piezoelectric ceramics”. In: (2014).

[139] RE Jones Jr, PD Maniar, R Moazzami, P Zurcher, JZ Witowski, YT Lii, P Chu, and SJ Gillespie. “Ferroelectric non-volatile memories for low-voltage, low-power applications”. In: *Thin Solid Films* 270.1-2 (1995), pp. 584–588.

[140] Dave HA Blank, Matthijn Dekkers, and Guus Rijnders. “Pulsed laser deposition in Twente: from research tool towards industrial deposition”. In: *Journal of physics D: applied physics* 47.3 (2013), p. 034006.

[141] R Uecker, B Velickov, D Klimm, R Bertram, M Bernhagen, M Rabe, M Albrecht, Roberto Fornari, and DG Schlom. “Properties of rare-earth scandate single crystals (Re= Nd-Dy)”. In: *Journal of Crystal Growth* 310.10 (2008), pp. 2649–2658.

[142] I Gaponenko, P Tückmantel, J Karthik, LW Martin, and P Paruch. “Towards reversible control of domain wall conduction in Pb (Zr0. 2Ti0. 8) O3 thin films”. In: *Applied Physics Letters* 106.16 (2015).

[143] Ludwig Feigl, Petr Yudin, Igor Stolichnov, Tomas Sluka, Konstantin Shapovalov, Mahamudu Mtebwa, Cosmin S Sandu, Xian-Kui Wei, Alexander K Tagantsev, and Nava Setter. “Controlled stripes of ultrafine ferroelectric domains”. In: *Nature communications* 5.1 (2014), p. 4677.

[144] Bert Voigtländer. *Atomic force microscopy*. Springer, 2019.

[145] Ronald G Reifenberger. *Fundamentals of atomic force microscopy: part I: foundations*. World Scientific Publishing Company Pte Limited Singapore, 2016.

[146] Graham K Hubler. “Pulsed laser deposition”. In: *Mrs Bulletin* 17.2 (1992), pp. 26–29.

[147] Michael J Aziz. “Film growth mechanisms in pulsed laser deposition”. In: *Applied Physics A* 93 (2008), pp. 579–587.

[148] T Thundat, X-Y Zheng, GY Chen, and RJ Warmack. “Role of relative humidity in atomic force microscopy imaging”. In: *Surface Science Letters* 294.1-2 (1993), pp. L939–L943.

[149] Lidia Aguilera, Wouter Polspoel, Alexander Volodin, Christian Van Haesendonck, Marc Porti, Wilfried Vandervorst, Montserrat Nafria, and Xavier Aymerich. “Influence of vacuum environment on conductive atomic force microscopy measurements of advanced metal-oxide-semiconductor gate dielectrics”. In: *Journal of Vacuum Science & Technology B: Microelectronics and Nanometer Structures Processing, Measurement, and Phenomena* 26.4 (2008), pp. 1445–1449.

[150] Solmates. *Operation and Maintenance Manual SMP series*. 3rd edition from 26-Jan-2018. (2018).

[151] Guus JHM Rijnders, Gertjan Koster, Dave HA Blank, and Horst Rogalla. “In-situ growth monitoring during PLD of oxides using RHEED at high oxygen pressure”. In: *Materials Science and Engineering: B* 56.2-3 (1998), pp. 223–227.

[152] Panagiotis Koutsogiannis, Felix Risch, José A. Pardo, Igor Stolichnov, and César Magén. “Atomic-scale characterization of 180° conductive domain walls in Pb(Zr,Ti)O3”. In: *ACS Applied Materials & Interfaces* (Manuscript submitted).

[153] Magnus Nord, Per Erik Vullum, Ian MacLaren, Thomas Tybell, and Randi Holmestad. “Atomap: a new software tool for the automated analysis of atomic resolution images using two-dimensional Gaussian fitting”. In: *Advanced structural and chemical imaging* 3 (2017), pp. 1–12.

[154] E.M. Eoghan O’Connell and Micheal Hennessy. *PinkShnack/TEMUL: Initial Temul-Toolkit Release (Version 0.1.1). Zenodo*. Tech. rep. 2021.

[155] Gertjan Koster, Mark Huijben, and Guus Rijnders. *Epitaxial growth of complex metal oxides*. Elsevier, 2015.

[156] Anoop R Damodaran, Joshua C Agar, Shishir Pandya, Zuhuang Chen, Liv Dedon, Ruijuan Xu, Brent Apgar, Sahar Saremi, and Lane W Martin. “New modalities of strain-control of ferroelectric thin films”. In: *Journal of Physics: Condensed Matter* 28.26 (2016), p. 263001.

[157] Enrique Zanardi, Silvana Radescu, Andrés Mujica, Plácida Rodrıguez-Hernández, and Alfonso Muñoz. “Ab Initio Theoretical Study of DyScO3 at High Pressure”. In: *Crystals* 13.2 (2023), p. 165.

[158] AHG Vlooswijk, Beatriz Noheda, G Catalan, A Janssens, B Barcones, G Rijnders, DHA Blank, S Venkatesan, B Kooi, and JTM De Hosson. “Smallest 90 domains in epitaxial ferroelectric films”. In: *Applied physics letters* 91.11 (2007).

[159] Xian-Kui Wei, Tomas Sluka, Barbara Fraygola, Ludwig Feigl, Hongchu Du, Lei Jin, Chun-Lin Jia, and Nava Setter. “Controlled charging of ferroelastic domain walls in oxide ferroelectrics”. In: *ACS applied materials & interfaces* 9.7 (2017), pp. 6539–6546.

[160] Masashi Kawasaki, Kazuhiro Takahashi, Tatsuro Maeda, Ryuta Tsuchiya, Makoto Shinohara, Osamu Ishiyama, Takuzo Yonezawa, Mamoru Yoshimoto, and Hideomi Koinuma. “Atomic control of the SrTiO3 crystal surface”. In: *Science* 266.5190 (1994), pp. 1540–1542.

[161] Alim Solmaz, Mark Huijben, Gertjan Koster, Ricardo Egoavil, Nicolas Gauquelin, Gustaaf Van Tendeloo, Jo Verbeeck, Beatriz Noheda, and Guus Rijnders. “Domain selectivity in BiFeO3 thin films by modified substrate termination”. In: *Advanced Functional Materials* 26.17 (2016), pp. 2882–2889.

[162] R Egoavil, H Tan, J Verbeeck, S Bals, B Smith, Bouwe Kuiper, G Rijnders, Gertjan Koster, and G Van Tendeloo. “Atomic scale investigation of a PbTiO3/SrRuO3/DyScO3 heterostructure”. In: *Applied physics letters* 102.22 (2013).

[163] Josée E Kleibeuker, Gertjan Koster, Wolter Siemons, David Dubbink, Bouwe Kuiper, Jeroen L Blok, Chan-Ho Yang, Jayakanth Ravichandran, Ramamoorthy Ramesh, Johan E Ten Elshof, et al. “Atomically Defined Rare-Earth Scandate Crystal Surfaces”. In: *Advanced functional materials* 20.20 (2010), pp. 3490–3496.

[164] Wolfgang Braun, Maren Jäger, Gennadii Laskin, Prosper Ngabonziza, Wolfgang Voesch, Pascal Wittlich, and Jochen Mannhart. “In situ thermal preparation of oxide surfaces”. In: *APL Materials* 8.7 (2020).

[165] JE Kleibeuker, Bouwe Kuiper, S Harkema, Dave HA Blank, Gertjan Koster, Guus Rijnders, P Tinnemans, E Vlieg, PB Rossen, Wolter Siemons, et al. “Structure of singly terminated polar DyScO 3 (110) surfaces”. In: *Physical Review B* 85.16 (2012), p. 165413.

[166] Tom Kuech. *Handbook of Crystal Growth: Thin Films and Epitaxy*. Elsevier, 2014.

[167] H Schraknepper, C Bäumer, F Gunkel, R Dittmann, and RA De Souza. “Pulsed laser deposition of SrRuO3 thin-films: The role of the pulse repetition rate”. In: *APL materials* 4.12 (2016).

[168] D Rubi, AHG Vlooswijk, and Beatriz Noheda. “Growth of flat SrRuO3 (111) thin films suitable as bottom electrodes in heterostructures”. In: *Thin solid films* 517.6 (2009), pp. 1904–1907.

[169] Arvind Baskaran and Peter Smereka. “Mechanisms of stranski-krastanov growth”. In: *Journal of Applied Physics* 111.4 (2012).

[170] Shu Ni, Evert Houwman, Nicolas Gauquelin, Dmitry Chezganov, Sandra Van Aert, Johan Verbeeck, Guus Rijnders, and Gertjan Koster. “Stabilizing Perovskite Pb (Mg0. 33Nb0. 67) O3–PbTiO3 Thin Films by Fast Deposition and Tensile Mismatched Growth Template”. In: *ACS Applied Materials & Interfaces* (2024).

[171] Linda Aissani, Akram Alhussein, Abdul Wasy Zia, Gcina Mamba, and Sami Rtimi. “Magnetron sputtering of transition metal nitride thin films for environmental remediation”. In: *Coatings* 12.11 (2022), p. 1746.

[172] Anoop R Damodaran, Shishir Pandya, Josh C Agar, Ye Cao, Rama K Vasudevan, Ruijuan Xu, Sahar Saremi, Qian Li, Jieun Kim, Margaret R McCarter, et al. “Three-state ferroelastic switching and large electromechanical responses in PbTiO3 thin films”. In: *Advanced materials* 29.37 (2017), p. 1702069.

[173] O Nesterov, Sylvia Matzen, César Magén, AHG Vlooswijk, Gustau Catalán, and Beatriz Noheda. “Thickness scaling of ferroelastic domains in PbTiO3 films on DyScO3”. In: *Applied Physics Letters* 103.14 (2013).

[174] André Chanthbouala, Vincent Garcia, Ryan O Cherifi, Karim Bouzehouane, Stéphane Fusil, Xavier Moya, Stéphane Xavier, Hiroyuki Yamada, Cyrile Deranlot, Neil D Mathur, et al. “A ferroelectric memristor”. In: *Nature materials* 11.10 (2012), pp. 860–864.

[175] Felix Risch, Yuri Tikhonov, Igor Lukyanchuk, Adrian M Ionescu, and Igor Stolichnov. “Giant switchable non thermally-activated conduction in 180° domain walls in tetragonal Pb (Zr, Ti) O3”. In: *Nature Communications* 13.1 (2022), p. 7239.

[176] Felix Risch, Panagiotis Koutsogiannis, Yuri Tikhonov, César Magén, José A. Pardo, Igor Lukyanchuk, Adrian M Ionescu, and Igor Stolichnov. “Non-volatile Domain-by-Domain Switchable Multistate Ferroelectric Memristor”. In: (Manuscript in preparation).

[177] Peter Maksymovych, Stephen Jesse, Pu Yu, Ramamoorthy Ramesh, Arthur P Baddorf, and Sergei V Kalinin. “Polarization control of electron tunneling into ferroelectric surfaces”. In: *Science* 324.5933 (2009), pp. 1421–1425.

[178] M Molotskii. “Generation of ferroelectric domains in atomic force microscope”. In: *Journal of applied physics* 93.10 (2003), pp. 6234–6237.

[179] Samuel D Bader and Stuart Stephen Papworth Parkin. “Spintronics”. In: *Annu. Rev. Condens. Matter Phys.* 1.1 (2010), pp. 71–88.

[180] SM Hosseini, Tayebeh Movlarooy, and Ahmad Kompany. “First-principles study of the optical properties of PbTiO 3”. In: *The European Physical Journal B-Condensed Matter and Complex Systems* 46 (2005), pp. 463–469.

[181] Felix Risch, Ali Gilani, Sadegh Kamaei, Adrian M Ionescu, and Igor Stolichnov. “Graphene-enhanced Ferroelectric Domain Wall High-Output Memristor”. In: *Applied physics letters* (Manuscript under Review).

[182] Hua Fan, Zhengwei Tan, Haoyang Liu, Luyong Zhang, Fengyuan Zhang, Wanshun Du, Zhen Fan, Xingsen Gao, Feng Pan, Dapeng Yu, et al. “Enhanced ferroelectric and piezoelectric properties in graphene-electroded Pb (Zr, Ti) O3 thin films”. In: *ACS Applied Materials & Interfaces* 14.15 (2022), pp. 17987–17994.

[183] Haidong Lu, Alexey Lipatov, Sangjin Ryu, DJ Kim, H Lee, M Ye Zhuravlev, Chang-Beom Eom, Evgeny Y Tsymbal, Alexander Sinitskii, and Alexei Gruverman. “Ferroelectric tunnel junctions with graphene electrodes”. In: *Nature communications* 5.1 (2014), p. 5518.

[184] Alexey Lipatov, Alexandra Fursina, Timothy H Vo, Pankaj Sharma, Alexei Gruverman, and Alexander Sinitskii. “Polarization-Dependent Electronic Transport in Graphene/Pb (Zr, Ti) O3 Ferroelectric Field-Effect Transistors”. In: *Advanced Electronic Materials* 3.7 (2017), p. 1700020.

[185] Willem F Van Dorp, Bob Van Someren, Cornelis W Hagen, Pieter Kruit, and Peter A Crozier. “Approaching the resolution limit of nanometer-scale electron beam-induced deposition”. In: *Nano letters* 5.7 (2005), pp. 1303–1307.

[186] A Botman, JJL Mulders, R Weemaes, and S Mentink. “Purification of platinum and gold structures after electron-beam-induced deposition”. In: *Nanotechnology* 17.15 (2006), p. 3779.

[187] Byeong-Seon An, Yena Kwon, Jin-Su Oh, Yeon-Ju Shin, Jae-seon Ju, and Cheol-Woong Yang. “Evaluation of ion/electron beam induced deposition for electrical connection using a modern focused ion beam system”. In: *Applied Microscopy* 49.1 (2019), pp. 1–5.

Publications

F. Risch, Y. Tikhonov, I. Lukyanchuk, A. M. Ionescu, and I. Stolichnov. "Giant switchable non thermally-activated conduction in 180° domain walls in tetragonal Pb (Zr, Ti) O3." In: Nature Communications 13.1 (2022), pp. 7239.

F. Risch, A. Gilani, S. Kamaei, A. M. Ionescu, and I. Stolichnov. "Graphene-enhanced Ferroelectric Domain Wall High-Output Memristor." In: Applied Physics Letters (under Review).

F. Risch, P. Koutsogiannis, Y. Tikhonov, C. Magén, J. A. Pardo, I. Lukyanchuk, A. M. Ionescu, and I. Stolichnov. "Non-volatile Domain-by-Domain Switchable Multistate Ferroelectric Memristor." Manuscript in preparation.

P. Koutsogiannis, **F. Risch**, J. A. Pardo, I. Stolichnov, and C. Magén. "Atomic-scale characterization of 180° conductive domain walls in Pb(Zr,Ti)O3." Manuscript submitted to ACS Applied Materials & Interfaces.

L. Capua, Y. Sprunger, H. Elettro, **F. Risch**, A. Grammoustianou, R. Midahuen, T. Ernst, S. Barraud, R. Gill, and A. M. Ionescu. "Label-free C-reactive protein Si nanowire FET sensor arrays with super-Nernstian back-gate operation." In: IEEE Transactions on Electron Devices 69.4 (2022), pp. 2159-2165.

A. Grammoustianou, A. Saeidi, J. Longo, **F. Risch**, and A. M. Ionescu. "Real-time detection of C-reactive protein in interstitial fluid using electrochemical impedance spectroscopy – towards wearable health monitoring." Manuscript submitted to ACS Sensors.